COMBINING ELECTROCALORIC AND MAGNETOCALORIC EFFECTS IN SINGLE-PHASE MULTIFERROICS

Uroš Prah

Doctoral Dissertation
Jožef Stefan International Postgraduate School
Ljubljana, Slovenia

Supervisor: Asst. Prof. Dr. Hana Uršič Nemevšek, Jožef Stefan Institute, Ljubljana, Slovenia
Co-Supervisor: Assoc. Prof. Dr. Tadej Rojac, Jožef Stefan Institute, Ljubljana, Slovenia

Evaluation Board:
Asst. Prof. Dr. Brigita Rožič, Chair, Jožef Stefan Institute, Ljubljana, Slovenia
Asst. Prof. Dr. Jaka Tušek, Member, Faculty of Mechanical Engineering, University of Ljubljana, Ljubljana, Slovenia
Dr. Emmanuel Defay, Member, Luxembourg Institute of Science and Technology, Luxembourg City, Luxembourg

MEDNARODNA PODIPLOMSKA ŠOLA JOŽEFA STEFANA
JOŽEF STEFAN INTERNATIONAL POSTGRADUATE SCHOOL



Uroš Prah

COMBINING ELECTROCALORIC AND MAGNETOCALORIC EFFECTS IN SINGLE-PHASE MULTIFERROICS

Doctoral Dissertation

KOMBINIRANI ELEKTROKALORIČNI IN MAGNETOKALORIČNI POJAVI V ENOFAZNIH MULTIFEROIKIH

Doktorska disertacija

Supervisor: Asst. Prof. Dr. Hana Uršič Nemevšek

Co-Supervisor: Assoc. Prof. Dr. Tadej Rojac

Ljubljana, Slovenia, October 2020

"Impossible only means that you haven't found the solution yet" – Anonymous

Acknowledgments

This work would not have been possible without the support of many people who helped me over the years.

First and foremost, I would like to express my deepest gratitude to my supervisor Asst. Prof. Dr. Hana Uršič Nemevšek for all her guidance, encouragement, patience, support, and extensive knowledge and countless ideas she has shared with me over the past 4 years. I can imagine that being my supervisor is sometimes quite a challenge, but she far exceeded all the duties of a PhD mentor. In addition, I would like to thank to my co-supervisor Assoc. Prof. Dr. Tadej Rojac for all his extensive knowledge and skills, numerous fruitful discussions, advice and ideas that have contributed significantly to my scientific work. I would also like to express my special thanks and gratitude to Prof. Dr. Barbara Malič for giving me the opportunity to work and study at the Electronic Ceramics Department (K5).

My special thanks go to all my friends and co-workers from the Electronic Ceramics Department at the Jožef Stefan Institute, especially to all former and current PhD students and young researchers who selflessly shared all their knowledge, skills, advice and at the same time made my PhD study easier and more pleasant. My thanks are extended to my first office-mate Marko, who together with our informal "electrocaloric subgroup" (Andraž, Lovro, Marko) and the indispensable Tanja were an exceptional support in all the ups and downs at the very beginning of my research career and their company was always the guarantee of a great atmosphere.

I highly appreciate the contribution of Assoc. Prof. Dr. Andreja Benčan Golob for the TEM analyses and all the support and discussions on all challenges related to electron microscopy, and dr. Magdalena Wencka from Institute of Molecular Physics, Polish Academy of Sciences for numerous magnetic and specific-heat-capacity measurements. Many thanks go to the incredible support of our technicians Brigita Kmet, Jena Cilenšek and Silvo Drnovšek, who made sure that my lab work went smoothly and without any problems. I would like to acknowledge Mr. Edi Kranjc from the Slovenian National Institute of Chemistry for the X-ray measurements, and finally all the Slovenian and foreign students who helped me with all kinds of laboratory work and measurements during these years.

I am also taking this opportunity to express my gratitude to the Slovenian Research Agency (young researcher project PR-07594, project *Multicaloric cooling* J2-9253, research core funding P2-0105), JECS Trust fund (Contract No. 2017137), joint research project between Polish Academy of Science and Slovenian Academy of Science and Art "*Multicaloric relaxor materials for new cooling technologies*," bilateral projects between Slovenia and United States of America (BI-US/19-21-062) and between Slovenia and Germany (BI-DE/19-20-010) for their financial support, and to the Centre of Excellence NAMASTE for enabling the use of laboratory equipment.

Most importantly, none of this would have been possible without the continuous support, motivation and inspiration of my family, who encouraged me to get outside my comfort zone. I will always be grateful to my brother Žiga, whose selfless daily support, perfectionism and hard work have been my greatest inspiration and motivation for pushing

boundaries and following my dreams. At the end, I would like to thank all my closest friends who occasionally dragged me away from work and the lab and showed me that life is not only about research.

Abstract

Solid-state refrigeration technology based on caloric effects represents a promising alternative for the replacement of the less energy efficient and environmentally problematic vapor-compression technology. Furthermore, it can be employed in fields where vapor-compression technology cannot be used, such as the cooling of small electronic devices and their components. There is considerable interest in the use of the electrocaloric (EC) and magnetocaloric (MC) effects, which are well-known and studied phenomena. In most cases, however, the individual caloric effects exhibit small cooling effects, with the highest values located in narrow temperature ranges, which limits their commercial use. An idea of how to solve this problem is to combine the EC and MC effects in the same multicaloric material and thus enhance the cooling performance and/or extend the operating temperature range of a cooling device.

In the first part of the thesis, single-phase $Pb(Fe_{0.5}Nb_{0.5})O_3$ (PFN) ceramics that combine EC and MC properties were successfully prepared by mechanochemical synthesis followed by sintering. The enhanced electrical conductivity was controlled with a careful optimization of the sintering conditions, resulting in the lowest value ($\sim 7 \cdot 10^{-12}\ \Omega^{-1}m^{-1}$) in a ceramic sintered at 1000 °C. In this sample, the maximum electrocaloric effect of ~0.9 °C at 28 °C and 100 $kV \cdot cm^{-1}$; and the maximum magnetocaloric effect of ~0.1 °C at −271 °C and 50 kOe were obtained. The EC as well as the MC properties of the PFN were further improved by doping with manganese. The addition of manganese successfully suppresses the excessive electrical conductivity at high temperatures, leading to superior EC effect of ~2.5 °C at 80 °C and 140 $kV \cdot cm^{-1}$. At the same time, the MC properties of the material were also improved, resulting in a maximum MC effect of ~0.4 °C at −271 °C and 50 kOe. Despite the promising room-temperature EC effect, the maximum value of the MC effect is still too small for practical usage.

In the second part, the ferroic properties of PFN were tailored by the addition of multiferroic $BiFeO_3$ (BFO). Seven single-phase PFN–100xBFO (x = 0–0.5) compositions were successfully prepared using mechanochemical synthesis followed by sintering. With a gradual increase in the BFO content, the temperature of the permittivity peak of the PFN–100xBFO solid solutions first decreased (reaching RT when $x = 0.2$), while at higher BFO contents ($x > 0.2$) it increased and reached ~200 °C in the PFN–50BFO. Introducing BFO into the PFN–100xBFO solid solution leads to the formation of a pseudocubic phase, consequently strengthening the relaxor behavior. This is accompanied by a broadening of the peak in the temperature-dependent permittivity, narrowing of ferroelectric P–E hysteresis loops and decreasing the size of the ferroelectric domains into polar nanoregions. Among the prepared compositions, PFN–20BFO exhibited low ferroelectric hysteresis losses and peak-permittivity near ambient temperature, making it a promising candidate for room-temperature multicaloric applications.

In the last part of this work, we focused on studying the multicaloric properties of PFN–BFO-based solid solutions. In PFN–20BFO, both the peak-permittivity anomaly as well as the paramagnetic-to-antiferromagnetic phase transition coincided at RT, making it one of the first such single-phase room-temperature multiferroic materials. Despite the

favorable room-temperature position of both ferroic anomalies, the excessive electrical conductivity and poor magnetic response of the material limit its EC and MC cooling capability. The further doping of PFN–20BFO with manganese and gadolinium ions successfully suppressed the excessive electrical conductivity and enhanced the magnetic response, leading to the improvement of the EC and MC properties. This results in a PFN–BFO composition with negligible Joule heating up to 75 °C, a room-temperature EC effect of more than 1 °C at 140 kV $\cdot$ cm^{-1}, a high MC effect above 3 °C at cryogenic temperatures and 50 kOe, and the highest room-temperature MC effect among all the prepared PFN-based multicalorics.

Povzetek

Tehnologija hlajenja na osnovi hladilnih elementov v trdnem stanju, ki izkazujejo kalorični učinek, predstavlja obetavno alternativo za zamenjavo energijsko manj učinkovite in okolju neprijazne parno-kompresijske tehnologije. Poleg tega se lahko uporablja na področjih, kjer parno-kompresijske tehnologije ni mogoče uporabiti, to je hlajenje majhnih elektronskih naprav in njihovih komponent. Med bolj razširjene ter dobro raziskane kalorične pojave uvrščamo elektrokalorični (EK) in magnetokalorični (MK) učinek, ki pa v večini primerov izkazujeta relativno nizke hladilne učinke. Poleg tega so njune maksimalne vrednosti omejene na ozka temperaturna območja, kar omejuje njihovo komercialno uporabo. Ena izmed rešitev tega problema je združitev EK in MK učinkov v istem multikaloričnemu materialu, kar lahko izboljša hladilno zmogljivost hladilne naprave oz. razširi njeno temperaturno območje delovanja.

V prvem sklopu doktorskega dela smo s pomočjo mehanokemijske sinteze in sledečim sintranjem uspešno pripravili enofazno $Pb(Fe_{0.5}Nb_{0.5})O_3$ (PFN) keramiko, ki združuje EK in MK lastnosti. Z optimizacijo pogojev sintranja smo znižali električno prevodnost materiala, ki doseže najnižjo vrednost ($\sim 7 \cdot 10^{-12}$ $\Omega^{-1}m^{-1}$) v keramiki, sintrani pri 1000 °C. V tem vzorcu je bila izmerjena najvišja vrednost EK učinka ~0,9 °C pri 28 °C in 100 kV $\cdot$ cm^{-1} ter dosežen največji magnetokalorični učinek ~0,1 °C pri −271 °C in 50 kOe. EK in MK lastnosti PFN keramike so bile nadalje izboljšane z dodatkom mangana. Dodatek mangana namreč uspešno zavira visoko električno prevodnost pri višjih temperaturah, kar vodi do dobrih EK lastnosti, ki dosežejo maksimalno vrednost EK učinka ~2,5 °C pri 80 °C in 140 kV $\cdot$ cm^{-1}. Hkrati se izboljšajo tudi MK lastnosti materiala, kar pripelje do višje maksimalne vrednosti MK učinka ~0,4 °C pri −271 °C in 50 kOe. Kljub obetavnemu EK učinku pripravljenega materiala so njegove najvišje vrednosti MK učinka še vedno premajhne za uporabo v hladilnih sistemih.

V drugem sklopu doktorskega dela smo spreminjali feroične lastnosti PFN keramike z dodatkom multiferoičnega $BiFeO_3$ (BFO). Z uporabo mehanokemijske sinteze, ki ji je sledilo sintranje, smo uspešno pripravili sedem enofaznih PFN–100xBFO ($x = 0$–0,5) trdnih raztopin. Ugotovili smo, da se s postopnim povečevanjem vsebnosti BFO temperatura vrha dielektrične konstante PFN–100xBFO trdnih raztopin najprej zniža (doseže sobno temperaturo pri $x = 0{,}2$), medtem ko se pri višjih vsebnostih dodanega BFO ($x > 0{,}2$) leta poviša ter doseže ~200 °C v PFN–50BFO. Uvajanje BFO v PFN–100xBFO trdno raztopino vodi do tvorbe psevdokubične faze in okrepi relaksorski značaj pripravljenih materialov. To je bilo razvidno iz širitve vrhov temperaturne odvisnosti dielektrične konstante, zožitve feroelektričnih P–E histereznih zank ter zmanjšanja velikosti feroelektričnih domen v nano-področja. Med pripravljenimi sestavami PFN–20BFO izkazuje nizke feroelektrične histerezne izgube in vrh dielektrične konstante v bližini sobne temperature, kar ga uvršča med obetavne kandidate za multikaloрično hlajenje pri sobni temperaturi.

V zadnjem sklopu doktorskega dela smo proučevali multikalorične lastnosti trdnih raztopin na osnovi PFN–BFO. V PFN–20BFO se temperatura, pri kateri se nahaja vrh dielektrične konstante, kot tudi temperatura paramagnetnega-antiferomagnetnega faznega

prehoda nahajata v bližini sobne temperature, kar ga uvršča med prve tovrstne enofazne multiferoične materiale. Kljub ugodnemu položaju obeh feroičnih anomalij v bližini sobne temperature povišana električna prevodnost ter šibek magnetni odziv materiala omejujeta njegove EK in MK učinke. Nadaljnja modifikacija PFN–20BFO z dodatkom manganovih in gadolinijevih ionov uspešno zavre prekomerno električno prevodnost ter poveča magnetni odziv, kar vodi do izboljšanja EK kot tudi MK lastnosti materiala. Posledično PFN–20BFO z dodatkom mangana in gadolinija izkazuje zanemarljivo Joulovo gretje vse do 75 °C, EK učinek višji od 1 °C pri sobni temperaturi in 140 $kV \cdot cm^{-1}$, visok MK učinek nad 3 °C pri kriogenih temperaturah in 50 kOe, ter najvišji MK učinek pri sobni temperaturi med vsemi do sedaj pripravljenimi multikaloričnimi materiali na osnovi PFN.

Contents

List of Figures **xv**

List of Tables **xvii**

Abbreviations **xix**

Symbols **xxi**

1 Introduction **1**
1.1 Definition of the Problem 1
1.2 Caloric Effect 2
1.2.1 Electrocaloric Effect 2
1.2.2 Magnetocaloric Effect 6
1.2.3 Multicaloric Effect 8
1.3 Ferroelectric Materials 13
1.4 Ferromagnetic Materials 16
1.5 Multiferroic Materials 18
1.5.1 Lead Iron Niobate, $Pb(Fe_{0.5}Nb_{0.5})O_3$ 19
1.5.2 Bismuth Ferrite, $BiFeO_3$ 21
1.5.3 $Pb(Fe_{0.5}Nb_{0.5})O_3$–$BiFeO_3$ Solid Solutions 22
1.6 Objectives and Hypotheses of the Dissertation 22

2 Improving the Multicaloric Properties of $Pb(Fe_{0.5}Nb_{0.5})O_3$ by Controlling the Sintering Conditions and Doping with Manganese **25**

3 Strengthened Relaxor Behavior in (1-*x*)$Pb(Fe_{0.5}Nb_{0.5})O_3$–*x*$BiFeO_3$ **51**

4 $Pb(Fe_{0.5}Nb_{0.5})O_3$–$BiFeO_3$-Based Multicalorics with Room-Temperature Ferroic Anomalies **79**

5 Conclusions and Outlook **99**

Appendix A Electrocaloric Measurements **101**
A.1 Direct Electrocaloric Measurements 101
A.2 Correction Factor 101
A.3 Estimation of measurement uncertainty 102

References **103**

Bibliography **111**

Biography **117**

List of Figures

Figure 1.1: Schematic representation of the working principles of four different caloric effects (EC, MC, eC and BC), where the application of external stimuli (electric field, magnetic field, uniaxial stress and pressure, respectively) causes a change in the material's temperature, accompanied by a subsequent heat flow. 2
Figure 1.2: Schematic representation of the EC cycle. 3
Figure 1.3: (a) Example of $Pb(Fe_{0.5}Nb_{0.5})O_3$-based ceramic pellet with attached thermistor and wires and (b) its directly measured temperature changes during the EC cycle, when a step-like electric field is applied. 5
Figure 1.4: Schematic representation of the MC cycle. 6
Figure 1.5: (a) An example of the temperature dependence of M at different applied H with (b) related indirectly calculated $\Delta T_{MC}(T,H)$ of $Pb(Fe_{0.5}Nb_{0.5})O_3$ ceramics. 8
Figure 1.6: Schematic representation of the individual caloric effects and their combinations forming different types of MultiC effects. 9
Figure 1.7: Schematic representation of the MultiC (EC+MC) cycle. 10
Figure 1.8: Schematic representation of different working principles and temperature ranges of the MultiC (EC+MC) effect. The MultiC effect can be defined as (a) a combination of ΔT_{EC} and ΔT_{MC} in the same temperature range, where both stimuli are simultaneously applied, (b) ΔT_{EC} and ΔT_{MC} that are located in different temperature regions, where a sequential application of external stimuli can broaden the operating temperature range, and (c) the MultiC effect ($\Delta T_{e,MultiC}$ and $\Delta T_{m,MultiC}$) can be achieved by the application of only one external stimulus (i.e., electric and magnetic field, respectively). 12
Figure 1.9: One of the possible classifications of materials according to their electro-thermo-mechanical properties. 14
Figure 1.10: Schematic representations of (a) the temperature dependence of ε' around the paraelectric-to-ferroelectric phase transition, (b) P–E hysteresis loop and (c) domain structure of typical ferroelectric material. 14
Figure 1.11: Schematic representations of (a) temperature and frequency (ν) dependences of ε' and (b) P–E hysteresis loop of typical relaxor material. (c) Schematic representation of two proposed models of relaxor's local domain structure. 16
Figure 1.12: One of the possible classifications of materials according to their magnetic properties. 17
Figure 1.13: Schematic representations of (a) the temperature dependence of M around the paramagnetic-to-ferromagnetic phase transition, (b) M–H hysteresis loop and (c) domain structure of typical ferromagnetic material. 18
Figure 1.14: Schematic representations of typical temperature dependence of M around the paramagnetic-to-antiferromagnetic phase transition. 18
Figure 1.15: Schematic representation of primary ferroic materials, i.e., ferroelectrics and ferromagnets, and their combination called multiferroics. 19

Figure 1.16: (a) Schematic representation of a perovskite unit cell, (b) temperature and frequency dependences of ε', (c) piezo-response force microscopy image of ferroelectric domain structure at RT and (d) temperature dependence of M measured at 10 kOe of PFN ceramics. 20

Figure 1.17: (a) Schematic representation of two BFO perovskite unit cells, (b) piezo-response force microscopy image of BFO ferroelectric domain structure at RT and (c) scanning electron microscopy image of polished BFO surface, where mullite and sillenite secondary phases are marked with blue and red arrows, respectively. 21

Figure A.1: Direct EC measurements of $Pb(Mg_{1/3}Nb_{2/3})O_3$ disk-shaped bulk ceramics. (a) Direct measurements of induced ΔT during the EC cycle using thermistor in modified DSC and IR camera. The ratio between both measured maximum ΔT values correspond to the correction factor of ~1.67. (b) Calculation of the correction factor according to the ratio of thermal masses of the whole sample assembly. (c) Numerical modeling of the temperature evolution in a few seconds after step-like electric field was applied..... 102

List of Tables

Table 5.1: Summary of room-temperature and maximum $\Delta T_{\mathrm{EC,eff}}$ and ΔT_{MC} of all PFN-based multicalorics. 99

Abbreviations

BC	. . . barocaloric
BFO	. . . bismuth ferrite, $BiFeO_3$
DC	. . . direct current
DSC	. . . differential scanning calorimetry
DW	. . . domain wall
EC	. . . electrocaloric
eC	. . . elastocaloric
IR	. . . infrared
MC	. . . magnetocaloric
mC	. . . mechanocaloric
ME	. . . magnetoelectric
MultiC	. . . multicaloric
PFN	. . . lead iron niobate, $Pb(Fe_{0.5}Nb_{0.5})O_3$
PFN–100xBFO	. . . (1-x)$Pb(Fe_{0.5}Nb_{0.5})O_3$–$x BiFeO_3$
PFN–100xPMW	. . . (1-x)$Pb(Fe_{0.5}Nb_{0.5})O_3$–$x Pb(Mg_{0.5}W_{0.5})O_3$
PNR	. . . polar nanoregion
RT	. . . room temperature

Symbols

B	. . . magnetic flux density
c_{E}	. . . specific heat capacity at electric field E
c_H	. . . specific heat capacity at magnetic field H
$C_{\mathrm{p,EC}}$	. . . heat capacity of the EC active component
$C_{\mathrm{p,i}}$	. . . heat capacity of the EC active and non-active component
D	. . . electric displacement
E	. . . electric field
E_{C}	. . . coercive electric field
G	. . . Gibbs free energy
H	. . . magnetic field
H_{C}	. . . coercive magnetic field
k	. . . correction factor
m	. . . mass
M	. . . magnetization
M_{R}	. . . remanent magnetization
M_{S}	. . . saturated magnetization
P	. . . polarization
P_{R}	. . . remanent polarization
P_{S}	. . . saturated polarization
Q	. . . heat
S	. . . entropy
T	. . . temperature
T_{C}	. . . ferroelectric Curie temperature
T_{C}^{*}	. . . ferromagnetic Curie temperature
T_{g}	. . . spin-glass phase transition
T_{N}	. . . Néel temperature
x	. . . strain
X	. . . stress
α	. . . magnetoelectric coupling coefficient
α_{e}	. . . electrically induced magnetoelectric coefficient
α_{m}	. . . magnetically induced magnetoelectric coefficient
ΔS	. . . entropy change
ΔS_{EC}	. . . electrocaloric entropy change
ΔS_{MC}	. . . magnetocaloric entropy change
ΔT	. . . temperature change
ΔT_{EC}	. . . electrocaloric temperature change, electrocaloric effect
$\Delta T_{\mathrm{EC,eff}}$	. . . electrocaloric effective cooling effect
$\Delta T_{\mathrm{e,MultiC}}$	. . . electrically induced multicaloric effect
ΔT_{MC}	. . . magnetocaloric temperature change, magnetocaloric effect

$\Delta T_{\mathrm{m,MultiC}}$ . . . magnetically induced multicaloric effect
$\Delta T_{\mathrm{MultiC}}$ . . . multicaloric temperature change, multicaloric effect
ε_0 . . . dielectric permittivity of vacuum
ε_{r} . . . relative dielectric permittivity
ε' . . . real part of the complex dielectric permittivity
μ_0 . . . magnetic permeability of vacuum
μ_{r} . . . relative magnetic permeability
ν . . . frequency
ρ . . . density
σ_{DC} . . . specific DC electrical conductivity
χ_{e} . . . electric susceptibility
χ_{m} . . . magnetic susceptibility

Chapter 1

Introduction

The Introduction provides a brief literature overview of the relevant topics of this thesis. It begins with the motivation and a brief description of the problem. The second section is focused on the basic definitions, characteristics and challenges related to the different caloric effects, while the following three sections cover the descriptions of promising candidates for caloric cooling applications, namely ferroelectric, ferromagnetic and multiferroic materials. At the end, the multiferroics lead iron niobate and bismuth ferrite, representing the two core materials investigated in this work, are introduced.

1.1 Definition of the Problem

With an increasing world population, better living standards and global warming, there is an increasing demand for refrigeration and air conditioning. According to the European Commission, a half of the European Union's energy consumption is spent on heating and cooling. The assumption is that by 2060, the consumption of energy consumed for cooling will exceed that for heating [1]. The majority of commercial refrigeration systems are still based on the vapor-compression refrigeration cycle, which was discovered at the beginning of the 19th century. Despite all the improvements, which were made with respect to higher energy efficiency and using less environmentally hazardous refrigerants, the method still exhibits some drawbacks. The next difficulties are the relatively large size of the cooling system, which prevents its miniaturization, and the emergence of noise and vibrations during its operation, making this method unsuitable for cooling small electronic devices and their components [2, 3]. All these disadvantages of conventional cooling systems have driven the development of more efficient and environmentally friendly cooling alternatives.

Solid-state refrigeration technology represents a promising alternative for their replacement, or better, for using it in fields where vapor-compression technology cannot be used, such as the cooling of small devices, electronic circuits or cooling in harsh environments [4, 5]. Most of the current activity in the research of new cooling technologies is oriented towards one of the caloric effects where the entropy of the material and thus its temperature changes during the application of external stimuli, such as an electric field, magnetic field, or stress [6-8]. However, all the individual caloric materials still face drawbacks, primarily a small caloric effect, which limits their commercial use. An interesting way to enhance the total caloric effect or, alternatively, expand the temperature range of their use, is to prepare a material exhibiting more than one caloric effect, commonly called a multicaloric material [6, 9, 10]. This a relatively new and promising area whose development has only just begun. The focus of this thesis is exactly the preparation and investigation of new, single-phase multicaloric materials, combining the

electrocaloric and magnetocaloric effects, which could potentially be used as active elements for future cooling devices.

1.2 Caloric Effect

The term caloric effect refers to the reversible thermal changes, namely the adiabatic temperature and isothermal entropy changes, of a material under the influence of external stimuli, such as an electric field, magnetic field or stress. Depending on the type of stimulus that causes the reversible temperature changes of the material, the caloric effects can be classified as electrocaloric (EC), magnetocaloric (MC) and mechanocaloric (mC). Based on the direction of the applied stress, i.e., uniaxial or isotropic (hydrostatic pressure), the mC effect can be further divided into two subgroups, namely the elastocaloric (eC) and barocaloric (BC) effects, respectively (Figure 1.1) [3, 6, 7, 11]. In this thesis we focus only on the EC effect, the MC effect and their combination, hereafter defined as the multicaloric effect. Therefore, their detailed descriptions, working principles, thermodynamics and measurement methods are presented in the next three subsections.

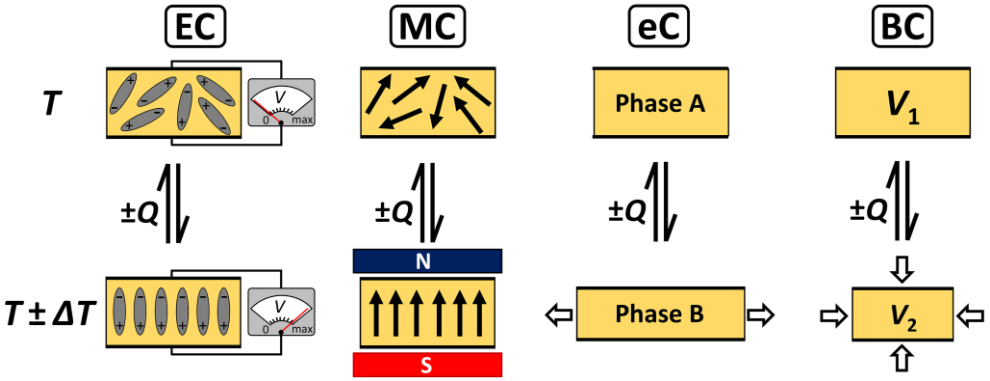


Figure 1.1: Schematic representation of the working principles of four different caloric effects (EC, MC, eC and BC), where the application of external stimuli (electric field, magnetic field, uniaxial stress and pressure, respectively) causes a change in the material's temperature, accompanied by a subsequent heat flow (after [3, 8]).

1.2.1 Electrocaloric Effect

The EC effect is defined as a reversible adiabatic temperature change and isothermal entropy change of a polar dielectric material under the influence of an external electric field. The working principle of the EC cooling/heating cycle can be divided into four periodic stages, i.e., two adiabatic and two iso-field processes (Brayton thermodynamic cycle process), which are schematically shown in Figure 1.2 [12-15]:

- **Stage I**. The application of an external electric field (E) causes partial alignment of the electric dipoles in the polar EC material, which consequently leads to a reduction in the entropy (S) of the dipolar subsystem. Under the adiabatic conditions (fast enough to prevent any heat exchange with the environment), the total entropy of the material remains constant. Therefore, in order to compensate for it, the lattice vibration entropy is increased, resulting in an increasing of the temperature (T) of the material by ΔT. This stage is often called the adiabatic polarization.

- **Stage II**. In this step the electric field remains applied, while the excessive heat (Q) is transferred to the heat sink, leading to cooling of the EC material back to the initial temperature (T).
- **Stage III**: In the third step of the cycle, also called adiabatic depolarization, the electric field is removed. The electric dipoles are returned back to the disordered state, which increases the entropy of the dielectric subsystem and consequently cools down the material by ΔT, hereafter called the EC temperature change (ΔT_{EC}).
- **Stage IV**. In the last step of the cycle, the temperature drop is compensated by heat transfer from the heat source, which heats up the EC material back to the initial temperature (T) and prepares the material for the next cycle. The heat sink and heat source now serve as the hot and cold parts of a refrigeration device [12-16].

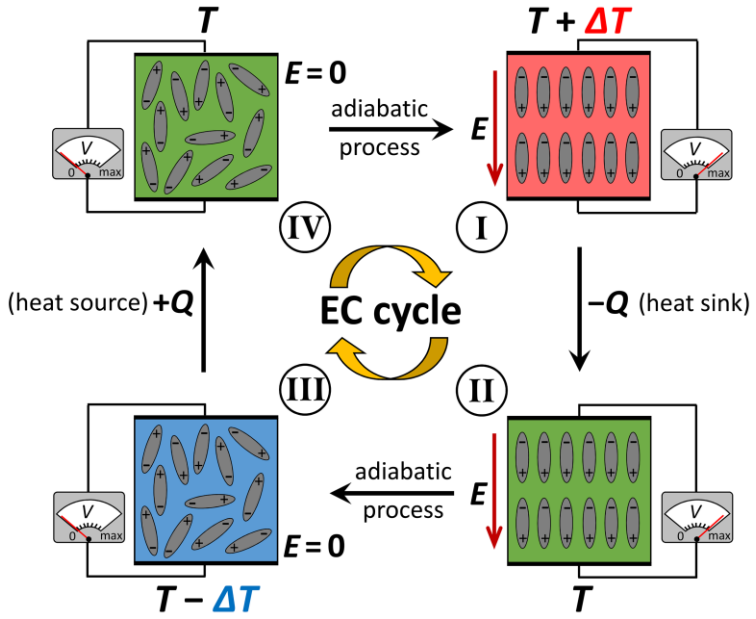


Figure 1.2: Schematic representation of the EC cycle (after [15, 16]).

The EC effect is a thermodynamic phenomenon that can be described using the so-called Maxwell thermodynamic approach [13, 17]. Referring to the first and second laws of thermodynamics, the differential form of the Gibbs free energy density (G) for a dielectric material is defined as:

$$dG = -SdT - x_{\mathrm{ij}}dX_{\mathrm{ij}} - P_{\mathrm{i}}dE_{\mathrm{i}}, \tag{1.1}$$

where x_{ij}, X_{ij} and P_{i} represent the strain, stress and electric polarization, respectively (indexes indicate their tensorial nature) [12, 13, 17]. With the assumption that X_{ij} is constant, the total entropy density change (dS) expressed according to E and T (independent variables are written as subscripts) can be represented as [13]:

$$dS = \left(\frac{\partial S}{\partial T}\right)_{X,E} dT + \left(\frac{\partial S}{\partial E_{\mathrm{i}}}\right)_{T,X} dE_{\mathrm{i}}. \tag{1.2}$$

The relation between the (S, T) and (P, E) pairs of parameters are described by the following Maxwell relation:

$$\left(\frac{\partial S}{\partial E_{\mathrm{i}}}\right)_{T,X} = \left(\frac{\partial P_{\mathrm{i}}}{\partial T}\right)_{X,E}, \tag{1.3}$$

and the expression for the specific heat capacity at electric field E (c_{E}) is given by:

$$c_{\mathrm{E}} = \frac{T}{\rho}\left(\frac{\partial S}{\partial T}\right)_{E}, \tag{1.4}$$

where ρ is the density of the material. By introducing Eqs. (1.3) and (1.4) into Eq. (1.2), the expression for dS is given as [13]:

$$dS = \frac{\rho\ c_{\mathrm{E}}}{T}dT + \left(\frac{\partial P_{\mathrm{i}}}{\partial T}\right)_{X,E} dE_{\mathrm{j}}. \tag{1.5}$$

Under isothermal conditions ($dT = 0$), the EC entropy density change (ΔS_{EC}) can be determined by integrating Eq. (1.5):

$$\Delta S_{\mathrm{EC}} = \int_{E_1}^{E_2} \left(\frac{\partial P_{\mathrm{i}}}{\partial T}\right)_{X,E} dE_{\mathrm{j}}, \tag{1.6}$$

where E_1 and E_2 are the starting (usually $E_1 = 0$) and final electric fields, respectively [12, 13]. Finally, the EC temperature change, or more briefly the EC effect (ΔT_{EC}), can be described by integrating Eq. (1.5) under adiabatic conditions ($dS = 0$) [12-14]:

$$\Delta T_{\mathrm{EC}} = -\int_{E_1}^{E_2} \frac{T}{\rho c_{\mathrm{E}}}\left(\frac{\partial P_{\mathrm{i}}}{\partial T}\right)_{X,E} dE_{\mathrm{j}}. \tag{1.7}$$

Based on Eq. (1.7), the properties of the effective EC material can be predicted. In order to obtain a large EC effect, the EC material must show a large change of polarization with the temperature and exhibit a low c_{E}. In addition, the size of the applied electric field (ΔE) also plays an important role in achieving large EC effects. However, it is strongly dependent on the dielectric breakdown strength of the material, which is usually the main limiting factor when it comes to achieving larger EC effects [18].

By definition, the EC effect can be determined as the adiabatic temperature change (ΔT) or isothermal entropy change (ΔS) at selected T and ΔE. Despite many decades from the first observation of the EC effect in Rochelle salt in 1930 [19], there is still no validated, commonly accepted and commercially available method for its determination [14]. However, many different techniques and approaches have been demonstrated so far, which can, in general, be divided into two main groups, namely, the direct and indirect EC measurement methods [12-14].

Direct EC measurement methods are based on a direct measurement of the adiabatic ΔT or isothermal heat flow (Q) when the electric field is applied/removed, while the isothermal ΔS cannot be measured directly. The majority of direct methods are based on a determination of the adiabatic ΔT using contact (e.g., thermistors and thermocouples) or non-contact (e.g., thermal cameras) thermometry, where ΔT is determined directly as a change of the temperature when the step-like electric field is applied (Figure 1.3). In most cases, especially for bulk samples, modified commercial differential scanning calorimeters (DSCs), or high-resolution calorimeters that enable precise temperature stabilization, are employed, where EC temperature changes are read out using small thermocouples or thermistors that are glued directly onto the samples (Figure 1.3) [12-14,

20]. In such measurements, the actually measured ΔT is usually lower than the intrinsic ΔT_{EC} of the material due to heat losses in the non-active parts of the measuring system (i.e., sample areas without electrodes, thermistor, wires, glue, electrodes and/or possible presence of a substrate). Such heat losses can be successfully compensated using the so-called correction factor (k):

$$\Delta T_{EC} = \Delta T \frac{\sum_i C_{\mathrm{p,i}}}{C_{\mathrm{p,EC}}} = k \cdot \Delta T, \tag{1.8}$$

where $C_{\mathrm{p,i}}$ represent the heat capacity of all the EC active and non-active parts, while $C_{\mathrm{p,EC}}$ is the heat capacity of the EC active sample (covered with electrodes) (details of the method used in this thesis are described in Appendix A) [12, 13]. In the case that $c_{\mathrm{E}}(E,T)$ is electric-field independent or only weakly dependent (i.e., exhibit no singularities), $c_{\mathrm{E}}(E,T)$ and $T(E)$ can be taken out of the integral and ΔS_{EC} can be calculated from the measured ΔT_{EC} using the following equation:

$$\Delta S_{\mathrm{EC}} = \frac{m \cdot c_{\mathrm{E}}}{T} \Delta T_{\mathrm{EC}}, \tag{1.9}$$

where m is the mass of the measured sample. In general, this equation is valid only at temperatures far from the absolute zero and far from any ferroelectric phase transitions, e.g. T_{C} [12, 13].

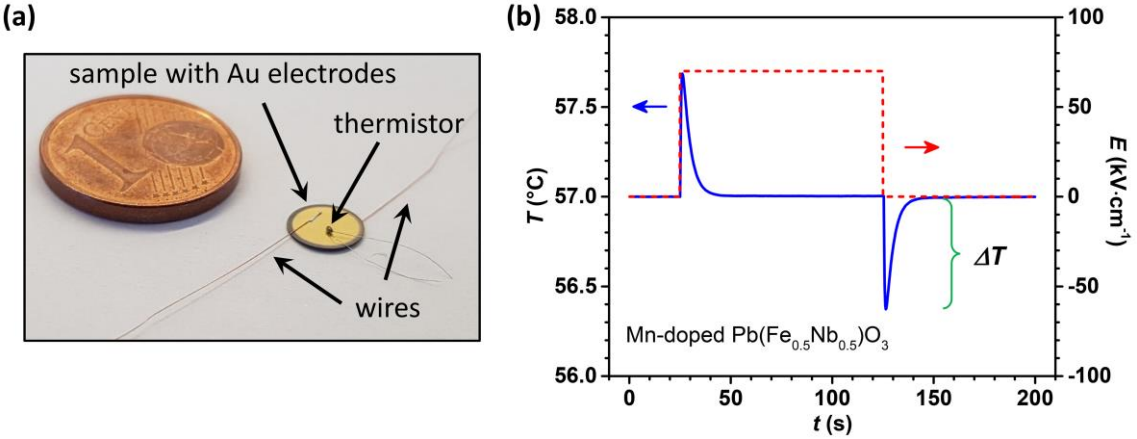


Figure 1.3: (a) Example of $Pb(Fe_{0.5}Nb_{0.5})O_3$-based ceramic pellet with attached thermistor and wires and (b) its directly measured temperature changes during the EC cycle, when a step-like electric field is applied [21].

On the other hand, in the case of the indirect EC measurement method, adiabatic ΔT and isothermal ΔS can be determined indirectly by integrating the aforementioned Eqs. (1.6) and (1.7). To solve both integral equations, experimental measurements of the temperature and electric-field dependence of polarization ($P(E,T)$), the temperature and electric-field dependence of the specific heat capacity ($c_{\mathrm{E}}(E,T)$) and the density (ρ) of the sample are needed. Note that the assumption of the electric-field independence of $c_{\mathrm{E}}(T)$, which significantly simplify the integration of Eq. (1.7), can lead to an erroneous estimate of ΔT_{EC}, especially close to the absolute zero and T_{C} [12-14]. Obviously, more reliable results are obtained with the direct methods; however, the indirect measurements are faster and more easily achievable [6, 12, 20].

1.2.2 Magnetocaloric Effect

The MC effect is analogous to the EC effect and is defined as the reversible adiabatic temperature change and isothermal entropy change of a magnetic material under the influence of an external magnetic field. In analogy with the EC effect (Figure 1.2), the working principle of MC cooling/heating cycle can be divided into four periodic stages, i.e., two adiabatic and two iso-field processes (Brayton thermodynamic cycle process), which are schematically shown in Figure 1.4 [22-25]:

- **Stage I**. The application of an external magnetic field (H) causes partial alignment of magnetic moments in the material, which consequently leads to a reduction in entropy (S) of the magnetic subsystem. Under the adiabatic conditions (fast enough to prevent any heat exchange with environment), the total entropy of the material remains constant. Therefore, in order to compensate for it, the lattice vibration entropy is increased, resulting in an increasing of the temperature (T) of the material by ΔT. This stage is often called the adiabatic magnetization.
- **Stage II**. In this step the magnetic field remains applied, while the excessive heat (Q) is transferred to the heat sink, leading to cooling of the MC material back to the initial temperature (T).
- **Stage III**: In the third step of the cycle, also called adiabatic demagnetization, the magnetic field is removed. The magnetic moments are returned to the disordered state, which increases the entropy of the magnetic subsystem and consequently cools the material by ΔT, hereafter called the MC temperature change (ΔT_{MC}).
- **Stage IV**. In the last step of the cycle, the temperature drop is compensated by heat transfer from the heat source, which heats up the MC material back to the initial temperature (T) and prepares the material for the next cycle. The heat sink and heat source now serve as the hot and cold parts of a refrigeration device [23-25].

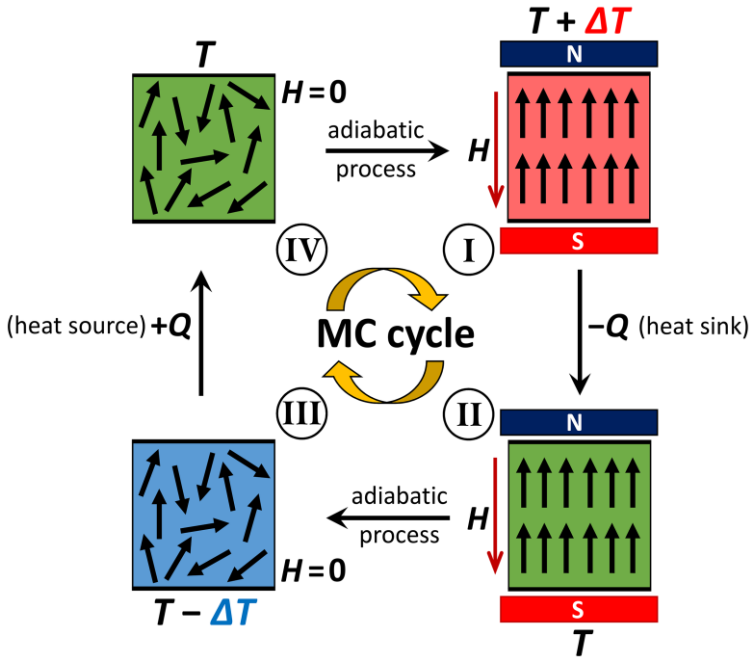


Figure 1.4: Schematic representation of the MC cycle (after [3, 15]).

The MC effect is a thermodynamic phenomenon that can be described using the so-called Maxwell thermodynamic approach [23, 24]. Referring to the first and second laws of

thermodynamics, similar to the EC effect, the differential form of the Gibbs free energy density for a magnetic material is defined as:

$$dG = -SdT - x_{\mathrm{ij}}dX_{\mathrm{ij}} - \mu_0 M_{\mathrm{i}} dH_{\mathrm{i}}, \tag{1.10}$$

where M_{i} represents the magnetization of the material (indexes indicate the tensorial nature) and μ_0 is magnetic permeability of a vacuum. With the assumption that X_{ij} is constant, the total entropy density changes of the system expressed according to H and T (independent variables are written as subscripts) can be represented as [23, 24]:

$$dS = \left(\frac{\partial S}{\partial T}\right)_{X,H} dT + \left(\frac{\partial S}{\partial H_{\mathrm{i}}}\right)_{T,X} dH_{\mathrm{i}}. \tag{1.11}$$

The relation between the (S, T) and (M, H) pairs of parameters are described by the following Maxwell relation:

$$\left(\frac{\partial S}{\partial H_{\mathrm{i}}}\right)_{T,X} = \mu_0 \left(\frac{\partial M_{\mathrm{i}}}{\partial T}\right)_{T,H}, \tag{1.12}$$

and the expression for the specific heat capacity at magnetic field H (c_{H}) is given by:

$$c_{\mathrm{H}} = \frac{T}{\rho}\left(\frac{\partial S}{\partial T}\right)_{H}. \tag{1.13}$$

By introducing Eqs. (1.12) and (1.13) into Eq. (1.11), the expression for dS is given as:

$$dS = \frac{\rho\, c_{\mathrm{H}}}{T} dT + \mu_0 \left(\frac{\partial M_{\mathrm{i}}}{\partial T}\right)_{X,H} dH_{\mathrm{j}}. \tag{1.14}$$

Under isothermal conditions ($dT = 0$), the MC entropy density change (ΔS_{MC}) can be determined by integrating Eq. (1.14):

$$\Delta S_{\mathrm{MC}} = \mu_0 \int_{H_1}^{H_2} \left(\frac{\partial M_{\mathrm{i}}}{\partial T}\right)_{X,H} dH_{\mathrm{j}}, \tag{1.15}$$

where H_1 and H_2 are the starting (usually $H_1 = 0$) and final magnetic fields, respectively [24]. Finally, the MC temperature change, or more briefly the MC effect (ΔT_{MC}), can be described by integrating Eq. (1.14) under adiabatic conditions ($dS = 0$) [23, 24]:

$$\Delta T_{\mathrm{MC}} = -\mu_0 \int_{H_1}^{H_2} \frac{T}{\rho c_{\mathrm{H}}} \left(\frac{\partial M_{\mathrm{i}}}{\partial T}\right)_{X,H} dH_{\mathrm{j}}. \tag{1.16}$$

Based on Eq. (1.16), the properties of the effective MC material can be predicted. In order to obtain a large MC effect, the MC material must show a large change of magnetization with the temperature and exhibit a low c_{H}. In addition, the size of the applied magnetic field (ΔH) also plays an important role in achieving large MC effects. However, unlike EC materials, MC materials can easily withstand very high external fields; therefore, the main limitation when it comes to achieving large MC effects lies in the magnetic field strength of the magnets. In general, more affordable permanent magnets and electromagnets are limited to a maximum magnetic flux density of 2 T.

Like the EC effect, the MC effect can be determined as an adiabatic temperature change (ΔT) or an isothermal entropy change (ΔS) at selected T and ΔH. So far, many different techniques and approaches have been demonstrated, which can in be general divided into two main groups, namely, the direct and indirect MC measurement methods.

In the case of the indirect MC measurement method, the adiabatic ΔT and isothermal ΔS can be determined indirectly by integrating the aforementioned Eqs. (1.15) and (1.16). To solve both integral equations, an experimental measurement of the temperature and magnetic-field dependence of magnetization ($M(H,T)$) (Figure 1.5), the temperature and magnetic-field dependence of the specific heat capacity ($c_H(H,T)$) and the density (ρ) of the sample are needed. Note that the assumption of the magnetic-field independence of $c_H(T)$, which significantly simplify the integration of Eq. (1.16), can lead to an erroneous estimate of ΔT_{MC}, especially close to the absolute zero and T^*_C. However, combining $M(H,T)$ data together with $c_H(T)$ measurements at different constant magnetic fields can lead to an accurate estimation of ΔT_{MC} effect with a relative uncertainty of 20-30%, which can increase at low ΔT_{MC} values [22, 23, 26, 27].

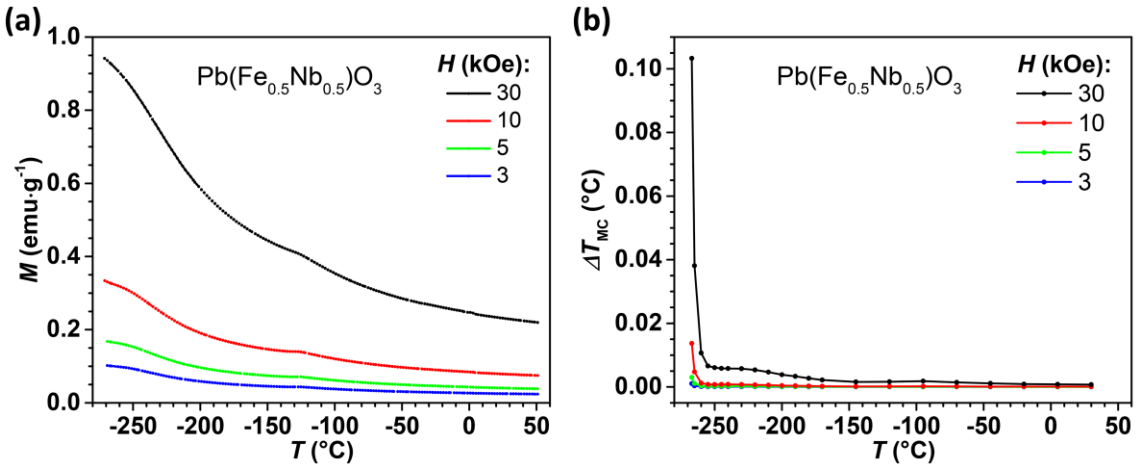


Figure 1.5: (a) An example of the temperature dependence of M at different applied H with (b) related indirectly calculated $\Delta T_{MC}(T,H)$ of $Pb(Fe_{0.5}Nb_{0.5})O_3$ ceramics [21].

On the other hand, direct MC measurement methods are based on a direct measurement of the adiabatic ΔT when a magnetic field is applied/removed using contact or non-contact thermometry, where ΔT is determined directly as a change of the temperature when the magnetic field suddenly changes. To ensure the adiabatic conditions, a rapid change of the magnetic field is required, which is achieved either by using pulsed magnetic fields or by moving the sample in and out of a uniform magnetic field. However, due to the challenges of providing a rapid change of the magnetic field and the possible influence of the magnetic field on the thermal sensors (e.g., induced parasitic signals, the appearance of eddy currents, etc.), direct measurements can be subject to large experimental errors. Because the direct MC measurement methods are challenging and time consuming, in most reported studies indirect methods are used to determine the MC effects of the materials [22, 23, 28, 29].

1.2.3 Multicaloric Effect

As the name implies, the multicaloric (MultiC) effect refers to a combination of more than one type of caloric effect in the same material. A combination of all three main individual caloric effects, namely, EC, MC and mC, leads to many different combinations, which are

schematically shown in Figure 1.6. The focus of this thesis is on a combination of the EC and MC effects in single-phase materials. Therefore, the definition of the multicaloric effect (EC+MC) in this study is related to the adiabatic and reversible temperature change that occurs in a material under the simultaneous or sequential application of an external electric and magnetic field [9, 10, 30, 31].

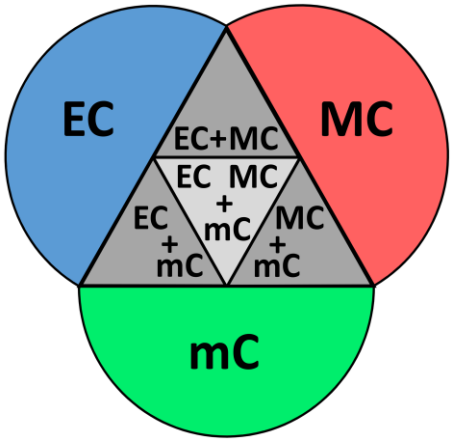


Figure 1.6: Schematic representation of the individual caloric effects and their combinations forming different types of MultiC effects (after [11]).

The working principle of MultiC cooling/heating cycle is simply a combination of the aforementioned EC and MC cycles, which is schematically shown in Figure 1.7. The MultiC material combining the EC and MC effects consists of two subsystems, i.e., electric dipoles and magnetic moments. Without the application of external electric and magnetic fields both subsystems are randomly oriented and possess the same temperature as the surroundings. The simultaneous or sequential application of both electric and magnetic fields causes the partial alignment of the electric dipoles and magnetic moments, which leads to a reduction in the entropy of the system and consequently an increase in the temperature of the material by ΔT. In the reverse process, when both fields are removed, the electric dipoles and magnetic moments are returned to the disordered state, which increases the entropy of the system and consequently cools the material by ΔT, hereafter called the multicaloric temperature change ($\Delta T_{\mathrm{MultiC}}$) [9, 32].

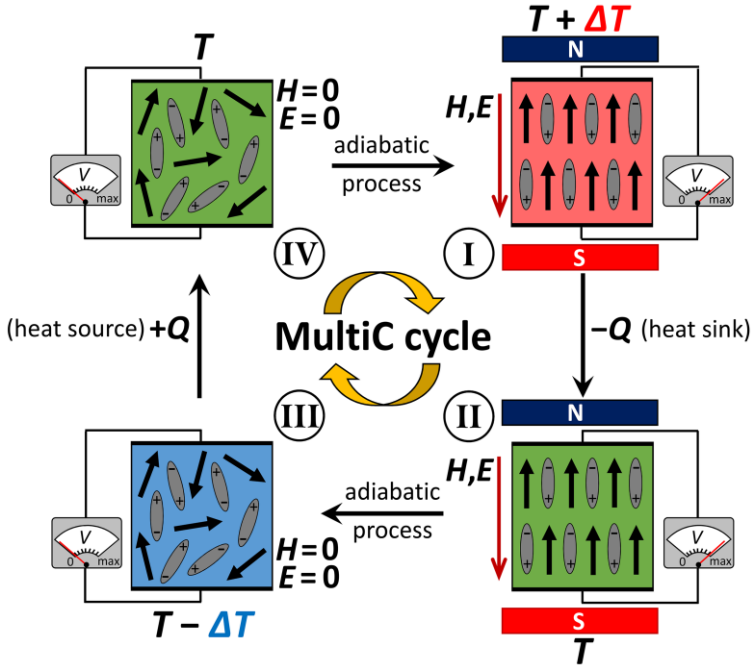


Figure 1.7: Schematic representation of the MultiC (EC+MC) cycle (after [3]).

The thermodynamic description of the MultiC effect follows from previously mentioned Maxwell approaches of both individual caloric effects. The MultiC temperature change, or more briefly the MultiC effect ($\Delta T_{\mathrm{MultiC}}$), can be described as the sum of both single EC and MC effects [30, 32]:

$$\Delta T_{\mathrm{MultiC}} = \Delta T_{\mathrm{EC}} + \Delta T_{\mathrm{MC}},$$

$$\Delta T_{\mathrm{MultiC}} = -\left[\int_{E_1}^{E_2} \frac{T}{\rho c_{\mathrm{H,E}}} \left(\frac{\partial P}{\partial T}\right)_{X,H,E} dE + \mu_0 \int_{H_1}^{H_2} \frac{T}{\rho c_{\mathrm{H,E}}} \left(\frac{\partial M}{\partial T}\right)_{X,H,E} dH\right]. \quad (1.17)$$

However, Eq. (1.17) stands for the systems where zero or negligible cross-coupling between the magnetic and electrical order parameters are present or in the case that electric and magnetic field are applied simultaneously (scenarios shown in Figures 1.8a and 1.8b). On the other hand, in the case of substantial magnetoelectric (ME) coupling or ME effect, which is defined as a change of M under the influence of external E or change of P under the influence of external H, an additional term must be introduced into the equation. This additional cross-coupling term is derived from the Maxwell relation between the (P, E) and (M, H) pairs of parameters:

$$\left(\frac{\partial M}{\partial E}\right)_{T,H} = \left(\frac{\partial P}{\partial H}\right)_{T,E} = \alpha, \quad (1.18)$$

where α is a linear ME coupling coefficient; and by assuming linear relations between P, M and their corresponding fields E, H:

$$dP = \varepsilon_0 \chi_{\mathrm{e}} dE, \quad (1.19)$$

$$dM = \mu_0 \chi_{\mathrm{m}} dH, \quad (1.20)$$

where ε_0 is the dielectric permittivity of vacuum, while χ_e and χ_m are the electric and magnetic susceptibilities, respectively [9, 30, 32]. By introducing Eqs. (1.18), (1.19) and (1.20) into Eq. (1.17), the expressions for the electrically induced MultiC effect ($\Delta T_{e,MultiC}$) and magnetically induced MultiC effect ($\Delta T_{m,MultiC}$) are given as:

$$\Delta T_{e,MultiC} = -\int_{E_1}^{E_2} \frac{T}{\rho c_E} \left[\left(\frac{\partial P}{\partial T} \right)_{X,H,E} + \frac{\alpha_e}{\mu_0 \chi_m} \left(\frac{\partial M}{\partial T} \right)_{H,E} \right] dE, \tag{1.21}$$

$$\Delta T_{m,MultiC} = -\mu_0 \int_{H_1}^{H_2} \frac{T}{\rho c_H} \left[\left(\frac{\partial M}{\partial T} \right)_{X,H,E} + \frac{\alpha_m}{\varepsilon_0 \chi_e} \left(\frac{\partial P}{\partial T} \right)_{H,E} \right] dH, \tag{1.22}$$

where α_e and α_m are the electrically and magnetically induced linear ME coefficients, respectively [9, 32]. From both equations it follows that in the case of large cross-coupling between the electrical and magnetic subsystems, the application of only one external field leads to a much higher MultiC effect compared to the individual EC or MC effects (Figure 1.8c). On the other hand, where $\alpha_e = \alpha_m = 0$, Eqs. (1.21) and (1.22) are simplified to the previously described equations for the single EC (1.7) and MC (1.16) effects, respectively [9, 32].

The combination of EC and MC effects in one material can lead to different working principles of the MultiC effect, which are schematically shown in Figure 1.8. The three most common scenarios of the MultiC effects are described below, along with their advantages over the individual caloric effects:

- **a.)** Both the EC and MC effects take place in the same temperature range, ideally close to room temperature (RT), where most refrigerators for everyday use operate (Figure 1.8a). In this case, the simultaneous application of both external fields can increase the overall cooling effect, as described in Eq. (1.17). This enables the use of smaller external fields to achieve a certain caloric effect.
- **b.)** Both the EC and MC effects take place in different temperature regions, which can extend the operating temperature range of a cooling device (Figure 1.8b). For example, the EC effect can be employed for cooling above 0 °C (i.e., kitchen refrigerator) and the MC effect for cooling below 0 °C (i.e., freezer) or using the EC effect at RT and the MC effect at cryogenic temperatures, *etc.*
- **c.)** In materials with high ME coupling, the MultiC effect can be driven by only one external field, as follows from Eqs. (1.21) and (1.22) (Figure 1.8c). This enables a larger cooling effect compared to a single EC or MC effect at the same strength of applied external field. This allows the use of smaller external fields to achieve a certain cooling effect, which can reduce the operating costs of a cooling device and improve the fatigue life of their active elements. Of particular interest for commercial use is the application of an external electric field to drive the EC and MC effects, because the electric field is relatively easy and cheap to deliver [33]. However, ME coupling is relatively large only in composite materials [34-37], while its value in single-phase materials is negligible. Therefore, this scenario is not covered in this thesis.

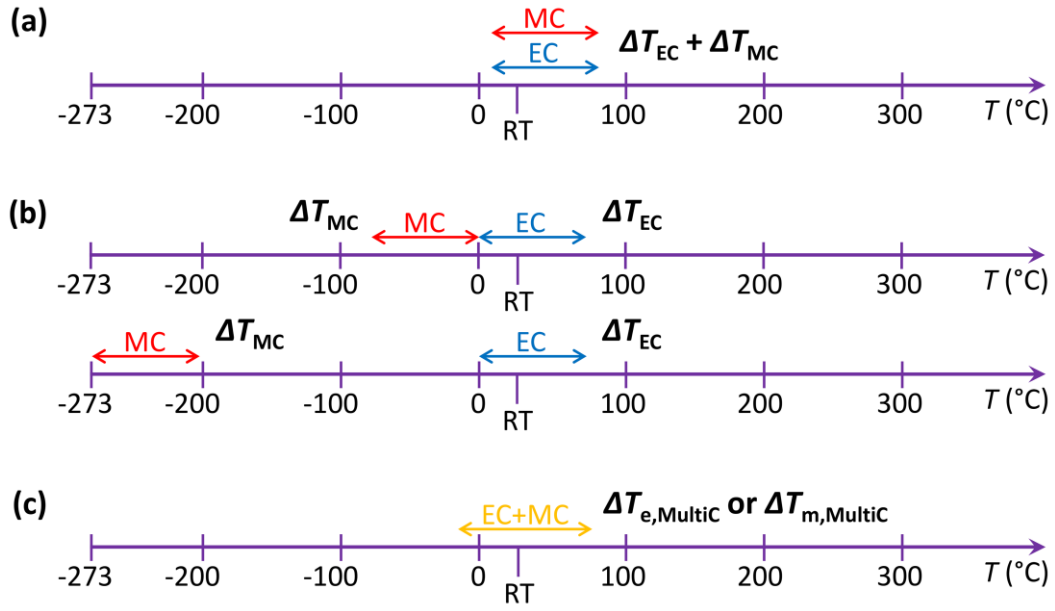


Figure 1.8: Schematic representation of different working principles and temperature ranges of the MultiC (EC+MC) effect. The MultiC effect can be defined as (a) a combination of ΔT_{EC} and ΔT_{MC} in the same temperature range, where both stimuli are simultaneously applied, (b) ΔT_{EC} and ΔT_{MC} that are located in different temperature regions, where a sequential application of external stimuli can broaden the operating temperature range, and (c) the MultiC effect ($\Delta T_{\mathrm{e,MultiC}}$ and $\Delta T_{\mathrm{m,MultiC}}$) can be achieved by the application of only one external stimulus (i.e., electric and magnetic field, respectively).

Since the field of multicaloric materials is relatively new, very few experimental studies combining the EC and MC effects in single-phase materials have been reported so far. In part, a reason for that could lie in the totally different origins and mechanisms for the occurrence of polar dielectric and magnetic subsystems and thus the appearance of the EC and MC effect, respectively. Usually, the occurrence of one order parameter (P or M) reduces the tendency for the emergence of the other one and vice versa, which subjects multicalorics to a compromise between good EC and MC properties.

The first experimental observation of both the EC and MC effect in a single-phase material was reported by J. Krishna Murthy *et al.* [38] in 2014. They indirectly obtained the EC and MC effects in Y_2CoMnO_6 double perovskite. The maximum ΔT_{MC} value of ~5.8 °C was obtained at ~−200 °C and using a very high magnetic flux density of 5 T. However, due to the improper ferroelectricity that is driven by a specific magnetic order rather than non-centrosymmetric crystal structure [39], the material exhibited very poor ferroelectric properties and thus a weak EC response. In addition, due to the very high electrical conductivity, the EC properties could only be measured at very low external electric fields (i.e., up to 4 kV · cm^{-1}). An indirect experimental observation of the EC and MC effects was also reported in $FeCr_2S_4$ and $CoCr_2S_4$ sulpho spinels [40], where similar behavior, namely, a relatively large MC effect and a poor EC effect, was observed.

In 2016, H. Uršič *et al.* [41] demonstrated the coexistence of EC and MC effects and thus the MultiC effect in relaxor $0.8Pb(Fe_{0.5}Nb_{0.5})O_3$–$0.2Pb(Mg_{0.5}W_{0.5})O_3$ (PFN–20PMW) ceramics, where the MC effect was measured using the indirect Maxwell approach, while the EC effect was measured directly using a high-resolution calorimeter. They reported a maximum EC effect of ~0.25 °C at −93 °C and 60 kV · cm^{-1} and a maximum MC effect of ~0.26 °C at −268 °C and 70 kOe. Despite the fact that both caloric effects are too low for

any practical applications and that their maximum values lie far below the desired RT, it is one of the first examples where the coexistence of the EC and MC effects in a single-phase material were unequivocally experimentally proven. This research work triggered our interest in such single-phase multicalorics and represented a starting point for this thesis.

1.3 Ferroelectric Materials

In this section, typical candidates and their requirements for achieving sufficient EC effects are introduced and their characteristics are described. In principle, in order to eliminate the Joule heating effect and other self-heating sources inside the material [42, 43], all EC candidates must exhibit a low electrical conductivity and small losses associated with the movement and switching of the domain walls [43]. Among them, the best EC properties are shown by ferroelectrics and relaxor ferroelectrics [6, 44, 45], which belong to the subgroup of dielectric materials (Figure 1.9).

Dielectrics are a group of electrically insulating materials, which can be polarized by an applied electric field (E). The electric field induces polarization (P), which is defined as a shift of the positive and negative electric charges relative to the direction of E. P is proportional to E:

$$P = \varepsilon_0(\varepsilon_r - 1)E = \varepsilon_0\chi_e E, \tag{1.23}$$

where ε_r is the relative dielectric permittivity of the material, representing a measure of the ability of materials to store the electric charge [46-49]. The total amount of charge, which is induced by the applied electric field, is equal to the electric displacement (D):

$$D = \varepsilon_0 E + P = \varepsilon_0\varepsilon_r E. \tag{1.24}$$

All crystal structures are classified into 32 different crystallographic point groups. 11 of them have a center of inversion and therefore they are not suitable for polar phenomena. Among 21 non-centrosymmetric crystal classes, 20 of them exhibit piezoelectric properties. Piezoelectrics are a group of materials that can be polarized under the influence of an external mechanical stress or inversely, the application of an external electric field causes an elastic strain. Among 20 piezoelectric point groups 10 of them shows spontaneous polarization in a given temperature range. This group of materials is called the pyroelectrics and they exhibit an electric dipole moment even in the absence of an applied external electric field [46-48].

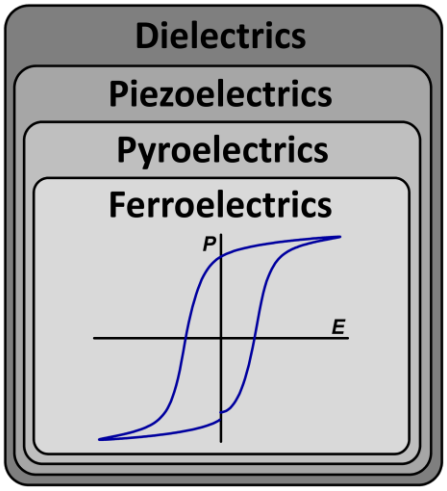


Figure 1.9: One of the possible classifications of materials according to their electro-thermo-mechanical properties (after [47]).

A subgroup of pyroelectrics is ferroelectrics (Figure 1.9). These materials exhibit two or more equilibrium orientations of the spontaneous polarization, which can be switched by the application of a sufficiently large external E [47-49]. Typically, ferroelectrics exhibit a structural phase transition from a high-temperature paraelectric (non-polar, with zero spontaneous polarization) to a low-temperature ferroelectric phase (polar, with non-zero spontaneous polarization) at the ferroelectric Curie temperature (T_C). This phase transition is accompanied by a high peak-permittivity anomaly, as evidenced by the temperature dependence of the real part of the complex dielectric permittivity (ε') shown in Figure 1.10a [46, 48, 50]. In addition, ferroelectrics exhibit a characteristic non-linear dependence of the polarization relative to the electric field, known as a P–E hysteresis loop (Figure 1.10b). Such a non-linear behavior is a consequence of the switching and alignment of regions with the uniformly oriented electric dipoles (Figure 1.10c), called ferroelectric domains, which are formed to minimize the electrostatic energy of the depolarizing field and elastic constraints [46-48]. In such materials, even in the absence of the external E, a relatively large P is maintained. The value of the polarization at zero field is called the remanent polarization (P_R), while the minimum electric field that is needed to switch the polarization orientation is called the coercive electric field (E_C). The maximum or saturated polarization is defined as P_S [48, 51].

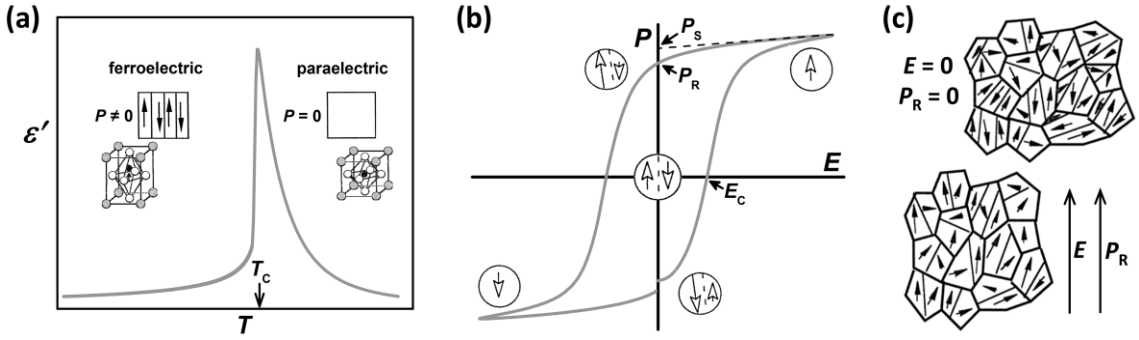


Figure 1.10: Schematic representations of (a) the temperature dependence of ε' around the paraelectric-to-ferroelectric phase transition, (b) P–E hysteresis loop and (c) domain structure of typical ferroelectric material (after [48, 21]).

According to Eq. (1.7), a large change of polarization with temperature is required to achieve large EC effects. Therefore, ferroelectrics near the paraelectric-ferroelectric phase transition, where P drastically changes, represent promising candidates for achieving high caloric performance [6, 30, 52, 53]. However, in ferroelectrics, the ferroic phase transition and thus the high EC effect is usually limited to a narrow temperature range, which limits their commercial use.

The narrow temperature range with the highest caloric effects can be extended using relaxor ferroelectrics or, more briefly, relaxors. These are materials where, unlike in normal ferroelectrics, no long-range structural order is present. A reason for that lies in the chemical or compositional heterogeneity at the nanoscale, which arises when differently sized ions with different valence states occupy a crystallographically equivalent site in the crystal lattice. The presence of this chemical disorder and thus the formation of random fields/bonds disturbs the long-range ferroelectric order and leads to the formation of "underdeveloped" nano-sized domain patterns, called polar nanoregions (PNRs) [54-58]. PNRs are responsible for the unique dielectric, ferroelectric and electromechanical behavior of relaxors. Relaxors typically exhibit very broad, diffuse and highly frequency-dependent dielectric peak-permittivity, reaching relatively high dielectric permittivity values through a wide temperature range (Figure 1.11a). Since there are no structural phase transitions in relaxors, such a peak-permittivity anomaly appears as a result of the dynamic response of PNRs to an external electric field [54-58]. The absence of long-range ferroelectric domains and a macroscopically zero polarization is also reflected in slim P–E hysteresis loops (Figure 1.11b).

It is experimentally proven that relaxors are composed of PNRs and exhibit macroscopic cubic symmetry. However, there is still a debate about which model best describes their local structure [58-60]. At the beginning of the studies on relaxors [61], the widely accepted model of relaxors assumes a local structure consisting of PNR islands embedded in a non-polar matrix [56-58] (Figure 1.11c, left). Recently, this initial model has been replaced with a one that assumes that relaxors are composed of a low-symmetry, nano-sized domains surrounded by high-density, low-angle domain walls (DWs). In this case, the non-polar matrix is nonexistent (Figure 1.11c, right) [58-60, 62, 63].

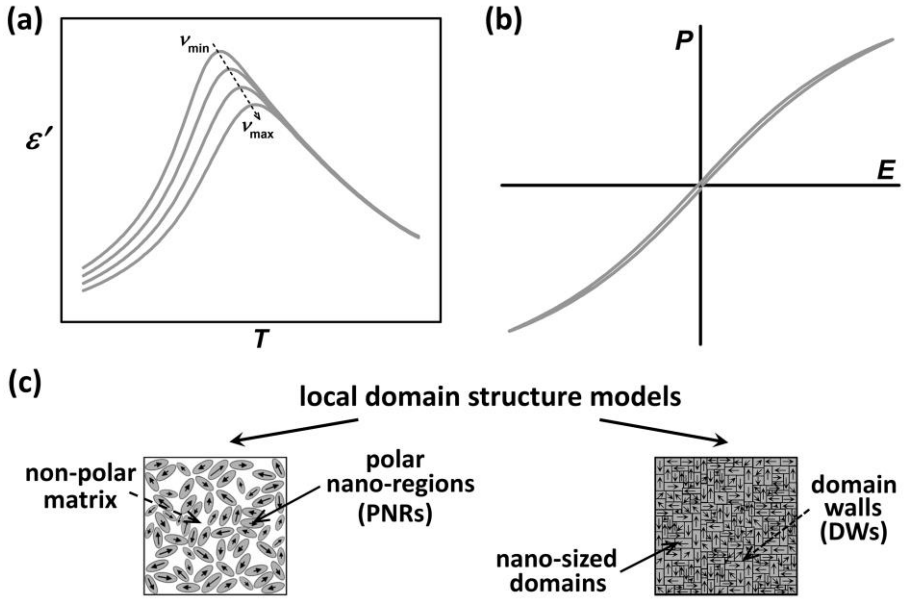


Figure 1.11: Schematic representations of (a) temperature and frequency (ν) dependences of ε' and (b) P–E hysteresis loop of typical relaxor material [21]. (c) Schematic representation of two proposed models of relaxor's local domain structure (after [48, 58]).

Relaxors have proven to be very good EC candidates, as PNRs are very responsive to external electric fields, leading to large changes in polarization and large EC effects [53, 64, 65]. Besides that, a broad peak-permittivity anomaly results in a large EC effect across a wide temperature range (a few tens of degrees) [66, 67]. In addition, the slim P–E loops of relaxors show low hysteresis losses and thus better cooling efficiency and better fatigue life compared to classic ferroelectrics [43, 68].

1.4 Ferromagnetic Materials

In this section, typical candidates and their requirements for achieving sufficient MC effects are introduced and their characteristics are described. All MC candidates must contain magnetic dipole moments and ideally show a large change of magnetization with the temperature. Among all the materials, the best MC properties are shown by ferromagnets [6, 69-71], which belong to the subgroup of diamagnetic materials (Figure 1.12).

Diamagnetism is a fundamental magnetic property and occurs in all materials. Diamagnetism arises from the interaction of an applied magnetic field (H) with the orbital motion of only paired electrons and it results in a very weak negative magnetization (M). H induces M, which is defined as magnetic dipole moment per unit volume and represents the material's response to the magnetic field:

$$M = (\mu_r - 1)H = \chi_m H, \tag{1.25}$$

where μ_r is the relative permeability, representing a measure of the degree to which the material can be magnetized [49, 72-74]. The materials' response to the magnetic field is described with the magnetization and magnetic flux density (B), which is analogous to the electric displacement (Eq. (1.24)):

$$B = \mu_0(H + M) = \mu_0\mu_r H. \tag{1.26}$$

As crystal structure and symmetry are important in the electrical properties, magnetic point groups govern the magnetic properties. Besides the common crystallographic symmetry, magnetic structures also possess time-reversed symmetry elements, which, with respect to 32 crystallographic point groups, increase the number of magnetic point groups to 90. Among the 90 point groups, 66 of them exhibit piezomagnetic properties, which are the magnetic analog of the piezoelectric properties and show a linear relationship between magnetization and mechanical stress. Among the 66 piezomagnetic point groups, 31 of them show spontaneous magnetization in a given temperature range. This group of materials is called the pyromagnets and they exhibit magnetic dipole moment even in the absence of an applied external magnetic field, which changes as the temperature is changed (hence, pyro term) [49].

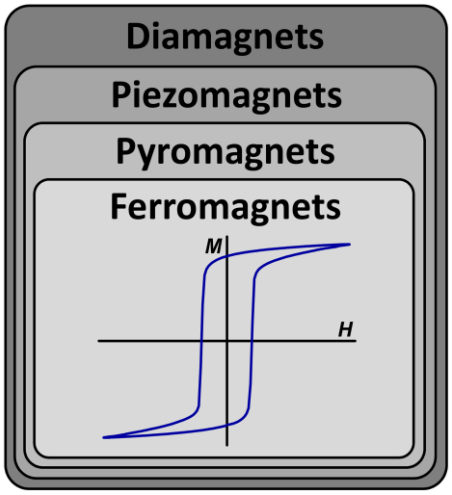


Figure 1.12: One of the possible classifications of materials according to their magnetic properties (after [49]).

Within the pyromagnets there is a subgroup of ferromagnets (Figure 1.12), which are a magnetic analogue of ferroelectrics. These materials exhibit two or more equilibrium orientations of the spontaneous magnetization, which can be switched by the application of a sufficiently large external H [49, 72-74]. Typically, ferromagnets exhibit a structural phase transition from a high-temperature paramagnetic (with zero macroscopic magnetization) to a low-temperature ferromagnetic phase (with non-zero macroscopic magnetization) at the ferromagnetic Curie temperature (T_C^*). This phase transition is typically accompanied by a drastic change of M, shown in Figure 1.13a [49, 72-74]. Similar to P–E loops in ferroelectrics, ferromagnets also exhibit a characteristic non-linear dependence of the magnetization relative to the magnetic field known as M–H hysteresis loop (Figure 1.13b). Such non-linear behavior is a consequence of the motion and rotation of domain walls (DWs), which separate the regions with the uniformly oriented magnetic dipoles (Figure 1.13c). Such regions are called ferromagnetic domains, which are formed to minimize the magnetostatic energy of the demagnetizing field [49, 72-74]. In such materials, even in the absence of the external H, a relatively large M is maintained. The value of the magnetization at zero field is called the remanent magnetization (M_R), while the minimum magnetic field, which is needed to switch magnetization orientation is called the coercive magnetic field (H_C). The maximum or saturated magnetization is defined as M_S [72-74].

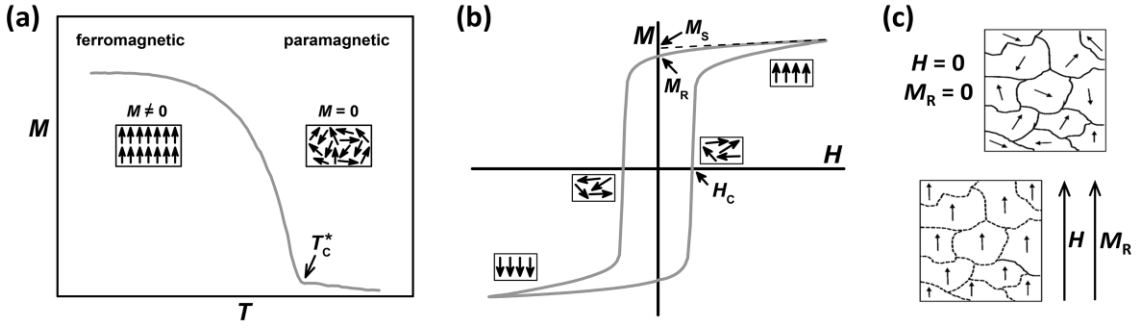


Figure 1.13: Schematic representations of (a) the temperature dependence of M around the paramagnetic-to-ferromagnetic phase transition, (b) M–H hysteresis loop and (c) domain structure of typical ferromagnetic material (after [21, 75, 76]).

According to Eq. (1.16), a large change of magnetization with temperature is required to achieve large MC effects. Therefore, ferromagnets near the paramagnetic-ferromagnetic phase transition represent promising candidates for good caloric performance [6, 69-71]. However, despite the outstanding performance of ferromagnets, a lot of complex oxide ceramics exhibit an antiferromagnetic arrangement. In these materials, magnetic moments are aligned in an antiparallel direction relative to each other, resulting in zero macroscopic magnetization at zero magnetic field. Such an arrangement often occurs in systems with two independent crystal sublattices, such as in complex perovskites. Typically, antiferromagnets exhibit a structural phase transition from a high-temperature paramagnetic to a low-temperature antiferromagnetic phase (both with zero macroscopic remanent magnetization) at the so-called Néel temperature, T_N (Figure 1.14) [49, 72-74].

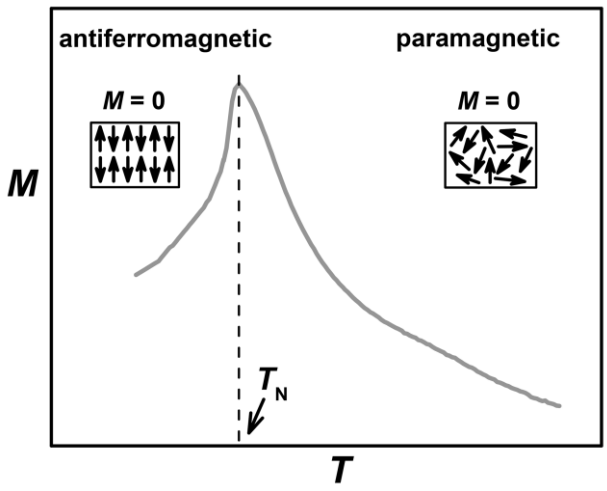


Figure 1.14: Schematic representations of typical temperature dependence of M around the paramagnetic-to-antiferromagnetic phase transition (after [21, 74]).

1.5 Multiferroic Materials

Multiferroics are a class of materials in which at least two primary ferroic orders – ferroelectric, ferromagnetic or ferroelastic – coexist in the same material. According to the latest definitions, also antiferroic and ferric orders (e.g., antiferromagnetic and ferrielectric) are included [34, 77-79]. Recently, a lot of attention is being paid to the so-called magnetoelectric (ME) multiferroics, combining ferroelectric and ferromagnetic properties

in the same material (Figure 1.15), which are attractive due to the completely different origins and opposite mechanisms of both ferroic orders [35, 77, 80].

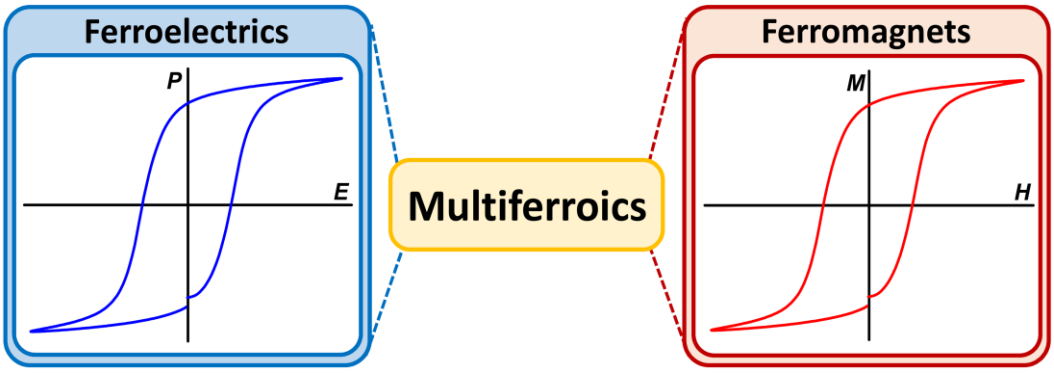


Figure 1.15: Schematic representation of primary ferroic materials, i.e., ferroelectrics and ferromagnets, and their combination called multiferroics (after [78]).

It is known that the highest caloric effects are obtained near the ferroic phase transitions, where the order parameters (i.e., P and M) are strongly temperature dependent [6, 30, 53]. Consequently, ME multiferroics with both ferroic phase transitions in the temperature ranges close together represent one of the most promising candidates for achieving large multicaloric (EC+MC) effects [30, 32]. However, single-phase ME multiferroics are rare, due to the numerous competing factors that are necessary for the appearance of one ferroic order, but at the same time reduce the tendency for the emergence of the other one [32, 36, 77, 80, 81]. Additionally, the majority of single-phase ME multiferroics exhibit ferroic phase transitions at different temperatures or temperature regions, resulting in a smaller multicaloric effect. Therefore, the search for new, single-phase multicalorics, especially those with both ferroic transitions close to RT, is challenging and timely [35, 80].

1.5.1 Lead Iron Niobate, $Pb(Fe_{0.5}Nb_{0.5})O_3$

Lead iron niobate, $Pb(Fe_{0.5}Nb_{0.5})O_3$ (PFN) is a well-known multiferroic material, where the ferroelectric and magnetic (antiferromagnetic) orders coexist [82, 83]. $Pb(Fe_{0.5}Nb_{0.5})O_3$ belongs to the class of lead-based complex perovskites with the general formula $A(B'_xB''_{1-x})O_3$ (Figure 1.16a), where multiferroic behavior arises from ferroelectrically active Pb^{2+} and Nb^{5+} ions (completely full or empty d-orbitals) and magnetically active Fe^{3+} ions (partially filled d-orbitals) that are randomly distributed on the B-site of the perovskite lattice [84, 85]. PFN exhibits a diffuse structural phase transition from the paraelectric to the ferroelectric phase (T_C) at ~95–115 °C (Figure 1.16b) [86-88]. Such a large range of reported T_C is most likely related to the diffuse nature of the transition, which arises from local fluctuations of similarly large Nb^{5+} and Fe^{3+} ions (ionic radii of 64 pm and 64.5 pm, respectively) [89] at the B-site sublattice. Consequently, the phase-transition temperature largely depends on the sample preparation, the variation of its local composition and the measurement technique used to determine T_C [90, 91]. Additionally, increased electrical conductivity as well as various charge point defects can lead to the frequency dependence of the peak-permittivity temperature. Therefore, there is still a debate about whether PFN exhibits more ferroelectric-like or relaxor-like behavior [87, 88, 92-94]. However, the frequency-independent peak-permittivity temperature (Figure 1.16b) and micron-sized ferroelectric domain structure (Figure 1.16c) [88, 92] clearly indicate long-range ferroelectric

order, confirming ferroelectric-like behavior at RT. Nevertheless, a minor role of the relaxor-like character of the material cannot be completely ruled out.

On the other hand, PFN exhibits two magnetic phase transitions that are visible as peak anomalies in the $M(T,H)$ curves, shown in Figure 1.16d. A structural phase transition from paramagnetic to long-range antiferromagnetic order (T_N) is located at approximately −125 °C, while at around −260 °C an additional magnetic phase transition related to the formation of short-range, spin-glass-like phase (T_g) is present [85, 95, 96]. The spin-glass-like phase arises from the local short-range order on the B-site perovskite sublattice (namely from the Nb-rich-Fe-poor regions), where long-range antiferromagnetic order (defined by Fe-O-Fe linkages) is disturbed due to the presence of the nonmagnetic Nb^{5+} ions [85, 95, 96].

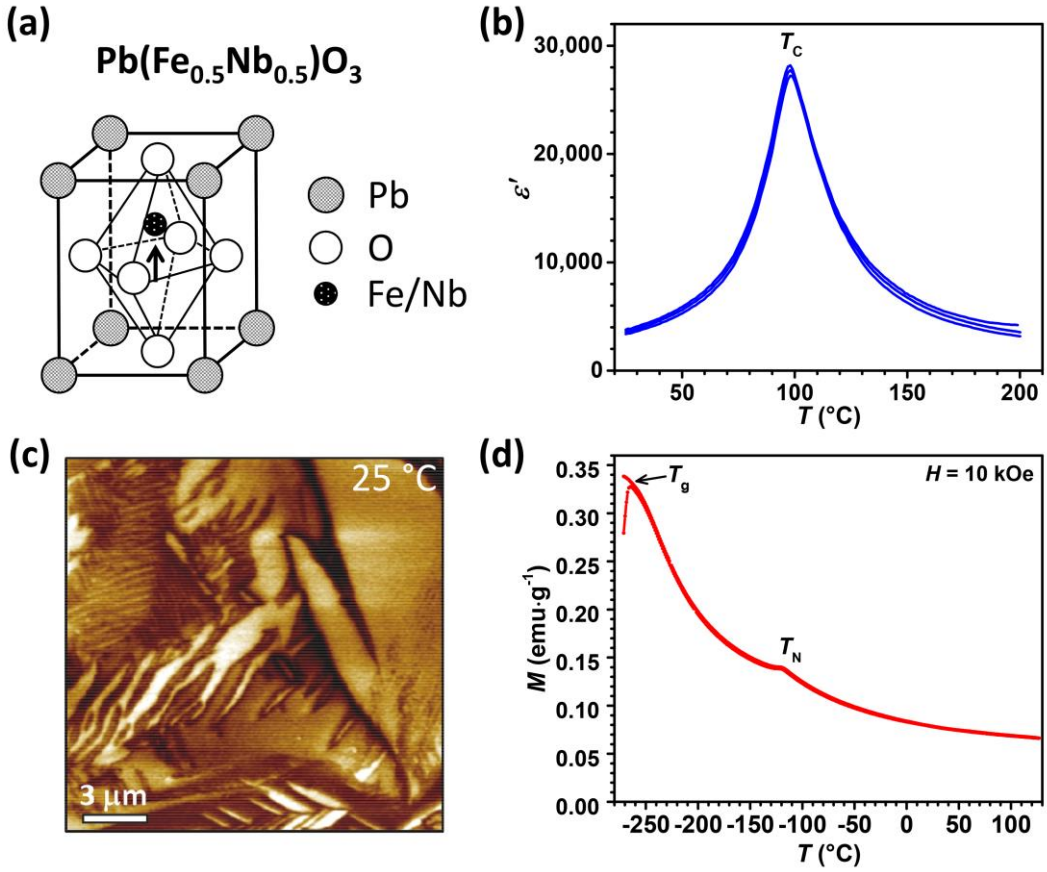


Figure 1.16: (a) Schematic representation of a perovskite unit cell, (b) temperature and frequency dependences of ε', (c) piezo-response force microscopy image of ferroelectric domain structure at RT and (d) temperature dependence of M measured at 10 kOe of PFN ceramics (after [21, 48, 88]).

Despite promising dielectric and ferroelectric properties, i.e., the peak-permittivity temperature slightly above RT and the large spontaneous polarization, prior to this thesis, no studies of EC properties of PFN have been reported. The main reason for this lies in the typically high electrical conductivity of PFN ceramics (in the range of 10^{-6}–10^{-10} $\Omega^{-1}m^{-1}$) [86, 87, 91, 97], which mostly originates from the presence of oxygen vacancies and/or various oxidation states of the Fe ions (2+, 3+ or 4+) [87, 91, 94] that is common for Fe-containing oxides [98, 99]. However, with proper optimization of the synthesis process and effective suppression of the excessive electrical conductivity, PFN-

based materials with their favorable peak-permittivity position, offer a good starting point for achieving improved EC as well as MultiC performance.

1.5.2 Bismuth Ferrite, $BiFeO_3$

Bismuth ferrite, $BiFeO_3$ (BFO), is one of the best-known and well-studied single-phase multiferroic materials, where the ferroelectric and magnetic (antiferromagnetic) orders coexist. In addition, it is a rare example of a single-phase material that exhibits multiferroic properties even above RT [100, 101]. $BiFeO_3$ belongs to the class of lead-free perovskites with the general formula ABO_3 (Figure 1.17a), where multiferroic behavior arises from the ferroelectrically active Bi^{3+} ions (full *d*-orbitals) on the A-site and the magnetically active Fe^{3+} ions (partially filled *d*-orbitals) on the B-site of a perovskite structure [101].

BFO exhibits a structural phase transition from the non-polar paraelectric to the polar ferroelectric phase (T_C) at ~825 °C [101, 102]. Long-range ferroelectric order is clearly evident from the ferroelectric domain structure, where at RT, micron-sized domains are present (Figure 1.17b). On the other hand, BFO exhibits a magnetic structural phase transition from the paramagnetic to the long-range antiferromagnetic order (T_N) at ~370 °C [101, 103, 104]. Similar to PFN, the antiferromagnetic arrangement in BFO derives from Fe-O-Fe linkages, where the magnetic moment of each Fe^{3+} ion is surrounded by six approximately antiparallel-oriented Fe^{3+} neighbors [100, 101, 103]. Additionally, the magnetic spin structure forms a long-range magnetic cycloidal spiral with a period of ~62 nm, resulting in very weak average macroscopic magnetization of the material [100, 104, 105].

Despite a seemingly simple chemical composition, the preparation of single-phase BFO material is extremely difficult. The thermodynamic instability of BFO, the reaction kinetics of the Bi_2O_3-Fe_2O_3 system, the presence of impurities and the volatility of Bi_2O_3 often favor the formation of undesired secondary phases, namely, Bi-rich sillenite (e.g. $Bi_{25}FeO_{39}$) and Fe-rich mullite (e.g. $Bi_2Fe_4O_9$) phases (Figure 1.17c) [102, 105-107]. All these processes can lead to the formation of various charged point defects, which were shown to have a strong influence on the functional properties of the material. This is often reflected in the increased electrical conductivity of the material (usually in the range of 10^{-10}–10^{-2} $\Omega^{-1}m^{-1}$), which can critically affect its dielectric, ferroelectric and electromechanical properties [102, 105, 106].

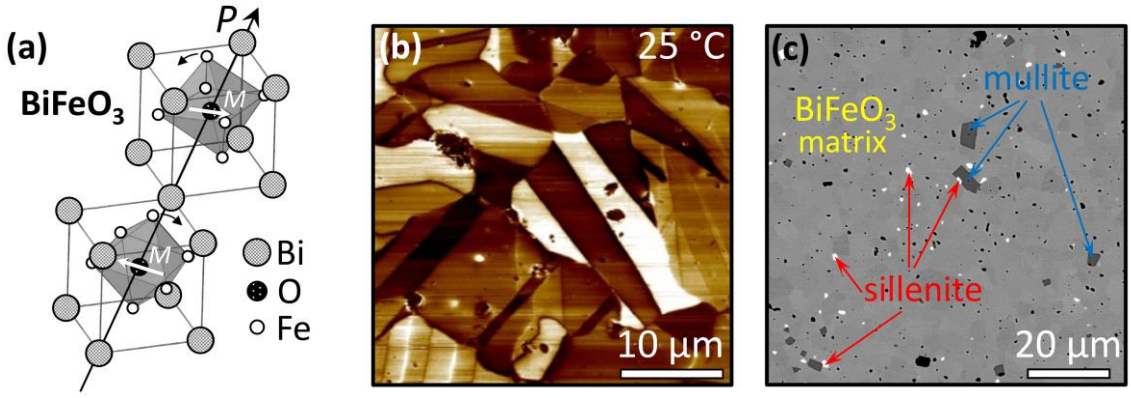


Figure 1.17: (a) Schematic representation of two BFO perovskite unit cells (after [108]), (b) piezo-response force microscopy image of BFO ferroelectric domain structure at RT (after [109]) and (c) scanning electron microscopy image of polished BFO surface, where mullite and sillenite secondary phases are marked with blue and red arrows, respectively (after [110]).

Due to the typically high electrical conductivity and weak spontaneous magnetization, BFO ceramics in unmodified form are not suitable for use in caloric applications. However, with appropriate modifications, i.e., by doping or the formation of solid solutions, as presented in the next section, BFO-based materials can represent promising candidates for achieving good MC as well as MultiC properties.

1.5.3 $Pb(Fe_{0.5}Nb_{0.5})O_3$–$BiFeO_3$ Solid Solutions

The first examples of $Pb(Fe_{0.5}Nb_{0.5})O_3$–$BiFeO_3$ solid solutions were reported in the 1960s [111-114], followed by other studies [115-119]. It was shown that the increasing amount of BFO in the (1-x)PFN–xBFO (PFN–100xBFO) solid solutions shifts the paramagnetic-to-antiferromagnetic phase transition to higher temperatures, i.e. towards the T_N of pure BFO [112, 116]. On the other hand, the addition of BFO to PFN also affects the paraelectric-to-ferroelectric phase-transition temperature. The reported studies indicate that in compositions with low BFO contents ($x < 0.2$) the T_C slightly decreases [111, 113, 118], while in compositions with a high BFO content ($x > 0.2$) the T_C shifts above the one of pure PFN [111, 113, 114, 116, 118, 119]. However, all compositions prepared by classic solid-state synthesis exhibit increased electrical conductivity, leading to high leakage currents and thus poor dielectric and ferroelectric properties [113, 116, 118, 119]. Therefore, for better understanding, a detailed systematic study of the dielectric and ferroelectric properties of this system is still needed.

Nevertheless, the formation of PFN–BFO solid solutions offers a bridge between the low-temperature phase transitions of PFN and the high-temperature phase transitions of BFO, which enables the tailoring of the multiferroic properties and, ideally, may bring both ferroic transitions closer to RT. Since the highest caloric effects are obtained near ferroic phase transitions [6, 30, 53, 71], this system offers a unique opportunity for designing new, room-temperature multicalorics that can be used as active elements in future cooling applications.

1.6 Objectives and Hypotheses of the Dissertation

The main goal of this thesis is to develop new singe-phase multicaloric materials with enhanced EC and MC properties. PFN material represents a good starting point due to its peak-permittivity position slightly above RT, which could lead to increased EC effects near RT. The addition of BFO to PFN and, accordingly, the formation of PFN–BFO solid solutions could further enable tailoring of the magnetic properties by shifting paramagnetic-to-antiferromagnetic phase transition towards RT, which offers the improvement of room-temperature multicaloric properties. In addition, doping with Mn ions can successfully compensate possible charge imbalances in the materials, which could suppress electrical conductivity and consequently enhance EC properties. On the other hand, rare earth elements, such as Gd ions possess strong localized magnetic moments, which can break the long-range antiferromagnetic order and increase the magnetization of the material.

The objectives of this doctoral dissertation are the following:

1.) To optimize the processing conditions of PFN ceramics using mechanochemical-activation-assisted synthesis followed by sintering at different temperatures aiming to prepare samples with low electrical conductivity ($< 10^{-10}\ \Omega^{-1}m^{-1}$) for caloric applications.

2.) To determine the EC and MC properties of optimized PFN ceramics.

3.) To modify PFN ceramics by doping with Mn to decrease the electrical conductivity and consequently enhance the effective EC cooling effect.
4.) To determine the EC and MC properties of optimized Mn-doped PFN ceramics.
5.) To prepare single-phase PFN–100xBFO ($x \leq 0.5$) solid solutions using mechanochemically-activation-assisted synthesis followed by heat treatment.
6.) To study how the addition of BFO into PFN influences the ferroelectric Curie temperature and ferroelectric properties.
7.) To modify selected PFN–100xBFO solid solutions by target doping with Mn and Gd ions, to reduce the electrical conductivity and improve their magnetic properties, respectively.
8.) To study caloric (EC and MC) properties of selected pure, Mn- and Gd-doped PFN–100xBFO solid solutions.

This doctoral dissertation is based on the following hypotheses:
1.) The EC effect of pure PFN is strongly affected by an increased electrical conductivity. Therefore, further modifications of PFN with dopants are required for its improvement.
2.) Due to the very high T_N of BFO, the addition of BFO into the PFN (the formation of PFN–100xBFO solid solution) will shift the magnetic anomalies towards room temperature. At the same time, the high ferroelectric Curie temperature of BFO will also affect the peak-permittivity temperature.
3.) The electrical conductivity of PFN–100xBFO solid solutions increases with increasing content of BFO.
4.) Modification of PFN–100xBFO with Mn will suppress the enhanced electrical conductivity, while Gd will improve the magnetic properties of the PFN–100xBFO solid solution.

Chapter 2

Improving the Multicaloric Properties of $Pb(Fe_{0.5}Nb_{0.5})O_3$ by Controlling the Sintering Conditions and Doping with Manganese

Multiferroic PFN exhibits a paraelectric-to-ferroelectric phase transition slightly above RT, which offers a good starting point for achieving a high room-temperature EC response and thus upgrading the caloric effects of the so-far only known single-phase relaxor PFN–20PMW multicaloric material [41].

In this study, single-phase PFN ceramics were successfully prepared using mechanochemical synthesis, followed by sintering at four different temperatures ranging from 950 °C to 1100 °C. Among them, the ceramic sintered at 1000 °C possessed low dielectric losses, the lowest specific electrical conductivity and, accordingly, exhibited no enhanced conduction at the grain boundaries. However, further evaluation of its multicaloric properties revealed that the excessive electrical conductivity still limits the material's cooling ability, leading to the appearance of Joule heating that degrades the EC cooling effect. For this reason, the multicaloric properties of PFN were further improved by doping with manganese. In fact, 0.5 mol% of added dopant successfully suppressed the excessive electrical conductivity, leading to a superior EC effective cooling effect of ~1.6 °C at RT, while reaching a maximum value of ~2.5 °C at 80 °C (at 140 $kV \cdot cm^{-1}$). At the same time, the MC properties of the material were also improved, resulting in a maximum value of 0.44 °C at −271 °C and 50 kOe.

The Mn-doped PFN multicaloric prepared in this work exhibits the highest EC and MC effects reported to date. The maximum EC and MC effects are located in two different temperature regions, one above and the other below RT, indicating a potential use of such materials in applications where the operating temperature is changing significantly. However, the maximum value of the MC effect is located at cryogenic temperatures and it is only 0.44 °C. Therefore, further work is needed to improve this value.

This chapter addresses thesis objectives 1, 2, 3 and 4.

Published in: U. Prah, T. Rojac, M. Wencka, M. Dragomir, A. Bradeško, A. Benčan, R. Sherbondy, G. Brennecka, Z. Kutnjak, B. Malič and H. Uršič, "Improving the multicaloric properties of $Pb(Fe_{0.5}Nb_{0.5})O_3$ by controlling the sintering conditions and doping with manganese," *J. Eur. Ceram. Soc.*, vol. 39, no. 14, pp. 4122–4130, 2019. (IF = 4.320, 2019)

My contribution: I optimized the synthesis process and prepared the powders and ceramic samples. I performed the scanning electron microscopy, energy-dispersive X-ray spectroscopy and thermal analysis studies, performed the characterization of the electrical properties, measured the EC and calculated the MC effects. I prepared the concept of the paper and jointly wrote the manuscript with the co-authors.

Journal of the European Ceramic Society 39 (2019) 4122–4130

Contents lists available at ScienceDirect

Journal of the European Ceramic Society

journal homepage: www.elsevier.com/locate/jeurceramsoc

Original Article

Improving the multicaloric properties of $Pb(Fe_{0.5}Nb_{0.5})O_3$ by controlling the sintering conditions and doping with manganese

Uroš Prah[a,b], Tadej Rojac[a,b], Magdalena Wencka[c], Mirela Dragomir[d], Andraž Bradeško[a,b], Andreja Benčan[a,b], Rachel Sherbondy[e], Geoff Brennecka[e], Zdravko Kutnjak[a,b], Barbara Malič[a,b], Hana Uršič[a,b,*]

[a] Jožef Stefan Institute, Jamova cesta 39, 1000 Ljubljana, Slovenia
[b] Jožef Stefan International Postgraduate School, Jamova cesta 39, 1000 Ljubljana, Slovenia
[c] Institute of Molecular Physics, Polish Academy of Sciences, ul. Smoluchowskiego 17, 61-179 Poznań, Poland
[d] Department of Chemistry and Chemical Biology, McMaster University, 1280 Main St. W., Hamilton, ON L8S 4L8, Canada
[e] Colorado School of Mines, 1500 Illinois St., Golden, CO 80401, USA

ARTICLE INFO

Keywords:
$Pb(Fe_{0.5}Nb_{0.5})O_3$
Multicaloric
Electrocaloric
Magnetocaloric
Multiferroic

ABSTRACT

Designing multicaloric single-phase materials with combined electro- and magnetocaloric effects is still at its initial stage and presents a number of challenges. One of the main challenges encountered so far is to reduce the excessive electrical conductivity, which leads to the appearance of Joule heating that might completely degrade the electrocaloric response. In this work, multicaloric $Pb(Fe_{0.5}Nb_{0.5})O_3$ material was successfully prepared exhibiting pronounced electrocaloric effect above room temperature and maximum magnetocaloric effect at cryogenic temperature. The conductivity was suppressed by controlling the sintering temperature. The ceramic sintered at 1000 °C exhibits maximum electrocaloric effective cooling of 0.88 °C at 28 °C and maximum magnetocaloric effect of 0.14 °C at −271 °C. The caloric properties can be further improved by doping $Pb(Fe_{0.5}Nb_{0.5})O_3$ with manganese. In comparison to the undoped sample, $Pb(Fe_{0.5}Nb_{0.5})O_3$ doped with 0.5 mol% of manganese exhibits three times higher maxima of electrocaloric effective cooling (2.47 °C at 80 °C) and magnetocaloric temperature change (0.44 °C at −271 °C).

1. Introduction

The majority of commercially used refrigeration systems are still using the vapor-compression refrigeration cycle, which was discovered at the beginning of the 19th century. A solid-state cooling technology represents a promising alterative for their replacement or for usage in fields where vapor-compression technology could not be used, such as cooling of small electronic devices or cooling in harsh environments. Most of the current activity in the research of new cooling technologies is oriented towards one of the caloric effects, either electrocaloric (EC), magnetocaloric (MC) or mechanocaloric (mC), where the material's entropy and consequently its temperature change under the application of external stimuli, i.e., electric field, magnetic field, or stress, respectively [1]. The highest caloric effects are obtained near ferroic phase transitions [1,2], which take place in a very narrow temperature range. For example, gadolinium shows a large MC temperature change of more than 10 °C, but high values are limited to only a few degrees close to the phase transition [3]. Such behavior is also characteristic of ferroelectrics, for example $BaTiO_3$-based ceramics [4]. This narrow temperature range of the highest caloric effects can be partially addressed using relaxor materials, where a high-caloric-effect temperature range coincides with a broad temperature range of typically few tens of degrees [2,5–7].

A possibility of how to extend the operating temperature range of caloric devices is to prepare a multicaloric material [8,9], where two or more single caloric modes can operate at different temperature intervals. This means that one caloric mode is active in one temperature range, while the other caloric mode is active in a different temperature range [10,11]. The principle was already demonstrated in composite $NiCoMnIn/(1–x)Pb(Mg_{1/3}Nb_{2/3})O_3–xPbTiO_3$ material, where the operating temperature window of the material was extended by combining MC and mC effects [11].

In our previous work [10], the multicaloric properties of $0.8Pb(Fe_{0.5}Nb_{0.5})O_3–0.2Pb(Mg_{0.5}W_{0.5})O_3$ (PFN–20PMW) were experimentally confirmed. However, this material possesses small MC and EC temperature changes (~0.25 °C), with the maximum values of both

* Corresponding author at: Jožef Stefan Institute, Jamova cesta 39, 1000 Ljubljana, Slovenia.
E-mail address: hana.ursic@ijs.si (H. Uršič).

https://doi.org/10.1016/j.jeurceramsoc.2019.05.062
Received 11 March 2019; Received in revised form 28 May 2019; Accepted 29 May 2019
Available online 30 May 2019
0955-2219/ © 2019 The Author(s). Published by Elsevier Ltd. This is an open access article under the CC BY license (http://creativecommons.org/licenses/BY/4.0/).

effects far below room temperature (−93 °C for EC and −268 °C for MC). Nevertheless, the PFN–20PMW may be treated as a proof-of-concept material that represent a good starting point for further development of combined MC and EC effects. In this work we focus on Pb($Fe_{0.5}Nb_{0.5}$)O_3 (PFN), which combines both effects with a maximum EC response above room temperature (RT) and a maximum MC response below RT.

In PFN, ferroelectric and magnetic (antiferromagnetic) orders co-exist in the same crystal structure [12]. The paraelectric-to-ferroelectric phase transition of PFN is located at ~100 °C [13,14] indicating that a maximum EC temperature change can be obtained a few ten degrees above RT. Additionally, two anomalies in the temperature dependence of the magnetic susceptibility are reported at −123 °C and −263 °C [15,16], hence a potentially enhanced MC effect is expected close to these temperatures. However, according to the literature, PFN exhibits high electrical conductivity ($10^{-6}-10^{-8}\ \Omega^{-1}\,m^{-1}$ [17,18]), which is common for Fe-containing oxides [19,20]. Such high conductivity may lead to Joule heating effect that lowers the EC cooling efficiency [21,22], but according to the literature the conductivity can be reduced when adding small amounts of manganese [23–26].

To suppress the elevated conductivity of PFN we propose in this study two strategies related to: (i) tailoring of the sintering temperature and (ii) doping with manganese. The results show that optimized sintering conditions as well as dopant concentration lead to significant improvement of the EC and MC properties of the material, pointing out the importance of the processing-composition-properties inter-correlations in PFN.

2. Experimental

2.1. Material synthesis

PFN ceramic powder was prepared by mechanochemical-activation-assisted synthesis using Nb_2O_5 (99.9%, Aldrich), Fe_2O_3 (99.9%, Alfa Aesar) and PbO (99.9%, Alfa Aesar) as starting oxides. Additionally, Fe_2O_3 was pre-milled in a planetary ball mill (Retsch PM 400, Retsch, Haan, Germany) with absolute ethanol at 200 min^{-1} for 6 h. In the case of Mn-doped PFN, 0.5 mol%, 1 mol% and 2 mol% of manganese in the form of MnO_2 (99.9%, Alfa Aesar) were added to the mixture of initial oxides as a substitution for B-site cations (Fe^{3+} and Nb^{5+}) according to the nominal formula Pb($Fe_{0.5-x/2}Nb_{0.5-x/2}Mn_x$)$O_3$. MnO_2 was pre-milled in an attrition mill (Netzsch, PE075/PR01, Selb, Germany) with absolute ethanol at 600 min^{-1} for 5 h using yttria-stabilized zirconia (YSZ) milling balls (ball diameters 3 mm). All the stoichiometric mixtures of starting oxides (110 g) were homogenized in a planetary ball mill at 200 min^{-1} for 4 h in absolute ethanol using YSZ milling balls (ball diameters 3 mm). The homogenized mixture was then dried and mechanochemically activated in a planetary ball mill for 6 h at 360 min^{-1} in a tungsten carbide milling vial (volume 250 cm^3), filled with 10 tungsten carbide milling balls (ball diameters 20 mm). After activation, the synthesized powder was re-milled in a planetary ball mill in an absolute ethanol at 200 min^{-1} for 4 h using YSZ milling balls (ball diameters 3 mm).

All the prepared powders were uniaxially pressed (50 MPa) into pellets of a diameter of 8 mm followed by isostatic pressing at 300 MPa. The powder compacts were reactively sintered in double alumina crucibles in the presence of a PFN packing powder with the same composition as that of the pellets. To examine the effect of the sintering temperature on the caloric properties, PFN compacts were sintered in a temperature range between 950 °C and 1100 °C (with a step of 50 °C) for 2 h in an oxygen atmosphere as previously suggested in Ref. [27]. PFN ceramics doped with 1 mol% and 2 mol% of manganese were sintered at 1000 °C for 2 h in an oxygen atmosphere, while PFN doped with 0.5 mol% of manganese was sintered at 800 °C due to the differences in the sintering behavior in comparison to the other samples (for more details see Supplementary material, S1). In all cases, heating and cooling rates of 2 °C min^{-1} were used.

2.2. Characterization

The densities of the sintered pellets were determined using a gas-displacement density analyzer (Micromeritics, AcuuPyc II 1340 Pycnometer) at RT. For the calculation of the relative density, the theoretical density of 8.46 $g{\cdot}cm^{-3}$ was used (PDF card no. 032-0522, [28]).

The mass loss that corresponds to PbO loss during the sintering process was estimated as the difference between the mass of the pellet heated to 600 °C for 1 h and sintered sample. The temperature of 600 °C for the pre-sintering heat treatment was determined from thermal analyses of the PFN powder with the goal to remove the adsorbed/chemisorbed H_2O and CO_2 prior to sintering. For more details, see Supplementary material, S2. The results were presented as average values of measurements done on three pellets.

The X-ray powder-diffraction (XRD) analyses of crushed ceramic pellets were performed with a PANalytical X'Pert PRO (PANalytical, Almelo, Netherlands) high-resolution diffractometer (Cu$K\alpha_1$ radiation) equipped with a 100 channel X'Celerator detector. Diffraction patterns were recorded in the 20–70° 2θ-range with a step of 0.017° and an integration time of 100 s per step at RT.

The microstructure and phase composition of sintered ceramics was examined using a field-emission scanning electron microscope (FE-SEM, JSM-7600 F, Jeol Ltd., Japan) equipped with an energy dispersive X-ray spectrometer (EDXS, Inca Oxford 350 EDS SSD, Oxford Instruments, Abingdon, U.K.). Prior to microstructural analyses, the samples were fractured for fracture-surface examination, ground and fine-polished using a colloidal silica suspension, followed by thermal etching at 100–350 °C below the sintering temperature of the sample. The average grain size and gran-size distribution were evaluated from the digitalized images of etched surfaces, processed using the Image Tool software (UTHSCSA Image Tool Version 3.00. 2002) [29] and by measuring more than 500 grains. The grain size is expressed as the Feret's diameter [30]. For the study of structural properties on the nanometer scale Cs corrected scanning transmission electron microscope Jeol ARM 200 CF (STEM), equipped with Centurio EDXS system was used. TEM samples were prepared by mechanical grinding, dimpling and final Ar-ion milling [31].

For characterization of electrical properties, the ceramic pellets were cut, thinned and polished to a thickness of ~200 μm. In order to release the internal stresses produced during the mechanical processing, the thinned ceramic pellets were heated up to 600 °C for 1 h (with 5 °C min^{-1} heating rate) and then slowly cooled down (1 °C min^{-1}) to RT. The surfaces of the pellets were coated with Au electrodes (diameter of 5 mm) using RF-magnetron sputtering machine (5Pascal, Italy). Current-density–electric-field (j–E) response was measured using a Keithley 237 (Keithley Instruments, Ohio, USA) high voltage source measure unit. For the j–E measurements, the samples were exposed to step-like voltages within the range of ± 0.5 kV·cm^{-1}. In this range, from negative to positive polarity, ~13 equal field steps were applied. Upon each of these steps, the voltage was maintained constant for 1.5 h for the current to stabilize, before being recorded. The specific DC electrical conductivity (σ_{DC}) was obtained at 0.5 kV·cm^{-1} assuming Ohm's law. The dielectric permittivity (ϵ) and dielectric losses ($tan\delta$) as a function of temperature were analyzed during cooling from 200 °C to 24 °C with a HP 4284A (Hewlett-Packard, California, USA) Precision LCR impedance meter in a frequency range of 1–100 kHz. The P–E loops were measured using an Aixacct TF analyzer 2000 (aixACCT Systems GmbH, Aachen, Germany) by applying single sinusoidal waveform with the frequency of 1 Hz at RT.

Conductive atomic force microscopy (cAFM) images were recorded with an atomic force microscope (AFM, Asylum Research, Molecular Force Probe 3D, Santa Barbara, CA, USA) equipped with an ORCA mode. Prior to the cAFM experiment, surfaces of ceramic samples were

prepared using standard metallographic procedure (thinning, grinding, polishing and fine polishing with SiO_2 particles) followed by heat treatment at 600 °C for 1 h with a cooling rate of 1 °C min^{-1}, in order to release internal stresses in the material. The final thicknesses of the as-prepared samples were ~70 µm. A tetrahedral Si tip (curvature diameter of ~15 nm) on a Si cantilever, both coated with Ti/Ir (Asyelec, AtomicForce F&E GmbH, Mannheim, Germany), was used. cAFM measurements were conducted by applying a DC voltage between the tip and the bottom electrode.

The EC effect was measured using the direct method. The measurements were performed on ~80 µm-thick ceramic samples with sputtered Au electrodes. The direct EC measurements were performed in a modified differential scanning calorimeter (Netzsch DSC 204 F1, Selb, Germany), which allowed a precise temperature stabilization. The temperature changes were measured with a small-bead thermistor glued to the sample; the temperature was measured using a digital multimeter. The EC temperature change (ΔT_{EC}) values presented in this work are the measured maximum temperature changes multiplied by a correction factor of ~1.85, which accounts for the passive part of the sample and also the thermal losses in the gold wires, the silver paste and the thermistor. The details of the method can be found in Ref. [32].

The MC effect was determined by the indirect method [33], where the MC temperature change (ΔT_{MC}) was calculated from the magnetization versus temperature measurements at different magnetic fields (1–50 kOe). Measurements were conducted using a physical property measurement system vibrating sample magnetometer (Quantum Design, California, USA) in a temperature range from −271 °C to 127 °C. The ~30 mg plate-shaped ceramic samples were used. For more details, see Supplementary material, S3.

3. Results and discussion

3.1. Multicaloric properties of PFN ceramics

The sintering conditions and consequently ceramic microstructures, in particular grain size and density, have a strong influence on the EC properties of the $Pb(Mg_{1/3}Nb_{2/3})O_3$–$PbTiO_3$ polycrystalline samples as previously shown in Refs. [34,35]. Therefore, in the first step we investigated the effect of sintering temperature on the electrical conductivity that strongly affects the EC properties in PFN through Joule heating as previously shown in $BaTiO_3$ [21]. In the second step, we investigated the EC as well as MC properties of PFN ceramics prepared at optimized sintering conditions.

We begin by analyzing the structure, phase composition and microstructure of the prepared PFN samples. In Fig. 1a the XRD patterns of crushed ceramic pellets are shown, while Fig. 1b shows the microstructures of the samples. Only peaks corresponding to the PFN perovskite phase are observed. All the ceramics are highly dense, > 98.5% of the theoretical density, with the exception of the sample sintered at 950 °C, which has 97.6% of relative density. This lower density is consistent with the increased number of visible pores in the microstructure of the sample sintered at 950 °C (Fig. 1b; note that some of the dark features are also pull-outs that form during sample cutting and polishing procedures). As expected, the average grain size of samples increases with increasing sintering temperature from 1.0 µm to 4.0 µm (see Fig. 1b). In all the samples unimodal grain size distributions, which indicates the normal grain growth during the sintering process, were observed (Supplementary material, S4).

The temperature dependence of the real permittivity ε' and dielectric loss tangent *tanδ* are shown in Fig. 2a. The measured ε' values are much higher in comparison to the values reported in the literature [13,14,36,37], where ceramic samples were prepared by solid-state synthesis. This could be a consequence of better chemical homogeneity of mechanochemically-activated powder, similar as already reported for $Pb(Sc_{0.5}Nb_{0.5})O_3$ ceramics [38]. The maximum ε' is the lowest for the sample sintered at 950 °C (i.e., ~29,900 at 1 kHz) and the highest for the sample sintered at 1100 °C (i.e., ~37,900 at 1 kHz). In all four samples, the Curie temperature (T_C) is at 99 °C, which is in agreement with the previously reported values [13,14,36]. High ε' were measured also at RT, for example the sample sintered at 1000 °C exhibits ε' of ~3600 at 1 kHz.

The enhanced electrical conductivity of the samples sintered above 1000 °C is reflected in the temperature behavior of *tanδ* (Fig. 2a), especially around RT. The value of *tanδ* at RT and 1 kHz is 0.03 for the sample sintered at 1000 °C, but it increases up to 0.21 when the sintering temperature reaches 1100 °C. The increased electrical conductivity with increasing sintering temperature is also seen in the high electric-field *P-E* hysteresis loops (Supplementary material, S5). At the lower sintering temperatures (950 °C and 1000 °C) sharp ferroelectric hysteresis loops were observed, while at higher sintering temperatures, *P-E* loops become rounded, which indicates the presence of a leakage current. This observation is important because enhanced electrical conductivity limits the EC efficiency of bulk ceramics through Joule heating effects [39]. Therefore, maintaining low electrical conductivity of the material is crucial for EC applications.

To investigate the electrical conductivity of PFN ceramics, *j-E* curves were measured at RT (Fig. 2b). The lowest σ_{DC} was obtained in the sample sintered at 1000 °C, that is $7.1 \cdot 10^{-12}\,\Omega^{-1}$. The sample sintered at 950 °C possesses slightly higher σ_{DC} of $1.9 \cdot 10^{-11}\,\Omega^{-1}\,m^{-1}$ most probably due to the slightly lower density. By increasing the sintering

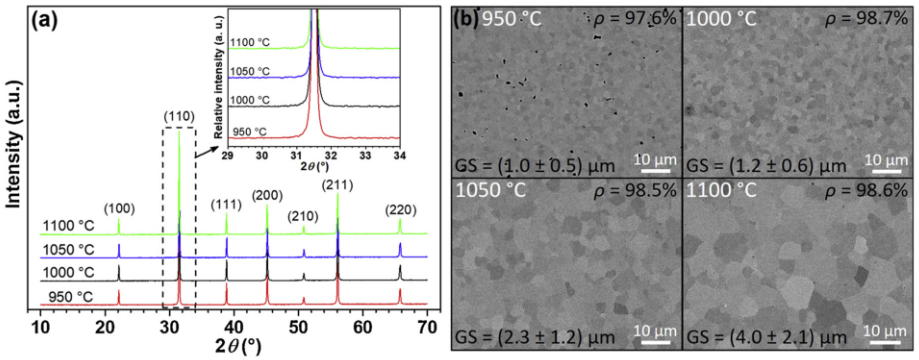


Fig. 1. (a) XRD patterns of PFN ceramics sintered at different temperatures from 950 °C to 1100 °C. The indexed peaks of the perovskite phase are shown in brackets (PDF 032-0522 [28]). Inset shows an enlarged view of the pattern in the 2θ region from 29° to 34°, where no peaks of secondary phases are observed. (b) SEM images of polished samples sintered at different temperatures.

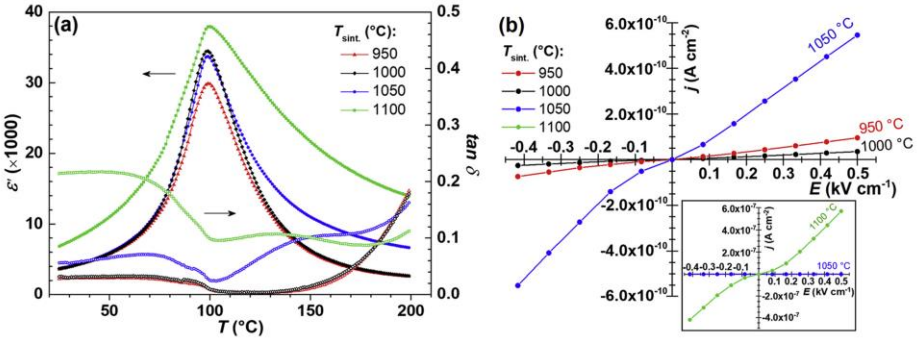


Fig. 2. (a) Temperature dependences of ε′, tanδ and (b) *j-E* curves of PFN ceramics sintered at 950, 1000, 1050 and 1100 °C. Inset shows *j-E* curves of samples sintered at 1050 and 1100 °C. These data are plotted separately due to the much larger electric current measured in the 1100 °C sample.

temperature above 1000 °C, the conductivity of the samples increases significantly. The σ_{DC} of the samples sintered at 1050 °C and 1100 °C are $1.1{\cdot}10^{-10}\Omega^{-1}\,m^{-1}$ and $1.1{\cdot}10^{-7}\,\Omega^{-1}\,m^{-1}$, respectively, which is about one to four orders of magnitude higher than the σ_{DC} measured in the sample sintered at 1000 °C.

To investigate the origin of the elevated conductivity of the sample sintered at the higher temperature (1100 °C), local conductivity measurements were performed using cAFM. As seen in Fig. 3a, in less conductive samples (sintered below 1050 °C) only current noise was detected at electric field of ~4 kV·cm^{-1}, while in the sample sintered at 1050 °C enhanced local conduction was identified at the grain-boundary areas. In the sample sintered at 1100 °C the local conduction was too high, exceeding the maximum current (a few nA), that can be measured with cAFM.

A possible explanation for the increased electrical conductivity of PFN sintered at elevated temperatures (1000, 1050 °C) is the PbO deficiency related to the high volatility of PbO [40]. As shown in Fig. 3b, PbO losses increase with increasing sintering temperature from 0.20 wt % for 950 °C to 0.37 wt% for 1100 °C. Furthermore, SEM and STEM analyses revealed a Pb-rich amorphous phase at the grain boundaries and triple grain junctions in the samples sintered above 1000 °C (Figs. 3c and d) indicating that PbO starts to concentrate in these regions, forms Pb-rich liquid phase before it leaves the system (Supplementary material, S6). Similar was previously observed in $Pb(Mg_{1/3}Nb_{2/3})O_3$–$PbTiO_3$ ceramics, where Pb-rich secondary phase was detected in the samples which experienced PbO losses [41,42].

On the other hand, Fe- and Nb-rich secondary phases were not found in these samples neither by XRD nor SEM analyses. Most probably, B-site cations compensate Pb-losses by stabilizing a Pb-deficient perovskite structure. This is supported by Rietveld refinement analysis that shows a slight decrease in the unit cell volume at higher sintering temperature, which could be related to A-site vacancies (Supplementary material, S7) [43,44].

In Fe-containing compounds, the reason for elevated electrical conductivity is often associated with a change in the oxidation state of iron, but in our samples only Fe^{3+} was detected by electron paramagnetic resonance (EPR) spectroscopy (Supplementary material, S8) that is in agreement with Ref. [45]. According to all these findings, a reason for enhanced electrical conductivity of samples sintered above 1000 °C is the accumulation of secondary phases at the grain

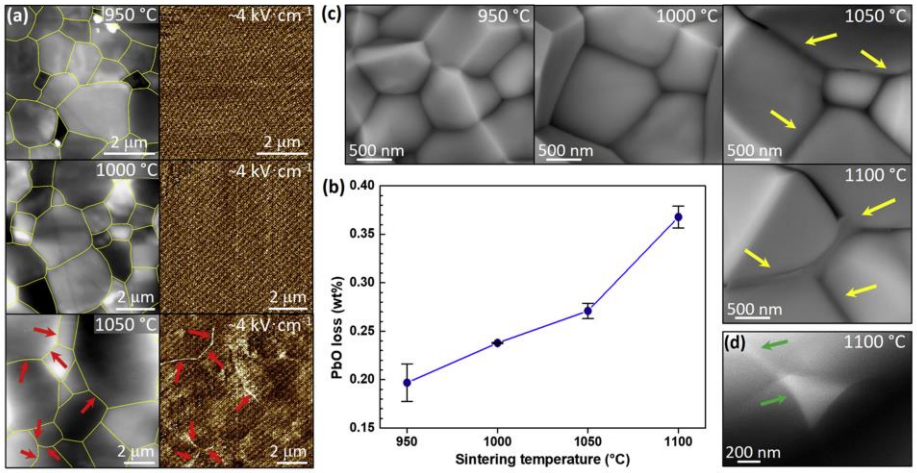


Fig. 3. (a) Topography-height (left) and cAFM (right) images of samples sintered at 950, 1000 and 1050 °C. Yellow lines mark the grain boundaries in the height images. Red arrows in the bottom cAFM image indicate the enhanced conduction measured close to grain boundaries. (b) PbO losses for samples sintered at 950, 1000 and 1100 °C. (c) SEM images of fractured PFN samples. Yellow arrows indicate secondary phase identified at the grain boundaries. (d) STEM image of the sample sintered at 1100 °C, where Pb-rich secondary phase observed at grain boundaries and triple grain junctions is marked by green arrows.

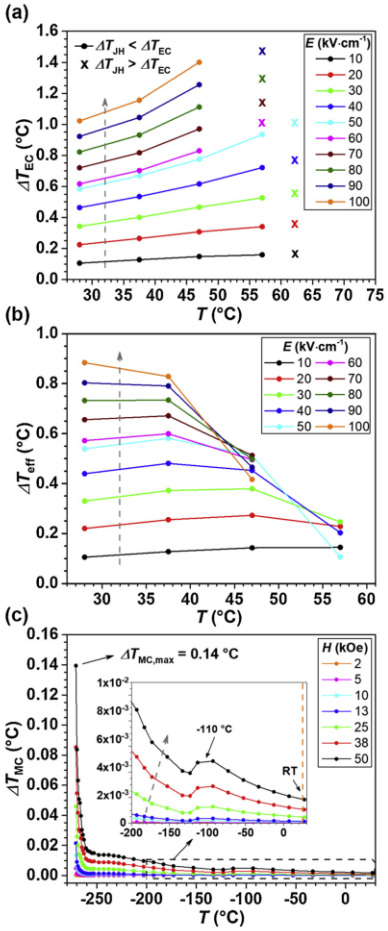


Fig. 4. EC and MC properties of PFN ceramic sintered at 1000 °C; temperature and electric field dependence of (a) ΔT_{EC} and (b) ΔT_{eff}. The crosses mark the measurements where $\Delta T_{JH} > \Delta T_{EC}$. (c) Temperature and magnetic field dependence of ΔT_{MC} with the inset showing an enlarged view of the data between −200 °C and 30 °C. The dashed arrows indicate the increase electric or magnetic field.

boundaries.

Among the PFN ceramics, the one sintered at 1000 °C possesses low dielectric losses, the lowest specific electrical conductivity and, accordingly, exhibits no enhanced conduction at the grain boundaries (the lowest detectable current of ORCA module is ~1 pA [46]). This ceramic is also highly dense (98.7%) and therefore it was chosen for further evaluation of multicaloric properties. Firstly, the EC response of this optimized ceramic sample was measured. The temperature and electric field dependence of ΔT_{EC} is shown in Fig. 4a. At 28 °C and 100 kV·cm^{-1}, ΔT_{EC} is 1.02 °C and it increases with increasing temperature reaching a maximum of 1.40 °C at 47 °C and 100 kV·cm^{-1}. However, at higher temperatures and applied electric fields, the electrical conductivity of the material is increased, which results in the appearance of Joule heating. At 28 °C only a small Joule heating (ΔT_{JH}) was detected, namely 0.14 °C at 100 kV·cm^{-1}, but it significantly increases at higher temperatures; to the value of 0.98 °C at 47 °C and 100 kV·cm^{-1}. At a certain point, the Joule heating starts to overlap the EC cooling effect (marked by crosses in Fig. 4a). Therefore, the EC effective cooling (ΔT_{eff}), defined as a difference between ΔT_{EC} and ΔT_{JH}, was introduced. For more details on Joule heating and EC effective cooling, see Supplementary material, S9. The temperature dependence of ΔT_{eff} is shown in Fig. 4b. As can be seen, the highest value of ΔT_{eff} is 0.88 °C at 28 °C and 100 kV·cm^{-1} and it drops quickly to half when temperature increases to 47 °C.

The temperature dependence of ΔT_{MC} is shown in Fig. 4c. At room temperature, ΔT_{MC} is low, i.e., $1.9 \cdot 10^{-3}$°C at 50 kOe, however, it increases with decreasing temperature and it reaches a maximum of 0.14 °C at −271 °C of sample temperature and 50 kOe. A small peak in the MC temperature response at ~−110 °C is shown in the inset of Fig. 4c. This anomaly is related to the paramagnetic-to-antiferromagnetic phase transition that is visible also in the magnetization versus temperature curves (Supplementary material, S3).

In conclusion of the first part of our study, we showed that PFN may exhibit large electrical conductivity, which critically degrade its EC response by the emergence of Joule heating effects. We demonstrated that the conductivity and thus Joule heating can be controlled with the sintering temperature. According to the literature [25,26,47–50], the electrical conductivity (and consequently Joule heating) of PFN-based materials can be further reduced by the addition of a small amount of manganese. Therefore, in the next part of this study, the caloric properties of Mn-doped PFN samples are discussed.

3.2. Multicaloric properties of Mn-doped PFN ceramics

The XRD patterns of Mn-doped PFN crushed pellets are shown in Fig. 5a. Only the peaks corresponding to the PFN perovskite phase are observed (Fig. 5a) with no additional secondary phase (see inset of Fig. 5a). Rietveld refinement analysis indicates that manganese incorporates into the crystal structure, which is demonstrated in a linear shrinkage of the unit cell volume with increasing content of manganese

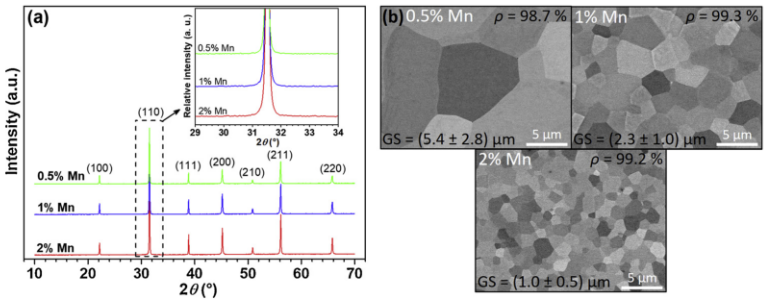


Fig. 5. (a) XRD patterns of PFN ceramics doped with different concentrations of Mn. The indexed peaks of the perovskite phase are shown in brackets (PDF 032-0522 [28]). Inset shows an enlarged view in the 2θ region from 29° to 34° where no peaks of secondary phases are observed. (b) SEM images of polished Mn-doped PFN samples.

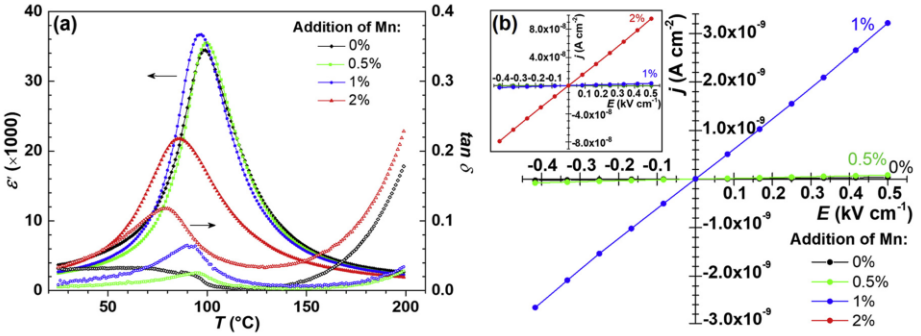


Fig. 6. (a) Temperature dependences of ε', tanδ and (b) *j-E* curves of PFN samples doped with 0.5 mol%, 1 mol% and 2 mol% of manganese. Inset: *j-E* curve of samples doped with 1 mol% and 2 mol% of manganese. These data are plotted separately due to the much larger electric current measured in the 2 mol% Mn-doped sample. The data for undoped PFN sample is added as a reference.

(Supplementary material, S7). As suggested in Ref. [49], the contraction of the crystal lattice is a consequence of a smaller ionic radius of Mn^{4+} compared to Fe^{3+} and Nb^{5+} on B-site of the PFN structure. Incorporation of the manganese ions into the PFN structure was additionally confirmed by EDXS analysis; in the samples with higher dopant concentration larger amount of manganese was detected (Supplementary material, S10).

All the ceramics are highly dense, i.e., equal or more than 98.7% of the theoretical density (Fig. 5b). The average grain size of doped samples decreases with increasing amount of added manganese, i.e., from 5.4 μm in the sample doped with 0.5 mol% to 1.0 μm in the sample with 2 mol% of manganese. Despite the fact that the sample doped with 0.5 mol% was sintered 200 °C lower than the other samples, it has the largest grain size, indicating a liquid-assisted sintering process [25] (detailed explanation in Supplementary material, S1). In all samples unimodal grain size distributions were observed (Supplementary material, S4).

The temperature dependence of ε' and *tanδ* is shown in Fig. 6a. In the samples with smaller amount of added dopant (0.5 mol% and 1 mol %), T_C is almost unchanged compared to pure PFN (99 °C), but in the sample doped with 2 mol% of Mn, T_C is shifted towards lower temperatures, i.e., 86 °C. A reason for this could also be related to a smaller ionic radius of Mn^{4+} compared to Fe^{3+} and Nb^{5+} [49]. The maximum value of ε' in the samples doped with 0.5 mol% and 1 mol% of manganese is comparable to the value obtained in undoped PFN (~36,000 at 1 kHz), while in the sample with 2 mol% of added dopant, the peak-permittivity value is lower (~22,000). The peak-permittivity values and T_C are comparable with previously reported studies [25,26,47].

At RT an increasing trend in *tanδ* with the addition of manganese was observed (Fig. 6a), where the lowest value of *tanδ* was obtained in 0.5 mol% Mn-doped sample (0.005 at 1 kHz) and the highest one in the 2 mol% Mn-doped sample (0.034 at 1 kHz). At higher temperatures, the difference is even more pronounced. For example, at 200 °C *tanδ* of 0.5 mol% Mn-doped sample is 0.028, however, it increases for almost ten times (0.228) by adding 2 mol% of Mn. The increased electrical conductivity in the sample is evident also in the high electric-field *P-E* hysteresis loops (Supplementary material, S5). In all the samples, typical ferroelectric hysteresis loops were obtained, but in samples with 1 mol% and 2 mol% of manganese slightly rounded edges indicate higher electrical conductivity. To further investigate the electrical conductivity of Mn-doped samples, *j-E* curves were measured at RT (Fig. 6b). The lowest σ_{DC} was obtained in the sample doped with 0.5 mol% of manganese, i.e. $1.6{\cdot}10^{-11}\ \Omega^{-1}\,m^{-1}$, but the value is slightly higher compared to the undoped sample ($7.1{\cdot}10^{-12}\ \Omega^{-1}\,m^{-1}$). However, at higher applied electric fields, the Mn-doped sample is less conductive than the pure one (Supplementary material, S5). With a further increase in the content of Mn, the conductivity of the samples is greatly increased. The σ_{DC} of the samples doped with 1 mol% and 2 mol % of manganese are $6.4{\cdot}10^{-10}\ \Omega^{-1}\,m^{-1}$ and $1.9{\cdot}10^{-8}\ \Omega^{-1}\,m^{-1}$, respectively, which is about one to three orders of magnitude higher in comparison to the 0.5 mol% Mn-doped sample, respectively.

To check the origin of elevated electrical conductivity at higher concentration of manganese, local conductivity measurements were performed using cAFM. Fig. 7 shows cAFM images at ~15 kV·cm^{-1}. In the 0.5 mol% Mn-doped sample no cAFM signal was detected, while in the sample with 1 mol% of added dopant, enhanced electrical conduction at the grain boundaries was observed (marked with arrows in Fig. 7). The effect is even more pronounced in the sample doped with 2 mol% of manganese. In the literature it is suggested [26,50,51] that at such high concentration of added dopant, MnO_2 can start to concentrate at the grain boundaries, resulting in increased electrical conductivity. The accumulation of manganese at the grain boundaries is supported by the EDXS analysis on the thermally etched surface of 2 mol% Mn-doped sample, where Mn-rich secondary phase was observed (Supplementary material, S4), but it was not directly observed by STEM, due to the problems with TEM-sample preparation (Supplementary material, S6).

Among the Mn-doped PFN ceramics, the PFN with 0.5 mol% of added manganese possesses the lowest dielectric losses, the lowest specific electrical conductivity and exhibits no enhanced conduction at the grain boundaries (within the sensitivity limit of cAFM). This ceramic is also highly dense (98.7%) and it was chosen for further evaluation of multicaloric properties. Firstly, the EC effect of this sample was measured. The temperature and electric field dependence of ΔT_{EC} and ΔT_{eff} are shown in Fig. 8a and 8b. At 28 °C and 140 kV·cm^{-1}, ΔT_{EC} is 1.62 °C and negligible Joule heating was detected (i.e. ΔT_{JH} ~0.03 °C), resulting in ΔT_{eff} of 1.59 °C. By increasing the temperature and applied electric field, ΔT_{EC} increases to high values, reaching 3.69 °C at 114 °C and 100 kV·cm^{-1}, which is comparable to the best EC values obtained in ceramic samples [34,52,53]. However, at the same time the Joule heating significantly increases, resulting in ΔT_{eff} of only 0.30 °C at 114 °C and 100 kV·cm^{-1} (Fig. 8b). At temperatures higher than 114 °C, the Joule heating starts to exceed the EC cooling effect ($\Delta T_{JH} > \Delta T_{EC}$). However, note that in 0.5 mol% doped PFN the values of ΔT_{eff} are higher than 1.5 °C in a broad temperature range (between RT and 95 °C) and reaches 2.47 °C at 80 °C and 140 kV·cm^{-1}. That makes Mn-doped PFN ceramic more promising for multicaloric cooling applications than pure PFN (Fig. 4b).

The temperature dependence of ΔT_{MC} is shown in Fig. 8c. Compared to the undoped PFN (Fig. 4c), the ΔT_{MC} values of 0.5 mol% Mn doped PFN are higher in the whole measured temperature range, which is related to higher magnetization values. At RT and 50 kOe, ΔT_{MC} is

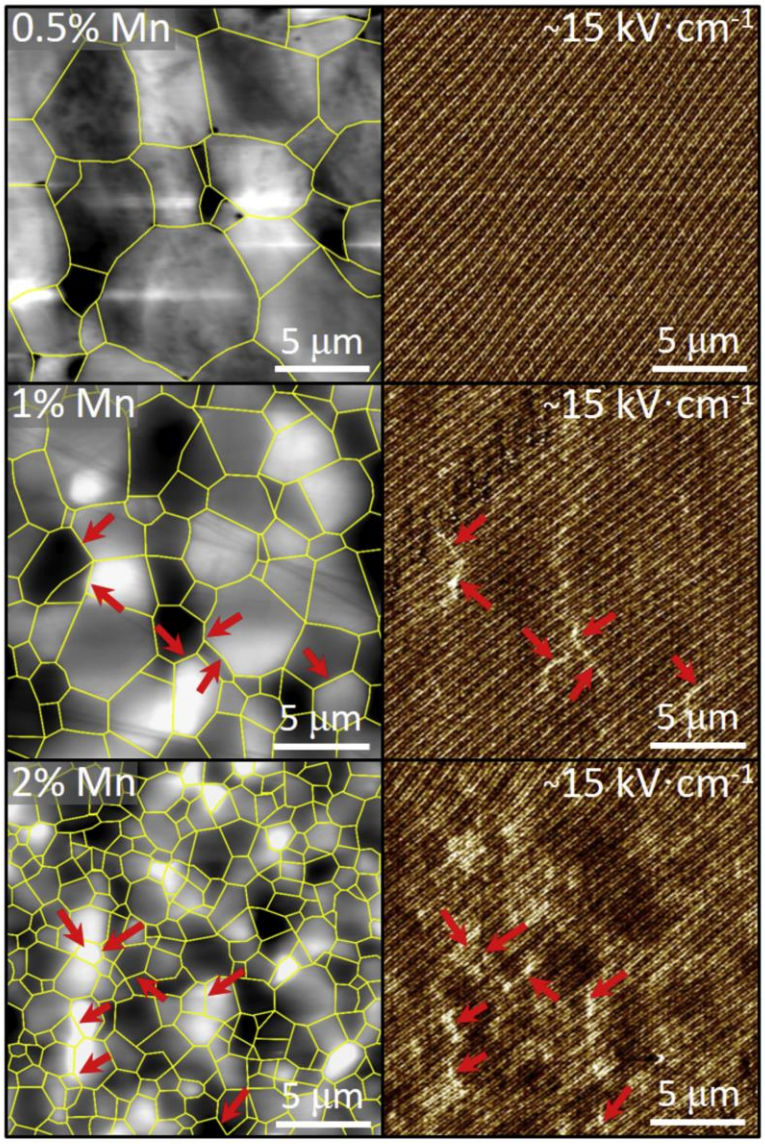


Fig. 7. Topography-height (left) and cAFM (right) images of Mn-doped PFN samples. Yellow lines mark the grain boundaries in the height images. Red arrows indicate the enhanced conduction at grain boundary regions.

$2.6 \cdot 10^{-3}$ °C, however it is increasing with decreasing temperature. At −125 °C a small peak in the ΔT_{MC} appears (inset of Fig. 8c) due to paramagnetic-to-antiferromagnetic phase transition that is visible also in the magnetization versus temperature curves (Supplementary material, S3), similarly as observed in the undoped PFN (Fig. 4c). The ΔT_{MC} reaches the maximum of 0.44 °C at −271 °C and 50 kOe. This value is more than three times higher than the one of undoped PFN (Fig. 4c).

4. Summary and conclusions

In this work, single-phase PFN ceramics that combine EC and MC properties were successfully prepared by mechanochemical synthesis followed by sintering at different temperatures. Electrical conductivity plays a crucial role in material's EC cooling ability, therefore, in the first part, the influence of sintering conditions on electrical conductivity and consequently on EC properties of PFN were investigated. The conductivity was successfully suppressed with a proper optimization of the sintering conditions, whereby the sample sintered at 1000 °C exhibits

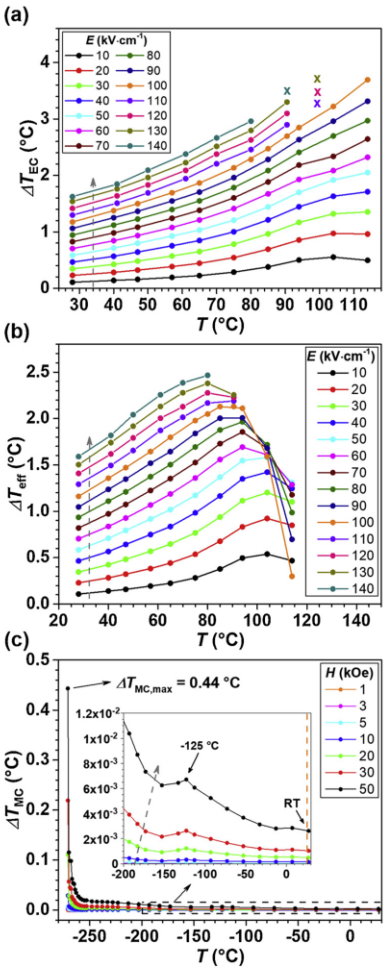


Fig. 8. EC and MC properties of PFN ceramics doped with 0.5 mol% of manganese; temperature and electric filed dependence of (a) ΔT_{EC} and (b) ΔT_{eff}. (c) Temperature and magnetic field dependence of ΔT_{MC} with the inset showing the enlarged view of the data between −200 °C and 30 °C. The dashed arrows indicate the increase electric or magnetic field.

the best properties, i.e., high density (98.7%), low dielectric losses (0.03 at RT and 1 kHz) and the lowest specific electrical conductivity ($7.1 \cdot 10^{-12}\ \Omega^{-1}\,m^{-1}$ at RT). The maximum values of ΔT_{eff} and ΔT_{MC} of this sample are 0.88 °C at 28 °C (100 kV·cm^{-1}) and 0.14 °C at −271 °C (50 kOe), respectively. At higher sintering temperature, PbO starts to concentrate at the grain boundaries, which results in increased electrical conductivity of the material and leads to the appearance of Joule heating.

EC as well as MC properties of PFN were further improved by doping with manganese. By adding 1 mol% and 2 mol% of manganese, enhanced conductivity, most probably related with the accumulation of MnO_2 at the grain boundaries, was observed. A smaller amount of dopant, i.e., 0.5 mol%, successfully suppresses the conductivity even at higher temperatures, leading to superior EC properties of 2.47 °C at 80 °C and 140 kV·cm^{-1}. At the same time, the MC properties of the material are improved, resulting in ΔT_{MC} of 0.44 °C at -271 °C and 50 kOe. Both caloric values are approximately three times higher than the ones of undoped PFN.

In conclusion, by appropriate optimization of the sintering conditions and doping with manganese, we managed to prepare a multicaloric material with the highest electrocaloric and magnetocaloric effects reported so far. The maximum effects are located in two different temperature regions, one above and the other below room temperature, indicating a potential use of such materials in applications where the operating temperature is significantly changing, for example in harsh environments such as space and extreme measurement conditions (liquid-nitrogen temperatures). However, the maximum value of MC effect is located at cryogenic temperatures and it is still too small for any practical use. Using our results as a starting point, further research in this area is needed to prepare better materials that can be used as multicaloric elements in hybrid solid-state cooling devices.

Acknowledgements

The authors thank the financial support from the Slovenian Research Agency (project *Multicaloric cooling* J2-9253, young researcher project PR-07594 and research core funding No. P2-0105), JECS Trust (Contract No. 2017137) and joint research project between Polish and Slovenian Academy of Sciences "*Multicaloric relaxor materials for new cooling technologies*". Technical support by Brigita Kmet, Ana Hedl from JSI and Ana Čukman, Marija Lovreković, Matija Buljan (Erasmus + programme) is gratefully acknowledged. Centre of Excellence NAMASTE is acknowledged for access to the AFM equipment.

Appendix A. Supplementary data

Supplementary material related to this article can be found, in the online version, at doi:https://doi.org/10.1016/j.jeurceramsoc.2019.05.062.

References

[1] X. Moya, S. Kar-Narayan, N.D. Mathur, Caloric materials near ferroic phase transitions, Nat. Mater. 13 (2014) 439–450, https://doi.org/10.1038/nmat3951.
[2] B. Rožič, M. Kosec, H. Uršič, J. Holc, B. Malič, Q.M. Zhang, R. Blinc, R. Pirc, Z. Kutnjak, Influence of the critical point on the electrocaloric response of relaxor ferroelectrics, J. Appl. Phys. 110 (064118) (2011) 1–5, https://doi.org/10.1063/1.3641975.
[3] V.K. Pecharsky, K.A. Gschneidner Jr, Magnetocaloric effect and magnetic refrigeration, J. Magn. Magn. Mater. 200 (1999) 44–56, https://doi.org/10.1016/S0304-8853(99)00397-2.
[4] Y. Bai, X. Han, X.-C. Zheng, L. Qiao, Both high reliability and giant electrocaloric strength in $BaTiO_3$ ceramics, Sci. Rep. 3 (02895) (2013) 1–5, https://doi.org/10.1038/srep02895.
[5] B. Rožič, B. Malič, H. Uršič, J. Holc, M. Kosec, Z. Kutnjak, Direct measurements of the electrocaloric effect in bulk $PbMg_{1/3}Nb_{2/3}O_3$ (PMN) ceramics, Ferroelectrics 421 (2011) 103–107, https://doi.org/10.1080/00150193.2011.594742.
[6] J. Peräntie, H.N. Tailor, J. Hagberg, H. Jantunen, Z.-G. Ye, Electrocaloric properties in relaxor ferroelectric $(1-x)Pb(Mg_{1/3}Nb_{2/3})O_3$–$xPbTiO_3$ system, J. Appl. Phys. 114 (174105) (2013) 1–6, https://doi.org/10.1063/1.4829012.
[7] T. Kimura, Y. Tomioka, R. Kumai, Y. Okimoto, Y. Tokura, Diffuse phase transition and phase separation in Cr-Doped $Nd_{1/2}Ca_{1/2}MnO_3$: a relaxor ferromagnet, Phys. Rev. Lett. 83 (1999) 3940–3943, https://doi.org/10.1103/PhysRevLett.83.3940.
[8] M.M. Vopson, The multicaloric effect in multiferroic materials, Solid State Commun. 152 (2012) 2067–2070, https://doi.org/10.1016/j.ssc.2012.08.016.
[9] E. Stern-Taulats, T. Castan, L. Manosa, A. Planes, N.D. Mathur, X. Moya, Multicaloric materials and effects, MRS Bull. 42 (2018) 295–299, https://doi.org/10.1557/mrs.2018.72.
[10] H. Uršič, V. Bobnar, B. Malič, C. Filipič, M. Vrabelj, S. Drnovšek, Y. Jo, M. Wencka, Z. Kutnjak, A multicaloric material as a link between electrocaloric and magnetocaloric refrigeration, Sci. Rep. 6 (26629) (2016) 1–5, https://doi.org/10.1038/srep26629.
[11] Y.-Y. Gong, D.-H. Wang, Q.-Q. Cao, E.-K. Liu, J. Liu, Y.-W. Du, Electric field control of the magnetocaloric effect, Adv. Mater. 27 (2015) 801–805, https://doi.org/10.1002/adma.201404725.
[12] T. Watanabe, K. Kohn, Magnetoelectric effect and low temperature transition of $PbFe_{0.5}Nb_{0.5}O_3$ single crystal, Phase Transit. A Multinatl. J. 15 (1989) 57–68, https://doi.org/10.1080/01411598908206837.

[13] C.C. Chiu, S.B. Desu, Microstructure and properties of lead ferroniobate ceramics ($Pb(Fe_{0.5}Nb_{0.5})O_3$), Mater. Sci. Eng. B21 (1993) 26–35, https://doi.org/10.1016/0921-5107(93)90261-K.
[14] S. Ananta, N.W. Thomas, Relationships between sintering conditions, microstructure and dielectric properties of lead Iron niobate, J. Eur. Ceram. Soc. 19 (1999) 1873–1881, https://doi.org/10.1016/S0955-2219(98)00290-8.
[15] R. Havlicek, J. Poltierova Vejpravova, D. Bochenek, Structure and magnetic properties of perovskite-like multiferroic $PbFe_{0.5}Nb_{0.5}O_3$, J. Phys. Conf. Ser. 200 (012058) (2010) 1–4, https://doi.org/10.1088/1742-6596/200/1/012058.
[16] S. Chillal, M. Thede, F.J. Litterst, S.N. Gvasaliya, T.A. Shaplygina, S.G. Lushnikov, A. Zheludev, Microscopic coexistence of antiferromagnetic and spin-glass states, Phys. Rev. B 87 (220403) (2013) 1–5, https://doi.org/10.1103/PhysRevB.87.220403.
[17] K. Wojcik, K. Zieleniec, M. Milata, Electrical properties of lead Iron niobate PFN, Ferroelectrics 289 (2003) 107–120, https://doi.org/10.1080/00150190390221331.
[18] E.V. Barabanova, O.V. Malyshkina, A.M. Lotonov, N.D. Gavrilova, The effect of conductivity on the dielectric response of PFN ceramics, Ferroelectrics 442 (2013) 144–148, https://doi.org/10.1080/00150193.2013.778569.
[19] V.L. Kozhevnikov, I.A. Leonidov, M.V. Patrakeev, E.B. Mitberg, K.R. Poeppelmeier, Electrical properties of the ferrite $SrFeO_y$ at high temperatures, J. Solid State Chem. 158 (2000) 320–326, https://doi.org/10.1006/jssc.2001.9120.
[20] E.T. Wefring, M.-A. Einarsrud, T. Grande, Electrical conductivity and thermopower of $(1 - x)BiFeO_3 - xBi_{0.5}K_{0.5}TiO_3$ (x = 0.1, 0.2) ceramics near the ferroelectric to paraelectric phase transition, Phys. Chem. Chem. Phys. 17 (2015) 9420–9428, https://doi.org/10.1039/C5CP00266D.
[21] M. Quintero, L. Ghivelder, F. Gomez-Marlasca, F. Parisi, Decoupling electrocaloric effect from Joule heating in a solid state cooling device, Appl. Phys. Lett. 99 (232908) (2011) 1–3, https://doi.org/10.1063/1.3665949.
[22] M. Quintero, P. Gaztanaga, I. Irurzun, Intrinsic leakage and adsorption currents associated with the electrocaloric effect in multilayer capacitors, Appl. Phys. Lett. 151901 (2015) 1–4, https://doi.org/10.1063/1.4933048.
[23] S.O. Leontsev, R.E. Eitel, Dielectric and piezoelectric properties in Mn-Modified $(1–x)BiFeO_3–xBaTiO_3$ ceramics, J. Am. Ceram. Soc. 92 (2009) 2957–2961, https://doi.org/10.1111/j.1551-2916.2009.03313.x.
[24] J. Kulawik, D. Szwagierczak, Dielectric properties of manganese and cobalt doped lead iron tantalate ceramics, J. Eur. Ceram. Soc. 27 (2007) 2281–2286, https://doi.org/10.1016/j.jeurceramsoc.2006.07.010.
[25] A.V. Pavlenko, N.A. Boldyrev, L.A. Reznichenko, I.A. Verbenko, G.M. Konstantinov, L.A. Shilkina, Microstructure and dielectric and piezoelectric properties of $PbFe_{0.5}Nb_{0.5}O_3$ ceramics modified with Li_2CO_3 and MnO_2, Inorg. Mater. Appl. Res. 50 (2014) 750–756, https://doi.org/10.1134/S0020168514070115.
[26] B. Fang, Y. Shan, H. Imoto, Charge compensation mechanism decreases dielectric loss in manganese-doped $Pb(Fe_{1/2}Nb_{1/2})O_3$ ceramics, Jap. J. Appl. Phys. 43 (2004) 2568–2571, https://doi.org/10.1143/Fjjap.43.2568.
[27] R. Font, O. Raymond-Herrera, L. Mestres, J. Portelles, J. Fuentes, J.M. Siqueiros, Improvement of the dielectric and ferroelectric properties of multiferroic $Pb(Fe_{1/2}Nb_{1/2})O_3$ ceramics processed in oxygen atmosphere, J. Mater. Sci. 51 (2016) 6319–6330, https://doi.org/10.1007/s10853-016-9928-1.
[28] D. Pfoertsch, C. Ruud, Penn State University, University Park, Pennsylvania, USA, ICDD Grant-in-Aid, PDF No. 032-0522, (1981).
[29] D. Wilcox, B. Dove, B. McDavid, D. Greer, UTHSCSA Image Tool for Windows Version 3.0, University of Texas Health Science Center, San Antonio, TX, 2002http://compdent.uthscsa.edu/dig/itdesc.html.
[30] W.H. Walton, Feret`s statistical diameter as a measure of particle size, Nature 162 (1948) 329–330, https://doi.org/10.1038/162329b0.
[31] D.B. Williams, C.B. Carter, Transmission Electron Microscopy. A Textbook for Materials Science, Springer, Boston, MA, USA, 2009, https://doi.org/10.1007/978-0-387-76501-3.
[32] Z. Kutnjak, B. Rožič, Indirect and direct measurements of the electrocaloric effect, in: T. Correia, Q. Zhang (Eds.), Electrocaloric Materials. New Generation of Coolers, Springer, Berlin, Heidelberg, 2014, pp. 147–182.
[33] A. Kitanovski, J. Tušek, U. Tomc, U. Plaznik, M. Ožbolt, A. Poredoš, Magnetocaloric Energy Conversion. From Theory to Applications, Springer International Publishing, Switzerland, 2015.
[34] M. Vrabelj, H. Uršič, Z. Kutnjak, B. Rožič, S. Drnovšek, A. Benčan, V. Bobnar, L. Fulanović, Barbara Malič, Large electrocaloroc effect in grain-size-engineered $0.9Pb(Mg_{1/3}Nb_{2/3})O_3$-$0.1PbTiO_3$, J. Eur. Ceram. Soc. 36 (2016) 75–80, https://doi.org/10.1016/j.jeurceramsoc.2015.09.031.
[35] H. Uršič, L. Fulanović, M. Vrabelj, Z. Kutnjak, B. Rožič, S. Drnovšek, B. Malič, Electrocaloric properties of $0.7Pb(Mg_{1/3}Nb_{2/3})O_3$–$0.3PbTiO_3$ ceramics with different grain sizes, Adv. Appl. Ceram. 115 (2016) 77–80, https://doi.org/10.1080/17436753.2015.1116724.
[36] M. Yokosuka, Electrical and electromechanical properties of hot-pressed $Pb(Fe_{1/2}Nb_{1/2})O_3$ ferroelectric ceramics, J. Appl. Phys. 32 (1993) 1142–1146, https://doi.org/10.1143/Fjjap.32.1142.
[37] D. Bochenek, Z. Surowiak, An influence of the synthesis conditions on the PFN ceramics properties, Acta Phys. Pol. A 116 (2009) 271–273, https://doi.org/10.12693/APhysPolA.116.271.
[38] H. Uršič, A. Benčan, G. Dražič, G. Esteves, J.L. Jones, T.-M. Usher, T. Rojac, S. Drnovšek, M. Deluca, J. Jouin, V. Bobnar, G. Trefalt, J. Holc, B. Malič, Unusual structural-disorder stability of mechanochemically derived-$Pb(Sc_{0.5}Nb_{0.5})O_3$, J. Mater. Chem. C 3 (2015) 10309–10315.
[39] M. Valant, Electrocaloric materials for future solid-state refrigeration technologies, Prog. Mater. Sci. 57 (2012) 980–1009, https://doi.org/10.1016/j.pmatsci.2012.02.001.
[40] A.I. Kingon, J.B. Clark, Sintering of PZT ceramics: I, atmosphere control, J. Am. Ceram. Soc. 66 (1983) 253–256, https://doi.org/10.1111/j.1151-2916.1983.tb15708.x.
[41] M. Villegas, A.C. Caballero, M. Kosec, C. Moure, P. Duran, J.F. Fernandez, Effect of PbO excess in $Pb(Mg_{1/3}Nb_{2/3})O_3$–$PbTiO_3$ ceramics: part I. Sintering and dielectric properties, J. Mater. Res. 14 (1999) 891–897, https://doi.org/10.1557/JMR.1999.0119.
[42] M. Villegas, J.F. Fernandez, A.C. Caballero, Z. Samardija, G. Drazic, M. Kosec, Effect of PbO excess in $Pb(Mg_{1/3}Nb_{2/3})O_3$–$PbTiO_3$ ceramics: part II. Microstructure development, J. Mater. Res. 14 (1999) 898–905, https://doi.org/10.1557/JMR.1999.0120.
[43] A.V. Kovalevsky, A.A. Yaremchenko, S. Populoh, A. Weidenkaff, J.R. Frade, Effect of A-Site cation deficiency on the thermoelectric performance of donor-substituted strontium titanate, J. Phys. Chem. C 118 (2014) 4596–4606, https://doi.org/10.1021/jp409872e.
[44] Y. Sun, J. Li, Y. Zeng, B. Shalchi Amirkhiz, M. Wang, Y. Behnamian, J. Luo, A-site deficient perovskite: the parent for in situ exsolution of highly active, regenerable nanoparticles as SOFC anodes, J. Mater. Chem. A Mater. Energy Sustain. 3 (2015) 11048–11056, https://doi.org/10.1039/c5ta01733e.
[45] R. Blinc, P. Cevc, A. Zorko, J. Holc, M. Kosec, Z. Trontelj, J. Pirnat, N. Dalal, V. Ramachandran, J. Krzystek, Electron paramagnetic resonance of magnetoelectric $Pb(Fe_{1/2}Nb_{1/2})O_3$, J. Appl. Phys. 101 (033901) (2007) 1–5, https://doi.org/10.1063/1.2432309.
[46] Orca – conductive AFM imaging using the MFP-3D, Manual, 2019.
[47] R. Sun, W. Tan, B. Fang, Perovskite phase formation and electrical properties of Pb $(Fe_{1/2}Nb_{1/2})O_3$ ferroelectric ceramics, Physica Status Solidi A Appl. Res. 206 (2009) 326–331, https://doi.org/10.1002/pssa.200824432.
[48] D. Bochenek, P. Guzdek, Ferroelectric and magnetic properties of ferroelectromagnetic $PbFe_{1/2}Nb_{1/2}O_3$ type ceramics, J. Magn. Magn. Mater. 323 (2011) 369–374, https://doi.org/10.1016/j.jmmm.2010.09.046.
[49] K.B. Park, K.H. Yoon, Dielectric properties of $xPb(Fe_{1/2}Nb_{1/2})O_3$-$(1-x)Pb(Co_{1/3}Nb_{2/3})O_3$ ceramic prepared by molten salt synthesis method, Ferroelectrics 145 (1993) 195–203, https://doi.org/10.1080/00150199308222447.
[50] H. Takahara, Effect of manganese oxide additive on the dielectric properties of mixed-sintering ceramics, J. Am. Ceram. Soc. 72 (1989) 1532–1535, https://doi.org/10.1111/j.1151-2916.1989.tb07700.x.
[51] V.V. Klimov, N.I. Selikova, A.N. Bronnikov, Effect of MnO_2, Bi_2O_3, and ZnO additions on the electrical properties of lead zirconate titanate piezoceramics, Inorg. Mater. Appl. Res. 42 (2006) 573–577, https://doi.org/10.1134/S0020168506050219.
[52] R. Zhang, S. Peng, D. Xiao, Y. Wang, B. Yang, J. Zhu, P. Yu, W. Zhang, Preparation and characterization of $(1–x)Pb(Mg_{1/3}Nb_{2/3})O_3$–$xPbTiO_3$ electrocaloric ceramics, Cryst. Res. Technol 33 (1998) 827–832, https://doi.org/10.1002/(SICI)1521-4079(1998)33:5<827::AID-CRAT827>3.0.CO;2-H.
[53] X.-S. Qian, H.-J. Ye, Y.-T. Zhang, H. Gu, X. Li, C.A. Randall, Q.M. Zhang, Giant electrocaloric response over a broad temperature range in modified $BaTiO_3$ ceramics, Adv. Funct. Mater. 24 (2014) 1300–1305, https://doi.org/10.1002/adfm.201302386.

SUPPLEMENTARY MATERIAL

Improving the multicaloric properties of $Pb(Fe_{0.5}Nb_{0.5})O_3$ by controlling the sintering conditions and doping with manganese

Uroš Prah,[a,b] Tadej Rojac,[a,b] Magdalena Wencka,[c] Mirela Dragomir,[d] Andraž Bradeško,[a,b] Andreja Benčan,[a,b] Rachel Sherbondy,[e] Geoff Brennecka,[e] Zdravko Kutnjak,[a,b] Barbara Malič,[a,b] and Hana Uršič[a,b]

[a] Jožef Stefan Institute, Jamova cesta 39, 1000 Ljubljana, Slovenia.
[b] Jožef Stefan International Postgraduate School, Jamova cesta 39, 1000 Ljubljana, Slovenia.
[c] Institute of Molecular Physics, Polish Academy of Sciences, ul. Smoluchowskiego 17, 61-179 Poznań, Poland.
[d] Department of Chemistry and Chemical Biology, McMaster University, 1280 Main St. W., Hamilton, ON, L8S 4L8 Canada.
[e] Colorado School of Mines, 1500 Illinois St., Golden, CO 80401, USA.

S1. Sintering behavior of samples

The dynamic sintering curves of the powder compacts were recorded during heating (5 °C·min^{-1}) using an optical dilatometer (Leitz Version 1A, Leitz, Wetzlar, Germany). In the undoped, 1 mol% and 2 mol% Mn-doped PFN samples almost identical sintering curves were obtained (Fig. S1a), while sample doped with 0.5 mol% of manganese shows different sintering behavior.

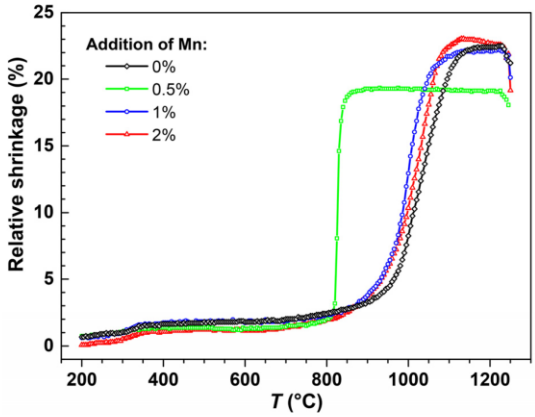


Figure S1a. Dynamic sintering curves of the undoped and Mn-doped PFN powder compacts.

Densification of the sample with 0.5 mol% of manganese occurs very rapidly in narrow temperature interval (from ~810 °C to ~860 °C), indicating a liquid-assisted sintering process [RS1]. Such sintering behavior is reproducible; the dynamic sintering curves of different powder batches were analyzed. In order to identify the liquid phase formed during the sintering of 0.5 mol% Mn-doped PFN, the microstructures of polished and fractured sample were investigated by FE-SEM. While the liquid phase was not detected in the polished samples, it was clearly visible in fracture, as shown in Fig. S1b. A presence of secondary phase was additionally confirmed by STEM, where EDXS analysis revealed the Pb-rich phase (not shown

here). A liquid-assisted sintering was already reported in Mn-doped PFN ceramic [RS2]. In this work authors suggest that the liquid phase could be related to the formation of eutectic mixture between PbO and pure PFN or/and between PbO and $Pb(Mn_{0.5}Nb_{0.5})O_3$, which might be locally formed in the sample during sintering [RS2, RS3].

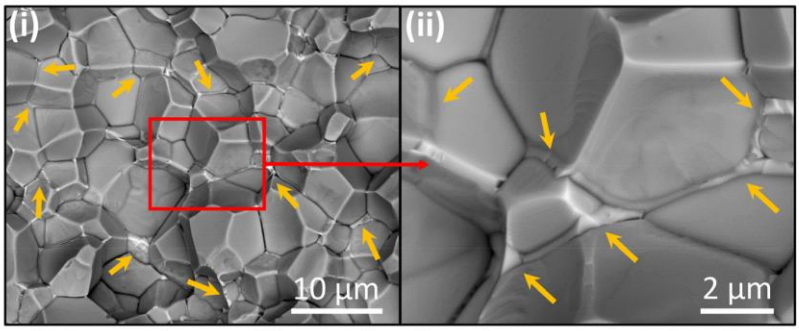


Figure S1b. (i) SEM image of fractured surface of 0.5 mol% Mn-doped sample. The secondary phase is marked by orange arrows. (ii) An enlarged view of the area marked with a red square.

S2. Thermal analysis

Thermogravimetric (TG), differential thermal (DTA) and evolved-gas (EGA) analyses of PFN powder after mechanochemical activation were carried out using a Netzsch STA 409 (Erich Netzsch, GmbH & Co. Holding KG, Selb, Germany) thermal analyzer coupled with a Balzers Thermostar GSD 300 T quadrupole mass spectrometer (Balzers Instruments, Balzers, Liechtenstein). For the measurements, ~50 mg of PFN powder was placed in Pt/Rh crucible and heated up to 640 °C with a heating rate of 10 °C·min^{-1} in an atmosphere of flowing synthetic air.

TG, DTA and EGA curves of PFN powder after mechanochemical activation are shown in Fig. S2. In the temperature range from 25 °C to ~140 °C, the observed mass loss of ~0.38% most likely corresponds to water evaporation and removal of adsorbed CO_2, as indicated by the small endothermic minimum on the DTA curve and the peaks of H_2O and CO_2 from the mass spectrometer signals. In the temperature interval between ~140 °C and ~380 °C, three coupled mass loss steps are observed, with a total mass loss of ~0.78%, that are associated with the decomposition and oxidation of the organic compounds. This is supported by the exothermic maximums on DTA curve and the EGA signals for H_2O and CO_2. Above 380 °C, the mass loss continuously decreases and stabilizes at ~600 °C. The total mass loss of the sample is ~1.42%. According to the results of thermal analyses, the temperature of 600 °C was chosen for pre-sintering heat treatment. At this temperature, all adsorbed molecules (H_2O, CO_2, etc.) and possible organic compounds (residues of polyethylene milling vials and spatulas) were removed and no changes in the composition of the PFN powder were observed. To estimate the deficiency of PbO in PFN ceramics related to PbO evaporation at the sintering temperature, green pellets were first heated up to 600 °C for 1 h with heating and cooling rates of 2 °C·min^{-1}. After the first heat treatment, the pellets were weighed and sintered as described in the main paper. After sintering, the pellets were weighed again. The difference in the mass before and after sintering was assumed to be a loss of mass due to the evaporation of PbO [RS4, RS5].

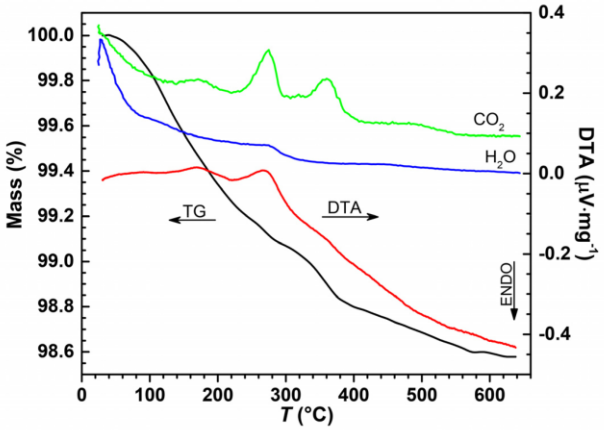


Figure S2. TG, DTA and EGA (H_2O, CO_2) curves of PFN powder before sintering.

S3. Measurements of magnetic properties

Zero-field-cooled (ZFC) and field-cooled (FC) DC magnetic susceptibilities (χ_m) vs. temperature were measured between -271 °C (2 K) and 127 °C (400 K) at different magnetic fields (1–50 kOe) using a physical property measurement system vibrating sample magnetometer (PPMS-VSM, Quantum Design, California, USA). First, χ_m measurements were performed under ZFC conditions. After that, the sample was heated back to 127 °C (400 K) and χ_m was measured under FC conditions. The M values were normalized according to the mass of the samples. Furthermore, the magnetization versus magnetic field (M–H) hysteresis loops were measured in magnetic fields up to 90 kOe at temperatures of -271 °C (2 K) and 27 °C (300 K).

Magnetic measurements of optimized PFN sample

The temperature dependence of M at different H of PFN sample sintered at 1000 °C is shown in Fig. S3a(i). At RT, the value of M is ~0.362 $Am^2 \cdot kg^{-1}$ at 50 kOe. M increases with decreasing temperature reaching a maximum value of ~1.374 $Am^2 \cdot kg^{-1}$ at -271 °C and 50 kOe. In the whole temperature range two anomalies were observed in $M(H)$ curves. The anomaly at -120 °C is known as the Néel temperature (T_N) and indicates a paramagnetic-to-antiferromagnetic (PM-AFM) phase transition [RS6, RS7]. On the other hand, the broad feature in the ZFC at lower temperatures (-263 °C) and the divergence of the ZFC-FC are typical characteristics of a spin glass transition (T_g). The spin glass behavior was previously confirmed by AC measurements from the temperature shift of the maxima in magnetic susceptibility with frequency by Chillal et al. [RS7]. The existence of a weak ferromagnetic component at -271 °C is evidenced in the slim M–H hysteresis loop (Fig. S3a(ii)), where the coercive filed (H_c), remanent magnetization (M_R) and saturated magnetization (M_S) are 2.0 kOe, 0.06 $Am^2 \cdot kg^{-1}$ and 2.2 $Am^2 \cdot kg^{-1}$, respectively. The existence of a ferromagnetic component at low temperatures further supports the spin glass state which is characterized by competing ferromagnetic–antiferromagnetic interactions. The origin of the ferromagnetic component is argued to be a spin canting in the AFM long-range order [RS7]. At RT typical paramagnetic behavior is evidenced by the absence of the hysteresis.

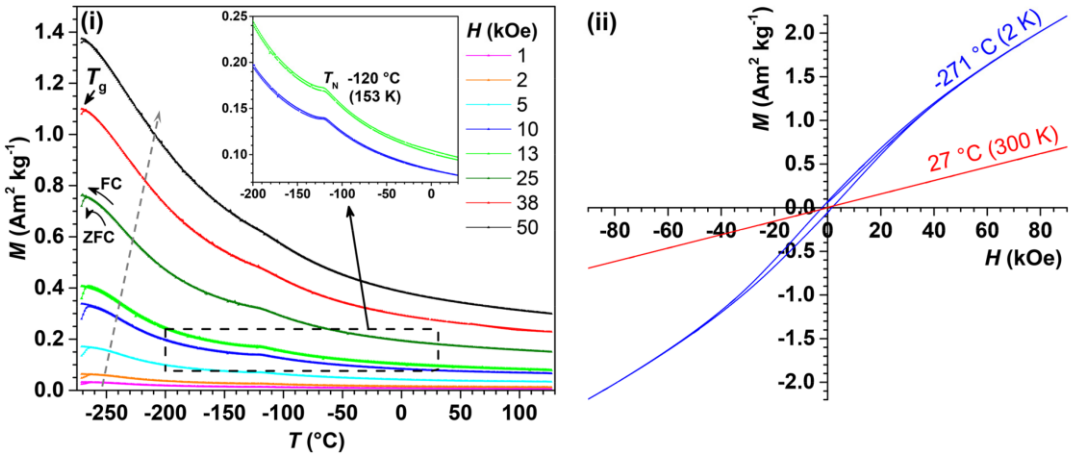


Figure S3a. (i) Temperature dependence of M at different applied H and (ii) M–H hysteresis loops of PFN ceramic sintered at 1000 °C. The dashed arrow indicates the increase magnetic field.

0.5 mol% Mn-doped PFN sample

The temperature dependence of M at different H of PFN ceramic doped with 0.5 mol% of manganese is shown in Fig. S3b(i). At RT and 50 kOe, the value of M is ~0.460 $Am^2 \cdot kg^{-1}$. The M increases with decreasing temperature reaching a maximum value of ~1.681 $Am^2 \cdot kg^{-1}$ at -271 °C and 50 kOe. In the whole temperature range two anomalies were observed in the $M(H)$ curves. The anomaly at -140 °C indicates a PM-AFM phase transition, while the anomaly at the lower temperature (-264 °C) indicates a spin glass transition, which is in agreement with the literature [RS8]. The existence of a weak magnetic component at -271 °C is evidenced in the slim M–H hysteresis loop (Fig. S3b(ii)). The H_c, M_R and M_S are 1.8 kOe, 0.11 $Am^2 \cdot kg^{-1}$ and 2.5 $Am^2 \cdot kg^{-1}$, respectively. At RT typical paramagnetic behavior is evidenced by the absence of the hysteresis.

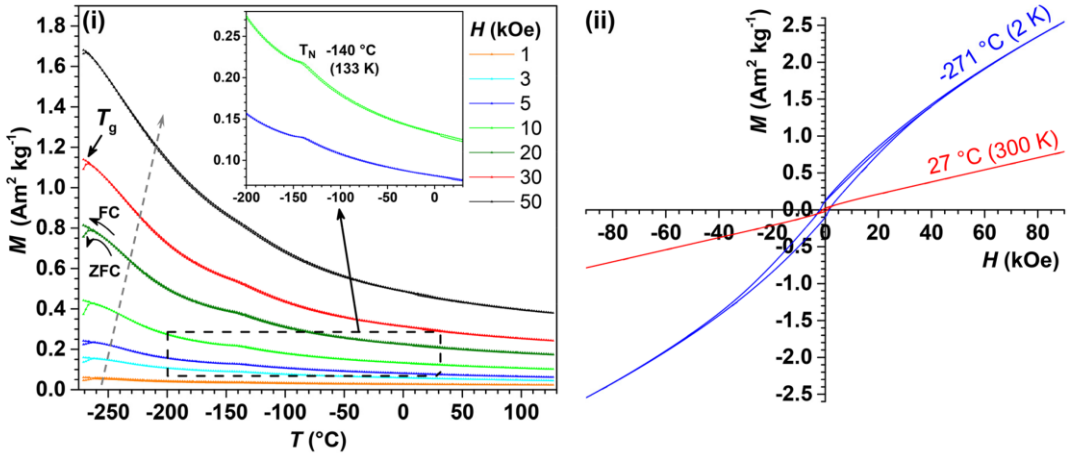


Figure S3b. (i) Temperature dependence of M at different applied H and (ii) M–H hysteresis loops of PFN ceramic doped with 0.5 mol% of manganese. The dashed arrow indicates the increase magnetic field.

Comparison of $M(T, H)$ curves of undoped and 0.5 mol% Mn-doped PFN ceramics is shown in Fig. S3c. The magnetization values of Mn-doped sample are higher throughout the entire temperature range in comparison to the ones of undoped sample. A similar trend is also reflected in M–H hysteresis loops where Mn-doped sample exhibits higher M_R and M_S values in comparison with the undoped one. The addition of manganese also affects the phase transition temperatures. Compared to the undoped PFN, T_N of Mn-doped PFN is shifted to lower temperatures, while T_g stays similar, which is in agreement with the previously reported study [RS8].

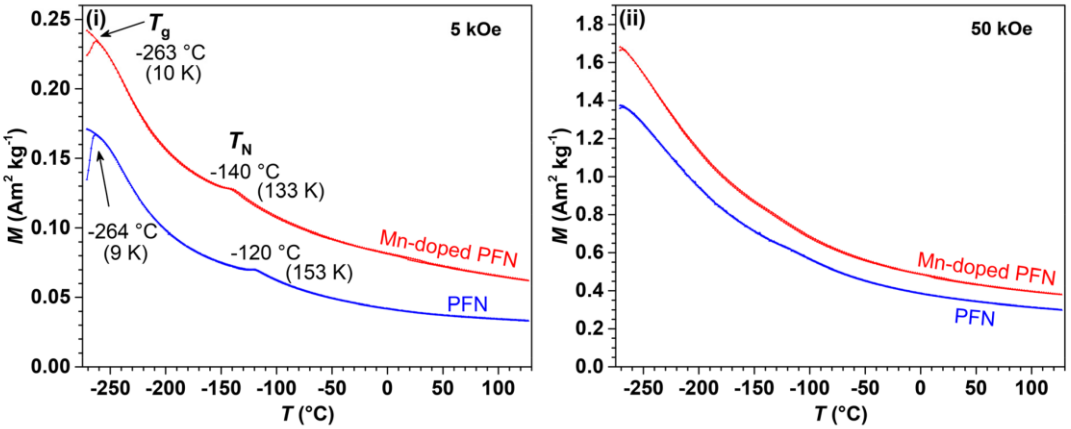


Figure S3c. Comparison of $M(T, H)$ curves of undoped and 0.5 mol% Mn-doped PFN ceramics measured at (i) 5 kOe and (ii) 50 kOe.

S4. Microstructure and grain size distributions

PFN samples

SEM images of the thermally etched surfaces and grain size distributions of PFN ceramics sintered at different temperatures (950 °C-1100 °C) are shown in Fig. S4a. The etched surfaces reveal highly dense and uniform microstructures, except the sample sintered at 950 °C, where some pull-outs, produced during the sample surface preparation, are present. The average grain size of the samples increases with increasing sintering temperature, which is also evident from grain size distributions, shown in Fig. S4a(ii).

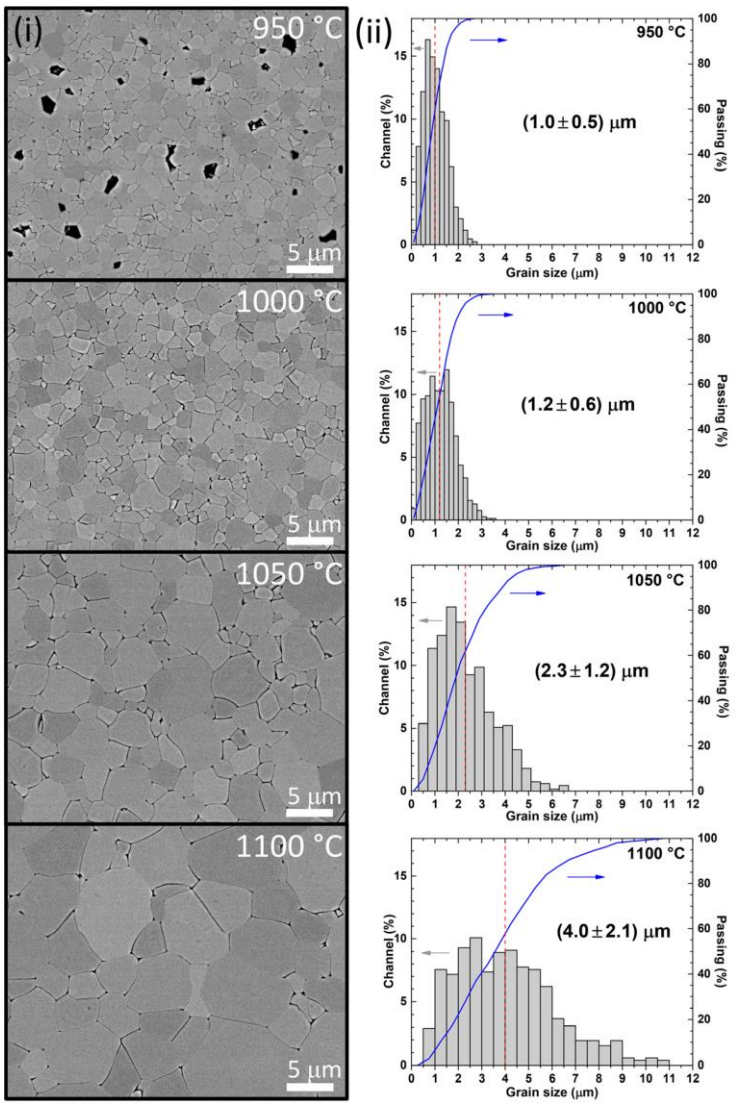


Figure S4a. (i) SEM images of thermally etched surfaces and (ii) the grain size distributions of PFN ceramics sintered at 950, 1000, 1050 and 1100 °C.

Mn-doped PFN samples

SEM images of the etched surfaces and grain size distributions of Mn-doped (0.5 mol%, 1 mol% and 2 mol%) PFN ceramics are shown in Fig. S4b. In all the samples, SEM images reveal highly dense microstructures. The average grain size of doped samples decreases with increasing amount of added manganese, which is also evident from grain size distributions, shown in Fig. S4b(ii). On the etched surface of the sample doped with 0.5 mol% of manganese, traces of Pb-rich secondary phase are visible (marked with orange arrows in Fig. S4b(i)), which is related to the liquid-assisted sintering process as described in S1. Furthermore, secondary phase is observed also on the etched surface of the sample doped with 2 mol% of manganese (marked with red arrows in Fig. S4b(i)). The SEM/EDXS analysis revealed that this secondary phase is rich on manganese (not shown here). According to the literature and as discussed in the main text, MnO_2 presumably concentrate at the grain boundaries. The Mn-rich secondary

phase that presumably pops out of the sample during the thermal etching (due to a low melting point of MnO_2 at ~535 °C) supports this idea.

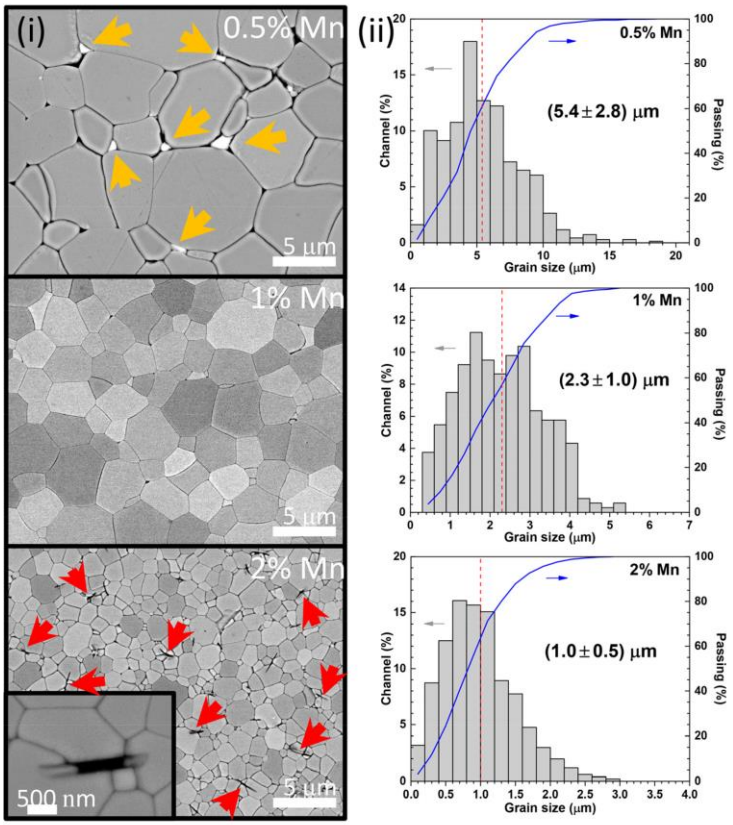


Figure S4b. (i) SEM images of thermally etched surfaces. Above: in the SEM image of 0.5 mol% Mn-doped sample, Pb-rich secondary phase is marked by orange arrows. Below: in the SEM image of 2 mol% Mn-doped sample, Mn-rich secondary phase is marked by red arrows. Inset: an enlarged view of Mn-rich secondary phase. (ii) Grain size distributions of Mn-doped PFN ceramics (note the different scales).

S5. Polarization versus electric field (*P–E*) and current density versus electric filed (*j–E*) hysteresis loops

PFN samples

P–E and *j–E* hysteresis loops of PFN ceramics are shown in Fig. S5a. In the samples sintered at 950 °C and 1000 °C ferroelectric hysteresis loops with sharp ends were observed, while at higher sintering temperatures, *P-E* loops become rounded due to a large polarization-field phase angle, indicating an increased electrical conductivity of the samples.

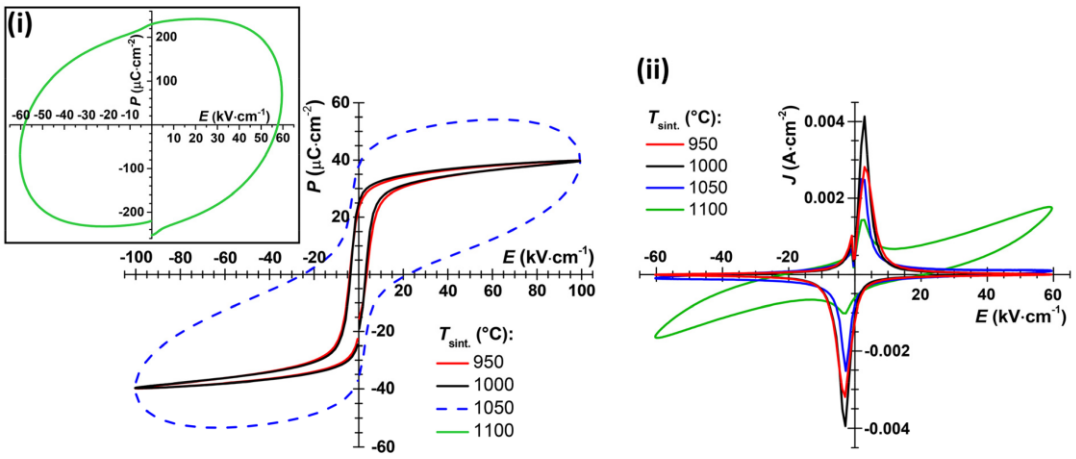


Figure S5a. (i) *P–E* and (ii) *j–E* hysteresis loops of PFN sintered at 950, 1000, 1050 and (inset) 1100 °C.

Mn-doped PFN samples

P–E and *j–E* hysteresis loops of Mn-doped PFN ceramics are shown in Fig. S5b. In all the samples, ferroelectric hysteresis loops were observed. Electrical conductivity of samples increases with increasing amount of added manganese, which is clearly visible from the sharpness of the loop ends (inset in Fig. S5b). Sample doped with 0.5 mol% of manganese exhibits very sharp *P–E* loop. With the increasing amount of added dopant, *P–E* loops become more rounded, which indicates higher electrical conductivity of the samples and therefore a presence of a leakage current.

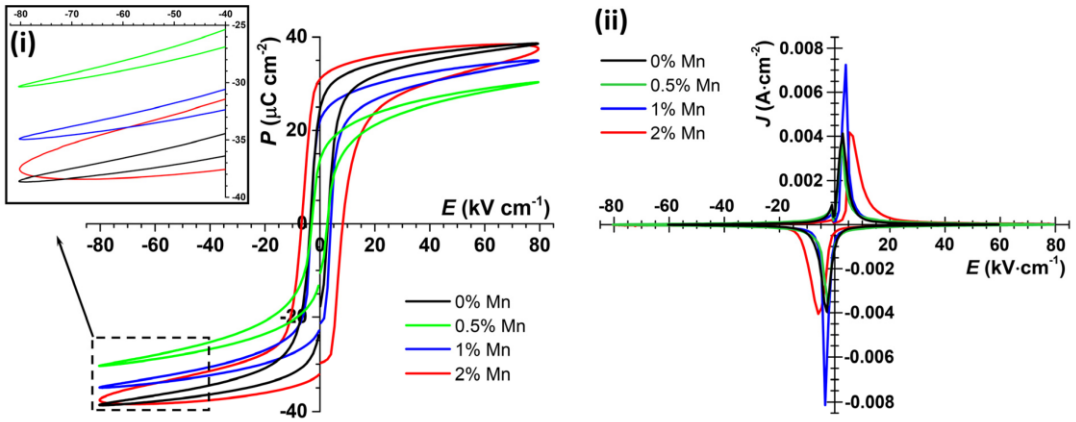


Figure S5b. (i) *P–E* and (ii) *j–E* hysteresis loops of undoped and Mn-doped (0.5 mol%, 1 mol% and 2 mol%) PFN samples. Inset: the enlarged view of a part of the measurements marked with dashed square.

S6. STEM micrographs and EDXS mapping analysis

PFN sample sintered at 1100 °C

STEM/EDXS elemental maps of the area shown in the main text (Fig. 3d) reveal that the observed secondary phase at the grain boundaries (marked with green arrows) is reach on lead (Fig. S6a). This is clearly demonstrated in composite image (combination of Pb L, Fe K and

Nb K-signals from EDXS mapping analysis), where reddish area at the grain boundary and in the triple grain junction (marked with black arrows) indicates Pb-rich phase.

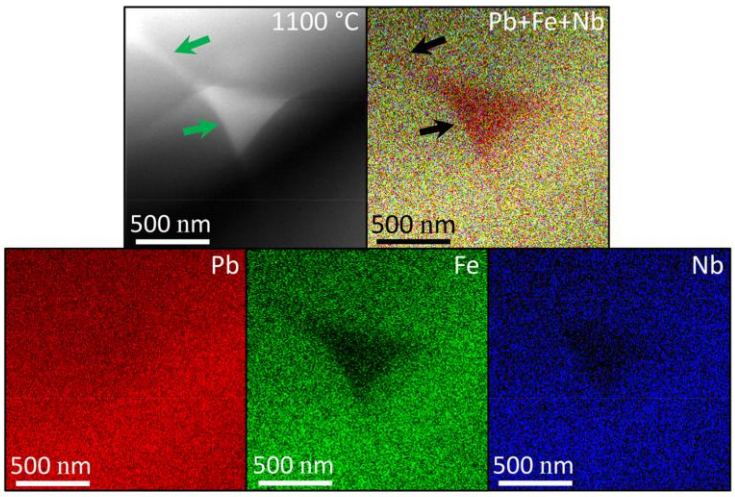


Figure S6a. STEM image of a secondary phase at the grain boundaries of the PFN sample sintered at 1000 °C (marked with green arrows) and EDXS mapping analysis of the corresponding area.

2 mol% Mn-doped PFN sample

In order to find a possible Mn-rich secondary phase at the grain boundaries, STEM analysis of PFN sample doped with 2 mol% of manganese was performed. It turned out that the classic TEM sample preparation (i.e., by mechanical grinding, dimpling and Ar-ion milling) is not appropriate for these samples, because they can easily break during the preparation and is therefore difficult to prepare sufficiently thin samples. However, despite the problems with the TEM-sample preparation, a few grain boundaries could be checked. In Fig. S6b STEM image of the sample doped with 2 mol% of manganese is shown, where only clean grain boundaries were observed (an example is shown in Fig. S6b(ii)). According to the results obtained with cAFM (Fig. 7 in the main text), increased electrical conductivity was observed only in some grain boundaries, which could mean that MnO_2 is unevenly distributed and thus not concentrated at all grain boundaries.

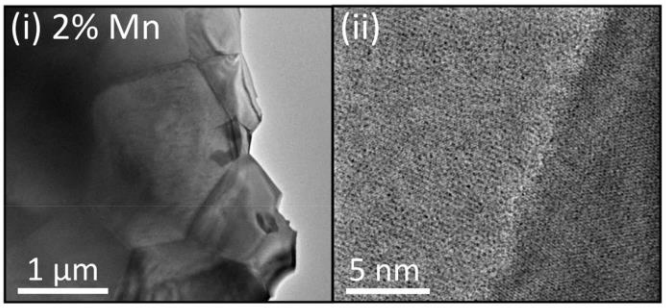


Figure 6b. STEM images of (i) the PFN sample doped with 2 mol% of manganese and (ii) example of a clean grain boundary.

S7. Rietveld refinement

For the purpose of Rietveld refinement analysis [RS9], the XRD patterns were recorded in the 15–120° 2θ-range with a step of 0.008° and an integration time of 100 s per step at RT. Rietveld refinement analysis of the diffraction data was performed with Topas R software package (version 6, Bruker, AXS, Karlsruhe, Germany). For the crystal structure refinement, monoclinic (space group *Cm*) PFN phase (ICSD 88357) [RS10] was used as the initial structural model. The fundamental parameters approach [RS11] was used to describe the peak profiles, while the background was estimated using a 7th order Chebychev polynomial. The specimen displacement, lattice parameters, scale factor, background, crystallite size, strain, the thermal displacement parameters and atomic coordinates were stepwise refined to obtain a calculated diffraction profile that best-fit the experimental pattern. All the occupancies were fixed at the nominal composition and kept constant during refinement. Finally, the quality of the fit was assessed from the fit parameters such as weighted profile *R*-factor (R_{wp}), profile *R*-factor (R_p), expected *R*-factor (R_{exp}), Bragg *R*-factor (R_B), and goodness of fit (G.O.F.) [RS12].

PFN samples

The effect of sintering temperature on the structural properties of PFN was investigated by the Rietveld refinement method. The agreement factors of the Rietveld analysis along with the cell parameters of PFN ceramics sintered at different temperatures are given in Table S7a.

Table S7a. Refined structural parameters for PFN ceramics sintered from 950 °C to 1100 °C.

$T_{sint.}$	**950 °C**	**1000 °C**	**1050 °C**	**1100 °C**
Phase	PFN			
Crystal system	Monoclinic			
Space group	*Cm*			
a (Å)	5.68011(5)	5.68025(4)	5.68037(5)	5.68071(4)
b (Å)	5.67304(3)	5.67298(3)	5.67304(4)	5.67303(4)
c (Å)	4.01584(4)	4.01580(4)	4.01560(4)	4.01571(4)
β (°)	89.8881(9)	89.8880(7)	89.8874(9)	89.8846(9)
V (Å^3)	129.4051(19)	129.4045(19)	129.4022(19)	129.2576(19)
R_{wp}	5.333	5.987	5.834	5.804
R_{exp}	4.288	5.122	4.447	4.904
R_p	4.015	4.641	4.348	4.386
G.O.F. (χ^2)	1.244	1.169	1.312	1.184
R_B	1.346	1.704	2.785	2.122

The results of Rietveld refinement show that the increase in the sintering temperature leads to a small decrease of the unit cell parameter *c*, β angle and the unit cell volume (Fig. S7a), which can be related to the presence of A-site vacancies [RS13-RS15].

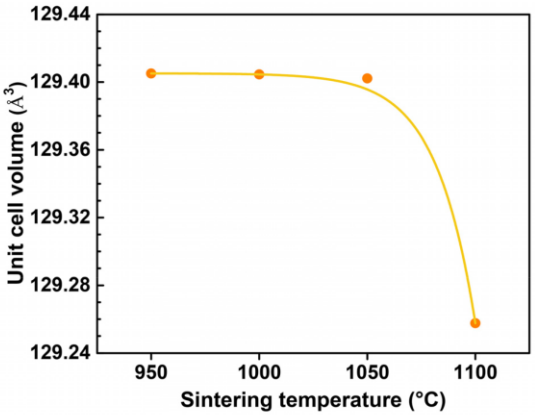


Figure S7a. The evolution of the unit cell volume with the sintering temperature. The line between the measured values is just a guide to the eye.

Mn-doped PFN samples

The effect of manganese doping on the structural properties of PFN was investigated by the Rietveld refinement method. The agreement factors of the Rietveld analysis along with the cell parameters of Mn-doped PFN ceramics are given in Table S7b.

Table S7b. Refined structural parameters for Mn-doped PFN ceramics.

Amount of Mn	**0 mol%**	**0.5 mol%**	**1 mol%**	**2 mol%**
Phase	PFN			
Crystal system	Monoclinic			
Space group	*Cm*			
a (Å)	5.68025(4)	5.67955(6)	5.67883(4)	5.67505(12)
b (Å)	5.67298(3)	5.67346(7)	5.66999(5)	5.66926(9)
c (Å)	4.01580(4)	4.01336(3)	4.01435(4)	4.01346(7)
β (°)	89.8850(7)	89.8845(9)	89.9032(4)	89.9216(12)
V (Å^3)	129.4045(19)	129.3420(30)	129.2576(19)	129.1260(40)
R_{wp}	5.987	6.202	4.913	5.031
R_{exp}	5.122	4.399	4.209	4.226
R_p	4.641	4.595	3.705	3.805
G.O.F. (χ^2)	1.169	1.410	1.167	1.191
R_B	1.704	4.214	1.060	1.490

The results of Rietveld refinement show that the increase in the concentration of manganese leads to a decrease of the unit cell volume (Fig. S7b), which could be consequence of a smaller ionic radius of Mn^{4+} (67 pm) compared to Fe^{3+} (69 pm for low spin and 78.5 pm for high spin configuration) and Nb^{5+} (78 pm) [RS16] on B-site of the PFN structure.

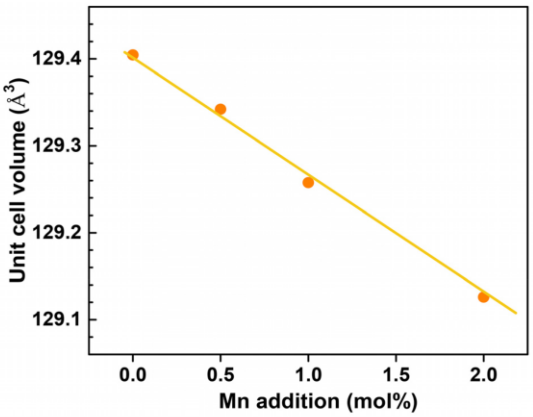


Figure S7b. The evolution of the unit cell volume with the addition of manganese. The line between the measured values is just a guide to the eye.

S8. EPR

EPR spectra were performed on ELEXSYS E500 X-band Bruker spectrometer at 25 °C and ambient atmosphere (microwave frequency 9.4035 GHz, microwave power 6.404 mW, amplitude of 2nd modulation of 1 G). For the measurements crushed ceramic pellets were used. G–factors at about 1.97 were determined using DPPH standard. EPR spectra (shown in Fig. S8) were normalized with the sample masses.

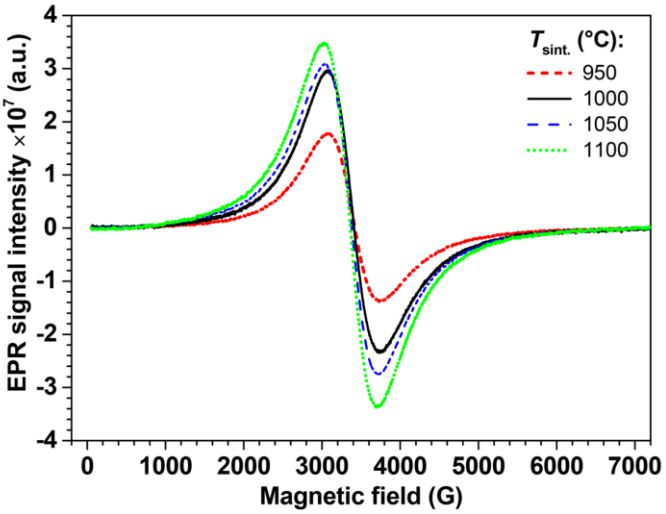


Figure S8. X-band EPR spectra of PFN ceramics sintered at 950, 1000, 1050 and 1100 °C.

S9. Effective cooling

In Fig. S9 two examples of the measured temperature changes during the EC cycle in PFN are shown. To determine the effect of Joule heating on the overall EC response, we introduce the term effective cooling (ΔT_{eff}) that is a difference between the EC temperature change (ΔT_{EC}) and temperature change corresponding to the Joule heating (ΔT_{JH}). In the first case, which is shown in Figure S9(i), no Joule heating is present, therefore ΔT_{eff} is equal to ΔT_{EC}. While, in the

second case (Figure S9(ii)), ΔT_{eff} is lower in comparison to ΔT_{EC}, due to the appearance of Joule heating.

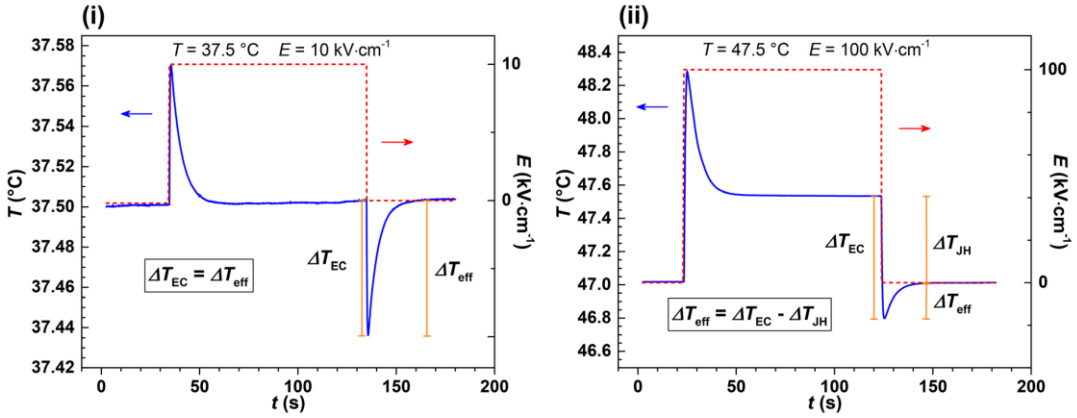


Figure S9. Measured temperature changes during the EC cycle of PFN sample sintered at 1000 °C. The measurements were obtained at (i) 37.5 °C and 10 kV·cm^{-1} and (ii) 47 °C and 100 kV·cm^{-1}. The applied electric field signal is marked by dotted line.

S10. Detected amount of manganese in the Mn-doped PFN (EDXS analysis)

The integration of manganese in PFN structure was investigated by SEM/EDXS analysis. The analyses were performed on polished surfaces of Mn-doped PFN samples. For each sample more than 10 randomly selected points were analyzed. The average values with the standard deviations are shown in Figure S10.

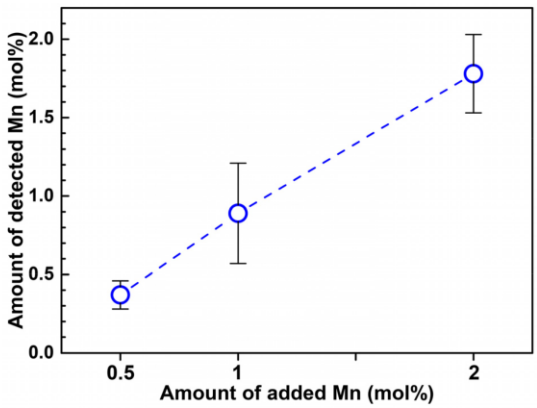


Figure S10. Added versus detected amount of manganese inside the grains. The line between the measured values is just a guide to the eye.

References

[RS1] S.-J. L. Kang. Sintering. Densification, grain growth & microstructure, Elsevier Butterworth-Heinemann, Oxford, 2005.
[RS2] A. V. Pavlenko, N. A. Boldyrev, L. A. Reznichenko, I. A. Verbenko, G. M. Konstantinov, L. A. Shilkina. Microstructure and dielectric and piezoelectric properties of $PbFe_{0.5}Nb_{0.5}O_3$ ceramics modified with Li_2CO_3 and MnO_2. Inorg. Mater. 50 (2014), 750–756. https://doi.org/10.1134/S0020168514070115.
[RS3] I. H. Brunskill, P. Tissot, H. Schmid. Determination of the phase diagrams, PbO–$Pb(Fe_{1/2}Nb_{1/2})O_3$ and PbO–$Pb(Mn_{1/2}Nb_{1/2})O_3$, Themochim. Acta 49 (1981), 351–355. https://doi.org/10.1016/0040-6031(81)80186-4.
[RS4] R. B. Atkin, R. M. Fulrath. Point Defects and Sintering of Lead Zirconate-Titanate. J. Am. Ceram. Soc. 54 (1971), 265–270. https://doi.org/10.1111/j.1151-2916.1971.tb12286.x.
[RS5] A. I. Kingon, J. B. Clark. Sintering of PZT Ceramics: I, Atmosphere Control. J. Am. Ceram. Soc. 66 (1983), 253–256. https://doi.org/10.1111/j.1151-2916.1983.tb15708.x.
[RS6] R. Havlicek, J. Poltierova Vejpravova, D. Bochenek. Structure and magnetic properties of perovskite-like multiferroic $PbFe_{0.5}Nb_{0.5}O_3$, J. Phys. Conf. Ser. 200 (2010), 012058 1–4. https://doi.org/10.1088/1742-6596/200/1/012058.
[RS7] S. Chillal, M. Thede, F. J. Litterst, S. N. Gvasaliya, T. A. Shaplygina, S. G. Lushnikov, A. Zheludev. Microscopic coexistence of antiferromagnetic and spin-glass states, Phys. Rev. B 87 (2013), 220403 1–5. https://doi.org/10.1103/PhysRevB.87.220403.
[RS8] D. Bochenek, P. Guzdek. Ferroelectric and magnetic properties of ferroelectromagnetic $PbFe_{1/2}Nb_{1/2}O_3$ type ceramics. J. Magn. Magn. Mater. 323 (2011), 369–374. https://doi.org/10.1016/j.jmmm.2010.09.046.
[RS9] R. A. Young, The Rietveld Method, International Union of Crystallograhy, Oxford University Press, Chester, England/Oxford, New York, 1993.
[RS10] N. Lampis, P. Sciau, A. G. Lehmann. Rietveld refinements of the paraelectric and ferroelectric structures of $PbFe_{0.5}Nb_{0.5}O_3$. J. Phys.: Condens. Matter. 11 (1999), 3489–3500. https://doi.org/10.1088/0953-8984/11/17/307.
[RS11] R. W. Cheary, A. Coelho. A fundamental parameters approach to X-Ray line-profile fitting, J. Appl. Crystallogr. 25 (1992), 109–1021. https://doi.org/10.1107/S0021889891010804.
[RS12] W. I. F. David. Powder Diffraction: Least-Squares and Beyond, J. Res. Natl. Inst. Stand. Technol. 109 (2004), 107–123. https://doi.org/10.6028/jres.008.
[RS13] M. Mori, K. Nakamura, T. Itoh. Crystal Structure and Anomalous Sintering Behaviour of $(Sr_{0.7}La_{0.3})_{1-x}TiO_{3+\delta}$ Perovskites ($0 \leq x \leq 0.12$) Synthesized by the Pechini Method. J. Fuel Cell Sci. Technol. 9 (2012) 021007 1–8. https://doi.org/10.1115/1.4005611.
[RS14] A. V. Kovalevsky, A. A. Yaremchenko, S. Populoh, A. Weidenkaff, J. R. Frade. Effect of A-Site Cation Deficiency on the Thermoelectric Performance of Donor-Substituted Strontium Titanate. J. Phys. Chem. C 118, (2014), 4596–4606. https://doi.org/10.1021/jp409872e.
[RS15] Y. Sun, J. Li, Y. Zeng, B. Shalchi Amirkhiz, M. Wang, Y. Behnamian, J. Luo. A-site deficient perovskite: the parent for in situ exsolution of highly active, regenerable nanoparticles as SOFC anodes. J. Mater. Chem. A 3 (2015), 11048–11056. https://doi.org/10.1039/c5ta01733e.
[RS16] R. D. Shannon, Revised Effective Ionic Radii and Systematic Studies of Interatomic Distances in Halides and Chalcogenides. Acta Crysr. A32 (1976) 751–767. https://doi.org/10.1107/S0567739476001551.

Chapter 3

Strengthened Relaxor Behavior in (1-x)Pb($Fe_{0.5}Nb_{0.5}$)O_3–xBiFeO_3

The formation of PFN–BFO solid solutions offers a bridge between the low-temperature ferroic phase transitions of PFN and the high-temperature phase transitions of BFO, which can lead to new materials with, ideally, room-temperature multiferroic anomalies. This chapter covers the preparation and structural, microstructural and functional characterization of various PFN–BFO solid solutions, with the emphasis on the systematic study of their dielectric, ferroelectric and electromechanical properties on the macroscopic as well as the local scale.

Seven single-phase PFN–100xBFO ($x = 0$–0.5) solid solutions were successfully prepared using mechanochemical synthesis followed by sintering at different temperatures. With a gradual increase in the BFO content, the peak-permittivity temperature of the PFN–100xBFO solid solutions first decreased (reaching RT when $x = 0.2$), while at higher BFO contents ($x > 0.2$) it increased and reached ~200 °C in PFN–50BFO. Introducing BFO into the PFN–100xBFO solid solution leads to the formation of a pseudocubic phase and consequently it strengthens the relaxor behavior. This is accompanied by a broadening of the peak in the temperature-dependent permittivity, narrowing of the ferroelectric P–E hysteresis loops and a decreasing of the size of ferroelectric domains into polar nanoregions.

Among the prepared compositions, PFN–20BFO exhibits low ferroelectric hysteresis losses and a peak permittivity near ambient temperature, making it a promising candidate for room-temperature electrocaloric and multicaloric applications.

This chapter addresses thesis objectives 5 and 6.

Published in: U. Prah, M. Dragomir, T. Rojac, A. Benčan, R. Broughton, C.-C. Chung, J. L. Jones, R. Sherbondy, G. Brennecka and H. Uršič, "Strengthened Relaxor Behavior in (1-x)Pb($Fe_{0.5}Nb_{0.5}$)O_3–xBiFeO_3," *J. Mater. Chem. C*, vol. 8, no. 10, pp. 3452–3462, 2020. (IF = 7.059, 2019)

My contribution: I optimized the synthesis process and prepared the powders and ceramic samples. I performed the scanning electron microscopy and differential scanning calorimetry analyses as well as the characterization of the electrical and electromechanical properties. I prepared the concept of the paper and jointly wrote the manuscript with the co-authors.

Journal of Materials Chemistry C

ROYAL SOCIETY OF CHEMISTRY

PAPER

View Article Online
View Journal | View Issue



Cite this: J. Mater. Chem. C, 2020, 8, 3452

Strengthened relaxor behavior in $(1-x)Pb(Fe_{0.5}Nb_{0.5})O_3-xBiFeO_3$†

Uroš Prah,[ab] Mirela Dragomir,[a] Tadej Rojac,[ab] Andreja Benčan,[ab] Rachel Broughton,[c] Ching-Chang Chung,[d] Jacob L. Jones,[c] Rachel Sherbondy,[e] Geoff Brennecka[e] and Hana Uršič*[ab]

A systematic study of $(1-x)Pb(Fe_{0.5}Nb_{0.5})O_3-xBiFeO_3$ (x = 0–0.5) was performed by combining dielectric and electromechanical measurements with structural and microstructural characterization in order to investigate the strengthening of the relaxor properties when adding $BiFeO_3$ into $Pb(Fe_{0.5}Nb_{0.5})O_3$ and forming a solid solution. $Pb(Fe_{0.5}Nb_{0.5})O_3$ crystalizes in monoclinic symmetry exhibiting ferroelectric-like polarization *versus* electric field (*P*–*E*) hysteresis loop and sub-micron-sized ferroelectric domains. Adding $BiFeO_3$ to $Pb(Fe_{0.5}Nb_{0.5})O_3$ favors a pseudocubic phase and a gradual strengthening of the relaxor behavior of the prepared ceramics. This is indicated by a broadening of the peak in temperature-dependent permittivity, narrowing of *P*–*E* hysteresis loops and decreasing size of ferroelectric domains resulting in polar nanodomains for x = 0.20 composition. The relaxor behavior was additionally confirmed by Vogel–Fulcher analysis. For the $x \geq 0.30$ compositions, broad high-temperature anomalies are observed in dielectric permittivity *versus* temperature measurements in addition to the frequency-dispersive peak located close to room temperature. These samples also exhibit pinched *P*–*E* hysteresis loops. The observed pinching is most probably related to the reorganization of polar nanoregions under the electric field as shown by synchrotron X-ray diffraction measurements as well as by piezo-response force microscopy analysis, while in part affected by the presence of charged point defects and anti-ferroelectric order, as indicated from rapid cooling experiments and high-resolution transmission electron microscopy, respectively.

Received 28th October 2019,
Accepted 4th February 2020

DOI: 10.1039/c9tc05883d

rsc.li/materials-c

I. Introduction

$BiFeO_3$ (BFO)[1,2] and $Pb(Fe_{0.5}Nb_{0.5})O_3$ (PFN)[3–5] are two of the most known and well-studied single-phase multiferroics, in which ferroelectric and antiferromagnetic orders can coexist. BFO exhibits a paraelectric–ferroelectric phase transition at 825 °C, known as the ferroelectric Curie temperature (T_C), and a paramagnetic–antiferromagnetic phase transition at 370 °C, denoted as the magnetic Néel temperature (T_N).[1] In PFN, both T_C and T_N occur at much lower temperatures, *i.e.*, ~100 °C and −120 °C, respectively.[4,6]

According to the literature reports, there is still a debate about whether PFN exhibits more ferroelectric-like or relaxor-like behavior.[4,7–9] At room temperature, it exhibits a monoclinic symmetry with *Cm* space group[10] exhibiting ferroelectric-like *P*–*E* hysteresis loops[11] and sub-micron-sized ferroelectric domains.[8,10] It possesses frequency independent (or only slightly dependent, *i.e.*, ±1 °C) peak-permittivity temperature for frequencies below 1 MHz.[11,12] However, it was shown[12] that the peak-permittivity temperature becomes frequency dependent in the microwave frequency region (GHz), indicating partial relaxor-like behavior. On the other hand, BFO shows ferroelectric behavior at room temperature and is also considered a high-temperature piezoelectric material due to its extremely high T_C.[13] What about the PFN–BFO solid solutions? Are they showing more ferroelectric- or relaxor-like behaviors at room temperature? This open question will be answered in this paper.

The preparation of different $(1-x)Pb(Fe_{0.5}Nb_{0.5})O_3-xBiFeO_3$ (PFN–100*x*BFO) solid solutions was demonstrated in the 1960s[14–17] and many other studies followed, all using classical solid-state synthesis.[18–25] Most of these reports focused on BFO-rich PFN–100*x*BFO ($x \geq 0.5$) compositions and investigation of their magnetic properties. However, as shown in this work,

[a] Jožef Stefan Institute, Jamova cesta 39, 1000 Ljubljana, Slovenia. E-mail: hana.ursic@ijs.si
[b] Jožef Stefan International Postgraduate School, Jamova cesta 39, 1000 Ljubljana, Slovenia
[c] Department of Materials Science and Engineering, North Carolina State University, Raleigh, NC 27695, USA
[d] Analytical Instrumentation Facility, North Carolina State University, Raleigh, NC 27695, USA
[e] Colorado School of Mines, 1500 Illinois St., Golden, CO 80401, USA

† Electronic supplementary information (ESI) available. See DOI: 10.1039/c9tc05883d

This journal is © The Royal Society of Chemistry 2020

PFN-rich compositions ($x < 0.5$) exhibit an interesting ferroelectric-relaxor behavior that is strengthened by adding BFO to PFN.

Large dielectric permittivity values across a broad temperature range, large electrostriction coefficients, low hysteresis losses and large change of field-induced polarization makes relaxors useful for capacitors, energy storage applications,[26] precision displacement actuators, transducers[26,27] and electrocaloric cooling elements.[28] One of the reasons that the ferroelectric-relaxor behavior has not yet been reported in PFN–BFO system may lay in the challenging preparation of single-phase ceramics with low electrical conductivity.

In this work, seven PFN–100xBFO (x = 0, 0.05, 0.1, 0.2, 0.3, 0.4 and 0.5) compositions were prepared by mechanochemical synthesis followed by sintering. This synthesis route has proven useful for the preparation of complex single-phase ceramics due to the better chemical homogeneity and partial amorphization of mechanochemically-activated powder, which can lead to lower sintering temperatures and more homogeneous and stoichiometric ceramics.[11,29,30] We show in this study that PFN–100xBFO ($x \leq 0.5$) is an interesting system exhibiting relaxor-like behavior. Electrical properties of ferroelectrics and relaxors are strongly dependent on the grain size of the material.[31,32] Therefore, in this work special attention was given in order to prepare all samples with similar grain size. Local domain structure was investigated at the sub-micron scale in addition to macroscopic measurements of dielectric permittivity and losses, polarization– and strain–electric field hysteresis loops and piezoelectric properties. The strengthened relaxor behavior by addition of BFO to PFN is therefore reported in detail here for the first time.

II. Experimental

A. Material synthesis

PFN–100xBFO (x = 0, 0.05, 0.1, 0.2, 0.3, 0.4 and 0.5) ceramic powders were prepared by mechanochemical-activation-assisted synthesis using PbO (99.9%, Alfa Aesar), Fe_2O_3 (99.9%, Alfa Aesar), Nb_2O_5 (99.9%, Aldrich) and Bi_2O_3 (99.999%, Alfa Aesar) as starting oxides. The preparation process of pure $Pb(Fe_{0.5}Nb_{0.5})O_3$ (PFN) powder is described in our previous work.[11] Prior to the preparation of BFO-containing compositions, all starting oxides were pre-milled in absolute ethanol using a planetary ball mill (Retsch PM400, Retsch, Haan, Germany) at 200 min^{-1} for 4–6 h or an attrition mill (Netzsch, PE075/PR01, Selb, Germany) at 500 min^{-1} for 6–8 h. In all cases, yttria-stabilized zirconia (YSZ) milling balls with a diameter of 3 mm were used. All stoichiometric mixtures of starting oxides (40 g) were homogenized in a planetary ball mill at 200 min^{-1} for 4 h in absolute ethanol using YSZ milling balls (ball diameters 3 mm). The homogenized mixtures were then dried and mechanochemically activated in the same planetary ball mill for 14 h at 400 min^{-1} in a tungsten carbide milling vial (volume 80 cm^3), filled with 7 tungsten carbide milling balls (ball diameters 15 mm). After activation, the synthesized powders, *i.e.*, mixtures of crystalline perovskite and amorphous phases (ESI† material, A), were re-milled in a planetary ball mill in absolute ethanol, at 200 min^{-1}, for 4 h, using YSZ milling balls (ball diameters 3 mm).

All prepared powders were uniaxially pressed (50 MPa) into pellets of a diameter of 8 mm followed by isostatic pressing at 300 MPa. The powder compacts were reactively sintered in double alumina crucibles in the presence of PFN packing powder. Sintering temperatures for each composition were estimated from sintering curves (details in ESI† material, B). In order to maintain similar grain size in all compositions (ESI† material, C), two different sintering temperatures were used. PFN–100xBFO samples with lower content of BFO (x = 0, 0.05 and 0.1) were sintered at 950 °C for 2 h, while samples with higher content of BFO (x = 0.2, 0.3, 0.4 and 0.5) were sintered 50 °C lower, *i.e.*, 900 °C. Sintering runs were performed in oxygen atmosphere as suggested in ref. 33 and used in our previous work.[11] The use of saturated oxygen atmosphere during the sintering prevents (or minimizes) the reduction of Fe^{3+} to Fe^{2+} and reduces the amount of oxygen vacancies, which consequently resulted in a lower electrical conductivity and dielectric losses of the material.[33] For all samples, heating and cooling rates of 2 °C min^{-1} were used.

B. Characterization

The densities of the sintered pellets were determined using a gas-displacement density analyzer (Micromeritics, AcuuPyc II 1340 Pycnometer) at room temperature (RT). For the calculation of the relative density of PFN, the crystallographic density of 8.46 g cm^{-3} was used (PDF card no. 032-0522),[34] while for other compositions, crystallographic densities were obtained from Rietveld refinement analysis (details in ESI† material, D).

X-ray powder diffraction (XRD) patterns of crushed ceramic pellets were recorded on a X'Pert Pro (PANalytical B.V., Netherlands) high-resolution powder diffractometer equipped with Cu $K\alpha_1$ radiation (45 kV, 40 mA), in reflection mode. Diffraction patterns were recorded in the 15–120° 2θ-range with a step size of 0.008° and an integration time of 100 s per step at RT. The phase identification was done with PDF-4+ database.

The quantitative phase composition analyses were performed using the Rietveld refinement method. The Topas R package (version 2.1, Bruker, AXS, Karlsruhe, Germany) was employed and a Fundamental Parameters Approach was used to describe the peak profile.[35] In this model, the background (10^{th} order Chebychev), unit cell parameters, crystallite size, scale factors, sample displacement, atomic coordinates, and thermal parameters were stepwise refined to obtain a calculated diffraction profile that best fits the experimental pattern. The quality of the fit was assessed from the goodness-of-fit parameters R_{wp}, R_p, R_{exp}, R_B, and G.O.F.

Electric field dependent synchrotron X-ray diffraction (sXRD) was conducted at the 11-ID-C beamline of the Advanced Photon Source (APS) at Argonne National Laboratory (Lemont, IL, USA). The wavelength used for the sXRD experiments was 0.1173 Å. Diffraction data for PFN–100xBFO (x = 0.4 and 0.5) were measured during application of various field amplitudes (from 0 to 5 kV cm^{-1} in 0.5 kV cm^{-1} increment) and after

release from electric field (0 kV cm^{-1}). The diffraction profiles represent scattering vectors oriented approximately parallel to the electric field. Debye–Scherrer rings of the samples under each electric field were measured with an exposure time of 0.5 s for 100 frames using a 2D PerkinElmer area detector. After that, a 1D pattern was calculated with FIT2D software by integrating a 2D diffraction image over an azimuthal 20° sector along the direction of the applied electric field. The beam center and distance were calibrated using a CeO_2 standard.

The microstructure of sintered ceramics was examined using a field-emission scanning electron microscope (FE-SEM, JSM-7600F, Jeol Ltd., Japan). Prior to microstructural analysis, the samples were fractured for fracture-surface examination, ground and fine-polished using a colloidal silica suspension, followed by thermal etching at 775 °C for 15 minutes in the presence of PFN packing powder. The average grain size and grain-size distribution were evaluated from the digitized images of etched surfaces, processed using the Image Tool software (UTHSCSA Image Tool Version 3.00. 2002)[36] by measuring more than 500 grains. The grain size is expressed as the Feret's diameter.[37] For the study of structural properties on the nanometer scale transmission electron microscope (TEM) JEM-2010F (Jeol Ltd., Japan) was used. TEM samples were prepared by mechanical grinding, dimpling and final Ar-ion milling.[38]

The local domain structure of sintered ceramics was recorded with an atomic force microscope (AFM, Asylum Research, Molecular Force Probe 3D, Santa Barbara, CA, USA) equipped with a piezoresponse force microscopy (PFM) dual AC resonance-tracking mode. Prior to the PFM measurements, surfaces of ceramic samples were prepared using standard metallographic procedures (thinning, grinding, polishing and fine polishing with SiO_2 particles) followed by heat treatment at 600 °C for 1 h with a cooling rate of 1 °C min^{-1}, in order to release internal stresses in the material. The final thicknesses of the as-prepared samples were ~70 μm. A tetrahedral Si tip (curvature diameter of 30 ± 10 nm) on a Si cantilever, both coated with Ti/Ir (Asyelec, AtomicForce F&E GmbH, Mannheim, Germany), was used. PFM out-of-plane amplitude images were conducted by applying an AC voltage of 10 and 20 V between the tip and the bottom electrode.

For characterization of electrical properties, the ceramic pellets were cut, thinned and polished to a thickness of ~200 μm (~600 μm for strain loops). In order to release the internal stresses produced during the mechanical processing, the thinned ceramic pellets were heated up to 600 °C for 1 h (with 5 °C min^{-1} heating rate) and then slowly cooled down (1 °C min^{-1}) to RT. The surfaces of the pellets were coated with Au electrodes (diameter of 5 mm) using RF-magnetron sputtering machine (5 Pascal, Italy). The relative dielectric permittivity (ε) and dielectric loss ($\tan\delta$) as a function of temperature were analyzed during cooling from 200 °C to −50 °C using an Aixacct TF analyzer 2000 (aixACCT Systems GmbH, Aachen, Germany) coupled with a HP 4284A (Hewlett-Packard, California, USA) Precision LCR impedance meter in a frequency range of 0.1–100 kHz. AC current density–electric field (J–E) and strain–electric field (S–E) loops were measured at RT using an Aixacct TF analyzer 2000 equipped with a laser interferometer by applying a single sinusoidal waveform with the frequency of 1 Hz (10 Hz for strain loops) and electric fields up to 70 kV cm^{-1}. Polarization–electric field (P–E) loops were automatically obtained by software using numerical integration of current signal. Piezoelectric coefficient (d_{33}) values were measured at RT and 100 Hz of stress frequency using a Berlincourt piezometer (Take Control PM10, Birmingham, UK). The measurements were performed 24 h after poling the samples. The results were presented in each composition as the mean value and standard deviation of the measurements done on three pellets. Prior to the measurements, the samples were poled in a silicone-oil bath at RT by applying a DC electric field of 30 kV cm^{-1} for 30 min.

III. Results and discussion

Firstly, the phase present, lattice parameters and microstructure of all seven PFN–100xBFO (x = 0–0.5) compositions were investigated. X-ray powder diffraction data indicate that all of the samples are pyrochlore-free, namely only the perovskite peaks are visible (see ESI,† material, D). Pure PFN crystallizes in monoclinic symmetry with Cm space group, which is in agreement with previous reports.[10,39,40] Substituting PFN with BFO leads to the formation of a pseudocubic (space group $Pm\bar{3}m$) phase as previously reported in ref. 14, 16 and 22. In compositions with smaller amounts of BFO (x = 0.05 and 0.1), Rietveld analysis revealed the coexistence of monoclinic and pseudocubic phases, while in samples with higher BFO contents ($0.2 \leq x \leq 0.5$) only a pseudocubic phase is present (Fig. 1a and b). According to the literature,[14,16] a transformation from cubic to rhombohedral symmetry (space group $R3c$) takes place in compositions with $x > 0.6$. Phase composition and lattice constants of all prepared samples are schematically shown in the form of a PFN–BFO phase diagram, presented in Fig. 1c. Details of Rietveld refinement analysis are shown in ESI† material, D.

Micrographs of polished and fractured sample surfaces are shown in Fig. 2. In all cases the microstructures are uniform, homogeneous and without the presence of visible secondary phases, which is in agreement with the results of the XRD analysis. All of the solid solutions are highly dense, from 97.6% to 99.7% of the theoretical density. The average grain size of all samples is comparable, *i.e.*, between 0.8 and 1.4 μm (see Fig. 2). Monomodal grain size distributions indicate a normal grain growth during the sintering process (ESI† material, C).

The temperature and frequency (ν) dependence of the real component of relative permittivity ε' and dielectric loss $\tan\delta$ for all compositions are shown in Fig. 3. In PFN, a paraelectric–ferroelectric phase transition with peak-permittivity values of ~30 000 (at 0.1 kHz) is observed at ~113 °C, showing a diffuse phase transition with a weak relaxor-like frequency dispersion, in agreement with literature data.[3,5,41,42] According to the high temperature of the paraelectric–ferroelectric phase transition in BFO (~825 °C),[1,2] it would be expected that the peak-permittivity

 This journal is © The Royal Society of Chemistry 2020

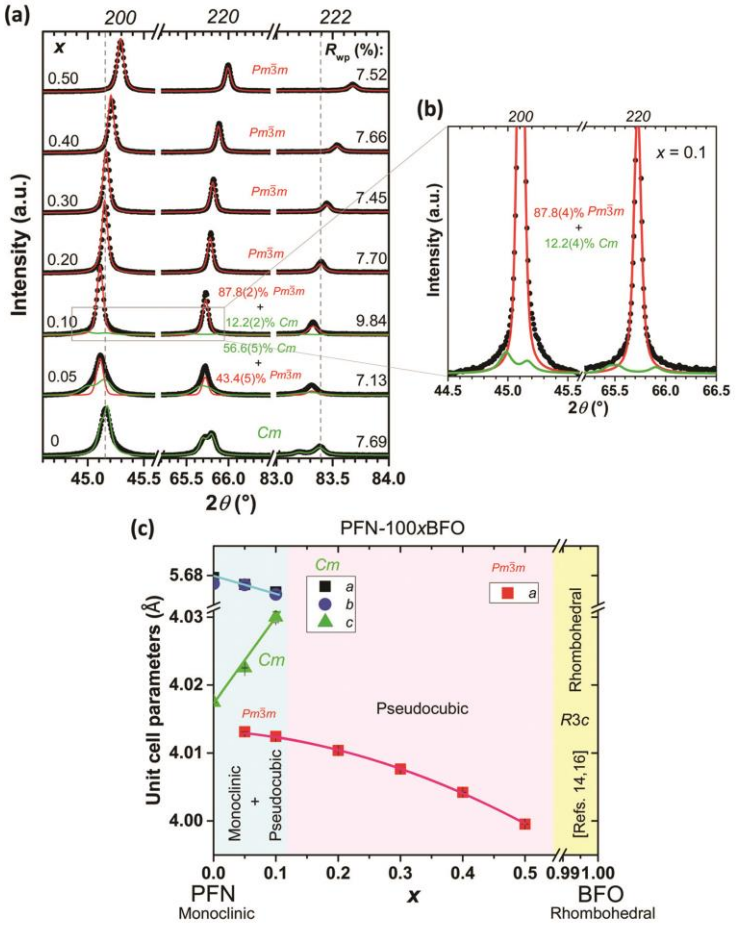


Fig. 1 (a) Room-temperature XRD profiles of the 200, 220, and 222 pseudocubic reflections (only from Cu $K\alpha_1$) for PFN–100*x*BFO (x = 0–0.5). The calculated profile for the monoclinic phase (*Cm* space group) is represented in green, while the pseudocubic phase ($Pm\bar{3}m$ space group) is displayed in red. (b) Zoom-in patterns of 200 and 220 reflections of the PFN–10BFO composition show the scattering contribution of both *Cm* and $Pm\bar{3}m$ phases to the diffraction pattern. (c) Lattice parameters of the PFN–100*x*BFO for compositions $0 \leq x \leq 0.5$.

temperature ($T_{\varepsilon,\max}$) of PFN–100*x*BFO system will be higher compared to PFN. Surprisingly, with a gradual increase in the BFO content up to x = 0.2, the $T_{\varepsilon,\max}$ of PFN–100*x*BFO solid solutions decreases, and dielectric peaks become more diffuse and frequency dependent, which indicates a strengthening of the relaxor behavior of the material.

Increasing relaxor behavior is clearly evident in the frequency dependence of a $T_{\varepsilon,\max}$ (Fig. 4a). The $T_{\varepsilon,\max}$ reaches the lowest value of 26 °C (at 0.1 kHz) in PFN–20BFO. In Fig. 4b the $\Delta T_{\varepsilon,\max}$ *versus* the sample composition is shown, where $\Delta T_{\varepsilon,\max}$ is defined as a difference between $T_{\varepsilon,\max}$ at 0.1 kHz and 100 kHz. $\Delta T_{\varepsilon,\max}$ is usually used to represent the relaxor behavior of the material.[43] As it can be seen, $\Delta T_{\varepsilon,\max}$ increases with addition of BFO with the maximum $\Delta T_{\varepsilon,\max}$ of 26 °C obtained in PFN–20BFO sample.

To further confirm the relaxor behavior of $x \leq 0.2$ compositions, Vogel–Fulcher analysis of ε' (T, ν) data was performed. The origin of the frequency-dispersive peak-permittivity of relaxors is related to the dynamics of polar nanoregions that freeze at the so-called freezing temperature (T_f).[44,45] The relationship between T_f, $T_{\varepsilon,\max}$ and driving frequency of the applied external electric field can be described with Vogel–Fulcher (V–F) relation, $\omega = \omega_0 \exp[-E_a/k_b(T_{\varepsilon,\max} - T_f)]$, where E_a represents activation energy, k_b is Boltzmann constant, ω ($2\pi\nu$) is angular frequency and ω_0 is a characteristic frequency.[45–47] $T_{\varepsilon,\max}(\omega)$ relations of $0 < x \leq 0.20$ compositions were fitted with V–F equation, where three parameters (ω_0, E_a and T_f) were obtained (Fig. 4c). The fitting formalism and the adequacy of our experimental data were validated on a well-known and studied $Pb(Mg_{1/3}Nb_{2/3})O_3$ relaxor material (ESI† material, E).

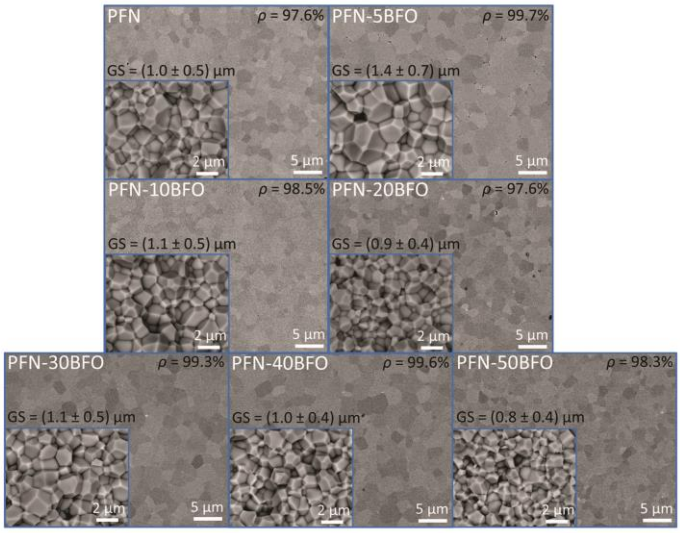


Fig. 2 SEM micrographs of polished and fractured (insets) PFN–100xBFO (x = 0–0.5).

Frequency-dependent dielectric permittivity responses of x = 0.05, 0.10 and 0.20 compositions nicely fit the V–F relation, confirming the relaxor behavior of these samples. The values of V–F parameters obtained by fitting, are shown in Fig. 4c. The T_f as well as E_a decreased with increasing the amount of BFO (up to x = 0.20), in agreement with the strengthening of relaxor behavior in these samples. It looks that the incorporation of BFO into the PFN crystal lattice stabilizes an ergodic relaxor phase. The reason for that could be related with an increased structural disorder, when different multivalence ions, such as Pb^{2+} and Bi^{3+}, occupy a crystallographically equivalent A-site of the perovskite structure.[26,48]

When increasing the BFO content (x = 0.3, 0.4 and 0.5), a more complex dielectric response is present. Slightly below or close to RT, a likely dispersive anomaly that could be related to traces of the frequency-dependent response seen in $x \leq 0.2$ compositions, is observed (marked by arrows in Fig. 3). On the other hand, it seems that in these compositions an additional anomaly starts to appear at temperatures higher than the permittivity maximum of pure PFN (Fig. 3). For PFN–30BFO this $T_{\varepsilon,max}$ is observed at ~150 °C, while for PFN–40BFO and PFN–50BFO, at ~200 °C and >200 °C, respectively. Due to the increased electrical conductivity at higher temperatures, which is also evident in the large increase of $\tan\delta$ with temperature (Fig. 3), a more precise determination of the $T_{\varepsilon,max}$ in these compositions was not possible.

To further investigate the origin of likely non-dispersive high temperature maximum of dielectric permittivity, differential scanning calorimetry (DSC) measurements were employed (ESI† material, F). DSC measurements of PFN–100xBFO (x = 0.3, 0.4 and 0.5) revealed an endothermic anomaly located in the vicinity of the peak-permittivity temperature, which might indicate a structural (anti)polar-to-non-polar phase transition. However, no detectable structural changes were observed in high-temperature XRD data (ESI† material, G).

A similar trend of $T_{\varepsilon,max}$ behavior was observed in ref. 14, 16 and 22, however the reported ε' values are much lower in comparison to the ones shown in Fig. 3. Furthermore, ε' were reported only at high frequencies (MHz range), most probably due to the high electrical conductivity of samples prepared by classical solid-state synthesis.[14,16] A possible reason for these differences could be a better chemical homogeneity and stoichiometry of mechanochemically-activated powder compared to those prepared by solid-state synthesis, as previously suggested for PFN[11] and $Pb(Sc_{0.5}Nb_{0.5})O_3$.[30]

The $\tan\delta$ values generally increase with increasing the BFO content (Fig. 3), are frequency-dependent and relatively low at the temperatures below 100 °C, namely 0.03 to 0.10 in a range between 0.1 and 100 kHz. The anomalies observed in $\tan\delta$ of PFN–100xBFO samples are correlated with the peak-permittivity values. Above 120 °C, the $\tan\delta$ increases with increasing temperature for all compositions. Comparison with previous reports is not possible due to the lack of given data or very high electrical conductivity of previously reported PFN–BFO samples.[14,16,22]

In order to verify the progressively increased relaxor behavior by the addition of BFO and to clarify the reason for the appearance of high-temperature anomaly observed by dielectric spectroscopy and DSC, the local structure of the samples was investigated using transmission electron microscopy (TEM). TEM micrographs of three solid solutions, *i.e.*, PFN, PFN–20BFO and PFN–50BFO, are shown in Fig. 5. In PFN, submicrometer-large wedge-type domains (marked by red arrows in Fig. 5a) indicate a more ferroelectric nature of the sample. On the other hand, in PFN–20BFO and PFN–50BFO only areas

 This journal is © The Royal Society of Chemistry 2020

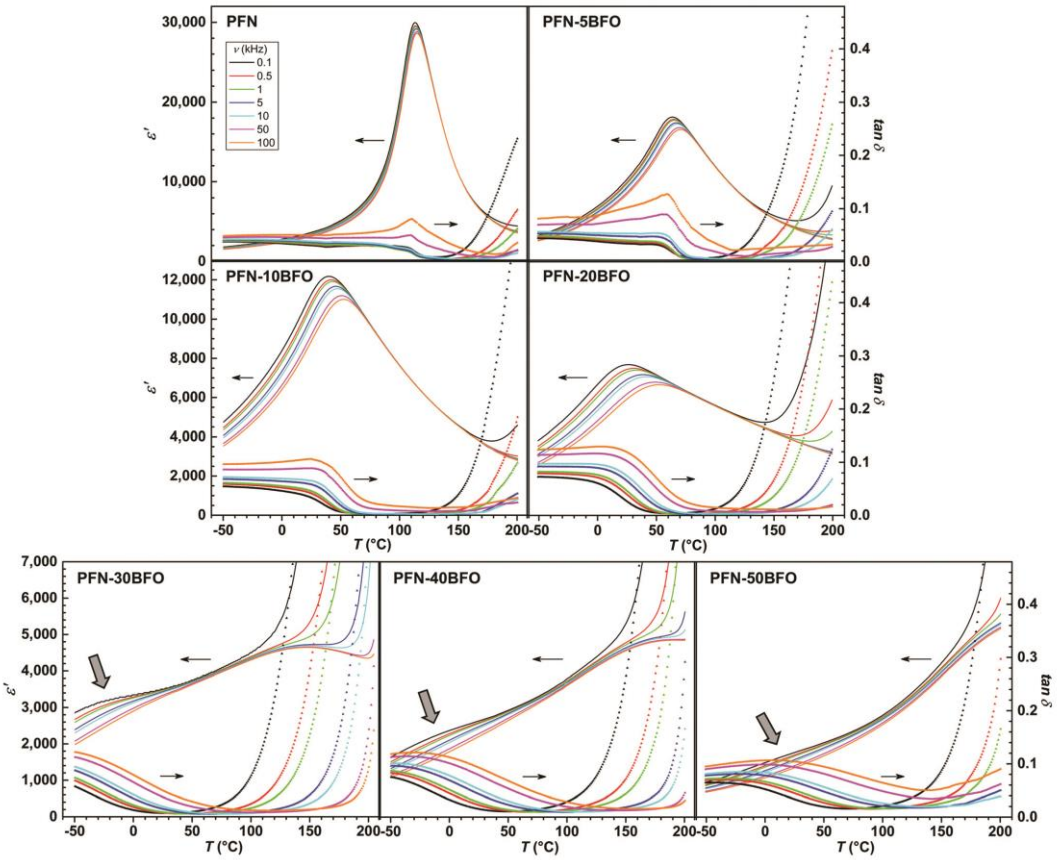


Fig. 3 Temperature and frequency dependences of ε' and $\tan\delta$ of PFN–100xBFO (x = 0–0.5). Note the differences in scales of ε'.

with nano-sized patterns (marked by green dashed circles in Fig. 5b and c) were observed.

The local short-range ordering was further investigated using high-resolution TEM (HRTEM). HRTEM image of PFN–50BFO with corresponding Fast Fourier Transform (FFT) is shown in Fig. 6a. FFT reveals superlattice $\frac{1}{2}\frac{1}{2}0$ reflections or so-called α spots.[49,50] Inverse FFT image using α spots (Fig. 6b) shows ~5 nm large regions whose origin could be related to anti-ferroelectric (AFE) fluctuations as already explained by A. Tkachuk *et al.*[50] However, it seems that the amount of the nano-AFE regions embedded in the pseudocubic relaxor phase is too small to be detected by XRD. HRTEM analyses were additionally performed for PFN–20BFO sample, but no α spots were found (ESI† material, H). The presence of AFE order could be the reason for the occurrence of high-temperature anomalies observed in dielectric permittivity measurements. These findings are supported by the results of the DSC analysis, where in PFN-rich compositions ($x \leq 0.2$) no anomalies were seen, while in BFO-rich compositions ($x \geq 0.3$) high-temperature phase changes were detected.

The local ferroelectric domain structure was additionally studied by piezoresponse force microscopy (PFM). PFM out-of-plane amplitude images, scanned at an AC drive amplitude of 10 V (the first scan of a virgin area) and 20 V, are shown in Fig. 7a and b, respectively. In PFN long-range ferroelectric order, evidenced by a sub-micrometer-large domain structure, was observed. Two different types of sub-micron-sized domains, wedged (marked by blue dashed arrows in Fig. 7a) and irregularly shaped (green dotted arrows in Fig. 7a) were also observed, in agreement a with previous study.[10] With increasing the amount of BFO, long-range ferroelectric domains gradually disappear. In the PFN–5BFO composition, irregularly shaped domains become smaller, a few hundred nm in size, and more rounded (marked by red solid arrows in Fig. 7a). In the PFN–10BFO composition, a PFM signal is still detected, but the size of irregular domains drops to a few tens of nanometers (marked by orange open arrows in Fig. 7a), which is close to the resolution limit of the PFM technique. In compositions with higher amounts of BFO ($x \geq 0.2$) zero piezo-response signal was observed at an AC drive amplitude of 10 V. These results

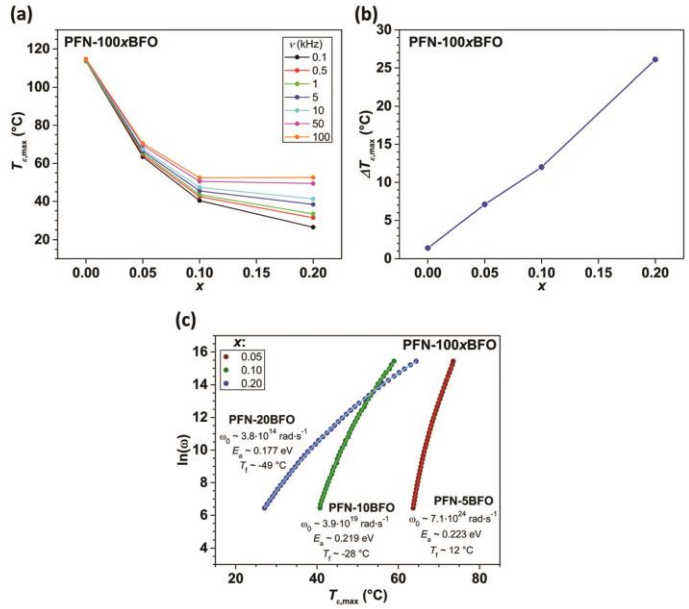


Fig. 4 (a) Frequency dependence of $T_{\varepsilon,max}$, (b) $\Delta T_{\varepsilon,max}$ and (c) $T_{\varepsilon,max}$ *versus* ln(ω) relations of PFN–100xBFO (x = 0–0.2). Line curves in (c) show the fits to our data using the V–F equation (see text) from where the ω_0, E_a and T_f parameters were obtained. Due to a too high electrical conductivity contribution, the values for x = 0.3–0.5 compositions could not be determined.

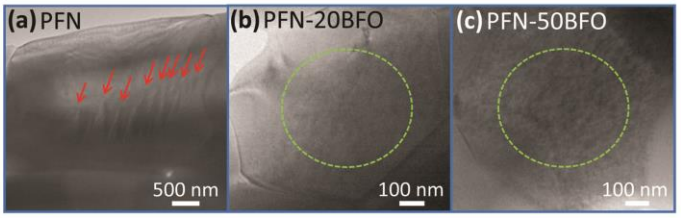


Fig. 5 TEM images of (a) PFN, (b) PFN–20BFO and (c) PFN–50BFO solid solutions. Sub-micron-sized wedge-type domains and nano-sized patterns are marked by red arrows and green dashed circles, respectively.

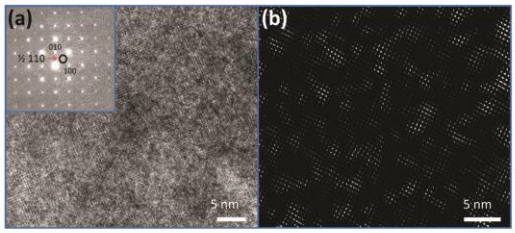


Fig. 6 (a) HRTEM image of a PFN–50BFO grain in [001] zone axis. Inset shows the FFT that reveals diffuse $\frac{1}{2}\frac{1}{2}$ 0 type spots (marked with red arrow). (b) The inverse FFT image using diffuse spots only highlights up to 5 nm large regions.

are consistent with the TEM study, where in PFN–50BFO only nano-range ordering is observed that is below the PFM detection limit (tip diameter ~30 nm).

When samples were scanned at an AC drive amplitude of 20 V (Fig. 7b), the piezo-response signal starts to appear in $x \geq 0.3$ compositions. This fine-grain response can be attributed to clusters of piezo-active polar nano-regions that reorganize under applied electric field as previously suggested for Pb-based relaxors.[51] These induced regions are several tens of nanometers in size. After 24 h, the same areas were scanned again with an AC drive amplitude of 10 V. During these scans, zero piezo-signal was observed again (similar to the ones in Fig. 7a for $x \geq 0.2$) indicating reversible electric field-induced phenomenon.

 This journal is © The Royal Society of Chemistry 2020

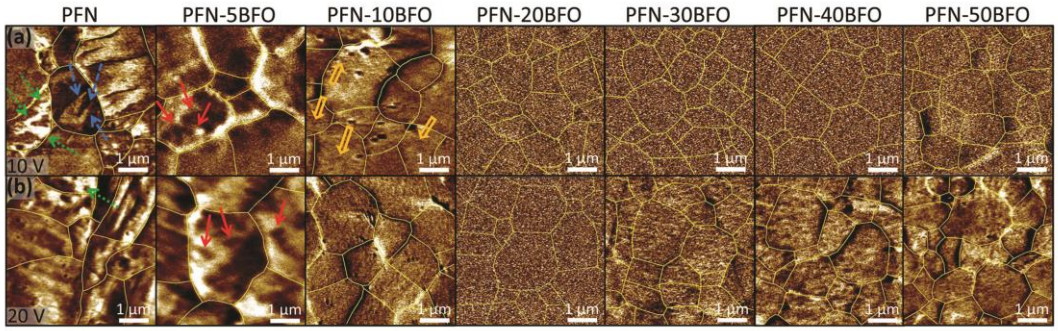


Fig. 7 PFM out-of-plane amplitude images obtained by scanning with AC drive signals of (a) 10 V and (b) 20 V of PFN–100*x*BFO (x = 0–0.5). Sub-micron-sized wedge domains are marked by blue dashed arrows. Irregular sub-micron-sized domains, a few hundred nm-large domains and a few tens of nm-large domains are marked by green dotted, red solid and orange open arrows, respectively.

P–E hysteresis loops of all PFN–100*x*BFO compositions are shown in Fig. 8. In pure PFN, ferroelectric square-like hysteresis loops were observed,[52] which is in agreement with previous reports.[11,42,53] The remanent polarization (P_r) and coercive filed (E_c) of pure PFN are ~22 μC cm^{-2} and ~3.5 kV cm^{-1}, respectively. With increasing contents of BFO up to x = 0.2, *P–E* loops become slimmer and tilted, indicating increased relaxor behavior in agreement with aforementioned analyses. Similar to the *P–E* loops, the more pronounced relaxor behavior is also reflected in the *S–E* measurements, which show a more quadratic-like response with diminished hysteresis, characteristic for electrostrictive response (ESI† material, I). This is the first time when *P–E* loops of PFN–100*x*BFO ($x \leq 0.5$) solid solutions were systematically studied, therefore a comparison with the literature data is not possible.

In compositions with higher BFO content (x = 0.2–0.5), *P–E* loops develop a pinched shape and gradually become thicker (show larger hysteresis). Pinching is more evident in the AC current density–electric field (*J–E*) hysteresis loops by the appearance of double current peaks (ESI† material, J). In general, there can be many reasons for the appearance of pinched *P–E* loops.[52] One reason could be related to the AFE ordering observed in HRTEM study. Due to the antisymmetric crystal sublattices this typically results in a double *P–E* hysteresis loop.[52] Often, pinching can also be related to electric-field-induced relaxor-to-ferroelectric phase transition that occurs during the measurement, as previously reported in $Pb(Sc_{0.5}Ta_{0.5})O_3$[54] and $Pb(Sc_{0.5}Nb_{0.5})O_3$[55] ceramics. In these two cases, the pinching was related to the coexistence of ferroelectric and relaxor phases and transition between them induced by application of high electric fields. Another reason for the pinched behavior is associated with the presence of charged point defects, such as oxygen vacancies or other type of defects which act as strong pinning centers for domain walls or similar interfaces. As previously demonstrated in $Pb(Zr,Ti)O_3$ ceramics,[56–58] an indirect evidence that pinching is indeed related to the pinning behavior of such charged point defects is obtained from a continues AC electric-field-cycling experiments and measurements of *P–E* and *J–E* hysteresis loops at different frequencies where the hysteresis loops eventually opens up or relaxes during field cycling. These experiments, provided for our PFN–BFO in ESI† material K, show that cycling of PFN–50BFO sample do not affect the shape of the *P–E* hysteresis loop, *i.e.*, the loop remains pinched. However, the additional rapid cooling (quenching) experiment shows that *P–E* hysteresis loops were partially de-pinched; in this experiment the loop is expected to completely depinch if the pinching is controlled by charged point defects because quenching leads to redistribution of the defects from an ordered (pinched) to a disordered (depinched) state (ESI† material, L).[59] Therefore, the influence of the charged point defects on pinching in PFN–50BFO cannot be completely excluded, however it appears as defects have still a minor role in the pinching behavior.

In order to further investigate the origin of electric-field induced phenomena, synchrotron X-ray diffraction (sXRD) measurements of PFN–50BFO were employed. Maps of the 111 and 200 pseudocubic reflections during *in situ* applied voltage up to 50 kV cm^{-1} and after release are shown in Fig. 9. From the measurements, it seems that PFN–50BFO does not exhibit a classical field-induced phase transition; however, the data contain some interesting features, including broadening and weakening in intensity of all peaks parallel to the field direction. These changes are isotropic and recoverable. Most probably, the transition involves changes at a length scale smaller than visible by diffraction, possibly deformation or reorganization of polar regions at the nanoscale (Fig. 7b) into larger clusters, which transform back when the electric field is removed. Similar behavior was also observed in $BiFeO_3$–$BaTiO_3$ based ceramics,[60] but in general, this phenomenon is not yet well described in the literature. *In situ* sXRD measurements were also performed for PFN–40BFO composition (ESI† material, M). However, the changes in intensity of peaks under the electric field are not so pronounced as in the case of PFN–50BFO, which is consistent with slimmer *P–E* and *S–E* hysteresis loops and consequently smaller pinching of PFN–40BFO.

The strengthening of the relaxor features in PFN–100*x*BFO solid solution is also reflected in piezoelectric properties. The values of piezoelectric coefficient d_{33} of all studied compositions

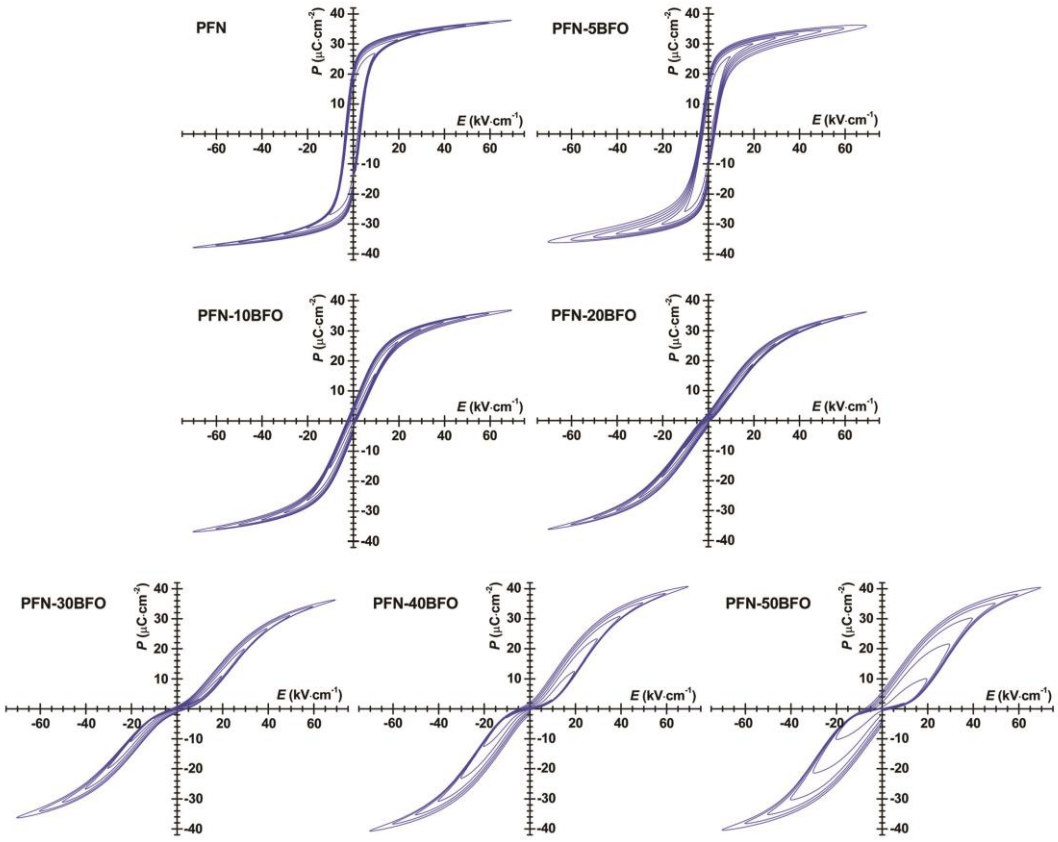


Fig. 8 *P*–*E* hysteresis loops of PFN–100*x*BFO (*x* = 0–0.5) at RT measured with increasing electric-field amplitude at driving frequency of 1 Hz.

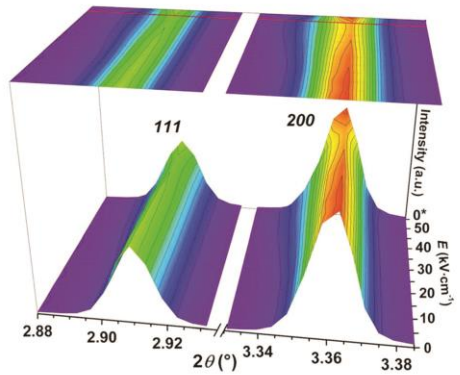


Fig. 9 Room-temperature *in situ* sXRD surface contour plots of the 111 and 200 pseudocubic reflections of PFN–50BFO with *in situ* applied voltage up to 50 kV cm^{-1} and after release (*0 kV cm^{-1}).

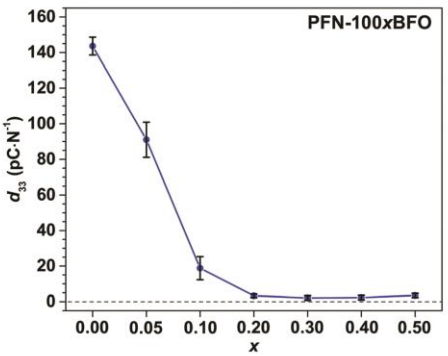


Fig. 10 Piezoelectric coefficient d_{33} of PFN–100*x*BFO (*x* = 0–0.5).

are shown in Fig. 10. The measurements were performed 24 h after poling so that any reversible electric-filed-induced changes that are observed in measurements under *in situ* applied electric field (see above sXRD and PFM measurements) are already relaxed back to the initial state. PFN exhibits the highest d_{33} of ~145 pC N^{-1}, which is consistent with previously

 This journal is © The Royal Society of Chemistry 2020

reported values.[5,10] d_{33} of PFN–100xBFO solid solutions gradually decreases with increasing BFO content and drops to almost zero in $x \geq 0.2$ compositions as expected for relaxor systems.

IV. Summary and conclusions

In this work, PFN–100xBFO (x = 0, 0.05, 0.1, 0.2, 0.3, 0.4 and 0.5) solid solutions were successfully prepared by mechanochemical synthesis followed by sintering at different temperatures. An optimized processing procedure resulted in the preparation of highly dense single-phase ceramics with comparable grain size and relatively low dielectric losses, which enable the systematic study of dielectric, ferroelectric and electromechanical properties of the PFN–BFO solid solutions.

PFN crystalizes in monoclinic symmetry. It exhibits well-defined and open *P–E* hysteresis loops with remanent polarization and coercive field values of $\sim$22 μC cm^{-2} and $\sim$3.5 kV cm^{-1}, respectively. Sub-micrometer-sized ferroelectric domains were observed by PFM and TEM. Introducing BFO into the PFN–BFO solid solution leads to the formation of a pseudocubic phase and consequently to enhanced relaxor-like behavior obeying the Vogel–Fulcher law.

The PFN–BFO compositions with small amounts of BFO (x = 0.05 and 0.1) exhibit coexistence of monoclinic and pseudocubic phases, which are accompanied by a broadening of dielectric peak-permittivity, slimmer *P–E* hysteresis loops, sub-micrometer irregularly shaped ferroelectric domains and a gradual decrease in the piezoelectric response compared to pure PFN. When adding extra BFO into the structure (x = 0.2–0.5), only pseudocubic symmetry is present. In these compositions, nanometer sized domains are observed by TEM. Additionally, superlattice $\frac{1}{2}\ \frac{1}{2}\ 0$ reflections are observed in PFN–50BFO form the HRTEM analysis, but not detected by XRD. These superlattice reflection indicate that antiferroelectric nanoislands are embedded in the pseudocubic relaxor phase.

During high-field electric properties measurements, recoverable electric-field phenomena appears, which is reflected in pinching of the *P–E* hysteresis loops. This is most probably related to several factors such as the reorganization of polar nano-domains into clusters under the electric field, AFE order and charged point defects present in the material.

In conclusion, PFN–10BFO and PFN-20BFO exhibit slim *P–E* hysteresis loops and peak-permittivity temperatures near ambient temperature, which make them promising for electrocaloric cooling applications. On the other hand, low hysteresis losses and electrostriction of PFN–20BFO and PFN–30BFO make these materials also potentially useful for energy storage applications and precision displacement actuators.

Conflicts of interest

There are no conflicts to declare.

Acknowledgements

The authors thank the financial support from the Slovenian Research Agency (project Multicaloric cooling J2-9253, young researcher project PR-07594, bilateral project BI-US/19-21-062 and research core funding No. P2-0105). Technical support by Brigita Kmet (from JSI), Milan Baricevic and Marko Mudri (Erasmus+ programme) is gratefully acknowledged. Centre of Excellence NAMASTE is acknowledged for access to the AFM equipment. This research used resources of the Advanced Photon Source, a U.S. Department of Energy (DOE) Office of Science User Facility operated for the DOE Office of Science by Argonne National Laboratory under Contract No. DE-AC02-06CH11357. Contributions from RS and GB were supported by a CoorsTek Fellowship and the US National Science Foundation (DMR-1555015), respectively.

References

1 G. Catalan and J. F. Scott, *Adv. Mater.*, 2009, **21**, 2463–2485.
2 T. Rojac, A. Bencan, B. Malic, G. Tutuncu, J. L. Jones, J. E. Daniels and D. Damjanovic, *J. Am. Ceram. Soc.*, 2014, **97**, 1993–2011.
3 V. A. Bokov, I. E. Mylnikova and G. A. Smolenskii, *J. Exp. Theor. Phys.*, 1962, **42**, 643–646.
4 C. C. Chiu and S. B. Desu, *Mater. Sci. Eng., B*, 1993, **21**, 26–35.
5 M. Yokosuka, *Jpn. J. Appl. Phys.*, 1993, **32**, 1142–1146.
6 R. Havlicek, J. Poltierova Vejpravova and D. Bochenek, *J. Phys.: Conf. Ser.*, 2010, **200**, 012058.
7 O. Raymond, R. Font, N. Suarez-Almondovar, J. Portelles and J. M. Siqueiros, *J. Appl. Phys.*, 2005, **97**, 084108.
8 S.-B. Lee, S.-H. Yoon and H. Kim, *J. Eur. Ceram. Soc.*, 2004, **24**, 2465–2470.
9 C. Stock, S. R. Dunsiger, R. A. Mole, X. Li and H. Luo, *Phys. Rev. B: Condens. Matter Mater. Phys.*, 2013, **88**, 094105.
10 H. Ursic, A. Bencan, U. Prah, M. Dragomir and B. Malic, *Materials*, 2019, **12**, 1327.
11 U. Prah, T. Rojac, M. Wencka, M. Dragomir, A. Bradesko, A. Bencan, R. Sherbondy, G. Brennecka, Z. Kutnjak, B. Malic and H. Ursic, *J. Eur. Ceram. Soc.*, 2019, **39**, 4122–4130.
12 R. Mackeviciute, V. Goian, S. Greicius, R. Grigalaitis, D. Nuzhnyy, J. Holc, J. Banys and S. Kamba, *J. Appl. Phys.*, 2015, **117**, 084101.
13 T. Rojac, M. Makarovic, J. Walker, H. Ursic, D. Damjanovic and T. Kos, *Appl. Phys. Lett.*, 2016, **109**, 042904.
14 C. F. Buhrer, *J. Chem. Phys.*, 1962, **36**, 798–803.
15 G. A. Smolenskii and V. M. Yudin, *Phys. Solid State*, 1965, **6**, 2936–2942.
16 N. N. Krainik, N. P. Khuchua, A. A. Berezhnoi and A. G. Tutov, *Phys. Solid State*, 1965, **7**, 100–107.
17 V. V. Zhdanova, *Phys. Solid State*, 1965, **7**, 108–111.
18 I. H. Ismailzade, R. M. Ismailov, A. I. Alekperov and F. M. Salaev, *Phys. Status Solidi A*, 1980, **57**, 99–103.
19 I. O. Troyanchuk, M. V. Bushinsky, A. N. Chobot, O. S. Mantytskaya, N. V. Pushkarev and R. Szymczak, *J. Exp. Theor. Phys.*, 2008, **107**, 245–250.

20 D. Bochenek, R. Zachariasz, J. Ilczuk and J. Dudek, *Acta Phys. Pol., A*, 2009, **116**, 274–276.
21 J. P. Patel, A. Singh and D. Pandey, *J. Appl. Phys.*, 2010, **107**, 104115.
22 L. A. Shilkina, A. V. Pavlenko, L. A. Reznitchenko and I. A. Verbenko, *Crystallogr. Rep.*, 2016, **61**, 263–269.
23 A. Stoch, J. Maurin, J. Kulawik and P. Stoch, *J. Eur. Ceram. Soc.*, 2017, **37**, 1467–1476.
24 D. Bochenek, P. Niemiec, P. Guzdek and M. Wzorek, *Mater. Chem. Phys.*, 2017, **195**, 199–206.
25 A. Stoch and P. Stoch, *Ceram. Int.*, 2018, **44**, 14136–14144.
26 F. Li, S. Zhang, D. Damjanovic, L.-Q. Chen and T. R. Shrout, *Adv. Funct. Mater.*, 2018, **28**, 1801504.
27 D. Damjanovic and R. E. Newnham, *J. Intell. Mater. Syst. Struct.*, 1992, **3**, 190–208.
28 M. Vrabelj, H. Ursic, Z. Kutnjak, B. Rozic, S. Drnovsek, A. Bencan, V. Bobnar, L. Fulanovic and B. Malic, *J. Eur. Ceram. Soc.*, 2016, **36**, 75–80.
29 T. Rojac and M. Kosec, in *High-Energy Ball Milling*, ed. M. Sopicka-Lizer, Woodhead Publishing, 1st edn, 2010, ch. 6, pp. 113–148.
30 H. Ursic, A. Bencan, G. Drazic, G. Esteves, J. L. Jones, T.-M. Usher, T. Rojac, S. Drnovsek, M. Deluca, J. Jouin, V. Bobnar, G. Trefalt, J. Holc and B. Malic, *J. Mater. Chem. C*, 2015, **3**, 10309–10315.
31 R. Jimenez, H. Amorin, J. Ricote, J. Carreaud, J. M. Kiat, B. Dkhil, J. Holc, M. Kosec and M. Alguero, *Phys. Rev. B: Condens. Matter Mater. Phys.*, 2008, **78**, 094103.
32 Y. Tan, J. Zhang, Y. Wu, C. Wang, V. Koval, B. Shi, H. Ye, R. McKinnon, G. Viola and H. Yan, *Sci. Rep.*, 2015, **5**(9953), 1–9.
33 R. Font, O. Raymond-Herrera, L. Mestres, J. Portelles, J. Fuentes and J. M. Siqueiros, *J. Mater. Sci.*, 2016, **51**, 6319–6330.
34 D. Pfoertsch and C. Ruud, Penn State University, University Park, Pennsylvania, USA, ICDD Grant-in-Aid, PDF No. 032-0522, 1981.
35 R. W. Cheary and A. Coelho, *J. Appl. Crystallogr.*, 1992, **25**, 109–121.
36 D. Wilcox, B. Dove, B. McDavid and D. Greer, *UTHSCSA Image Tool for Windows Version 3.0*, University of Texas Health Science Center, San Antonio, TX, 2002.
37 W. H. Walton, *Nature*, 1948, **162**, 329–330.
38 D. B. Williams and C. B. Carter, Transmission Electron Microscopy, *A Textbook for Materials Science*, Springer, Boston, MA, USA, 2009.
39 N. Lampis, P. Sciau and A. G. Lehmann, *J. Phys.: Condens. Matter*, 1999, **11**, 3489–3500.
40 I.-K. Jeong, J. S. Ahn, B. G. Kim, S. Yoon, S. Pal Singh and D. Pandey, *Phys. Rev. B: Condens. Matter Mater. Phys.*, 2011, **83**, 064108.
41 S. Ananta and N. W. Thomas, *J. Eur. Ceram. Soc.*, 1999, **19**, 2917–2930.
42 R. Font, O. Raymond, E. Martinez, J. Portelles and J. M. Siqueiros, *J. Appl. Phys.*, 2009, **105**, 114110.
43 I. Grinberg, P. Juhas, P. K. Davies and A. M. Rappe, *Phys. Rev. Lett.*, 2007, **99**, 267603.
44 R. Pirc and R. Blinc, *Phys. Rev. B: Condens. Matter Mater. Phys.*, 2007, **76**, 020101.
45 H. Ursic and D. Damjanovic, *Appl. Phys. Lett.*, 2013, **103**, 072907.
46 H. Vogel, *Phys. Z.*, 1921, **22**, 645.
47 G. S. Fulcher, *J. Am. Ceram. Soc.*, 1925, **8**, 339–355.
48 A. A. Bokov and Z. G. Ye, *J. Mater. Sci.*, 2006, **41**, 31–52.
49 A. M. Glazer, *Acta Crystallogr., Sect. A: Found. Crystallogr.*, 1975, **31**, 756–762.
50 A. Tkachuk and H. Chen, *AIP Conf. Proc.*, 2003, **677**, 55–64.
51 V. V. Shvartsman, A. L. Kholkin, A. Orlova, D. Kiselev, A. A. Bogomolov and A. Sternberg, *Appl. Phys. Lett.*, 2005, **86**, 202907.
52 T. Schenk, E. Yurchuk, S. Mueller, U. Schroeder, S. Starschich, U. Böttger and T. Mikolajick, *Appl. Phys. Rev.*, 2014, **1**, 041103.
53 B. Fraygola, N. Frizon, W. J. Nascimento, A. A. Coelho, D. Garcia and J. A. Eiras, *Ferroelectrics*, 2014, **470**, 221–226.
54 F. Chu, N. Setter and A. K. Tagantsev, *J. Appl. Phys.*, 1993, **74**, 5129–5134.
55 F. Chu, I. M. Reaney and N. Setter, *J. Appl. Phys.*, 1995, **77**, 1671–1676.
56 M. I. Morozov and D. Damjanovic, *J. Appl. Phys.*, 2008, **104**, 034107.
57 T. Rojac, S. Drnovsek, A. Bencan, B. Malic and D. Damjanovic, *Phys. Rev. B*, 2016, **93**, 014102.
58 K. Carl and K. H. Hardtl, *Ferroelectrics*, 1978, **17**, 473–486.
59 D. Damjanovic, in *The Science of Hysteresis*, ed. I. Mayergoyz and G. Bertotti, Elsevier, vol. 3, 2006, ch. 4, pp. 337–465.
60 G. Wang, Z. Fan, S. Murakami, Z. Lu, D. A. Hall, D. C. Sinclair, A. Feteira, X. Tan, J. L. Jones, A. K. Kleppe, D. Wang and I. M. Reaney, *J. Mater. Chem. A*, 2019, **7**, 21254–21263.

 This journal is © The Royal Society of Chemistry 2020

Supplementary material

Strengthened relaxor behavior in $(1-x)Pb(Fe_{0.5}Nb_{0.5})O_3–xBiFeO_3$

Uroš Prah,[a,b] Mirela Dragomir,[a] Tadej Rojac,[a,b] Andreja Benčan,[a,b] Rachel Broughton,[c] Ching-Chang Chung,[d] Jacob L. Jones,[c] Rachel Sherbondy,[e] Geoff Brennecka[e] and Hana Uršič[a,b,*]

[a] Jožef Stefan Institute, Jamova cesta 39, 1000 Ljubljana, Slovenia.
[b] Jožef Stefan International Postgraduate School, Jamova cesta 39, 1000 Ljubljana, Slovenia.
[c] Department of Materials Science and Engineering, North Carolina State University, Raleigh, NC 27695, USA.
[d] Analytical Instrumentation Facility, North Carolina State University, Raleigh, NC 27695, USA.
[e] Colorado School of Mines, 1500 Illinois St., Golden, CO 80401, USA.
[*] Corresponding author: hana.ursic@ijs.si

A. XRD analysis of mechanochemically activated powder

The optimal total milling time of mechanochemical activation process of PFN–100xBFO (x = 0.05–0.50) was determined from XRD analysis of powders, which were analyzed after certain time of high-energy milling. XRD patterns of PFN–50BFO powder after certain time of activation are shown in Fig. S1. Similar behavior was also observed in all other PFN–100xBFO (x = 0.05–0.40) compositions.

Initially, during the first 6 h, mainly amorphization of starting oxides takes place, which is reflected in a decrease in the intensity of the diffraction peaks and an increase in the background. Between 6 and 8 h of milling, the perovskite phase begins to form. After 14 h all the starting oxides were transformed either to amorphous or crystalline perovskite phase (approximate mass ratio of 50:50). Because perovskite phase was already formed during the high-energy milling, no additional calcination step before sintering was needed.

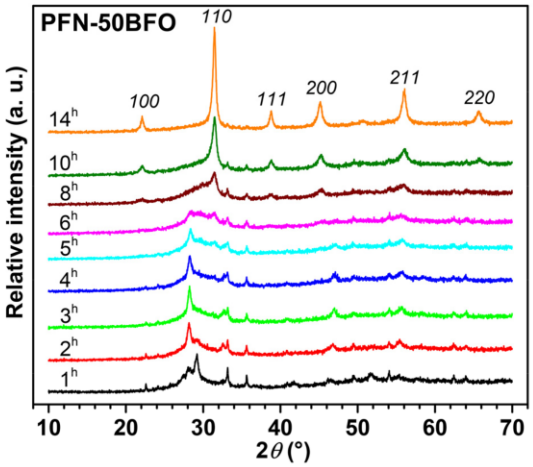


Figure S1. Room-temperature XRD patterns of PFN–50BFO powder after certain time of mechanochemical activation (1–14 h). Diffraction peaks corresponding to perovskite phase are indexed according to the cubic notation.

B. Sintering behavior of samples

The dynamic sintering curves of the powder compacts were recorded during heating using an optical dilatometer (Leitz Version 1A, Leitz, Wetzlar, Germany). In all cases heating rate of 5 °C·min^{-1}, which is the lowest calibrated temperature rate of our instrument, was used. Sintering curves of all PFN–100*x*BFO (*x* = 0–0.5) solid solutions are shown in Fig. S2. With increasing amount of BFO the densification of the samples, evidenced as a rapid shrinkage of the powder compact, shifts toward lower temperatures.

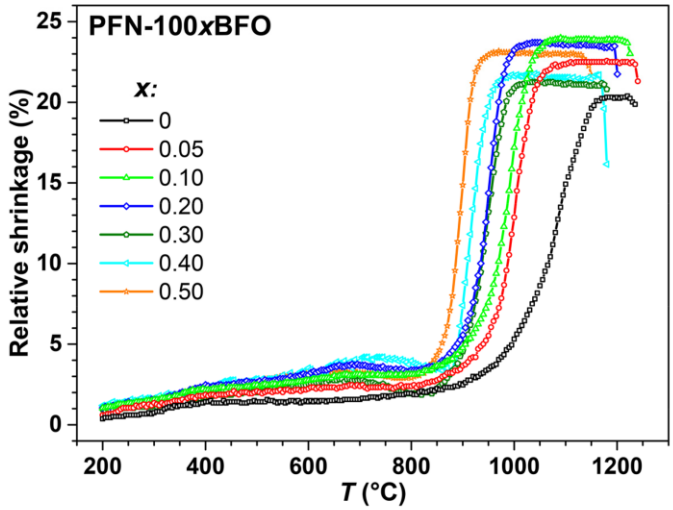


Figure S2. Dynamic sintering curves of different PFN–100*x*BFO (*x* = 0–0.5) powder compacts.

We point out that for the actual sintering process heating rate of 5 °C·min^{-1} did not result in sufficiently dense ceramics, while prolonged duration time of sintering process led to higher PbO losses and consequently more electrically conductive samples. Therefore, to achieve sufficient densification and at the same time to minimize the evaporation of PbO, the heating rate of 2 °C·min^{-1} was used. Note that due to the use of different heating rates in sintering process and in dynamic sintering curve measurement, the direct comparison of densification process is not possible. The dynamic sintering curves serve only to estimate the approximate sintering temperature.

C. Microstructure and grain size distributions

SEM images of the thermally etched surfaces and grain size distributions of different PFN–100*x*BFO (x = 0–0.5) solid solutions are shown in Fig. S3. In all compositions, SEM images reveal uniform and dense microstructures (note that in some samples also some pull-outs, produced during the sample surface preparation, are present). In all samples, a unimodal grain size distribution is observed.

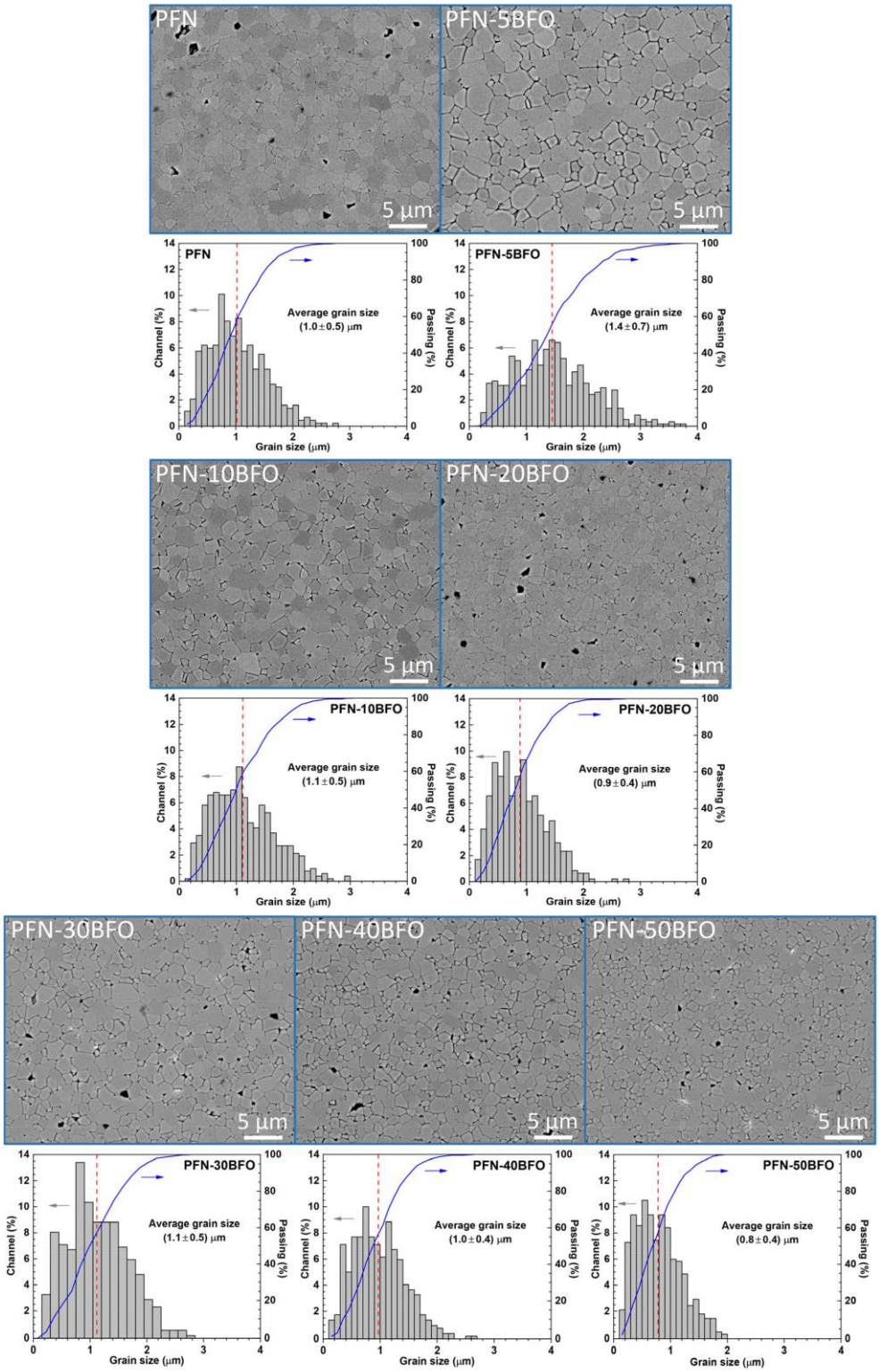


Figure S3. SEM images of thermally etched surfaces and the grain size distributions of different PFN–100*x*BFO (*x* = 0–0.5) solid solutions.

D. Rietveld refinement

The XRD patterns of crushed PFN–100*x*BFO (*x* = 0–0.5) ceramic pellets are shown in Fig. S4. Only the peaks corresponding to the perovskite phase are observed with no additional secondary phase (see inset of Fig. S4).

The phase composition, crystal structure and lattice parameters of PFN–100*x*BFO (*x* = 0–0.5) were investigated by the Rietveld refinement method. The agreement factors of the Rietveld analysis along with the cell parameters of all the samples are given in Table S1.

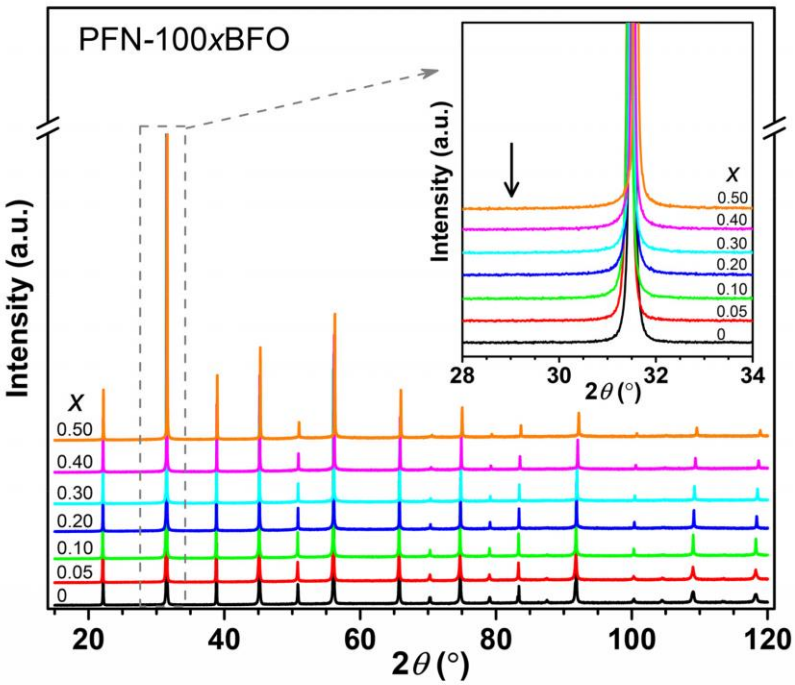


Figure S4. Room-temperature XRD patterns of PFN–100*x*BFO (*x* = 0–0.5) solid solutions. The inset shows an enlarged 2θ region with an arrow marking the position where the strongest pyrochlore peak would appear.

Table S1: Refined structural parameters for PFN–100xBFO (x = 0–0.5) solid solutions.

Composition	**PFN**	**PFN-5BFO**		**PFN-10BFO**		**PFN-20BFO**	**PFN-30BFO**	**PFN-40BFO**	**PFN-50BFO**
Crystal system	Monoclinic	Monoclinic	Cubic	Monoclinic	Cubic	Cubic	Cubic	Cubic	Cubic
Space group	*Cm*	*Cm*	$Pm\bar{3}m$	*Cm*	$Pm\bar{3}m$	$Pm\bar{3}m$	$Pm\bar{3}m$	$Pm\bar{3}m$	$Pm\bar{3}m$
Weight fraction (%)	100	56.73(5)	43.27(5)	12.22(2)	87.78(2)	100	100	100	100
a (Å)	5.67774(7)	5.67084(9)	4.01314(2)	5.66320(6)	4.01245(2)	4.01038(9)	4.00764(1)	4.00420(4)	3.99951(6)
b (Å)	5.67196(4)	5.67056(9)	/	5.66078(5)	/	/	/	/	/
c (Å)	4.01775(7)	4.02244(7)	/	4.02999(3)	/	/	/	/	/
β (°)	89.8843(9)	89.9867(9)	/	89.5823(8)	/	/	/	/	/
V (Å^3)	129.3873(3)	129.3491(9)	63.6329(7)	129.1906(9)	64.5993(6)	64.4999(9)	64.3674(4)	64.2020(1)	63.9767(6)
ρ (g·cm^{-3})	8.4595(1)	8.4619(4)	8.3768(1)	8.4724(6)	8.2565(8)	8.4123(5)	8.3727(1)	8.3509(1)	8.3368(6)
R_{wp} (%)	7.693	7.125		9.837		7.703	7.449	7.665	7.520
R_{exp} (%)	5.125	5.053		4.937		4.931	5.054	4.997	4.866
R_p (%)	5.644	5.374		6.874		5.885	5.638	5.710	5.621
G. O. F.	1.501	1.410		1.992		1.562	1.474	1.534	1.545
R_b (%)	2.399	1.636	4.736	8.161	7.816	2.456	2.123	2.696	2.895

E. Vogel-Fulcher analysis

The fitting formalism and the adequacy of the data obtained from our setup were first tested on a prototype relaxor material, $Pb(Mg_{1/3}Nb_{2/3})O_3$ (PMN). PMN ceramic was prepared from oxides using mechanochemical-activation-assisted synthesis followed by sintering at 1200 °C for 2 h in the presence of PMN packing powder with the same composition as the pellets. Details of the synthesis procedure are described in Ref. [1].

$T_{e,max}(\omega)$ relations of PMN ceramics were fitted with V-F equation (details can be found in the manuscript), where three V-F parameters were obtained (Fig. S5). The dielectric permittivity data fits well with the V-F law resulting in ω_0, E_a and T_f of ~$3.5 \cdot 10^{14}$ rad·s^{-1}, ~0.087 eV and −48 °C, respectively. The results are in a good agreement with literature data.[1-3]

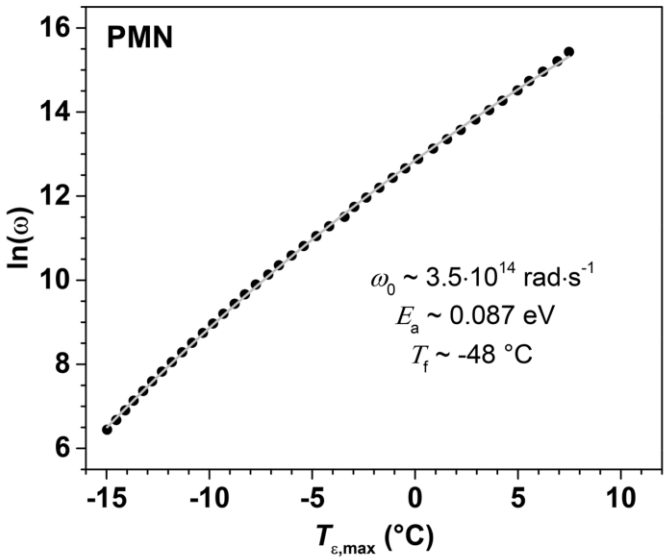


Figure S5. $T_{\varepsilon,max}$ versus ln(ω) relation of PMN. Line curve shows the fit of data with V-F equation (see text in the manuscript) from where V-F parameters ω_0, E_a *and* T_f are obtained.

F. Differential Scanning Calorimetry

Thermal changes that correspond to structural phase transitions of the ceramic samples were determined from the differential scanning calorimetry curves measured using a differential scanning calorimeter, DSC (Netzsch, DSC 204 F1, Selb, Germany). The measurements were performed on ceramic pellets of ~6 mm in diameter and thickness of ~0.25 mm, which were placed in Pt crucible with lid. In order to eliminate the possible thermal effects related to water evaporation and desorption of gasses from the surface of the sample, two heating and cooling cycles were performed for each composition. In the first cycle, the samples were heated from 25 °C to 500 °C followed by cooling down to −50 °C using liquid nitrogen. Afterwards the samples were heated again to 500 °C followed by cooling back to 25 °C. For all measurements heating and cooling rates of 10 °C·min^{-1} were used.

Temperature dependences of DSC signals of all compositions, obtained from the second heating run, are shown in Fig. S6. In pure PFN an endothermic anomaly at ~100 °C, which according to dielectric permittivity measurements belongs to paraelectric-to-ferroelectric phase transition, was observed (Fig. S6a). In PFN–100*x*BFO compositions with $x \leq 0.20$ no detectable thermal

changes were seen, which is in a good agreement with the nature of canonical relaxor materials, where no structural phase transitions should be present. On the other hand, in compositions with $x \geq 0.30$ (Fig. S6b and c) endothermic anomalies were detected in the vicinity or slightly below the temperatures where the high-temperature anomalies appeared in dielectric permittivity measurements (Fig. 3 in the manuscript). The reason for the difference in the temperature of the anomaly occurrence may be partly due to the different measurement conditions of the both techniques (i.e., different heating/cooling rates, furnace configuration, measurement principle, etc.)

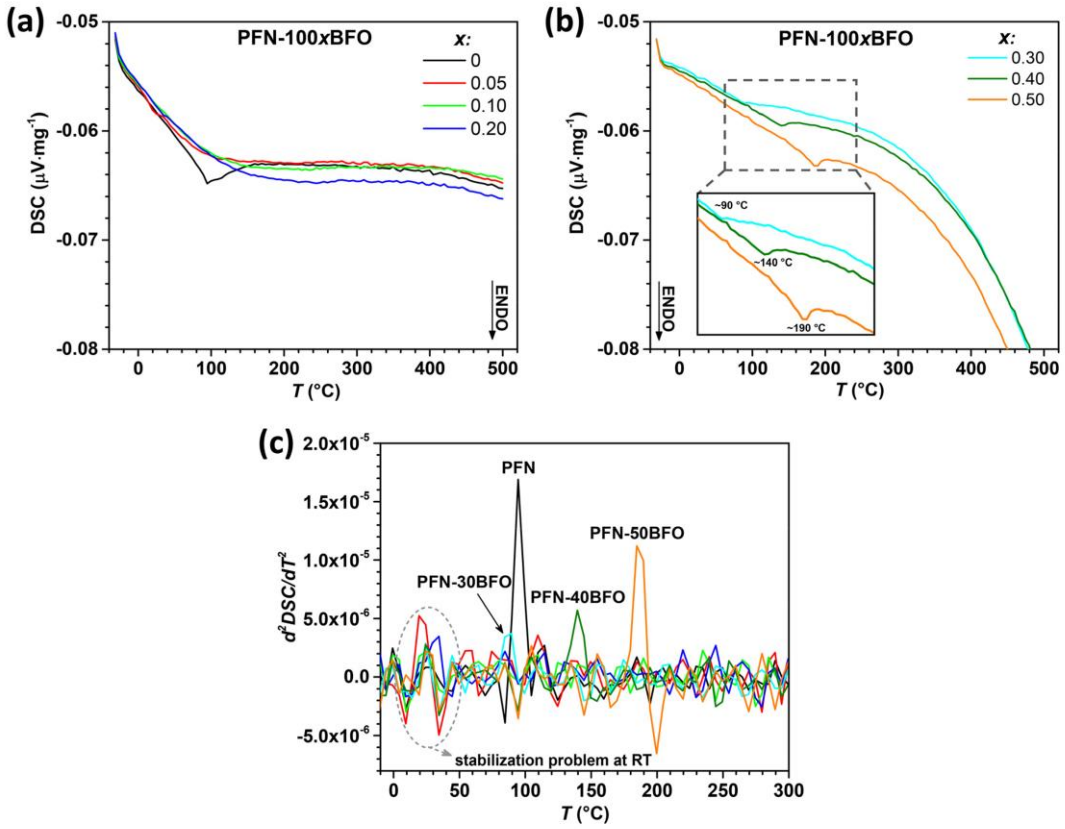


Figure S6. Temperature dependences of DSC signals of (a) $x \leq 0.20$ and (b) $x \geq 0.30$ PFN–100xBFO solid solutions. (c) The second derivative of DSC signals of all PFN–100xBFO (x = 0–0.5) compositions.

G. High temperature XRD

High temperature XRD (HT XRD) patterns of PFN–50BFO ceramic pellet were recorded on PANalytical Empyrean X-ray diffractometer (PANalytical B.V., Netherlands) equipped with Cu $K\alpha$ radiation (containing both $K\alpha_1$ and $K\alpha_2$) and a furnace heating stage. Diffraction patterns were recorded in the 15–80° 2θ-range with a step size of 0.013° and an integration time of 100 s per step. The measurements were performed in a temperature range from 25 °C to 300 °C with the step of 25 °C. The phase identification was done with PDF-4+ database. For the measurements, disk-like shaped ceramic pellet with a diameter of ~14 mm and thickness of ~1 mm were used.

A series of XRD patterns of PFN–50BFO, recorded in a temperature range of 25–300 °C, are shown in Fig. S7. Beside an increase in the lattice parameter (peak shift to lower 2θ) due to thermal expansion, there is no other changes in the structure with the temperature. The change of lattice parameters with temperature were additionally investigated by the Rietveld refinement analysis (details in section C), where no specific anomalies were observed (Fig. S8).

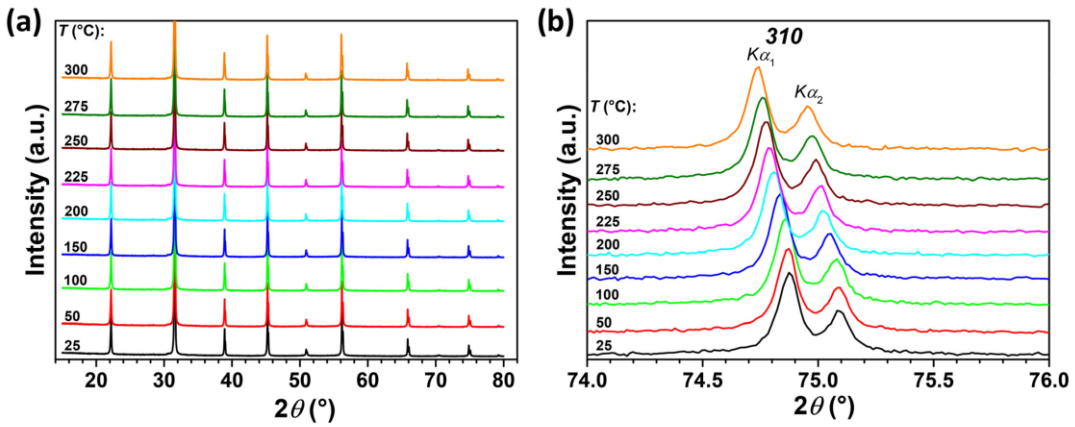


Figure S7. (a) Temperature dependence of XRD patterns of PFN–50BFO with (b) enlarged view of *310* pseudocubic reflection (from Cu $K\alpha_1$ and $K\alpha_2$).

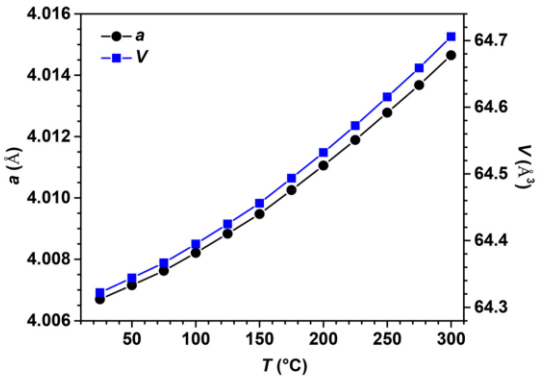


Figure S8. Temperature dependences of lattice parameter and unit cell volume of PFN–50BFO. The blue and black lines are guides to the eye.

H. High resolution TEM

HRTEM images of PFN–20BFO and PFN–50BFO and corresponding FFTs are shown in Figs. S9a and S9b, respectively. As it can be seen from FFTs, superlattice *½ ½ 0* reflections (α spots) are only observed in the PFN–50BFO sample, which might indicate the existence of antiferroelectric order in the material. As indicated by the inverse FFT image using α spots, nanometer large regions can be found (Fig. S9c). On the other hand, no sign of those spots were seen in PFN–20BFO.

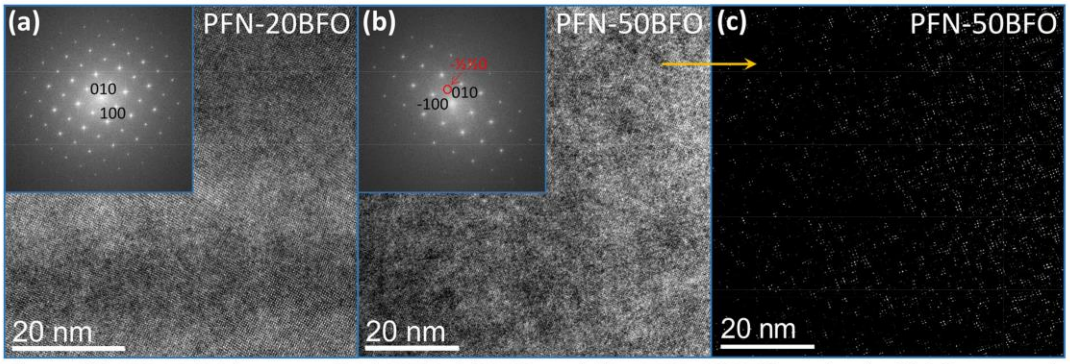


Figure S9. HRTEM images of (a) PFN–20BFO and (b) PFN–50BFO grains in [*001*] zone axis with corresponding FFTs in the insets. The FFT of PFN–50BFO reveals diffuse superlattice *½ ½ 0* spots (marked with red arrow). (c) The inverse FFT image of PFN–50BFO using marked diffuse spots indicates 5 nm large regions.

I. *S–E* hysteresis loops and *S–P* plots

S–E hysteresis loops of PFN–100*x*BFO (*x* = 0–0.5) compositions are shown in Fig. S10. In pure PFN, ferroelectric butterfly-like hysteresis loops, typically observed due to switching of ferroelastic domain walls in ferroelectric materials,[4] were obtained. With increasing content of BFO up to *x* = 0.3, the *S–E* loops become slimmer and more quadratic-like indicating increased contribution probably from electrostriction. In *x* = 0.4 and 0.5 compositions, the *S–E* loops start again to open up and gradually become more hysteretic.

During the *S–E* loop measurements, the *P–E* loops were simultaneously measured. The decreasing piezoelectric response (as shown in Fig. 10 of the main paper) and strengthening of the electrostrictive-like response with increasing amount of BFO in PFN–100*x*BFO solid solutions are also visible from the strain–polarization (*S–P*) plots (Figs. S10). In order to highlight how the electromechanical behavior of the samples deviates from pure electrostrictive response, the *S–P* plots were fitted with quadratic function of the type $S = Q \cdot P^2$, where the fitted parameter *Q* represents the electrostriction coefficient.[5]

As seen in Fig. S11, in pure PFN, a hysteretic *S–P* response with the largest deviation from the quadratic relation is observed. With increasing content of BFO up to *x* = 0.2, the hysteresis gradually diminishes and smaller deviation from the pure quadratic response is observed, indicating an increasing contribution of the electrostrictive-like response. In compositions with higher BFO contents ($x \geq 0.3$), small deviation from pure electrostrictive response is maintained, while the *S–P* response gradually become more hysteretic, which is consistent with the appearance of the pinched *P–E* loops (see Fig. 8 in the main paper).

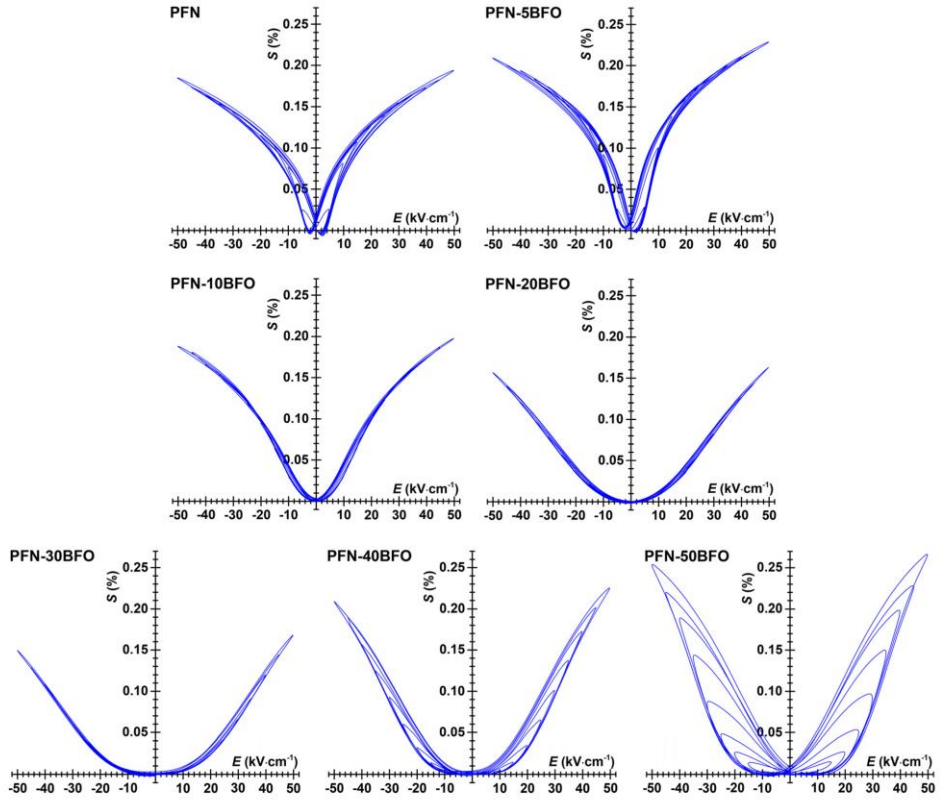


Figure S10. *S*–*E* hysteresis loops of PFN–100*x*BFO (*x* = 0–0.5) at room temperature measured with increasing electric-field amplitude at driving frequency of 10 Hz.

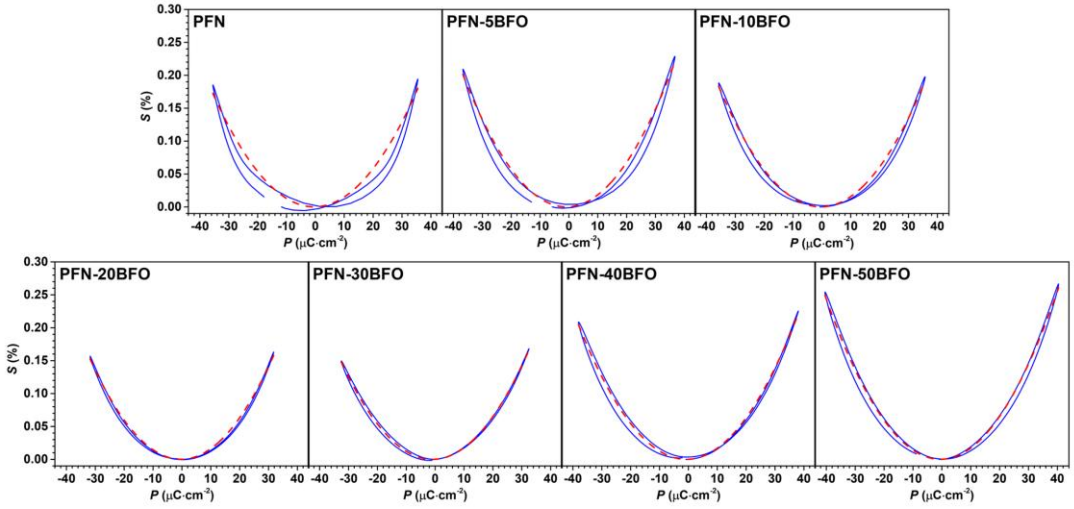


Figure S11. *S*–*P* plots of PFN–100*x*BFO (*x* = 0–0.5) at room temperature shown for 50 kV·cm^{-1} and driving frequency of 10 Hz. With red dashed curve fitted quadratic relation between *S* and *P* are shown.

J. *J–E* hysteresis loops

J–E hysteresis loops of PFN–100*x*BFO ($x = 0$–0.5) compositions are shown in Fig. S12. Pinching of *P–E* hysteresis loops of composition with $x \geq 0.2$ is clearly visible as a splitting of peaks (double current peaks) obtained from *J–E* hysteresis loop measurements (marked by arrows in Fig. S12).

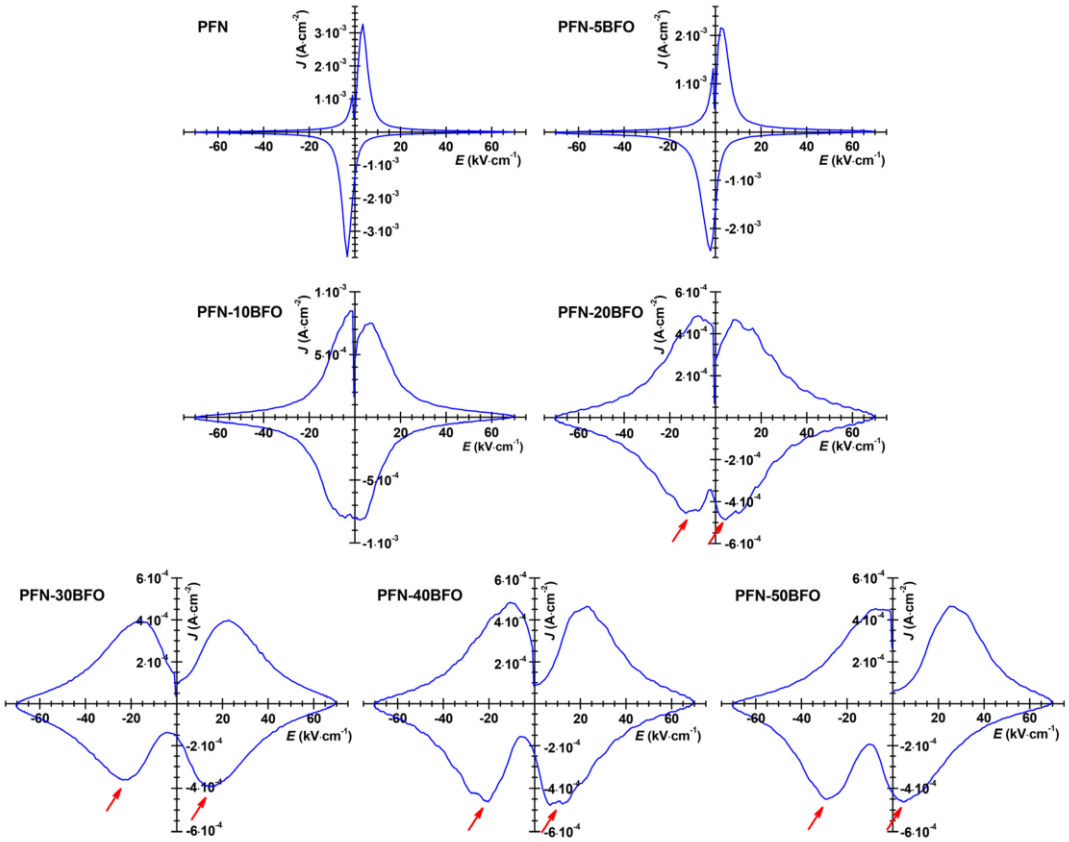


Figure S12. *J–E* hysteresis loops of PFN–100*x*BFO ($x = 0$–0.5) solid solutions measured at room temperature and 70 kV·cm^{-1}.

K. AC electric-field-cycling experiments

In order to investigate the origin of pinching observed in *P–E* measurements, AC electric-field-cycling experiments were performed on a PFN–50BFO sample. The *P–E* loops were continuously measured 50 times at room temperature by applying a single sinusoidal waveform with a frequency and electric field of 1 Hz and 60 kV·cm^{-1}, respectively. As can be seen in Fig. S13a, no changes in the shape of the *P–E* loops (i.e., de-pinching) were observed regardless of the cycle number. After cycling, the sample was aged for 1 hour in zero-field conditions and the *P–E* measurement was performed again. As can be seen in Fig. S13b, even after aging experiment, practically no change in the shape of *P–E* loop was observed.

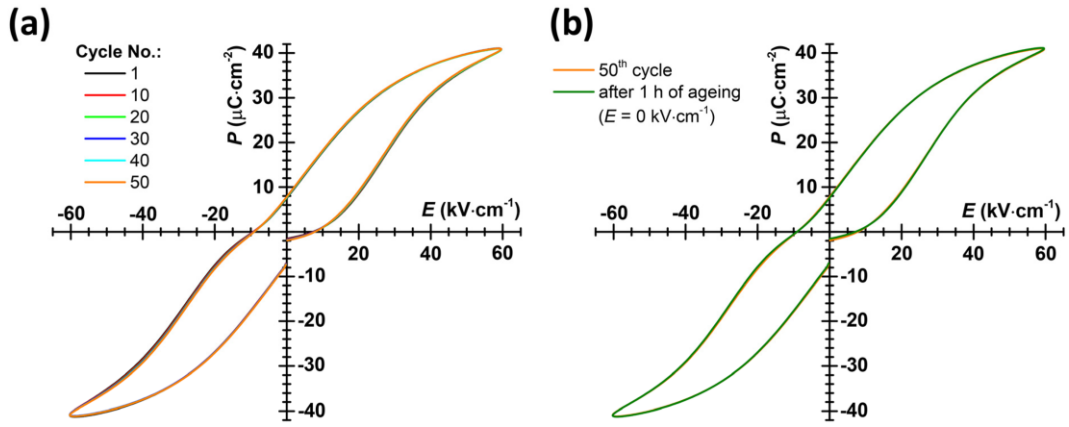


Figure S13. AC electric-field-cycling and aging experiments of PFN–50BFO; (a) The *P*–*E* measurement at 60 kV·cm^{-1} of every tenth cycle. (b) The *P*–*E* measurement after aging compared with the *P*–*E* measurement of 50th cycle.

In order to further investigate the origin of pinching observed in *P*–*E* loops measurements, the measurements of *J*–*E* and *P*–*E* loops at different frequencies were performed. Firstly, the loops were measured at the driving frequency of 10 Hz, where the pinching of the loop was observed (Fig. S14a). In the next step, the driving frequency of the measurement was stepwise reduced from 10 Hz to 0.01 Hz by performing one cycle at each frequency, i.e., 1, 0.1 and 0.01 Hz. During this experiment, performed at low driving frequency, the defects may in principle migrate due to the longer period under the electric field; this is seen in the larger contribution of the electrical conductivity of the material resulting in rounded and leaky *P*–*E* hysteresis loop (Fig. S14a). Finally, after the cycles performed at low frequencies, the driving frequency was increased back to 10 Hz. In principle, if the defects redistribution (migration) under the low-frequency field has any role in the original pinched shape, measured at 10 Hz, the low frequency driving should affect this pinched shape measured at 10 Hz. Only a slight change in the loop shape was observed at 10 Hz after the low-frequency cycles, relative to the first measured 10 Hz loop (see Fig. S14a). This is also seen in the *J*–*E* loops, where little changes are observed between the first and last 10 Hz cycle (compare black and dashed orange loops in Fig. S14b).

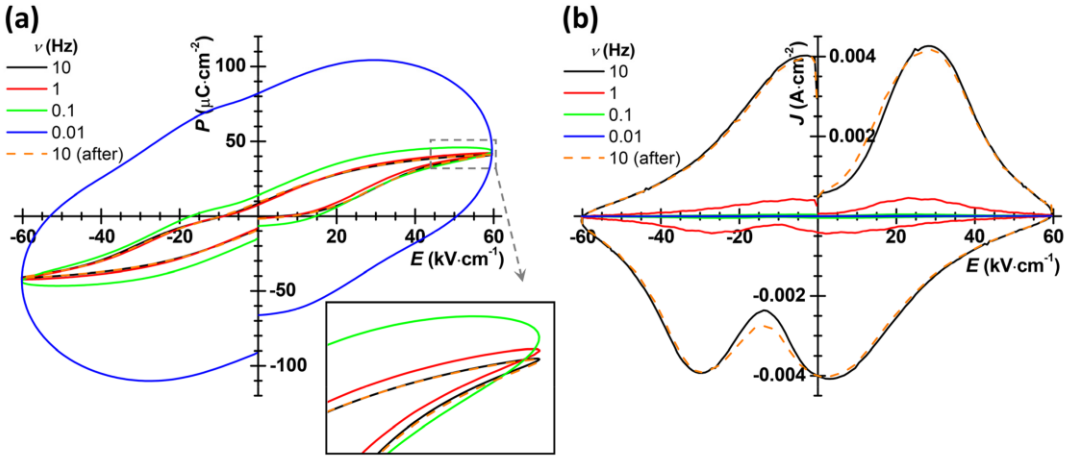


Figure S14. (a) *P–E* and (b) *J–E* hysteresis loops of PFN-50BFO measured at 60 kV·cm^{-1} using different driving frequencies at room temperatures.

L. Rapid cooling (quenching) experiment

The role of charged defects on pinching of *P–E* loop was additionally investigated by controlling the post-sintering heat-treatment cooling rate. Distribution of defects can be controlled by the processing cooling rate, namely, quenching from above the Curie temperature induces defect disorder, while slow cooling favors defect ordering. Ideally, in the former the loops should be completely open up, while in the latter should be pinched (if defect distribution has any role in the pinching behavior).[6]

In this experiment, first, the thinned (~200 μm) PFN-50BFO ceramic pellet was heated to 600 °C for 1 h and then slowly cooled down to room temperature with the cooling rate of 1 °C·min^{-1} (named as non-quenched sample). The surfaces of the pellets were coated with Au electrodes and the *J–E* and *P–E* loops were obtained at 1 Hz and 60 kV·cm^{-1}. After that, the same pellet was heated to 400 °C for 5 min and immediately cooled down by quenching in water (quenched sample). The measurement of *J–E* and *P–E* loops were repeated using the same measurement conditions.

The *J–E* and *P–E* loops of both experiments are shown in Fig. S15. Compared to the non-quenched sample, the degree of pinching was slightly decreased when the sample was quenched. Small difference in *J–E* and *P–E* responses of the sample exposed to different cooling rates show that the ordering of charged defects can be partially responsible for the pinching of the loop.

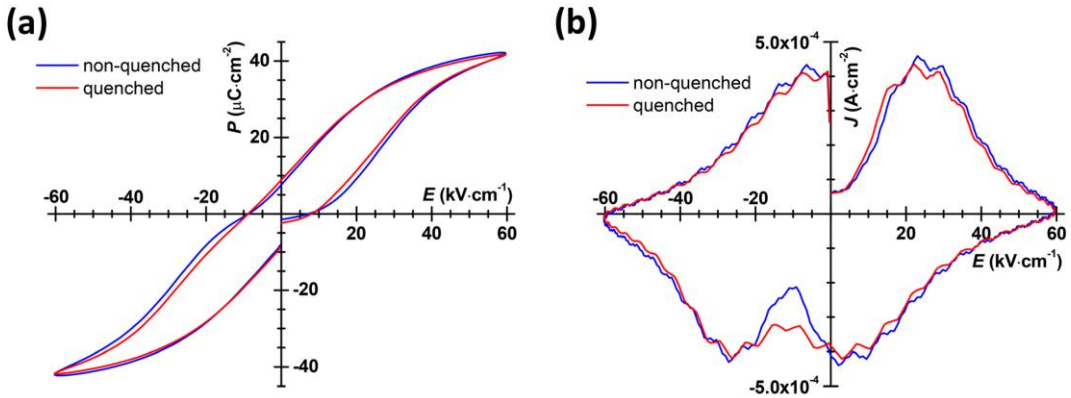


Figure S15. (a) *P*–*E* and (b) *J*–*E* hysteresis loops of PFN-50BFO measured after slowly (1 °C·min^{-1}) and rapid cooling of sample.

M. *in situ* sXRD

In situ sXRD measurements of PFN–40BFO were employed. Maps of the *111* and *200* pseudocubic reflections during *in situ* applied voltage up to 50 kV·cm^{-1} and after release are shown in Fig. S16. In contrast to PFN–50BFO, the electric-field-induced phenomenon, namely the broadening and weakening in peak intensity parallel to the field is substantially less pronounced.

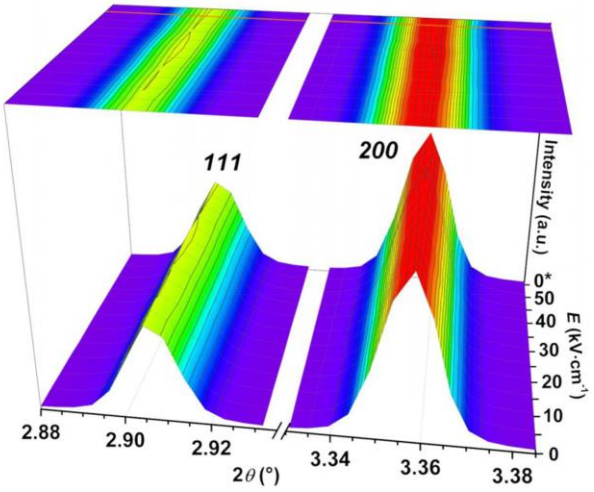


Figure S16. Room-temperature *in situ* sXRD surface contour plots of the (a) *111* and (b) *200* pseudocubic reflections of PFN–40BFO with *in situ* applied voltage up to 50 kV·cm^{-1} and after release (*0 kV·cm^{-1}).

References

[1] H. Ursic and D. Damjanovic, *Appl. Phys. Lett*., 2013, **103**, 072907 1–4.
[2] A. E. Glazounov and A. K. Tagantsev, *Appl. Phys. Lett*., 1998, **73**, 856–858.
[3] D. Viehland, S. J. Jang, L. E. Cross and M. Wuttig, *J. Appl. Phys*., 1990, **68**, 2916–2921.
[4] D. Damjanovic, *Rep. Prog. Phys.*, 1998, **61**, 1267–1324.
[5] S. Nomura and K. Uchino, *Ferroelectrics*, 1982, **41**, 117–132.
[6] D. Damjanovic, in *The Science of Hysteresis*, eds. I. Mayergoyz and G. Bertotti, Elsevier, Volume 3, 2006, Chapter 4, 337–465.

Chapter 4

$Pb(Fe_{0.5}Nb_{0.5})O_3$–$BiFeO_3$-Based Multicalorics with Room-Temperature Ferroic Anomalies

This chapter is focused on the study of multicaloric properties of PFN–BFO-based solid solutions. In PFN–20BFO, the peak-permittivity anomaly as well as paramagnetic-to-antiferromagnetic phase transition coincide at RT, making it one of the first such single-phase materials and thus a promising candidate for room-temperature multicaloric cooling applications. Despite the favorable positions of the ferroic anomalies, the excessive electrical conductivity and poor magnetic response of the material limit its EC and MC cooling capability.

Further doping of PFN–20BFO with Mn and Gd ions successfully suppresses the excessive electrical conductivity and enhances the magnetic response, leading to improvement of the EC and MC properties. This results in a composition with negligible Joule heating up to 75 °C, with a room-temperature EC effect of more than 1 °C, and a high MC effect of ~3 °C at cryogenic temperatures. Furthermore, this material also exhibits the highest room-temperature MC effect among all the known PFN-based multicalorics.

This chapter addresses thesis objectives 7 and 8.

Published in: U. Prah, M. Wencka, T. Rojac, A. Benčan and H. Uršič, "$Pb(Fe_{0.5}Nb_{0.5})O_3$–$BiFeO_3$-based multicalorics with room-temperature ferroic anomalies," *J. Mater. Chem. C*, vol. 8, no. 32, pp. 11282–11291, 2020. (IF = 7.059, 2019)

My contribution: I prepared the powders and ceramic samples. I performed the scanning electron microscopy, energy-dispersive X-ray spectroscopy and Rietveld analyses, performed the characterization of electrical properties, measured the EC and calculated the MC effects. I prepared the concept of the paper and jointly wrote the manuscript with the co-authors.

Journal of Materials Chemistry C

ROYAL SOCIETY OF CHEMISTRY

PAPER



Cite this: *J. Mater. Chem. C*, 2020, **8**, 11282

$Pb(Fe_{0.5}Nb_{0.5})O_3$–$BiFeO_3$-based multicalorics with room-temperature ferroic anomalies†

Uroš Prah, *[ab] Magdalena Wencka,[c] Tadej Rojac,[ab] Andreja Benčan[ab] and Hana Uršič [ab]

The search for new single-phase multicaloric materials, combining electrocaloric and magnetocaloric effects, is just at its beginning. Since the highest caloric effects are obtained near ferroic phase transitions, multiferroics with room-temperature ferroic anomalies are promising candidates for multicaloric cooling. In this work, such materials were prepared by tailoring the temperature of the ferroic anomalies by introducing $BiFeO_3$, a material possessing high-temperature ferroic phase transitions, into the multicaloric $Pb(Fe_{0.5}Nb_{0.5})O_3$ to form a solid solution. A series of $(1-x)Pb(Fe_{0.5}Nb_{0.5})O_3$–$xBiFeO_3$ (x = 0–0.5) were prepared. Among them, $0.8Pb(Fe_{0.5}Nb_{0.5})O_3$–$0.2BiFeO_3$ exhibits both dielectric permittivity and magnetic susceptibility anomalies at room temperature and is therefore one of the first such single-phase materials. However, at higher temperatures the material exhibits excessive Joule heating that critically degrades the electrocaloric cooling effect, while the antiferromagnetic nature of the material results in a low magnetocaloric response. Because of that, the multicaloric properties of $0.8Pb(Fe_{0.5}Nb_{0.5})O_3$–$0.2BiFeO_3$ were further improved by doping the material with Mn and Gd ions. This results in a composition with negligible Joule heating up to 75 °C and with room-temperature electrocaloric effect of more than 1 °C, and a high magnetocaloric effect of ~3 °C at cryogenic temperatures. Furthermore, this material also exhibits the highest room-temperature magnetocaloric effect (~8×10^{-3} °C) among all already known $Pb(Fe_{0.5}Nb_{0.5})O_3$-based multicalorics.

Received 14th May 2020,
Accepted 7th July 2020

DOI: 10.1039/d0tc02329a

rsc.li/materials-c

I. Introduction

Multiferroics are a class of materials, where in general more than one ferroic (including relaxor), antiferroic or ferric orders coexist.[1,2] A lot of attention is paid to the so-called single-phase magnetoelectric multiferroics, combining ferroelectric and ferromagnetic properties in the same material, which are attractive due to the different origins and opposite mechanisms of both ferroic orders.[2–5] Magnetoelectric multiferroics are promising candidates for future environmental friendly solid-state cooling based on the caloric effect,[6–9] which refers to the reversible adiabatic temperature changes of the material under the influence of external stimuli, such as electric or magnetic fields.[9–11]

Electrocaloric (EC) and magnetocaloric (MC) materials show drawbacks that limit their cooling capacity and consequently prevent their commercial use.[6,8] An interesting idea for improving their cooling capacity is to prepare a material that combines both EC and MC effects, hereafter called the multicaloric material.[11–13] The highest caloric effects are obtained near ferroic phase transitions, where the order parameters (*i.e.*, polarization and magnetization) are strongly temperature dependent.[11,14,15] The majority of commercially used cooling devices operate at room temperature (RT), and therefore multiferroics with broad room-temperature ferroic anomalies are promising candidates for efficient multicalorics.[14,16] However, the vast majority of them exhibit anomalies at different temperature regions, therefore, the search for single-phase multiferroics exhibiting both ferroic anomalies at RT is just at its beginning.[3,4]

The topic of multicaloric (EC + MC) materials is relatively new.[13,17–21] In 2016, the coexistence of EC and MC effects was experimentally confirmed in $0.8Pb(Fe_{0.5}Nb_{0.5})O_3$–$0.2Pb(Mg_{0.5}W_{0.5})O_3$ relaxor ceramics.[22] However, this material exhibits very low EC and MC effects (both ~0.25 °C) with the maximum values far below RT. Recently, in our previous work, careful control of sintering conditions and doping with manganese resulted in improved EC and MC properties of $Pb(Fe_{0.5}Nb_{0.5})O_3$ (PFN) ceramics with the maximal values of 2.47 °C (at 80 °C and 140 kV cm^{-1}) and 0.44 °C (at −271 °C and 50 kOe), respectively.[23] Despite a relatively large EC effect at RT (1.59 °C at 140 kV cm^{-1}), the highest MC effect in this material is located at temperatures far below the desired RT.

[a] *Jožef Stefan Institute, Jamova cesta 39, 1000 Ljubljana, Slovenia. E-mail: uros.prah@ijs.si*
[b] *Jožef Stefan International Postgraduate School, Jamova cesta 39, 1000 Ljubljana, Slovenia*
[c] *Institute of Molecular Physics, Polish Academy of Sciences, ul. Smoluchowskiego 17, 61-179 Poznań, Poland*

† Electronic supplementary information (ESI) available: online Supplementary material. See DOI: 10.1039/d0tc02329a

This journal is © The Royal Society of Chemistry 2020

PFN is a well-known complex perovskite, whose multiferroic behavior arises from ferroelectrically active Nb^{5+} (empty d-orbitals) and magnetically active Fe^{3+} ions (partially filled d-orbitals) that are randomly distributed in the B-site of the perovskite lattice. PFN exhibits paraelectric-to-ferroelectric phase transition (Curie temperature, T_C) at $\sim$100 °C[23,24] and paramagnetic-to-antiferromagnetic phase transition (Néel temperature, T_N) at ~ -120 °C.[23,25] At temperatures below −250 °C, an additional magnetic phase transition from long-range antiferromagnetic to short-range spin-glass-like magnetic order is present.[25,26] Because PFN already exhibited the paraelectric-to-ferroelectric phase transition together with high EC effects slightly above desired RT, it seems a promising starting point for designing multiferroic materials with room-temperature ferroic phase transitions. An idea to modify the PFN in order to shift its paramagnetic-to-antiferromagnetic phase transition (−120 °C) closer to RT is to mix PFN with $BiFeO_3$ (BFO) and form a solid solution. BFO is a well-known multiferroic material, which exhibits a paramagnetic-to-antiferromagnetic phase transition at 370 °C,[27] therefore adding BFO to PFN should ideally move the T_N of the material towards RT.

In general, BFO exhibits high specific electrical conductivity that typically occurs in the range of 10^{-10}–10^{-2} Ω^{-1} m^{-1},[27,28] while PFN is less conductive ($\sim 10^{-12}$ Ω^{-1} m^{-1}).[23] Consequently, the increasing BFO content in PFN–BFO solid solution will increase the electrical conductivity of the material, leading to the appearance of the Joule heating effect and thus lowering of the EC cooling efficiency.[29–31] According to reports on PFN[23,32] as well as BFO-based materials,[33,34] the excessive electrical conductivity can be suppressed by the addition of small amounts of Mn ions. In our previous work it was shown that adding 0.5 mol% of Mn ions efficiently suppresses the electrical conductivity of PFN.[23] Another drawback of using PFN and BFO as multicalorics is their antiferromagnetic order that leads to low magnetization, namely <0.4 emu g^{-1} at magnetic fields of 60 kOe in BFO.[35] According to the literature, in BFO, breaking the antiferromagnetic ordering and increasing the magnetic susceptibility can be achieved by the substitution of A-site of the crystal lattice with rare earth elements, such as Gd ions.[36–39] Rare earth elements possess strong localized magnetic moments that arise from the partially filled 4f inner electron shell, making them promising candidates for enhancing the magnetic properties of the materials.[40] In previous Gd-doped BFO studies,[36–39] it was shown that the addition of 12 mol% of Gd ions enhances the ferromagnetic properties and at the same time does not increase the electrical conductivity and does not lead to the formation of a non-polar phase.[37,41] However, no studies on doping of PFN–BFO have been reported, and therefore in this work, a similar approach as reported for pure PFN and BFO, namely doping with 0.5 mol% of Mn and 12 mol% of Gd ions, is employed.

In this work, seven different multiferroic $(1-x)Pb(Fe_{0.5}Nb_{0.5})O_3$–$xBiFeO_3$ (x = 0–0.5) solid solutions were prepared. Among them, PFN–20BFO exhibits both dielectric permittivity and magnetic susceptibility anomalies close to RT and is therefore a promising candidate for multicalorics. Further doping of PFN–20BFO with 0.5 mol% of Mn and 12 mol% of Gd ions suppresses the electrical conductivity and enhances the magnetic ordering leading to the improvement of the EC and MC properties. The results of this study show the importance of composition–caloric-property inter-correlations in PFN–BFO-based ceramics.

II. Experimental

Material synthesis

PFN–100xBFO (x = 0, 0.05, 0.1, 0.2, 0.3, 0.4 and 0.5) ceramic powders were prepared by mechanochemical-activation-assisted synthesis using PbO (99.9%, Alfa Aesar), Fe_2O_3 (99.9%, Alfa Aesar), Nb_2O_5 (99.9%, Sigma Aldrich) and Bi_2O_3 (99.999%, Alfa Aesar) as starting oxides. The preparation process of unmodified PFN–100xBFO powders is described in detail in our previous work.[23,42] The same synthesis procedure was employed also for Mn-doped PFN–20BFO, where 0.5 mol% of Mn in the form of MnO_2 (99.9%, Alfa Aesar) were added to the mixture of initial oxides as a substitution for B-site cations (Fe^{3+} and Nb^{5+}) according to the nominal formula $0.8Pb(Fe_{0.5}Nb_{0.5})_{0.995}Mn_{0.005}O_3$–$0.2BiFe_{0.995}Mn_{0.005}O_3$. MnO_2 was pre-milled in an attrition mill (Netzsch, PE075/PR01, Selb, Germany) with absolute ethanol at 600 min^{-1} for 5 h using yttria-stabilized zirconia (YSZ) milling balls (ball diameter, 3 mm).

The composition with 0.5 mol% of Mn (substitution for B-site cations, Fe^{3+} and Nb^{5+}) and 12 mol% of Gd (substitution for Bi^{3+}) was prepared according to the nominal formula $0.8Pb(Fe_{0.5}Nb_{0.5})_{0.995}Mn_{0.005}O_3$–$0.2Bi_{0.88}Gd_{0.12}Fe_{0.995}Mn_{0.005}O_3$. Due to the problems with aggregation and dispersion of Gd_2O_3, for the preparation of Gd and Mn co-doped PFN–20BFO, in all starting oxides, surfactant ammonium polyacrylate (PAA) was used. The PAA, used as a steric stabilizer, was formed by mixing poly(acrylic acid) (50 wt% solution in H_2O, Sigma Aldrich) and 1-butlyamine (99%, Alfa Aesar) in absolute ethanol.[43,44] Gd_2O_3 (99.99%, Metall) was pre-milled in a planetary ball mill (Retsch PM400, Retsch, Haan, Germany) at 150 min^{-1} for 4 h in an ethanol/PAA mixture using YSZ milling balls (ball diameters 3 mm). PAA was added also to all other pre-milled starting oxides and the mixtures were homogenized by milling in a planetary ball mill at 150 min^{-1} for 2 h using YSZ milling balls (ball diameter, 3 mm). A stoichiometric mixture of all starting oxides (40 g) was homogenized in a planetary ball mill at 150 min^{-1} for 4 h in absolute ethanol using YSZ milling balls (ball diameter, 3 mm). The homogenized mixture was dried and heat-treated at 350 °C for 30 min (heating and cooling rates of 2 °C min^{-1}) in order to remove PAA from the powder. The powder mixture was mechanochemically activated in the same planetary ball mill for 14 h at 400 min^{-1} in a tungsten carbide milling vial (volume 80 cm^3), filled with 7 tungsten carbide milling balls (ball diameter, 15 mm). After activation, the synthesized powder, *i.e.*, mixtures of crystalline perovskite and amorphous phases, was re-milled in a planetary ball mill in absolute ethanol, at 200 min^{-1}, for 4 h, using YSZ milling balls (ball diameter, 3 mm).

All prepared powders were uniaxially pressed (50 MPa) into pellets of a diameter of 8 mm followed by isostatic pressing at

300 MPa. The powder compacts were reactively sintered in double alumina crucibles in the presence of PFN packing powder. Sintering temperatures for each composition were estimated from sintering curves (details in ref. 42). To maintain similar grain sizes, PFN–100xBFO samples with a lower content of BFO ($x \leq 0.1$) were sintered at 950 °C for 2 h, while samples with a higher content of BFO ($x \geq 0.2$) were sintered at 900 °C for 2 h. Similar thermal treatment was performed also for Mn-doped PFN–20BFO (900 °C for 2 h), while in the Mn,Gd co-doped sample, due to the different sintering behavior, a higher sintering temperature (1000 °C for 2 h) was used (shown in ESI,† A). Sintering runs were performed under an oxygen atmosphere as suggested in ref. 45 and used in our previous work.[23,42] The use of the saturated oxygen atmosphere during the sintering prevents (or minimizes) the reduction of Fe^{3+} to Fe^{2+} and reduces the amount of oxygen vacancies, which consequently resulted in a lower electrical conductivity and dielectric losses of the material.[45] For all samples, a heating and cooling rate of 2 °C min^{-1} was used.

Characterization

The densities of the sintered pellets were determined using a gas-displacement density analyzer (Micromeritics, AcuuPyc II 1340 Pycnometer) at RT. For the calculation of the relative density, the crystallographic densities were obtained from Rietveld refinement analysis (details in the ESI,† B). X-ray powder diffraction (XRD) patterns of crushed ceramic pellets were recorded on a X'Pert Pro (PANalytical B.V., Netherlands) high-resolution powder diffractometer equipped with Cu Kα_1 radiation (45 kV, 40 mA), in reflection mode. Diffraction patterns were recorded in the 10–70° 2θ-range with a step size of 0.017° and an integration time of 100 s per step at RT. The phase identification was performed with the PDF-4+ database.

The microstructure of sintered ceramics was examined using a field-emission scanning electron microscope (FE-SEM, JSM-7600F, Jeol Ltd, Japan) equipped with an energy dispersive X-ray spectrometer (EDXS, Inca Oxford 350 EDS SSD, Oxford Instruments, Abingdon, UK). Prior to microstructural analysis, the samples were fractured for fracture-surface examination, ground and fine-polished using a colloidal silica suspension, followed by thermal etching at 775 °C for 15 minutes in the presence of PFN packing powder. The average grain size and grain-size distribution were evaluated from the digitized images of etched surfaces, processed using the Image Tool software (UTHSCSA Image Tool Version 3.00. 2002)[46] by measuring more than 500 grains. The grain size is expressed as the Feret's diameter.[47]

For characterization of electrical properties, the ceramic pellets were cut, thinned and polished to a thickness of ~200 μm. In order to release the internal stresses produced during the mechanical processing, the thinned ceramic pellets were heated up to 600 °C for 1 h (with 5 °C min^{-1} heating rate) and then slowly cooled down (1 °C min^{-1}) to RT. The surfaces of the pellets were coated with Au electrodes (diameter of 5 mm) using a RF-magnetron sputtering machine (5Pascal, Italy).

The relative dielectric permittivity (ε) and dielectric loss ($\tan\delta$) as a function of temperature were analyzed during cooling from 200 °C to −50 °C using an Aixacct TF analyzer 2000 (aixACCT Systems GmbH, Aachen, Germany) coupled with a HP 4284A Precision LCR impedance meter (Hewlett-Packard, California, USA) in the frequency range of 0.1–100 kHz. The DC current-density–electric-field (j–E) response was measured using a Keithley 237 (Keithley Instruments, Ohio, USA) high voltage source measuring unit. For the j–E measurements, the samples were exposed to step-like voltages within the range of ±0.5 kV cm^{-1}. In this range, from negative to positive polarity, 13 equal field steps were applied. Upon each of these steps, the voltage was maintained constant for 1.5 h for the current to stabilize, before being recorded. The specific DC electrical conductivity (σ_{DC}) was obtained from the slope assuming Ohm's law. AC current density–electric field (j–E) loops were measured at RT using an Aixacct TF analyzer 2000 by applying a single sinusoidal waveform with a frequency of 1 Hz and electric fields up to 80 kV cm^{-1}. Polarization–electric field (P–E) loops were automatically obtained with software using numerical integration of the current signal.

The EC effect was measured using the direct method. The measurements were performed on ~80 μm-thick ceramic samples with sputtered Au electrodes. The direct EC measurements were performed using a modified differential scanning calorimeter (Netzsch DSC 204 F1, Selb, Germany), which allowed a precise temperature stabilization. The temperature changes were measured with a small-bead thermistor glued to the sample; the temperature was measured using a digital multimeter. The EC temperature change (ΔT_{EC}) values presented in this work are the measured maximum temperature changes multiplied by a correction factor of 1.60–1.75, which accounts for the passive part of the sample and also the thermal losses in the gold wires, the silver paste and the thermistor. The used correction factor agrees well with the results of the numerical simulation.[48] The details of the method can be found in ref. 49.

Field-cooled (FC) DC magnetic moment *vs.* temperature was measured between −270 °C and 127 °C at different magnetic fields (0.02–90 kOe) using a physical property measurement system vibrating sample magnetometer (PPMS-VSM, Quantum Design, California, USA). Furthermore, the magnetization–magnetic field (M–H) hysteresis loops were obtained in magnetic fields up to 90 kOe at temperatures of −270 °C and RT. For the measurements rod-like-shaped ceramic samples were used. The M values were obtained by normalizing the magnetic moment values by the mass of the samples. The MC effect was determined by the indirect method,[50] where the MC temperature change (ΔT_{MC}) was calculated from the magnetization *versus* temperature measurements at different magnetic fields (0.5–90 kOe).

III. Results and discussion

A. $(1-x)Pb(Fe_{0.5}Nb_{0.5})O_3$–$xBiFeO_3$

In the first part, multiferroic properties of PFN–100xBFO (x = 0–0.5) solid solutions were investigated. All prepared ceramics were single-phase, homogeneous and highly dense (>97.6% of the crystallographic density), as previously reported in ref. 42. The temperature

 This journal is © The Royal Society of Chemistry 2020

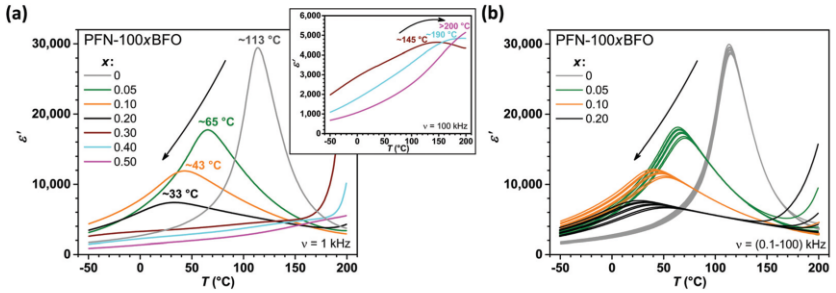


Fig. 1 (a) Temperature dependences of ε' for PFN–100xBFO measured at 1 kHz (x = 0–0.5) and (inset) 100 kHz ($x \geq 0.3$). (b) Temperature and frequency dependence of ε' for PFN–100xBFO ($x \leq 0.2$) measured in the frequency range of 0.1–100 kHz.

dependences of the real component of the relative permittivity ε' for all compositions measured at 1 kHz are shown in Fig. 1a. The peak-permittivity of PFN–100xBFO is shifting towards RT with an increasing amount of BFO ($x \leq 0.2$) and it reaches the lowest value in PFN–20BFO, *i.e.*, 33 °C (Fig. 1a). This is accompanied with an increasing relaxor behavior, as seen in Fig. 1b and reported in ref. 42. By further increasing the BFO content ($x \geq 0.3$), the peak-permittivity temperature seemingly shifts to temperatures above the one of PFN (*i.e.*, 113 °C), as visible from ε' measurements at 100 kHz (inset of Fig. 1a). A reason for the progressively increased relaxor behavior by the addition of BFO is most probably related to the increased compositional disorder at the A-site of the perovskite structure, which arises when different multivalence ions occupy a crystalographically equivalent place in the crystal lattice.[42,51,52] Heterovalent substitution of the differently sized Pb^{2+} (119 pm)[53] and Bi^{3+} (103 pm)[53] ions appears to disturb a long-range ferroelectric order in PFN-rich PFN–BFO solid solutions as previously suggested for Pb-based relaxors.[54]

In the next step, the influence of BFO addition on the magnetic properties of PFN–100xBFO was studied. The $M(T)$ curves of all compositions, measured at magnetic field of 1 kOe, are shown in Fig. 2a. In all the samples M increases with the decreasing temperature reaching a maximum value of $\sim$0.032 emu g^{-1} at −270 °C in PFN. PFN exhibits the paramagnetic-to-antiferromagnetic phase transition (T_N) at −120 °C. With an increase in the amount of BFO, T_N is almost linearly shifted towards higher temperatures reaching RT in PFN–20BFO (Fig. 2b). In PFN–50BFO T_N is probably shifted beyond the measured temperature range (*i.e.*, above 130 °C), which is in agreement with previously reported studies.[55] As demonstrated in Fig. 2b, increasing T_N values with an increasing amount of BFO in PFN–BFO solid solutions are directly related to the higher amount of Fe^{3+} on the B-site perovskite lattice. These results agree well with the previously reported studies, where it was shown that in pure PFN[56] as well as in PFN–50BFO[57,58] the magnetic properties and thus T_N depend on the number of Fe–O–Fe linkages in the structure. Therefore, in our case, the substitution of similarly large Nb^{5+} with Fe^{3+} ions ($\sim$64 pm)[53] increases the Fe/Nb atomic ratio on the B-site sublattice, leading to a higher temperature of the paramagnetic-to-antiferromagnetic phase transition. On the other hand, a decrease in the Nb^{5+} concentration reduces the tendency for the formation of a short-range spin-glass-like phase at low temperatures, which is reflected in lower M values in BFO-rich compared to PFN-rich PFN–BFO solid solutions (Fig. 2a).[25,59] In all compositions slim antiferromagnetic M–H hysteresis loops with almost zero remanent magnetization were obtained at −270 °C (ESI,† C), which

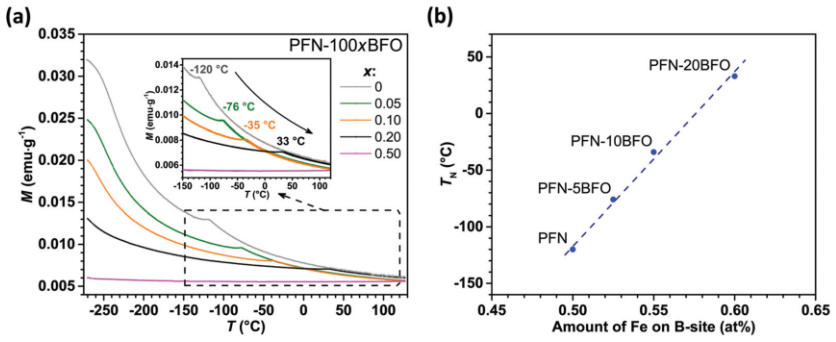


Fig. 2 (a) Temperature dependences of M for PFN–100xBFO (x = 0–0.5) measured at 1 kOe. Inset: The enlarged view of the data between −150 °C and 120 °C where T_N is highlighted. (b) Relationship between T_N and the amount of Fe on B-site perovskite sublattice for PFN–100xBFO (x = 0–0.2).

indicates that in the PFN–BFO system the increasing BFO content does not significantly affect the long-range antiferromagnetic ordering.

Among all the compositions, PFN–20BFO exhibits the dielectric permittivity anomaly as well as the paramagnetic-to-antiferromagnetic phase transition at RT, which makes this material a promising candidate for room-temperature multicaloric cooling. However, further evaluation of its EC and MC properties revealed some issues, namely excessive electrical conductivity and poor magnetic response, which limit its cooling capability (ESI,† D). At higher temperatures and applied electric fields the increased electrical conductivity leads to the appearance of Joule heating (JH), which significantly reduces material's EC response reaching the maximum EC effective cooling (ΔT_{eff}, defined as the difference between ΔT_{EC} and ΔT_{JH}) of 0.50 °C at RT and 90 kV cm^{-1} (ESI†, D and E). On the other hand, the antiferromagnetic nature of the sample results in a low MC effect over the entire measured temperature range (from −270 to 130 °C) with the maximum value of only 0.07 °C at −270 °C and 50 kOe. Furthermore, despite the vicinity of T_{N}, no increase in the MC effect at RT in comparison to the previously published PFN[23] was observed (ESI†, D). According to the literature, in PFN and BFO-based materials excessive electrical conductivity and consequently JH can be suppressed by the addition of small amounts of Mn ions,[23,32–34] while the ferromagnetic response can be enhanced by the addition of Gd ions.[36–39] Based on that, in the second part of this study the influence of Mn and Gd doping on the multiferroic and multicaloric properties of PFN–20BFO is discussed.

B. Mn-doped and Gd,Mn co-doped PFN–20BFO

In the second part of this study, the effect of Mn and Gd addition on the structural, microstructural and functional properties of PFO–20BFO was investigated. Firstly, the phase composition, crystal symmetry and microstructure of pure, Mn-doped and Gd,Mn co-doped PFN–20BFO were studied. The X-ray powder diffraction patterns of crushed ceramic pellets are shown in Fig. 3a. In all three samples only the peaks corresponding to the perovskite phase are present and no additional peaks corresponding to the secondary phases are observed. Rietveld refinement analysis (ESI,† B) revealed that all three compositions exhibit a pseudocubic symmetry at RT ($Pm\bar{3}m$ space group), which is consistent with the previous studies of pure PFN–20BFO.[42,60,61]

The SEM images of the polished sample surfaces are shown in Fig. 3b. All three samples are highly dense, *i.e.*, equal or more than 97.6% of the crystallographic density, exhibiting homogeneous and uniform microstructures. In the microstructure of pure and Mn-doped PFN–20BFO no visible secondary phases are present, while in the Gd,Mn co-doped sample small dark inclusions are observed. A qualitative EDXS analysis revealed that these dark phase regions correspond to Fe-rich and Gd,Nb-rich secondary phases (details in ESI†, F). The average grain sizes of pure and Mn-doped PFN–20BFO are in the range of 1 μm, while the grain size of the Gd,Mn co-doped sample is larger (∼4.8 μm) due to the higher sintering temperature. In all three samples, monomodal grain size distribution, indicating the normal grain growth during the sintering, was observed (ESI†, G).

The temperature and frequency (ν) dependence of the real component of relative permittivity ε' and dielectric loss tan δ of all three PFN–20BFO-based compositions are shown in Fig. 4. Pure PFN–20BFO exhibits broad and diffusive peak-permittivity with the maximal value of ∼7700 at 0.1 kHz and 27 °C indicating relaxor-like behavior (Fig. 4a).[42] The sample shows a large frequency dependence of peak-permittivity temperature ($T_{\varepsilon,\mathrm{max}}$) that is spanning from 27 °C at 0.1 kHz to 53 °C at 100 kHz (*i.e.*, $\Delta T_{\varepsilon,\mathrm{max}}$ of 26 °C). The addition of 0.5 mol% Mn resulted in slightly lower peak-permittivity values with $T_{\varepsilon,\mathrm{max}}$ shifted to higher temperatures, reaching the maximum value of ∼6200 at 0.1 kHz and 65 °C (Fig. 4b). While further addition of 12 mol% Gd shifts the $T_{\varepsilon,\mathrm{max}}$ to slightly lower temperatures compared to pure PFN–20BFO with the maximum value of ∼5800 at 0.1 kHz and 18 °C (Fig. 4c). Both modifications of PFN–20BFO lead to a weakening of the relaxor behavior, which is reflected in smaller $\Delta T_{\varepsilon,\mathrm{max}}$, namely ∼5 °C in both

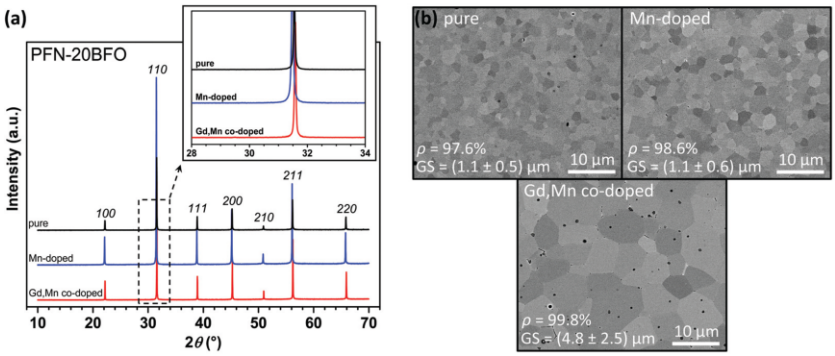


Fig. 3 (a) Room-temperature XRD patterns of PFN–20BFO-based compositions. The indexed peaks of the perovskite phase are labeled according to the cubic notation. The inset shows an enlarged 2θ region from 28° to 34°, where no peaks of secondary phases are observed. (b) SEM micrographs of polished PFN–20BFO-based compositions.

 This journal is © The Royal Society of Chemistry 2020

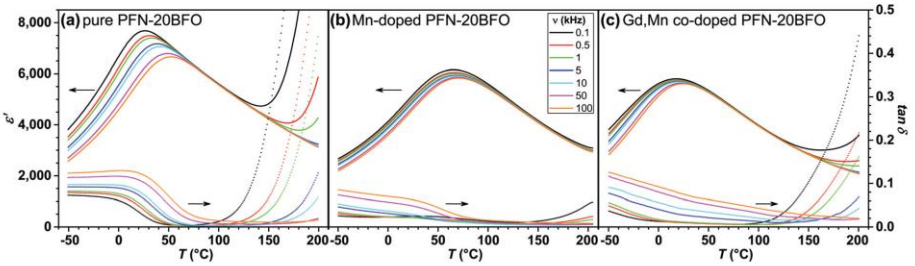


Fig. 4 Temperature and frequency dependences of ε' and $\tan\delta$ of (a) pure, (b) Mn-doped and (c) Gd,Mn co-doped PFN–20BFO.

samples. In all three samples high room-temperature ε' values are observed, ranging from ~5200 to ~7700 at 0.1 kHz.

The $\tan\delta$ of all three compositions are frequency-dependent with relatively low values at RT, namely from 0.05 to 0.01 at 1 kHz (Fig. 4). Due to the enhanced electrical conductivity in pure PFN–20BFO, above 120 °C the $\tan\delta$ significantly increases. The addition of Mn ions successfully reduces the $\tan\delta$ throughout the entire temperature range showing very low values even at high temperatures, *i.e.*, ~0.05 at 200 °C and 0.1 kHz (Fig. 4b). Further modification of the material by Gd ions leads back to an increase in $\tan\delta$, but the values remain comparable or even slightly lower than that in pure PFN–20BFO.

To further investigate the influence of Mn and Gd doping on electrical conductivity, the DC *j*–*E* responses of samples were measured at RT (Fig. 5a). As expected, the highest σ_{DC} was obtained in pure PFN–20BFO, namely $\sim 3.0 \times 10^{-10}\ \Omega^{-1}\ m^{-1}$. The addition of 0.5 mol% Mn successfully reduces the electrical conductivity of the material, leading to ~20 times lower room-temperature σ_{DC} value, *i.e.*, $\sim 1.7 \times 10^{-11}\ \Omega^{-1}\ m^{-1}$. On the other hand, further addition of Gd does not significantly increase the electrical conductivity at RT, which still remains low and comparable to that of the Mn-doped one (*i.e.*, $\sim 2.0 \times 10^{-11}\ \Omega^{-1}\ m^{-1}$).

The influence of Mn and Gd doping on room-temperature *P*–*E* hysteresis loop measurements was investigated (Fig. 5b). Pure PFN–20BFO exhibits relatively slim and tilted relaxor-like *P*–*E* hysteresis loops with a coercive electric field (E_C) and saturated polarization (P_S) of ~2.8 kV cm^{-1} and ~38 μC cm^{-2}, respectively. The results are in agreement with the previous study.[42] The addition of 0.5 mol% Mn does not significantly affect the *P*–*E* response, where E_C remains comparable to the one in pure PFN–20BFO, while P_S is slightly lower, *i.e.*, ~34 μC cm^{-2}. Further addition of Gd resulted in even slimmer room-temperature hysteresis loops with lower E_C and P_S values, namely ~1.5 kV cm^{-1} and ~32 μC cm^{-2}, respectively. Note that this is most probably related to the lower peak-permittivity temperature and more pronounced cubic symmetry in this composition at RT (ESI,† B). In addition, both modified compositions exhibit sharp *P*–*E* loop ends, indicating low electrical conductivity of the materials even at higher applied electric fields.

As previously demonstrated in PFN[23,62] as well as BFO-based[33,34] ceramics, a reason that such a small amount of Mn successfully suppresses the enhanced electrical conductivity of the material could be related to the nature of the Mn ions, which are known to undergo different oxidation states (for example 4+, 3+ or 2+ in this case) and thus easily compensate possible charge imbalances in the system. Consequently, Mn ions most likely lead to a lower concentration of charge point defects, leading to suppressed electrical conductivity at high temperatures and high electric fields. On the other hand, further addition of Gd does not significantly affect the ferroelectric and dielectric properties of the material, where dilution of ferroelectrically active Bi^{3+} ions by magnetic Gd^{3+} ions causes only a slight shift of $T_{\varepsilon,max}$ towards lower temperatures.

After structural, microstructural and electrical characterization, the influence of Mn and Gd doping on the magnetic properties

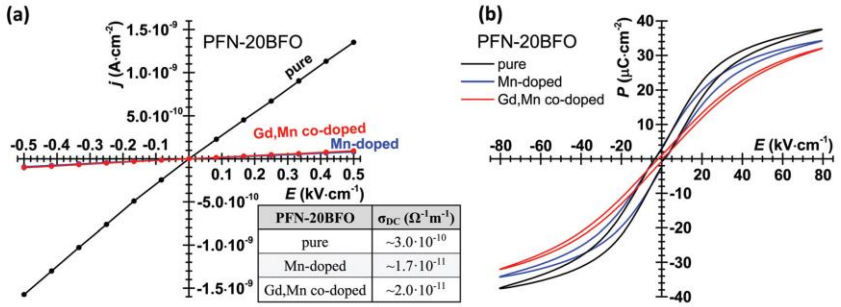


Fig. 5 (a) *j*–*E* curves with (inset) related σ_{DC} values and (b) *P*–*E* hysteresis loops of PFN–20BFO-based compositions measured at RT.

of PFN–20BFO was studied. The $M(T)$ curves of all three PFN–20BFO-based compositions, measured at a magnetic field of 1 kOe, are shown in Fig. 6a. In all three cases an increasing trend of M with a decreasing temperature is observed. Even the addition of only 0.5 mol% Mn ions slightly affects the magnetic properties of the material, where compared to pure PFN–20BFO, ~10% higher magnetization values are obtained over the entire measuring temperature range. As already mentioned, Fe–O–Fe linkages define the magnetic properties in this system.[56–58] The substitution of larger Fe^{3+} ions (64.5 pm, $3d^5$)[53] with smaller Mn^{4+} ions (53 pm, $3d^3$)[53] changes the local structure of FeO_6 octahedra,[63,64] leading to contraction of the lattice parameters (ESI,† B). Consequently, a shorter Mn–O bond and thus different angles of Fe–O–Mn linkages in comparison to the initial Fe–O–Fe lead to a slightly different magnetic arrangement in the structure.[64,65] According to the previous studies, it was found that Fe–O–Mn can slightly distort the long-range antiferromagnetic order, inducing more ferrimagnetic-like spin configuration and thus slightly larger macroscopic magnetization.[66] The same trend, namely slightly increased magnetization in the entire temperature range, was also observed in Mn-doped PFN ceramics.[23]

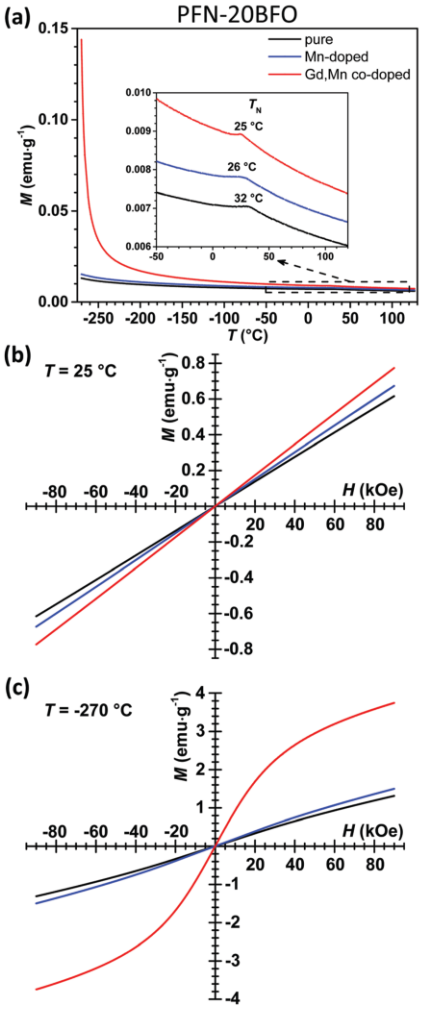


Fig. 6 (a) Temperature dependences of M for PFN–20BFO-based composition measured at 1 kOe. Inset: The enlarged view of the data between −50 °C and 120 °C where T_N is highlighted. M–H hysteresis loops of PFN–20BFO-based compositions measured at (b) RT and (c) −270 °C.

Further doping with Gd ions results in a significant enhancement of magnetic properties, especially at low temperatures. Compared to pure PFN–20BFO, the Gd,Mn co-doped sample exhibits ~30% larger room-temperature magnetization (inset of Fig. 6a and b). While at lower temperatures more than 11 times higher maximum value of M is obtained, namely ~0.144 emu g^{-1} at −270 °C and 1 kOe. This significantly higher magnetic response of the Gd, Mn co-doped sample is also reflected in M–H hysteresis loop measurements at −270 °C (Fig. 6c). Similarly, a large enhancement of M at low temperatures was also reported for Gd-doped BFO,[36,38,39,67] where such an enhanced magnetic response is described by the alignment of Gd^{3+} and Fe–O–Fe magnetic moments in the same direction. At low temperatures, paramagnetic Gd^{3+} ions (partially filled seven 5f-orbitals) that possess high magnetic moments align with the antiferromagnetic Fe–O–Fe subsystem (f–d exchange orbital interaction), leading to significant enhancement of magnetization.[36,67,68] This contribution is less pronounced at higher temperatures, which is reflected in lower magnetization values.

As seen above, the addition of Mn and Gd enhances the magnetic properties of PFN–20BFO but at the same time, it does not influence its relaxor behavior that remains comparable to that of pure PFN–20BFO. Even more, both modified compositions exhibit relaxor-like hysteresis loops with sharp ends indicating low electrical conductivity even at higher applied electric fields, which make them promising candidates for multicalorics. Therefore, in the next step, the EC and MC effects of Mn and Gd,Mn modified compositions were studied.

The temperature dependence of ΔT_{EC} at different applied electric fields for Mn-doped PFN–20BFO is shown in Fig. 7a. The addition of 0.5 mol% Mn reduces the electrical conductivity, which enables the measurements of EC effects at higher temperatures and applied electric fields compared to pure PFN–20BFO (see Fig. S5a (ESI†) and compare with Fig. 7a). Mn-doped PFN–20BFO exhibits a high room-temperature ΔT_{EC} value of ~1.5 °C at 150 kV cm^{-1}, which is comparable to that of previously studied Mn-doped PFN.[23] By increasing the temperature, ΔT_{EC} increases and reaches the maximum value of ~1.8 °C at 76 °C and 150 kV cm^{-1} (Fig. 7a). Additional doping with Gd resulted in a slightly lower ΔT_{EC}, namely ~1.13 °C at RT and 140 kV cm^{-1}. As seen in Fig. 4c, the peak-permittivity temperature of the Gd,Mn co-doped sample is below RT. As the temperature increases, no additional anomalies are observed, resulting in a nearly constant ΔT_{EC} of 1.15 °C ± 0.02 °C.

In Mn-doped PFN–20BFO at temperatures below 70 °C almost negligible JH (<3%) is present, resulting in a good

 This journal is © The Royal Society of Chemistry 2020

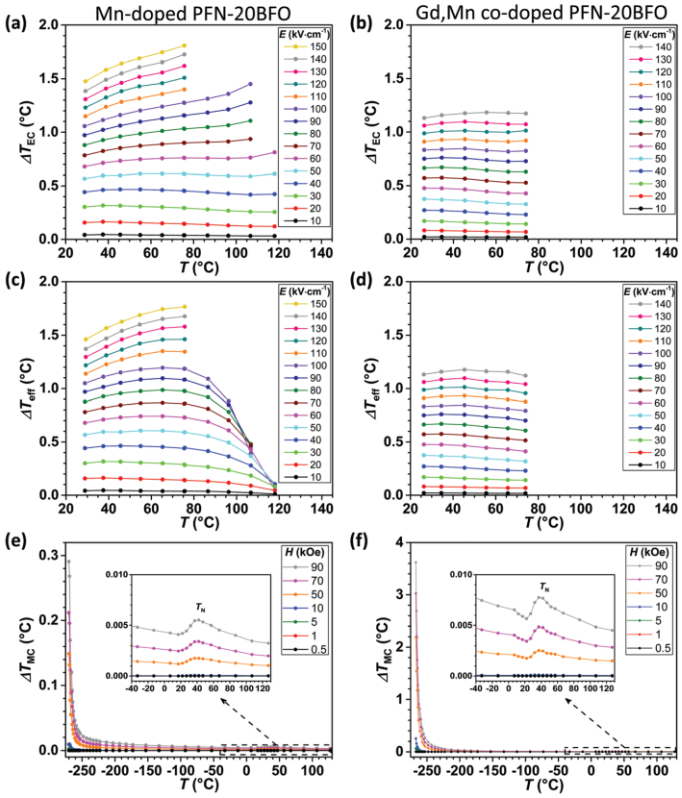


Fig. 7 Multicaloric properties of (a,c and e) Mn-doped and (b,d and f) Gd,Mn co-doped PFN–20BFO; (a and b) ΔT_{EC} and (c and d) ΔT_{eff} measured at different temperatures and applied electric fields. Due to the constant trend, EC measurements of the Gd,Mn co-doped sample were performed only up to 75 °C. (e and f) ΔT_{MC} measured at different temperatures and applied magnetic field with the inset showing an enlarged view of the data between −40 °C and 130 °C. Note the differences in scales of ΔT_{MC}. Lines between the measured values are just a guide to the eye.

match of ΔT_{eff} with the ΔT_{EC} values (Fig. 7c). Above 80 °C, the JH starts to increase, causing a gradual lowering of the effective EC cooling effect. Negligible JH (<5%) was also observed in the Gd,Mn co-doped sample, where ΔT_{eff} remains more or less identical to ΔT_{EC} until 75 °C (Fig. 7d).

The temperature dependences of ΔT_{MC} (calculated from $M(T)$ curves shown in ESI†, C) at different applied magnetic fields for Mn-doped and Gd,Mn co-doped PFN–20BFO are shown in Fig. 7e and f, respectively. A slight improvement in the magnetization of the Mn-doped sample in comparison to pure PFN–20BFO (see Fig. 6a) is also reflected in the MC effect, where ∼20% higher room-temperature ΔT_{MC} is observed. However, at low temperatures ∼2 times higher ΔT_{MC} of ∼0.15 °C at −270 °C and 50 kOe is obtained (insets of Fig. 7e). In agreement with enhanced magnetic properties, further addition of Gd ions causes a significant improvement of the MC effect over the entire temperature range, resulting in ∼65% higher ΔT_{MC} at RT and more than 30 times higher ΔT_{MC} at −270 °C (∼2.2 °C at 50 kOe) compared to pure PFN–20BFO (Fig. 7f). Furthermore, in this material room-temperature ΔT_{MC} $\sim 8 \times 10^{-3}$ °C is obtained at 90 kOe, which is so far the highest value among the PFN-based multicalorics.[22,23,69] On the other hand, the sample exhibits an extremely high ΔT_{MC} value of 3.6 °C at −270 °C and 90 kOe. Considering that this is an indirect measurement and that temperature of −273.15 °C (0 K) cannot be reached, we estimate that the ΔT_{MC} value is below 3 °C.

IV. Summary and conclusions

In this work, a series of single-phase PFN–100xBFO solid solutions (x = 0–0.5) were prepared by mechanochemical synthesis followed by sintering. The influence of BFO addition on the temperatures of magnetic susceptibility and dielectric permittivity anomalies was studied. With an increase in the amount of BFO, the paramagnetic–antiferromagnetic phase transition of PFN–BFO shifts toward higher temperatures, while the peak-permittivity temperature first decreases (to RT when x = 0.2) and then increases to higher temperatures (in x > 0.2 compositions). The dielectric

Table 1 Summary of room-temperature and maximum (a) EC and (b) MC effect values for PFN–20BFO-based compositions

(a)	Sample	T (°C)	E (kV cm^{-1})	ΔT_{eff} (°C)
EC effect	Pure	RT	90	0.50
	Mn-doped	RT	90	0.97
			150	1.5
		$T_{EC,max}$ (76 °C)	150	1.8
	Gd,Mn co-doped	RT	90	0.75
			140	1.1

(b)	Sample	T (°C)	H (kOe)	ΔT_{MC} (°C)
MC effect	Pure	RT	50	0.0015
		$T_{MC,max}$ (−270 °C)	50	0.07
	Mn-doped	RT	50	0.0018
		$T_{MC,max}$ (−270 °C)	50	0.15
	Gd,Mn co-doped	RT	50	0.0025
		$T_{MC,max}$ (−270 °C)	50	2.2

permittivity and magnetic susceptibility anomalies coincide at RT in PFN–20BFO composition, making it a promising candidate for multicaloric applications. However, due to the excessive Joule heating and its antiferromagnetic nature, PFN–20BFO exhibits low EC and MC effects in the entire measuring temperature range with the maximum values of 0.50 °C (at RT and 90 kV cm^{-1}) and 0.07 °C (at −270 °C and 50 kOe), respectively (Table 1). Therefore, the EC and MC properties of PFN–20BFO were further improved by doping with Mn and Gd ions.

The addition of 0.5 mol% Mn successfully suppresses the electrical conductivity and consequently the Joule heating effect in the material, which resulted in a high room-temperature EC effect of 1.5 °C, and even a higher maximum value of 1.8 °C at 76 °C (Table 1a). At the same time, the addition of Mn also slightly improves the MC properties of the material, resulting in ∼20% higher room-temperature and ∼2 times higher maximum ΔT_{MC} compared to pure PFN–20BFO (Table 1b). Further addition of 12 mol% Gd leads to a significant enhancement of the MC effect in the entire measurement temperature range, exhibiting ∼65% higher room-temperature and more than 30 times higher maximum ΔT_{MC} compared to pure PFN–20BFO (Table 1b). At the same time, the room-temperature electrical conductivity remains comparable to that of Mn-doped PFN–20BFO, which resulted in negligible Joule heating and EC effects of more than one degree over a wide temperature range.

Despite the fact that in the prepared PFN–20BFO-based materials both ferroic anomalies are located at RT, the maximum MC and EC effects are located in two different temperature regions. The use of such multicaloric materials could be in applications where the operating temperature is significantly changing, for example in deep space and extreme measurement under liquid-helium temperature conditions. Further research in this area is needed to prepare better room-temperature single-phase multicalorics that can be used as cooling elements in future solid-state cooling devices for everyday use.

Conflicts of interest

There are no conflicts to declare.

Acknowledgements

The authors acknowledge the financial support from the Slovenian Research Agency (project *Multicaloric cooling* J2-9253, young researcher project PR-07594 and research core funding No. P2-0105) and the joint research project between the Polish Academy of Science and the Slovenian Academy of Science and Art "*Multicaloric relaxor materials for new cooling technologies*". The authors thank Julian Walker for fruitful discussions and valuable advices.

References

1 W. Eerenstein, N. D. Mathur and J. F. Scott, *Nature*, 2006, **442**, 759–765.
2 M. Fiebig, T. Lottermoser, D. Meier and M. Trassin, *Nat. Rev. Mater.*, 2016, **1**, 16046.
3 N. A. Spaldin and R. Ramesh, *Nat. Mater.*, 2019, **18**, 203–212.
4 P. Chandra, *Nat. Mater.*, 2019, **18**, 197–198.
5 N. A. Hill, *J. Phys. Chem. B*, 2000, **104**, 6694–6709.
6 I. Takeuchi and K. Sandeman, *Phys. Today*, 2015, **68**, 48–54.
7 J. Shi, D. Han, Z. Li, L. Yang, S.-G. Lu, Z. Zhong, J. Chen, Q. M. Zhang and X. Qian, *Joule*, 2019, **3**, 1–26.
8 S. Fahler and V. K. Pecharsky, *MRS Bull.*, 2018, **43**, 264–268.
9 L. Manosa, A. Planes and M. Acet, *J. Mater. Chem. A*, 2013, **1**, 4925–4936.
10 S. Fahler, U. K. Rossler, O. Kasther, J. Eckert, G. Eggeler, H. Emmerich, P. Entel, S. Muller, E. Quandt and K. Albe, *Adv. Eng. Mater.*, 2012, **14**, 10–19.
11 X. Moya, S. Kar-Narayan and N. D. Mathur, *Nat. Mater.*, 2014, **13**, 439–450.
12 M. M. Vopson, *Crit. Rev. Solid State Mater. Sci.*, 2015, **40**, 223–250.
13 M. M. Vopson, *Solid State Commun.*, 2012, **152**, 2067–2070.
14 E. Stern-Taulats, T. Castan, L. Manosa, A. Planes, N. D. Mathur and X. Moya, *MRS Bull.*, 2018, **43**, 295–299.
15 B. Rozic, M. Kosec, H. Ursic, J. Holc, B. Malic, Q. M. Zhang, R. Blinc, R. Pirc and Z. Kutnjak, *J. Appl. Phys.*, 2011, **110**, 064118.
16 M. M. Vopson, *J. Phys. D: Appl. Phys.*, 2013, **46**, 345304.
17 H. Meng, B. Li, W. Ren and Z. Zhang, *Phys. Lett. A*, 2013, **377**, 567–571.
18 A. Planes, T. Castan and A. Saxena, *Philos. Mag.*, 2014, **94**, 1893–1908.
19 A. Kumar and K. L. Yadav, *J. Appl. Phys.*, 2014, **116**, 083907.
20 A. S. Starkov and I. A. Starkov, *J. Exp. Theor. Phys.*, 2014, **119**, 258–263.
21 J. Krishna Murthy and A. Venimadhav, *J. Phys. D: Appl. Phys.*, 2014, **47**, 445002.
22 H. Ursic, V. Bobnar, B. Malic, C. Filipic, M. Vrabelj, S. Drnovsek, Y. Jo, M. Wencka and Z. Kutnjak, *Sci. Rep.*, 2016, **6**, 26629.
23 U. Prah, T. Rojac, M. Wencka, M. Dragomir, A. Bradesko, A. Bencan, R. Sherbondy, G. Brennecka, Z. Kutnjak, B. Malic and H. Ursic, *J. Eur. Ceram. Soc.*, 2019, **39**, 4122–4130.
24 M. Yokosuka, *Jpn. J. Appl. Phys.*, 1993, **32**, 1142–1146.

 This journal is © The Royal Society of Chemistry 2020

25 V. V. Laguta, J. Rosa, L. Jastrabik, R. Blinc, P. Cevc, B. Zalar, M. Remskar, S. I. Raevskaya and I. P. Raevski, *Mater. Res. Bull.*, 2010, **45**, 1720–1727.

26 A. Kumar, R. S. Katiyar, C. Rinaldi, S. G. Lushnikov and T. A. Shaplygina, *Appl. Phys. Lett.*, 2008, **93**, 232902.

27 G. Catalan and J. F. Scott, *Adv. Mater.*, 2009, **21**, 2463–2485.

28 T. Rojac, A. Bencan, B. Malic, G. Tutuncu, J. L. Jones, J. E. Daniels and D. Damjanovic, *J. Am. Ceram. Soc.*, 2014, **97**, 1993–2011.

29 A. Bradesko, A. Hedl, L. Fulanovic, N. Novak and T. Rojac, *APL Mater.*, 2019, **7**, 071111.

30 M. Quintero, L. Ghivelder, F. Gomez-Marlasca and F. Parisi, *Appl. Phys. Lett.*, 2011, **99**, 232908.

31 M. Quintero, P. Gaztanaga and I. Irurzun, *Appl. Phys. Lett.*, 2015, **107**, 151901.

32 D. Bochenek and P. Guzdek, *J. Magn. Magn. Mater.*, 2011, **323**, 369–374.

33 M. Makarovic, J. Walker, E. Khomyakova, A. Bencan, B. Malic and T. Rojac, *Informacije MIDEM*, 2016, **46**, 154–159.

34 S. O. Leontsev and R. E. Eitel, *J. Am. Ceram. Soc.*, 2009, **92**, 2957–2961.

35 G. L. Yuan, S. W. Or, Y. P. Wang, Z. G. Liu and J. M. Liu, *Solid State Commun.*, 2006, **138**, 76–81.

36 V. A. Khomchenko, V. V. Shvartsman, P. Borisov, W. Kleemann, D. A. Kiselev, I. K. Bdikin, J. M. Vieira and A. L. Kholkin, *Acta Mater.*, 2009, **57**, 5137–5145.

37 J. Walker, H. Ursic, A. Bencan, B. Malic, H. Simons, I. Reaney, G. Viola, V. Nagarajan and T. Rojac, *J. Mater. Chem. C*, 2016, **4**, 7859–7868.

38 V. Sobol, B. Korzun, O. Mazurenko, T. Bizhigitov and S. Tomaev, *MRS Adv.*, 2019, **4**, 1989–1999.

39 D. Lukovic Golic, A. Radojkovic, A. Dapcevic, D. Pajic, J. Dragovic, F. Toric, J. Cirkovic, G. Brankovic and Z. Brankovic, *Ceram. Int.*, 2019, **45**, 19158–19165.

40 J. J. Rhyne and T. R. McGuire, *IEEE Trans. Magn.*, 1972, **8**, 105–130.

41 S. Karimi, I. M. Reaney, Y. Han, J. Pokorny and I. Sterianou, *J. Mater. Sci.*, 2009, **44**, 5102–5112.

42 U. Prah, M. Dragomir, T. Rojac, A. Bencan, R. Broughton, C.-C. Chung, J. L. Jones, R. Sherbondy, G. Brennecka and H. Ursic, *J. Mater. Chem. C*, 2020, **8**, 3452–3462.

43 D. Kuscer, T. Bakaric, B. Kozlevcar and M. Kosec, *J. Phys. Chem. B*, 2013, **117**, 1651–1659.

44 J. Walker, P. Bryant, V. Kurusingal, C. Sorrell, D. Kuscer, G. Drazic, A. Bencan, V. Nagarajan and T. Rojac, *Acta Mater.*, 2015, **83**, 149–159.

45 R. Font, O. Raymond-Herrera, L. Mestres, J. Portelles, J. Fuentes and J. M. Siqueiros, *J. Mater. Sci.*, 2016, **51**, 6319–6330.

46 D. Wilcox, B. Dove, B. McDavid and D. Greer, *UTHSCSA Image Tool for Windows Version 3.0.*, University of Texas Health Science Center, San Antonio, TX, 2002.

47 W. H. Walton, *Nature*, 1948, **162**, 329–330.

48 A. Bradesko, L. Fulanovic, M. Vrabelj, M. Otonicar, H. Ursic, A. Henriques, C.-C. Chung, J. L. Jones, B. Malic, Z. Kutnjak and T. Rojac, *Acta Mater.*, 2019, **169**, 275–283.

49 Z. Kutnjak and B. Rožič, Indirect and Direct Measurements of the Electrocaloric Effect, in *Electrocaloric Materials. New Generation of Coolers*, ed. T. Correia and Q. Zhang, Springer, Berlin, Heidelberg, 2014, vol. 147.

50 A. M. Tishin and Y. I. Spichkin, *The Magnetocaloric Effect and its Applications*, Institute of Physics Publishing, Bristol, UK, 2003.

51 A. A. Bokov and Z.-G. Ye, *J. Mater. Sci.*, 2006, **41**, 31–52.

52 F. Li, S. Zhang, D. Damjanovic, L.-Q. Chen and T. R. Shrout, *Adv. Funct. Mater.*, 2018, **28**, 1801504.

53 R. D. Shannon, *Acta Crystallogr., Sect. A: Cryst. Phys., Diffr., Theor. Gen. Crystallogr.*, 1976, **32**, 751–767.

54 F. Chu, I. M. Reaney and N. Setter, *J. Appl. Phys.*, 1995, **77**, 1671–1676.

55 G. A. Smolenskii and V. M. Yudin, *Phys. Solid State*, 1965, **6**, 2936–2942.

56 V. V. Bhat, K. V. Ramanujachary, S. E. Lofland and A. M. Umarji, *J. Magn. Magn. Mater.*, 2004, **280**, 221–226.

57 A. Stoch, J. Maurin, J. Kulawik and P. Stoch, *J. Eur. Ceram. Soc.*, 2017, **37**, 1467–1476.

58 A. Stoch and P. Stoch, *Ceram. Int.*, 2018, **44**, 14136–14144.

59 S. Chillal, M. Thede, F. J. Litterst, S. N. Gvasaliya, T. A. Shaplygina, S. G. Lushnikov and A. Zheludev, *Phys. Rev. B: Condens. Matter Mater. Phys.*, 2013, **87**, 220403.

60 N. N. Krainik, N. P. Khuchua, A. A. Berezhnoi and A. G. Tutov, *Phys. Solid State*, 1965, **7**, 100–107.

61 L. A. Shilkina, A. V. Pavlenko, L. A. Reznitchenko and I. A. Verbenko, *Crystallogr. Rep.*, 2016, **61**, 263–269.

62 B. Fang, Y. Shan and H. Imoto, *Jpn. J. Appl. Phys.*, 2004, **43**, 2568–2571.

63 L. Chen, L. Zheng, Y. He, J. Zhang, Z. Mao and X. Chen, *J. Alloys Compd.*, 2015, **633**, 216–219.

64 Y. Zhang, Y. Wang, J. Qi, Y. Tian, M. Sun, J. Zhang, T. Hu, M. Wei, Y. Liu and J. Yang, *Nanomaterials*, 2018, **8**, 711.

65 I. Sosnowska, W. Schäfer, W. Kockelmann, K. H. Andersen and I. O. Troyanchuk, *Appl. Phys. A: Mater. Sci. Process.*, 2002, **74**, 1040–1042.

66 H. Naganuma, J. Miura and S. Okamura, *Appl. Phys. Lett.*, 2008, **93**, 052901.

67 A. I. Iorgu, F. Maxim, C. Matei, L. P. Ferreira, P. Ferreira, M. M. Cruz and D. Berger, *J. Alloys Compd.*, 2015, **629**, 62–68.

68 I. I. Makoed and A. F. Revinskii, *Phys. Solid State*, 2015, **57**, 1787–1792.

69 U. Prah, M. Wencka, Z. Kutnjak, M. Vrabelj, S. Drnovsek, B. Malic and H. Ursic, *Informacije MIDEM*, 2017, **47**, 165–170.

Supplementary material

$Pb(Fe_{0.5}Nb_{0.5})O_3$–$BiFeO_3$-based multicalorics with room-temperature ferroic anomalies

Uroš Prah,[a,b,*] Magdalena Wencka,[c] Tadej Rojac,[a,b] Andreja Benčan[a,b] and Hana Uršič[a,b]

[a] Jožef Stefan Institute, Jamova cesta 39, 1000 Ljubljana, Slovenia.
[b] Jožef Stefan International Postgraduate School, Jamova cesta 39, 1000 Ljubljana, Slovenia.
[c] Institute of Molecular Physics, Polish Academy of Sciences, ul. Smoluchowskiego 17, 61-179 Poznań, Poland.
[*] Corresponding author: uros.prah@ijs.si

A. Sintering behavior of PFN–20BFO-based compositions

The optimal sintering temperatures were selected and verified by performing two dynamic sintering curve experiments. The measurements were recorded during heating using an optical dilatometer (Leitz Version 1A, Leitz, Wetzlar, Germany), where in all cases heating rate of 2 °C·min^{-1} was used. In the first step, dynamic sintering curve measurement was performed by heating the sample to its melting point (i.e., up to ~1200 °C), representing a reference for the total shrinkage and densification level of each composition (solid lines in Fig. S1). Based on that, the temperature at which the powder compact start to densify was selected. The temperature 900 °C was selected for pure and Mn-doped samples, while for Gd,Mn co-doped sample 1000 °C is required to obtain a sufficient degree of densification. In the next step, the dynamic sintering curve measurements were repeated by creating the entire sintering process, namely heating the powder compact to previously selected temperature followed by 2 hours of holding time at this temperature (open symbols in Fig. S1). In all three compositions, the selected thermal processes have led to sufficient densification of the powder compacts.

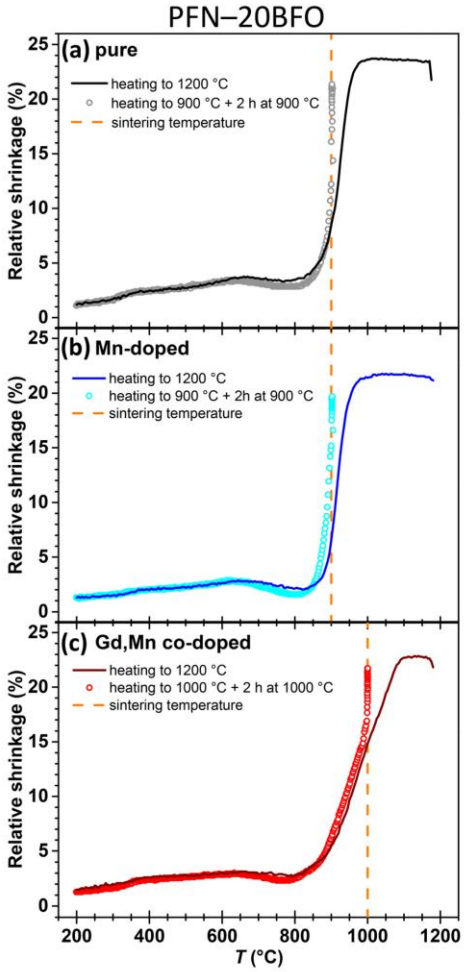


Fig. S1. Dynamic sintering curves measurements of (a) pure, (b) Mn-doped and (c) Gd,Mn co-doped PFN–20BFO powder compacts. Solid lines and open symbols represent shrinkage during heating to 1200 °C and during thermal treatment at selected sintering conditions, respectively.

B. Rietveld refinement of PFN–20BFO-based compositions

The quantitative phase composition analyses were performed using the Rietveld refinement method. For this purpose, the XRD patterns were recorded in the 15–120° 2θ-range with a step of 0.008° and an integration time of 100 s per step at RT. The *Topas R* package (version 2.1, Bruker, AXS, Karlsruhe, Germany) was employed and a Fundamental Parameters Approach was used to describe the peak profile.[a] In this model, the background (10^{th} order Chebychev), unit cell parameters, crystallite size, scale factors, sample displacement, atomic coordinates, and thermal parameters were stepwise refined to obtain a calculated diffraction profile that best fits the experimental pattern. The quality of the fit was assessed from the goodness-of-fit parameters R_{wp}, R_p, R_{exp}, R_B, and *G.O.F.*

The effects of Mn and Gd doping on the phase composition, crystal structure and lattice parameters of PFN–20BFO were investigated. The agreement factors of the Rietveld analysis along with the cell parameters of all PFN–20BFO-based compositions are given in Table S1.

Table S1: Refined structural parameters for PFN–20BFO-based compositions at RT.

PFN–20BFO	**Pure**	**Mn-doped**	**Gd,Mn co-doped**
Crystal system	Cubic	Cubic	Cubic
Space group	$Pm\bar{3}m$	$Pm\bar{3}m$	$Pm\bar{3}m$
a (Å)	4.01038(9)	4.00917(5)	4.00441(1)
V (Å^3)	64.4999(9)	64.4414(3)	64.2119(1)
ρ (g·cm^{-3})	8.4123(5)	8.4062(6)	8.4042(2)
R_{wp} (%)	7.70	7.39	7.07
R_{exp} (%)	4.93	6.30	6.47
R_p (%)	5.89	5.69	5.49
G.O.F.	1.56	1.17	1.09
R_B (%)	2.46	3.19	4.39

The results of Rietveld refinement show that the addition of Mn as well as further doping with Gd ions does not affect the crystal symmetry at RT, which in all three PFN–20BFO-based compositions remains pseudocubic with $Pm\bar{3}m$ space group (Fig. S2a). Furthermore, doping with Mn ions leads to a slight decrease of the lattice parameter and unit cell volume (Fig. S2b). This could be consequence of a smaller ionic radius of Mn^{4+} (53 pm) compared to Fe^{3+} (64.5 pm for high spin configurations) and Nb^{5+} (64 pm) on B-site of the perovskite structure.[b] The decrease is even more pronounced in Gd,Mn co-doped sample, where additional contraction of lattice constants most probably arise from smaller ionic radius of Gd^{3+} (93.8 pm) compared to Bi^{3+} (103 pm) on A-site of the perovskite structure.[b]

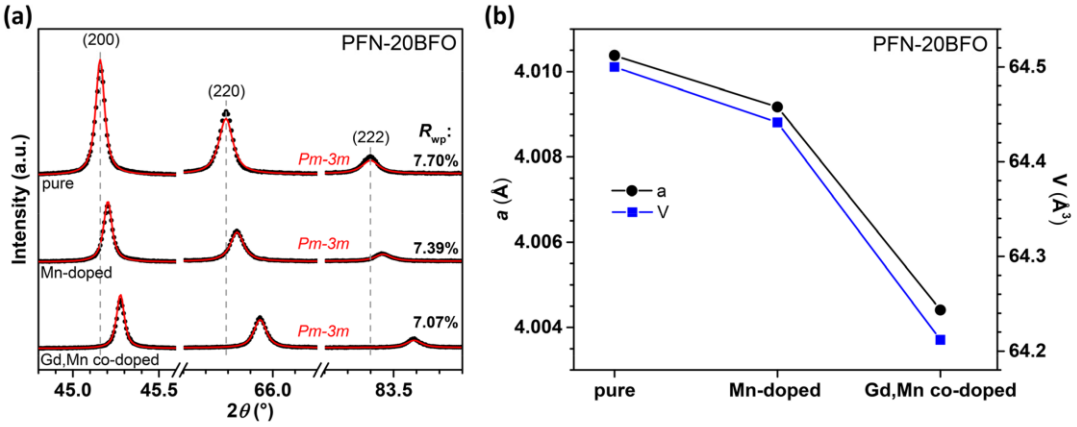


Fig. S2. (a) Room-temperature XRD profiles of the *200*, *220*, and *222* pseudocubic reflections (only from Cu $K\alpha_1$) for PFN–20BFO-based compositions. The calculated profile for the pseudocubic phase ($Pm\bar{3}m$ space group) is displayed in red. (b) Lattice parameters and unit cell volumes of PFN–20BFO-based compositions. Lines between the measured values are just a guide to the eye.

C. Measurements of magnetic properties of PFN–BFO-based compositions

M–H hysteresis loops of PFN–100*x*BFO (*x* = 0–0.5) solid solutions measured at 25 °C and −270 °C at the magnetic field of 90 kOe are shown in Fig. S3. At RT, compositions with *x* < 0.5 exhibit linear, paramagnetic-like *M–H* response (Fig. S3a), while in PFN–50BFO a weak antiferromagnetic behavior is present (inset of Fig. S3a). This is consistent with the results of *M*(*T*) measurements (Fig. 2 in the main text), which reveal that PFN–50BFO exhibits paramagnetic-antiferromagnetic phase transition above RT. At −270 °C, the presence of antiferromagnetic behavior is observed in all compositions (Fig. S3b). The coercive magnetic field (H_c), remanent magnetization (M_R) and saturated magnetization (M_S) are decreased with increasing amount of BFO, reaching the maximum values in PFN, namely ~1.8 kOe, ~0.1 emu·g^{-1} and ~2.2 emu·g^{-1}, respectively. This is in agreement with the *M*(*T*) measurements (Fig. 2 in the main text), where in PFN the highest *M* values are obtained. A reason for such behavior at low temperatures is the formation of a spin-glass-like phase in PFN-rich compositions, which arises from local short range order on the B-site perovskite sublattice (namely from Nb-rich-Fe-poor regions), where long range antiferromagnetic order is disturbed due to the presence of nonmagnetic Nb^{5+} ions. Therefore, an increase in Nb^{5+} concentration and thus Nb/Fe ratio increases the tendency for the formation of short-range spin-glass-like phase at low temperatures, which is reflected in higher *M* values in PFN-rich PFN–BFO compositions.[c,d,e]

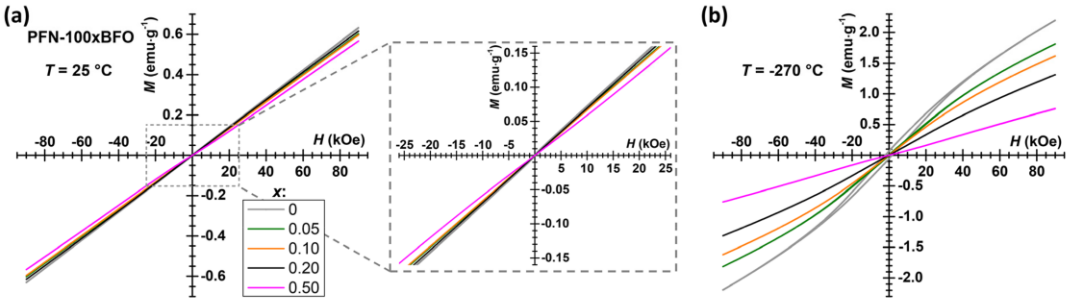


Fig. S3. *M–H* hysteresis loops of PFN–100*x*BFO (*x* = 0–0.5) measured at (a) 25 °C and (b) −270 °C. Inset: the enlarged view of the data between ±25 kOe at 25 °C.

The temperature dependences of *M* at different *H* for all three PFN–20BFO-based compositions are shown in Fig. S4. In all cases, *M* increases with decreasing temperature reaching maximum values at −270 °C. Such *M*(*T*,*H*) measurements were used for calculation of MC effect using indirect method.[f]

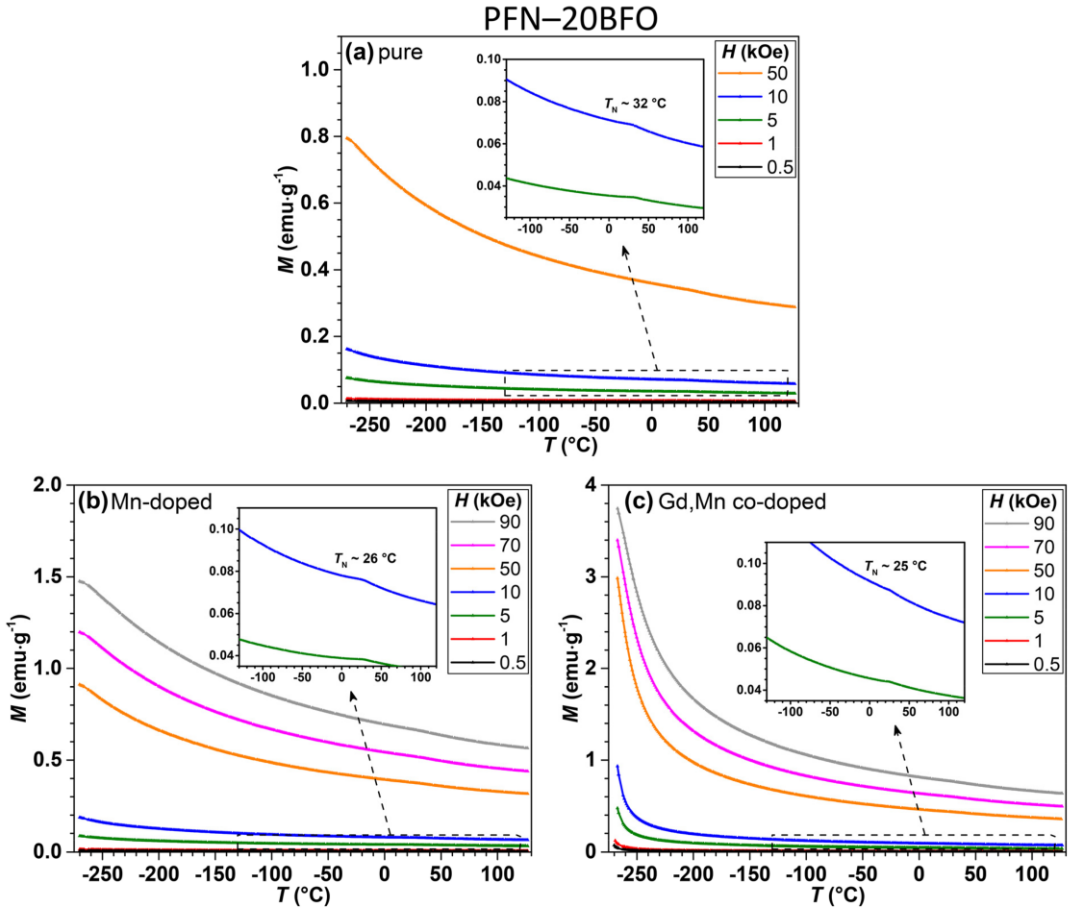


Fig. S4. Temperature dependences of M at different applied H for (a) pure, (b) Mn-doped and (c) Gd,Mn co-doped PFN–20BFO. Insets: the enlarged view of the data between −130 °C and 120 °C where T_N is highlighted.

D. Multicaloric properties of pure PFN–20BFO

First, the EC effect of PFN–20BFO solid solution was measured. The temperature dependence of ΔT_{EC} at different applied electric fields is shown in Fig. S5a. The ΔT_{EC} of 0.91 °C was obtained at RT and 90 kV·cm^{-1} (determined directly from measured temperature change during the EC cycle, shown in Fig. S5b). At higher temperatures ΔT_{EC} slightly increases reaching a maximum value of 0.94 °C at 45 °C and 90 kV·cm^{-1}. Measurements at higher temperatures and larger applied electric fields were not possible due to the excessive electrical conductivity. Namely, the increased electrical conductivity leads to the appearance of Joule heating (JH) that can slightly or completely overlap the ΔT_{EC} (marked with crosses in Fig. S5a) and thus critically degrade the cooling ability of the material[g] (details in the next section, E). For example, the JH is 0.41 °C at RT and 90 kV·cm^{-1} (Fig. S5b). Taking into account the influence of JH on total EC cooling effect, the term EC effective cooling (ΔT_{eff}), defined as a difference between ΔT_{EC} and ΔT_{JH}, was introduced (shown in Figs. S5b and S6). The temperature and electric field dependence of ΔT_{eff} is shown in Fig. S5c. The highest ΔT_{eff} value

of 0.50 °C was obtained at RT and 90 kV·cm^{-1}. Due to increased JH, ΔT_{eff} is significantly reduced at higher temperatures, namely to only 0.17 °C at 45 °C and 90 kV·cm^{-1}.

The temperature dependences of ΔT_{MC} (calculated from $M(T)$ curves shown in the previous section, C) at different applied magnetic fields are shown in Fig. S5d. In general, ΔT_{MC} is low through the entire measuring temperature range reaching the maximum value of only 0.07 °C at −270 °C and 50 kOe. Additionally, at RT a peak in ΔT_{MC} response is observed (inset of Fig. S5d) in agreement with paramagnetic-antiferromagnetic phase transition. The peak value of ΔT_{MC} is ~$1.5 \cdot 10^{-3}$ °C at 42 °C and 50 kOe, which is comparable to the room-temperature value of PFN ceramics.[g]

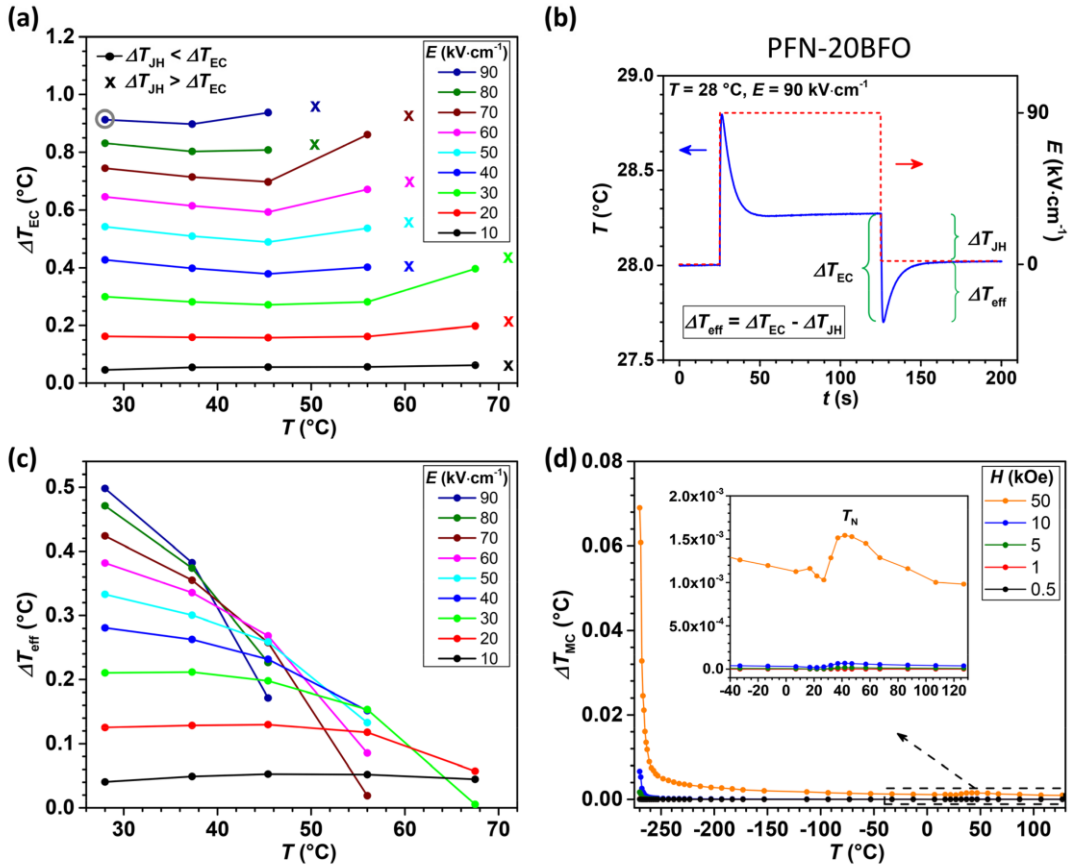


Figure S5. Multicaloric properties of PFN–20BFO; (a) ΔT_{EC} with (b) corresponding measured temperature change during the EC cycle at 28 °C and 90 kV·cm^{-1} (marked with gray circle in panel a) and (c) ΔT_{eff} measured at different temperatures and applied electric fields. The crosses in (a) mark the measurements where ΔT_{JH} overlap ΔT_{EC}. Note that temperature changes in (b) are not multiplied by a correction factor of 1.6. (d) ΔT_{MC} measured at different temperatures and applied magnetic fields with the inset showing an enlarged view of the data between −40 °C and 130 °C. Lines between the measured values are just a guide to the eye.

E. Electrocaloric effective cooling

Two examples of the measured temperature changes during the EC cycle in PFN–20BFO-based compositions are shown in Fig. S6. To determine the influence of Joule heating on the overall EC cooling response, the term EC effective cooling (ΔT_{eff}), defined as a difference between the EC temperature change (ΔT_{EC}) and temperature change corresponding to the Joule heating (ΔT_{JH}), was introduced. In the first example, i.e., the temperature change during the EC cycle of Gd,Mn co-doped sample at 56 °C and 100 kV·cm^{-1}, no Joule heating is present, therefore ΔT_{eff} is identical to ΔT_{EC} (Fig. S6a). While, in the second example, i.e., the temperature change during the EC cycle of pure PFN–20BFO at 28 °C and 50 kV·cm^{-1}, ΔT_{eff} is lower in comparison to ΔT_{EC}, due to the appearance of Joule heating effect (Fig. S6b).

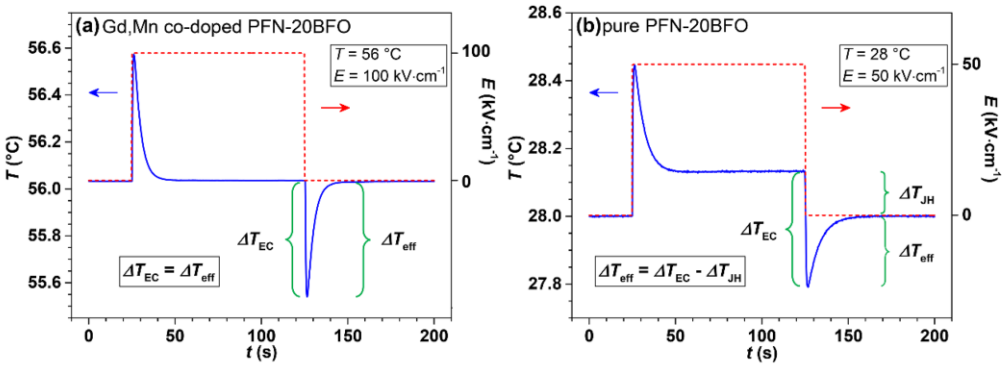


Fig. S6. Measured temperature changes during the EC cycle. The measurements were obtained (a) in Gd,Mn co-doped PFN–20BFO at 56 °C and 100 kV·cm^{-1} and (b) in pure PFN–20BFO at 28 °C and 50 kV·cm^{-1}. The applied electric field signal is marked by red dotted line. Note that temperature changes in (a) and (b) are not multiplied by a correction factor of 1.6 and 1.7, respectively.

F. EDXS analysis of Gd,Mn co-doped PFN–20BFO

Identification of the secondary phases present in Gd,Mn co-doped PFN–20BFO sample was performed by SEM-EDXS point analysis using accelerating voltage of 15 kV. SEM image of polished surface reveals the presence of two different secondary phases, which are marked with red and blue arrows in Fig. S7a. The EDXS analyses of identified secondary phases together with the matrix phase are shown in Fig. S7b. EDXS analysis reveal that areas marked with red arrows correspond to Fe-rich secondary phase, while areas marked with blue arrows indicating the presence of Gd,Nb-rich secondary phase. Considering the standard deviation error, the composition of a matrix phase is very close to the nominal value. Note that due to the small size of both secondary phases in comparison to ~1 μm large interaction volume of EDXS analysis, the results are only used for qualitative comparison. In addition, the amount of Mn is below the detection limit of the technique.

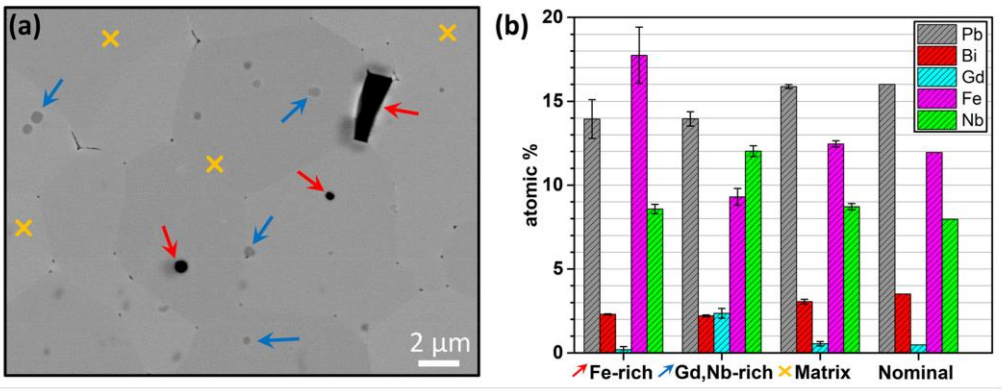


Fig. S7. (a) SEM micrograph of polished Gd,Mn co-doped PFN–20BFO with red arrows, blue arrows and orange crosses indicating Fe-rich, Gd,Nb-rich secondary phases and the matrix phase, respectively. (b) Corresponding EDXS analysis of phases marked with red arrows, blue arrows, orange crosses and nominal composition, respectively. Results are presented as average values with standard deviations of at least three areas.

G. Microstructure and grain size distributions of PFN–20BFO-based compositions

SEM images of the fractured, thermally etched surfaces and grain size distributions of all three PFN–20BFO-based compositions are shown in Fig. S8. In all compositions, SEM images reveal uniform and dense microstructures. Furthermore, in the thermally etched image of pure PFN–20BFO also some pull-outs, produced during the sample surface preparation, are present, while in Gd,Mn co-doped sample traces of Fe- and Gd,Nb-rich secondary phases are visible as a dark phase regions (described in the previous section, F). In all samples, a unimodal grain size distribution is observed (Fig. S8c).

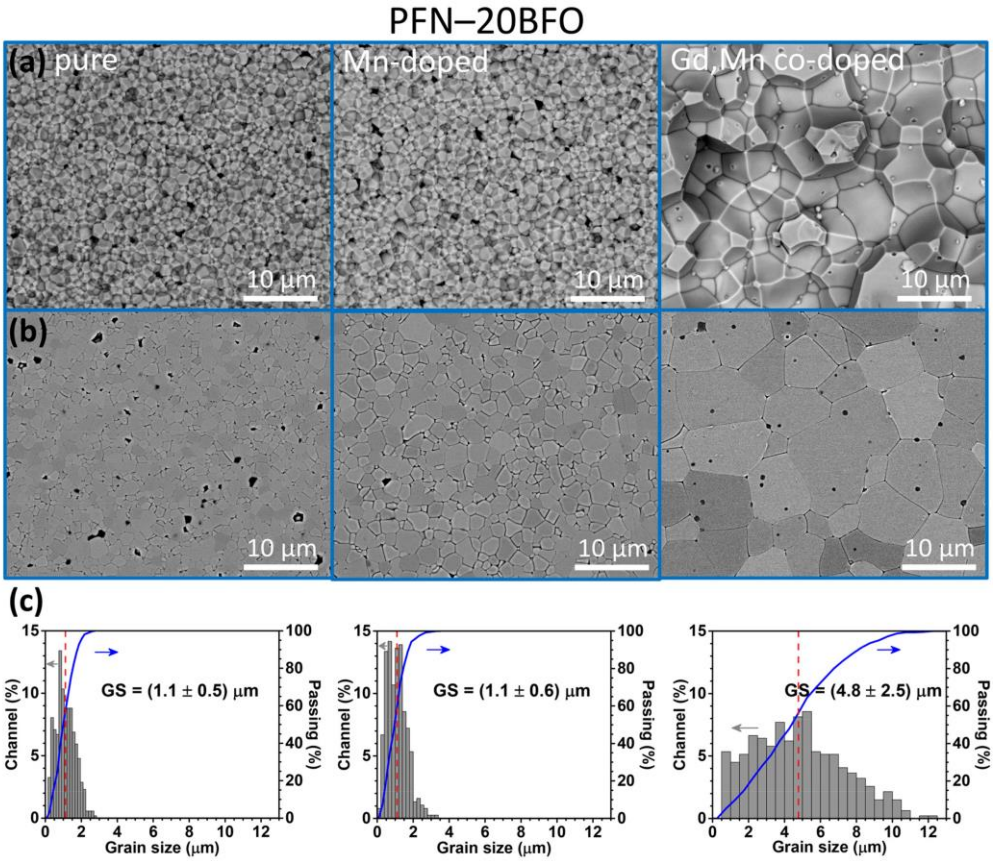


Fig. S8. SEM images of (a) fractured, (b) thermally etched surfaces and (c) the grain size distributions of PFN–20BFO-based compositions.

References

[a] R. W. Cheary and A. Coelho, *J. Appl. Crystallogr.*, 1992, **25**, 109–121.
[b] R. D. Shannon, *Acta Cryst. A*, 1976, **32**, 751–767.
[c] A. Kumar, R. S. Katiyar, C. Rinaldi, S. G. Lushnikov and T. A. Shaplygina, *Appl. Phys. Lett.*, 2008, **93**, 232902 1–3.
[d] G. M. Rotaru, B. Roessli, A. Amato, S. N. Gvasaliya, C. Mudry, S. G. Lushnikov and T. A. Shaplygina, *Phys. Rev. B*, 2009, **79**, 184430 1–5.
[e] V. V. Laguta, J. Rosa, L. Jastrabik, R. Blinc, P. Cevc, B. Zalar, M. Remskar, S. I, Raevskaya and I. P. Raevski, *Mater. Res. Bull.*, 2010, **45**, 1720–1727.
[f] A. M. Tishin and Y. I. Spichkin. The Magnetocaloric Effect and its Applications, Institute of Physics Publishing, Bristol, UK, (2003).
[g] A. Bradesko, A. Hedl, L. Fulanovic, N. Novak and T. Rojac, *APL Mater.*, 2019, **7**, 071111 1–6.
[h] U. Prah, T. Rojac, M. Wencka, M. Dragomir, A. Bradesko, A. Bencan, R. Sherbondy, G. Brennecka, Z. Kutnjak, B. Malic and H. Ursic, *J. Eur. Ceram. Soc.*, 2019, **39**, 4122–4130.

Chapter 5

Conclusions and Outlook

In this thesis we report and discuss the preparation and characterization of new, single-phase multicaloric materials that combine the EC and MC effects and represent promising candidates for active elements in future refrigeration technologies. The multicaloric properties of the prepared materials are summarized in Table 5.1, where for comparison also EC and MC properties of previously known PFN–20PMW multicaloric [41] are included.

Table 5.1: Summary of room-temperature and maximum $\Delta T_{EC,eff}$ and ΔT_{MC} of all PFN-based multicalorics.

Multicaloric material	$\Delta T_{EC,eff}$ (°C)				ΔT_{MC} (°C)			
	room-temp.		maximum		room-temp.		maximum [IV]	
	E (kV · cm^{-1})		E (kV · cm^{-1})		H (kOe)		H (kOe)	
	90	140	90	140	50	90	50	90
PFN–20PMW [41]	×	×	×	×	0.002	/	0.2 [V]	/
PFN	0.8	×	0.8 [I]	×	0.002	/	0.1	/
PFN–20BFO	0.5	×	0.5 [I]	×	0.001	/	0.1	/
Mn-doped PFN	1.0	1.6	1.9 [II]	2.5 [II]	0.003	/	0.4	/
Mn-doped PFN–20BFO	1.0	1.4	1.1 [II]	1.7 [II]	0.001	0.004	0.2	0.3
Gd,Mn co-doped PFN–20BFO	0.7	1.1	0.8 [III]	1.2 [II]	0.002	0.006	2.2	3.6

*The estimated relative uncertainty of determined ΔT_{EC} (Appendix A.3) and ΔT_{MC} (Subsection 1.2.2) are ~10% and ~25%, respectively.

(×) - cannot be determined due to high Joule heating or dielectric breakdown
(/) - not measured
Measured at: (I) RT, (II) 75 °C, (III) 45 °C, (IV) −270 °C and (V) −268 °C.

Based on the results, the following main conclusions can be drawn:

- We prepared five new, single-phase multicaloric materials that exhibit both the EC and MC effects.
- The addition of BFO to PFN and, accordingly, the formation of PFN–BFO solid solutions successfully shifts the paramagnetic-to-antiferromagnetic phase transition towards higher temperatures, reaching room temperature in the PFN–20BFO composition. In addition, PFN–20BFO also exhibits a room-temperature peak-permittivity anomaly, making it one of the first single-phase multiferroic materials with both ferroic anomalies at RT. These results confirm the hypothesis 2, where it was predicted that the addition of BFO into the PFN would shift the magnetic

anomalies towards RT and at the same time also affect the peak-permittivity temperature of PFN–BFO solid solutions.

- The electrical conductivity of PFN–BFO solid solutions increases with an increasing amount of BFO, leading to a higher Joule heating effect, which results in lower EC properties of PFN–20BFO compared to PFN (Table 5.1). This finding fully supports the hypothesis 3.
- Due to the excessive electrical conductivity and thus the occurrence of Joule heating, PFN and PFN–20BFO cannot withstand high applied electric fields and elevated temperatures (Table 5.1), which narrows the operating range of both materials. These findings confirm the hypotheses 1, which assumed that increased electrical conductivity would have a significant effect on unmodified compositions.
- Doping with 0.5 mol% of manganese successfully suppresses the enhanced electrical conductivity of the PFN and PFN–20BFO, resulting in σ_{DC} ~10^{-11} $\Omega^{-1}m^{-1}$ at RT for both samples. This allows the use of materials at high temperatures (up to 100 °C) and improves the resistance to large electric fields, which increases the EC effect as well as broadening the operating temperature and electric-field ranges. At the same time, the addition of manganese also induces a more ferromagnetic-like spin arrangement, resulting in improved MC effects in both compositions. These results support the hypothesis 1, where suppression of excessive electrical conductivity by dopants was proposed.
- Simultaneous doping with Gd and Mn successfully enhances the magnetic response and consequently the MC effect of PFN–20BFO, while, at the same time, does not significantly degrade the dielectric and ferroelectric properties. This results in EC and MC effects above 1 °C in both cases, which fully confirms the hypothesis 4.

In conclusion, careful control of the material's composition, an optimal synthesis procedure and target doping can lead to an improvement of the material's EC and MC effects, and thus the multicaloric properties. Among all the newly prepared materials, Gd,Mn co-doped PFN–20BFO exhibits so far the best multicaloric properties (Table 5.1) and low hysteresis losses resulting from its relaxor-like behavior. Nevertheless, the highest values of both individual caloric effects are still located in different temperature regions. This can be useful for applications where the ambient temperature varies significantly and a wider operating temperature range of the multicaloric material is required. However, most of the cooling devices for everyday use are operating at RT; therefore, there is still room for new room-temperature multicaloric materials. Using our results as a starting point, further work in this area is needed to prepare materials with high room-temperature multicaloric effects. Among all the possible external stimuli to drive caloric responses, the electric field is the easiest and cheapest to produce and apply, therefore, in my opinion, electrically induced multicaloric effects in highly coupled ME multiferroics represent the most promising path to efficient multicaloric refrigeration technologies in the future.

Appendix A

Electrocaloric Measurements

A.1 Direct Electrocaloric Measurements

The EC effect in this thesis was measured using the direct EC measurement method. The measurements were performed on 60–100 µm-thick disk-shaped ceramic pellets with sputtered Au electrodes (Figure 1.3a). The direct EC measurements were performed in a modified differential scanning calorimeter (Netzsch DSC 204 F1, Selb, Germany), which allowed a precise temperature stabilization (±0.001 °C). The temperature changes were measured with a small-bead thermistor glued to the sample (Figure 1.3a). The electrical signal was applied using a Keithley High Voltage Source-Measure Unit 237 and the thermistor resistance was monitored using a Keithley 2100 digital multimeter (Keithley Instruments, Solon, Ohio, USA). For the determination of the ΔT_{EC} a square electric-field waveform of 10–150 kV $\cdot$ cm^{-1} of magnitude and a period of 200 s (i.e., 100 s on-field and 100 s off-field) was used. Such long on-field and off-field periods allow relaxation of the whole induced temperature change to the surroundings and thus its easier determination (Figure 1.3b).

The EC temperature change (ΔT_{EC}) values presented in this work are the measured maximum temperature changes multiplied by a correction factor (Eq. (1.8)) of 1.60–1.85, which accounts for the passive (non-electroded) part of the sample and also the thermal losses in the wires, thermistor, Au electrodes and glue that is used to mount the thermistor and wires to the sample. The details of the method can be found in Refs. [12, 13]. The used correction factors agree with the values typically obtained in bulk materials [12].

A.2 Correction Factor

The direct EC measurement set-up and the adequacy of the calculated correction factor obtained from Eq. (1.8) were tested by A. Bradeško et al. [120-122] on similarly sized $Pb(Mg_{1/3}Nb_{2/3})O_3$ ceramic pellets using infrared (IR) camera (Flir A6700sc, FLIR Systems, Inc., Wilsonville, Oregon, USA). Due to much better time resolution for detection of ΔT, IR camera were able to detect EC temperature change before the heat starts to leak to the passive parts of the sample assembly, resulting in determination of intrinsic EC effect of the sample. Comparison of ΔT obtained by the thermistor in modified DSC and ΔT_{EC} detected by IR camera (Figure A.1a) deviates for almost identical correction factor as the one calculated from the ratio of relevant thermal masses (Figure A.1b). The result confirms the correctness of determining the correction factor using the Eq. (1.8), which was further used to determine the correction factors of all the samples used in this thesis.

In addition, the size of the correction factor was also confirmed by numerical modeling (Figure A.1c)[121, 122], where temperature evolution in a few seconds after the adiabatic

application of electric field was simulated. Simulations showed that the measured ΔT of the thermistor is lower than the actual intrinsic EC effect of the material due to the much longer thermalization time of the thermistor (>0.5 s), which allows more time to transfer induced heat to passive parts of the sample assembly [121, 122]. The correction factor obtained from simulations agree well with the ones obtained by calculations and IR-camera measurements.

We note that the analysis described in paragraphs above is specific for the disc-shaped single layer (bulk) ceramic samples (identical as used in this thesis). Alteration of the geometry, materials and configuration of the EC sample (i.e., electrode placement, thickness and surface) would significantly alter the boundary conditions and thus possibly the thermalization process.

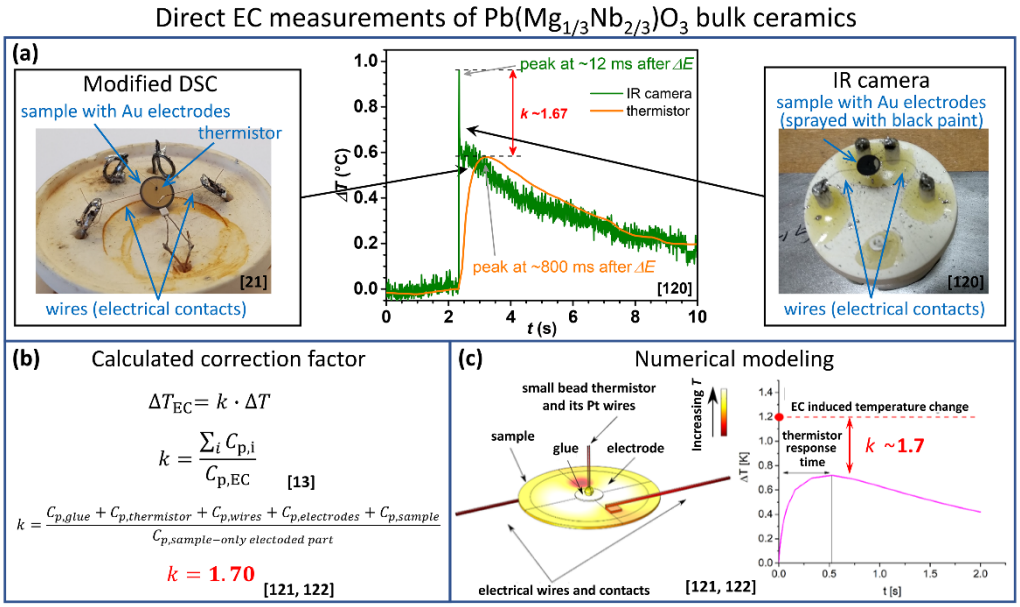


Figure A.1: Direct EC measurements of $Pb(Mg_{1/3}Nb_{2/3})O_3$ disk-shaped bulk ceramics. (a) Direct measurements of induced ΔT during the EC cycle using thermistor in modified DSC and IR camera [21, 120]. The ratio between both measured maximum ΔT values correspond to the correction factor of ~1.67. (b) Calculation of the correction factor according to the ratio of thermal masses of the whole sample assembly [13, 121, 122]. (c) Numerical modeling of the temperature evolution in a few seconds after step-like electric field was applied [121, 122].

A.3 Estimation of measurement uncertainty

The relative uncertainty of determined ΔT_{EC} (details of the method are described in Appendix A.1) is estimated to ~10% [122, 123]. The main reasons for this uncertainty are [122]:

- temperature gradient in the sample due to inhomogeneous heat distribution,
- inaccurate positioning of the thermistor on the sample surface,
- non-homogeneous electric field due to the off-centered position of the upper and lower electrodes,
- determination of the correction factor due to the uncertainty of heat capacity values of active and passive components (electrodes, glue, wires and thermistor) and
- heat transfer between the surface of the sample and the thermistor, which is conditioned by the amount of glue between them.

References

[1] M. Isaac and D. P. van Vuuren, "Modeling global residential sector energy demand for heating and air conditioning in the context of climate change," *Energy Policy*, vol. 37, no. 2, pp. 507–521, 2009.

[2] M. Ožbolt, A. Kitanovski, J. Tušek and A. Poredoš, "Electrocaloric vs. magnetocaloric energy conversion," *Int. J. Refrig.*, vol. 37, pp. 16–27, 2014.

[3] S. Crossley, N. D. Mathur and X. Moya, "New developments in caloric materials for cooling applications," *AIP Adv.*, vol. 5, no. 6, pp. 067153 1–8, 2015.

[4] S. Fahler, U. K. Rossler, O. Kastner, J. Eckert, G. Eggeler, H. Emmerich, P. Entel, S. Muller, E. Quandt and K. Albe, "Caloric Effects in Ferroic Materials: New Concepts for Cooling," *Adv. Eng. Mater.*, vol. 14, no. 8, pp. 10–19, 2012.

[5] I. Takeuchi and K. Sandeman, "Solid-state cooling with caloric materials," *Phys. Today*, vol. 68, no. 12, pp. 48–54, 2015.

[6] X. Moya, S. Kar-Narayan and N. D. Mathur, "Caloric materials near ferroic phase transitions," *Nature Mater.*, vol. 13, no. 5, pp. 439–450, 2014.

[7] L. Manosa, A. Planes and M. Acet, "Advanced materials for solid-state refrigeration," *J. Mater. Chem. A*, vol. 1, no. 16, pp. 4925–4936, 2013.

[8] S. Fahler and V. K. Pecharsky, "Caloric effect in ferroic materials," *MRS Bull.*, vol. 43, no. 4, pp. 264–268, 2018.

[9] M. M. Vopson, "The multicaloric effect in multiferroic materials," *Solid State Commun.*, vol. 152, no. 23, pp. 2067–2070, 2012.

[10] A. Planes, T. Castan and A. Saxena, "Thermodynamics of multicaloric effects in multiferroics," *Philos. Mag.*, vol. 94, no. 17, pp. 1893–1908, 2014.

[11] A. Barman, S. Kar-Narayan and D. Mukherjee, "Caloric Effects in Perovskite Oxides," *Adv. Mater. Interfaces*, vol. 6, no. 15, pp. 1900291 1–31, 2019.

[12] T. Correia and Q. Zhang, Eds., *Electrocaloric materials: New Generation of Coolers*, 1st ed., Berlin, Heidelberg, Germany: Springer-Verlag Berlin Heidelberg, 2014.

[13] Z. Kutnjak, B. Rožič and R. Pirc, *Electrocaloric Effect: Theory, Measuring, and Applications*, Wiley Encyclopedia of Electrical and Electronics Engineering, 2015.

[14] M. Valant, "Electrocaloric materials for future solid-state refrigeration technologies," *Prog. Mater. Sci.*, vol. 57, no. 6, pp. 980–1009, 2012.

[15] J. F. Scott, "Electrocaloric Materials," *Annu. Rev. Mater. Res.*, vol. 41, no. 1, pp. 229–240, 2011.

[16] M. Ožbolt, A. Kitanovski, J. Tušek and A. Poredoš, "Electrocaloric refrigeration: Thermodynamics, state of the art and future perspectives," *Int. J. Refrig.*, vol. 40, pp. 174–188, 2014.

[17] X. Li, S.-G. Lu, X.-Z. Chen, H. Gu, X.-S. Qian and Q. M. Zhang, "Pyroelectric and electrocaloric materials," *J. Mater. Chem. C*, vol. 1, no. 1, pp. 23–37, 2013.

[18] M. Valant, A.-K. Axelsson, F. L. Goupil and N. M. Alford, "Electrocaloric temperature change constrained by the dielectric strength," *Mater. Chem. Phys.*, vol. 136, no. 2-3, pp. 277–280, 2012.

[19] P. Kobeko and I. Kurtschatov, "Dielektrische Eigenshaften der Seignettesalzkristalle," *Z. Phys.*, vol. 66, pp. 192–205, 1930.

[20] Y. Liu, J. F. Scott and B. Dkhil, "Direct and indirect measurements on electrocaloric effect: Recent developments and perspectives," *Appl. Phys. Rev.*, vol. 3, no. 3, pp. 031102 1–18, 2016.

[21] Archive of the Electronic Ceramics Department, Jožef Stefan Institute, Ljubljana, Slovenia.

[22] V. K. Pecharsky and K. A. Gschneidner Jr., "Magnetocaloric effect and magnetic refrigeration," *J. Magn. Magn. Mater.*, vol. 200, no. 1-3, pp. 44–56, 1999.

[23] A. M. Tishin and Y. I. Spichkin, *The Magnetocaloric Effect and its Applications*, Institute of Physics Publishing, Bristol, UK, 2003.

[24] J. R. Gomez, R. F. Garcia, A. M. Catoira and M. R. Gomez, "Magnetocaloric effect: A review of the thermodynamic cycles in magnetic refrigeration," *Energy Rev.*, vol. 17, pp. 74–82, 2013.

[25] A. Kitanovski, J. Tušek, U. Tomc, U. Plaznik, M. Ožbolt and A. Poredoš, *Magnetocaloric Energy Conversion: From Theory to Applications*, Springer International Publishing, Switzerland, 2015.

[26] V. K. Pecharsky and K. A. Gschneidner, "Magnetocaloric effect from indirect measurements: Magnetization and heat capacity," *J. Appl. Phys.*, vol. 86, no. 1, pp. 565–575, 1999.

[27] V. K. Pecharsky, K. A. Gschneidner Jr., A. O. Pecharsky and A. M. Tishin, "Thermodynamics of the magnetocaloric effect," *Phys. Rev. B*, vol. 64, pp. 144406 1–13, 2001.

[28] K. A. Gschneidner Jr. and V. K. Pecharsky, "Magnetocaloric Materials," *Annu. Rev. Mater. Sci.*, vol. 30, pp. 387–429, 2000.

[29] V. Franco, J. S. Blazques, J. J. Ipus, J. Y. Law, L. M. Moreno-Ramirez and A. Conde, "Magnetocaloric effects: From materials research to refrigeration devices," *Prog. Mater. Sci.*, vol. 93, pp. 112–232, 2018.

[30] E. Stern-Taulats, T. Castan, L. Manosa, A. Planes, N. D. Mathur and X. Moya, "Multicaloric materials and effects," *MRS Bull.*, vol. 43, no. 4, pp. 295–299, 2018.

[31] J.-Z. Hao, F.-X. Hu, Z.-B. Yu, F.-R. Shen, H.-B. Zhou, Y.-H. Gao, K.-M. Qiao, J. Li, C. Zhang, W.-H. Liang, J. Wang, J. He, J.-R. Sun and B.-G. Shen, "Multicaloric and coupled-caloric effects," *Chin. Phys. B*, vol. 29, no. 4, pp. 047504 1–10, 2020.

[32] M. M. Vopson, "Theory of giant-caloric effect in multiferroic materials," *J. Phys. D: Appl. Phys.*, vol. 46, no. 34, pp. 345304 1–7, 2013.

[33] E. Defay, R. Faye, G. Despesse, H. Strozyk, D. Sette, S. Crossley, X. Moya and N. D. Mathur, "Enhanced electrocaloric efficiency via energy recovery," *Nat. Commun.*, vol. 9, no. 1, pp. 1827 1–9, 2018,

[34] N. A. Spaldin and M. Fiebig, "The Renaissance of Magnetoelectric Multiferroics," *Science*, vol. 309, no. 5733, pp. 391–392, 2005.

[35] M. Fiebig, "Revival of the magnetoelectric effect," *J. Phys. D: Appl. Phys.*, vol. 38, no. 8, pp. 123–152, 2005.

[36] M. M. Vopson, "Fundamentals of Multiferroic Materials and Their Possible Applications," *Crit. Rev. Solid State Mater. Sci.*, vol. 40, no. 4, pp. 223–250, 2015.

[37] M. M. Vopson, D. Zhou and G. Caruntu, "Multicaloric effect in bi-layer multiferroic composites," *Appl. Phys. Lett.*, vol. 107, no. 18, pp. 182905 1–4, 2015.

[38] J. K. Murthy and A. Venimadhav, "Multicaloric effect in multiferroic Y_2CoMnO_6," *J. Phys. D: Appl. Phys.*, vol. 47, no. 44, pp. 445002 1–6, 2014.

[39] G. Sharma, J. Saha, S. D. Kaushik, V. Siruguri and S. Patnaik, "Magnetism driven ferroelectricity above liquid nitrogen temperature in Y_2CoMnO_6," *Appl. Phys. Lett.*, vol. 103, no. 1, pp. 012903 1–4, 2013.

[40] K. Dey, A. Indra, A. Karmakar and S. Giri, "Multicaloric effect in multiferroic sulpho spinel $M Cr_2S_4$ (M = Fe & Co)," *J. Magn. Magn. Mater.*, vol. 498, pp. 166090 1–6, 2020.

[41] H. Ursic, V. Bobnar, B. Malic, C. Filipic, M. Vrabelj, S. Drnovsek, Y. Jo, M. Wencka and Z. Kutnjak, "A multicaloric material as a link between electrocaloric and magnetocaloric refrigeration," *Sci. Rep.*, vol. 6, pp. 26629 1–5, 2016.

[42] M. Quintero, P. Gaztanaga and I. Irurzun, "Intrinsic leakage and adsorption currents associated with the electrocaloric effect in multilayer capacitors," *Appl. Phys. Lett.*, vol. 107, no. 15, pp. 151901 1–4, 2015.

[43] A. Bradeško, A. Hedl, L. Fulanović, N. Novak and T. Rojac, "Self-heating of relaxor and ferroelectric ceramics during electrocaloric field cycling," *APL Mater.*, vol. 7, no. 7, pp. 071111 1–6, 2019.

[44] S.-G. Lu and Q. Zhang, "Electrocaloric Materials for Solid-State Refrigeration," *Adv. Mater.*, vol. 21, no. 19, pp. 1983–1987, 2009.

[45] B. Nair, T. Usui, S. Crossley, S. Kurdi, G. G. Guzman-Verri, X. Moya, S. Hirose and N. D. Mathur, "Large electrocaloric effects in oxide multilayer capacitors over a wide temperature range," *Nature*, vol. 575, no. 7783, pp. 468–472, 2019.

[46] M. E. Lines and A. M. Glass, *Principles and Applications of Ferroelectrics and Related Materials*, Clarendon Press, Oxford, UK, 1977.

[47] R. Waser, U. Böttger and S. Tiedke, Eds., *Polar Oxides: Properties, Characterization, and Imaging*, WILEY-VCH Verlag GmbH & Co. KGaA, Weinheim, Germany, 2005.

[48] D. Damjanovic, "Ferroelectric, dielectric and piezoelectric properties of ferroelectric thin films and ceramics," *Rep. Prog. Phys.*, vol. 61, no. 9, pp. 1267–1324, 1998.

[49] R. E. Newnham, *Properties of Materials: Anisotropy, Symmetry, Structure*, OUP Oxford, UK, 2005.

[50] D. Damjanovic, "Hysteresis in Piezoelectric and Ferroelectric Materials," in *The Science of Hysteresis*, vol. 3, I. Mayergoyz and G. Bertotti (Eds.), Elsevier, 2006.

[51] G. H. Heartling, "Ferroelectric Ceramics: History and Technology," *J. Am. Ceram. Soc.*, vol. 82, no. 4, pp. 797–818, 1999.

[52] E. Defay, S. Crossley, S. Kar-Narayan, X. Moya and N. D. Mathur, "The Electrocaloric Efficiency of Ceramic and Polymer Films," *Adv. Mater.*, vol. 25, no. 24, pp. 3337–3342, 2013.

[53] B. Rožič, M. Kosec, H. Uršič, J. Holc, B. Malič, Q. M. Zhang, R. Blinc, R. Pirc and Z. Kutnjak, "Influence of critical point on the electrocaloric response of relaxor ferroelectrics," *J. Appl. Phys.*, vol. 110, no. 6, pp. 064118 1–5, 2011.

[54] L. E. Cross, "Relaxor Ferroelectrics," *Ferroelectrics*, vol. 76, no. 1, pp. 241–267, 1987.

[55] D. Damjanovic and R. E. Newnham, "Electrostrictive and Piezoelectric Materials for Actuator Applications," *J. Intell. Mater. Syst. Struct.*, vol. 3, no. 2, pp. 190–208, 1992.

[56] T. Tsurumi, K. Soejima, T. Kamiya and M. Daimon, "Mechanism of Diffuse Phase Transition in Relaxor Ferroelectrics," *Jpn. J. Appl. Phys.*, vol. 33, no. 4A, pp. 1959–1964, 1994.

[57] A. A. Bokov and Z.-G. Ye, "Universal relaxor polarization in $Pb(Mg_{1/3}Nb_{2/3})O_3$ and related materials," *Phys. Rev. B*, vol. 66, no. 6, pp. 064103 1–9, 2002.

[58] A. A. Bokov and Z.-G. Ye, "Recent progress in relaxor ferroelectrics with perovskite structure," *J. Mater. Sci.*, vol. 41, no. 1, pp. 31–52, 2006.

[59] M. Eremenko, V. Krayzman, A. Bosak, H. Y. Playford, K. W. Chapman, J. C. Woicik, B. Ravel and I. Levin, "Local atomic order and hierarchical polar nanoregions in a classical relaxor ferroelectric," *Nature Commun.*, vol. 10, no. 1, pp. 2728 1–9, 2019.

[60] F. Li, S. Zhang, D. Damjanovic, L.-Q. Chen and T. R. Shrout, "Local Structural Heterogeneity and Electromechanical Responses of Ferroelectrics: Learning from Relaxor Ferroelectrics," *Adv. Funct. Mater.*, vol. 28, no. 37, pp. 1801504 1–21, 2018.

[61] G. Burns and F. H. Dacol, "Ferroelectrics with a glassy polarization phase," *Ferroelectrics*, vol. 104, pp. 25–35, 1990.

[62] H. Takenaka, I. Grinberg, S. Liu and A. M. Rappe, "Slush-like polar structures in single-crystal relaxors," *Nature*, vol. 546, no. 7658, pp. 391–395, 2017.

[63] M. J. Cabral, S. Zhang, E. C. Dickey and J. M. LeBeau, "Gradient chemical order in the relaxor $Pb(Mg_{1/3}Nb_{2/3})O_3$," *Appl. Phys. Lett.*, vol. 112, no. 8, pp. 082901 1–5, 2018.

[64] S. G. Lu, B. Rožič, Q. M. Zhang, Z. Kutnjak, X. Li, E. Furman, L. J. Gorny, M. Lin, B. Malič, M. Kosec, R. Blinc and R. Pirc, "Organic and inorganic relaxor ferroelectrics with giant electrocaloric effect," *Appl. Phys. Lett.*, vol. 97, no. 16, pp. 162904 1–3, 2010.

[65] R. Pirc, Z. Kutnjak, R. Blinc and Q. M. Zhang, "Electrocaloric effect in relaxor ferroelectrics," *J. Appl. Phys.*, vol. 110, no. 7, pp. 074113 1–7, 2011.

[66] B. Rožič, B. Malič, H. Uršič, J. Holc, M. Kosec and Z. Kutnjak, "Direct Measurements of the Electrocaloric Effect in Bulk $PbMg_{1/3}Nb_{2/3}O_3$ (PMN) Ceramics," *Ferroelectrics*, vol. 421, no. 1, pp. 103–107, 2011.

[67] M. Vrabelj, H. Uršič, Z. Kutnjak, B. Rožič, S. Drnovšek, A. Benčan, V. Bobnar, L. Fulanović and B. Malič, "Large electrocaloric effect in grain-size-engineered $0.9Pb(Mg_{1/3}Nb_{2/3})O_3$–$0.1PbTiO_3$," *J. Eur. Ceram. Soc.*, vol. 36, no. 1, pp. 75–80, 2016.

[68] U. Plaznik, M. Vrabelj, Z. Kutnjak, B. Malič, A. Poredoš and A. Kitanovski, "Electrocaloric cooling: The importance of electric-energy recovery and heat regeneration," *EPL*, vol. 112, no. 1, pp. 57009 1–6, 2015.

[69] V. K. Pecharsky and K. A. Gschneidner Jr., "Giant Magnetocaloric Effect in $Gd_5(Si_2Ge_2)$," *Phys. Rev. Lett.*, vol. 78, no. 23, pp. 4494–4497, 1997.

[70] V. K. Pecharsky and K. A. Gschneidner Jr., "Advanced magnetocaloric materials. What does the future hold?," *Int. J. Refrig.*, vol. 29, no. 8, pp. 1239–1249, 2006.

[71] J. Liu, T. Gottschall, K. P. Skokov, J. D. Moore and O. Gutfleisch, "Giant magnetocaloric effect driven by structural transitions," *Nature Mater.*, vol. 11, no. 7, pp. 620–626, 2012.

[72] S. Blundell, *Magnetism in Condensed Matter*, Oxford University Press, UK, 2001.

[73] W. D. Callister Jr., *Fundamentals of Materials Science and Engineering*, 5th Ed., John Wiley & Sons, Inc., New York, USA, 2001.

[74] N. A. Spaldin, *Magnetic Materials: Fundamentals and Applications*, 2nd Ed., Cambridge University Press, UK, 2010.

[75] M. E. McHenry and D. E. Laughlin, *Magnetic Properties of Metals and Alloys*, in Physical Metallurgy, 5th ed., D. E. Laughlin and K. Hono (Eds.), Elsevier, 2014.

[76] R. Nistico, F. Cesano and F. Garello, "Magnetic Materials and Systems: Domain Structure Visualization and Other Characterization Techniques for the Application in the Materials Science and Biomedicine," *Inorganics*, vol. 8, no. 1, pp. 1–59, 2020.

[77] W. Eerenstein, N. D. Mathur and J. F. Scott, "Multiferroic and magnetoelectric materials," *Nature*, vol. 442, no. 7104, pp. 759–765, 2006.

[78] D. Khomskii, "Classifying multiferroics: Mechanisms and effects," *Physics*, vol. 2, no. 20, pp. 1–8, 2009.

[79] M. Fiebig, T. Lottermoser, D. Meier and M. Trassin, "The evolution of multiferroics," *Nat. Rev. Mater.*, vol. 1, no. 8, pp. 16046 1–14, 2016.

[80] N. A. Spaldin and R. Ramesh, "Advances in magnetoelectric multiferroics," *Nature Mater.*, vol. 18, no. 3, pp. 203–212, 2019.

[81] N. A. Hill, "Why Are There so Few Magnetic Ferroelectrics?," *J. Phys. Chem. B*, vol. 104, no. 29, pp. 6694–6709, 2000.

[82] G. A. Smolenskii, A. I. Agranovskaia, S. N. Popov and V. A. Isupov, "New ferroelectrics of complex composition. Pb_2FeNbO_6 and Pb_2YbNbO_6," *Sov. Phys.-Tech. Phys.*, vol. 3, pp. 1981–1982, 1958.

[83] V. A. Bokov, I. E. Mylnikova and G. A. Smolenskii, "Ferroelectric Antiferromagnetics," *J. Exptl. Theoret. Phys.*, vol. 42, pp. 643–646, 1962.

[84] G. A. Smolenskii and V. A. Bokov, "Coexistence of Magnetic and Electric Ordering in Crystals," *J. Appl. Phys.*, vol. 35, no. 3, pp. 915–918, 1964.

[85] V. V. Laguta, J. Rosa, L. Jastrabik, R. Blinc, P. Cevc, B. Zalar, M. Remskar, S. I. Raevskaya and I. P. Raevski, "^{93}Nb NMR and Fe^{3+} EPR study of local magnetic properties of magnetoelectric $Pb(Fe_{1/2}Nb_{1/2})O_3$," *Mater. Res. Bull.*, vol. 45, no. 11, pp. 1720–1727, 2010.

[86] M. Yokosuka, "Electrical and Electromechanical Properties of Hot-Pressed $Pb(Fe_{1/2}Nb_{1/2})O_3$ Ferroelectric Ceramics," *Jpn. J. Appl. Phys.*, vol. 32, no. 3A, pp. 1142–1146, 1993.

[87] R. Font, O. Raymond-Herrera, L. Mestres, J. Portelles, J. Fuentes and J. M. Siqueiros, "Improvement of the dielectric and ferroelectric properties of multiferroic $Pb(Fe_{1/2}Nb_{1/2})O_3$ ceramics processed in oxygen atmosphere," *J. Mater. Sci.*, vol. 51, no. 13, pp. 6319–6330, 2016.

[88] H. Ursic, A. Bencan, U. Prah, M. Dragomir and B. Malic, "Structure and Dynamics of Ferroelectric Domains in Polycrystalline $Pb(Fe_{1/2}Nb_{1/2})O_3$," *Materials*, vol. 12, no. 8, pp. 1329 1–9, 2019.

[89] R. D. Shannon, "Revised Effective Ionic Radii and Systematic Studies of Interatomic Distances in Halides and Chalcogenides," *Acta Cryst. A*, vol. 32, no. 5, pp. 751–767, 1976.

[90] N. Lampis, P. Sciau and A. G. Lehmann, "Rietveld refinements of the paraelectric and ferroelectric structures of $PbFe_{0.5}Nb_{0.5}O_3$," *J. Phys.: Condens. Matter.*, vol. 11, no. 17, pp. 3489–3500, 1999.

[91] D. Bochenek and P. Guzdek, "Ferroelectric and magnetic properties of ferroelectromagnetic $PbFe_{1/2}Nb_{1/2}O_3$ type ceramics," *J. Magn. Magn. Mater.*, vol. 323, no. 3-4, pp. 369–374, 2011.

[92] S.-B. Lee, S.-H. Yoon and H. Kim, "Positive temperature coefficient of resistivity in $Pb(Fe_{1/2}Nb_{1/2})O_3$ ceramics," *J. Eur. Ceram. Soc.*, vol. 24, no. 8, pp. 2465–2470, 2004.

[93] H. Sim, D. C. Peets, S. Lee, S. Lee, T. Kamiyama, K. Ikeda, T. Otomo, S.-W. Cheong and J.-G. Park, "High-resolution structure studies and magnetoelectric coupling of relaxor multiferroic $Pb(Fe_{0.5}Nb_{0.5})O_3$," *Phys. Rev. B*, vol. 90, no. 21, pp. 214438 1–8, 2014.

[94] R. Mackeviciute, V. Goian, S. Greicius, R. Grigalaitis, D. Nuzhnyy, J. Holc, J. Banys and S. Kamba, "Lattice dynamics and broad-band dielectric properties of multiferroic $Pb(Fe_{1/2}Nb_{1/2})O_3$ ceramics," *J. Appl. Phys.*, vol. 117, no. 8, pp. 084101 1–6, 2015.

[95] S. Chillal, M. Thede, F. J. Litterst, S. N. Gvasaliya, T. A. Shaplygina, S. G. Lushnikov and A. Zheludev, "Microscopic coexistence of antiferromagnetic and spin-glass states," *Phys. Rev. B*, vol. 87, no. 21, pp. 220403 1–5, 2013.

[96] R. Blinc, V. V. Laguta, B. Zalar, B. Zupancic and M. Itoh, "^{17}O and ^{93}Nb NMR investigation of magnetoelectric effect in $Pb(Fe_{1/2}Nb_{1/2})O_3$," *J. Appl. Phys.*, vol. 104, no. 8, pp. 084105 1–4, 2008.

[97] K. Wojcik, K. Zieleniec and M. Milata, "Electrical Properties of Lead Iron Niobate PFN," *Ferroelectrics*, vol. 289, no. 1, pp. 107–120, 2003.

[98] V. L. Kozhevnikov, I. A. Leonidov, M. V. Patrakeev, E. B. Mitberg and K. R. Poeppelmeier, "Electrical Properties of the Ferrite $SrFeO_y$ at High Temperatures," *J. Solid State Chem.*, vol. 158, no. 2, pp. 320–326, 2000.

[99] E. T. Wefring, M.-A. Einarsrud and T. Grande, "Electrical conductivity and thermopower of $(1–x)BiFeO_3–xBi_{0.5}K_{0.5}TiO_3$ (x = 0.1, 0.2) ceramics near the ferroelectric to paraelectric phase transition," *Phys. Chem. Chem. Phys.*, vol. 17, no. 4, pp. 9420–9428, 2015.

[100] A. M. Kadomtseva, Y. F. Popov, A. P. Pyatakov, G. P. Vorobev, A. K. Zvezdin and D. Viehland, "Phase transitions in multiferroic $BiFeO_3$ crystals, thin-layers, and ceramics: enduring potential for a single phase, room-temperature magnetoelectric 'holy grail'," *Phase Transit.*, vol. 79, no. 12, pp. 1019–1042, 2006.

[101] G. Catalan and J. F. Scott, "Physics and Applications of Bismuth Ferrite," *Adv. Mater.*, vol. 21, no. 24, pp. 2463–2485, 2009.

[102] T. Rojac, A. Bencan, B. Malic, G. Tutuncu, J. L. Jones, J. E. Daniels and D. Damjanovic, "$BiFeO_3$ Ceramics: Processing, Electrical, and Electromechanical Properties," *J. Am. Ceram. Soc.*, vol. 97, no. 7, pp. 1993–2011, 2014.

[103] J. M. Moreau, C. Michel, R. Gerson and W. J. James, "Ferroelectric $BiFeO_3$ X-ray and Neutron Diffraction Study," *J. Phys. Chem. Solids*, vol. 32, no. 6, pp. 1315–1320, 1971.

[104] I. Sosnowska, T. Peterlin-Neumaier and E. Steichele, "Spiral magnetic ordering in bismuth ferrite," *J. Phys. C: Solid State Phys.*, vol. 15, no. 23, pp. 4835–4846, 1982.

[105] G. L. Yuan, S. W. Or, Y. P. Wang, Z. G. Liu and J. M. Liu, "Preparation and multi-properties of insulated single-phase $BiFeO_3$ ceramics," *Solid State Commun.*, vol. 138, no. 2, pp. 76–81, 2006.

[106] T. Rojac, M. Kosec, B. Budic, N. Setter and D. Damjanovic, "Strong ferroelectric domain-wall pinning in $BiFeO_3$ ceramics," *J. Appl. Phys.*, vol. 108, no. 7, pp. 074107 1–8, 2010.

[107] M. Valant, A.-K. Axelsson and N. Alford, "Peculiarities of a Solid-State Synthesis of Multiferroic Polycrystalline $BiFeO_3$," *Chem. Mater.*, vol. 19, no. 22, pp. 5431–5436, 2007.

[108] A. Lubk, S. Gemming and N. A. Spaldin, "First-principles study of ferroelectric domain walls in multiferroic bismuth ferrite," *Phys. Rev. B*, vol. 80, no. 10, pp. 104110 1–8, 2009.

[109] T. Rojac, A. Bencan, G. Drazic, N. Sakamoto, H. Ursic, B. Jancar, G. Tavcar, M. Makarovic, J. Walker, B. Malic and D. Damjanovic, "Domain-wall conduction in ferroelectric $BiFeO_3$ controlled by accumulation of charged defects," *Nature Mater.*, vol. 16, no. 3, pp. 322–327, 2017.

[110] M. Makarovic, N. Kanas, A. Zorko, K. Ziberna, H. Ursic, D. R. Smabraten, S. M. Selbach and T. Rojac, "Tailoring the electrical conductivity and hardening in $BiFeO_3$ ceramics," *J. Eur. Ceram. Soc.*, vol. 40, no. 15, pp. 5483–5493, 2020.

[111] C. F. Buhrer, "Some Properties of Bismuth Perovskites," *J. Chem. Phys.*, vol. 36, no. 3, pp. 798–803, 1962.

[112] G. A. Smolenskii and V. M. Yudin, "Weak ferromagnetism of some $BiFeO_3$–$Pb(Fe_{0.5}Nb_{0.5})O_3$ perovskites," *Phys. Solid State*, vol. 6, no. 12, pp. 2936–2942, 1965.

[113] N. N. Krainik, N. P. Khuchua, A. A. Berezhnoi and A. G. Tutov, "Nature of phase transformations in solid solutions of $BiFeO_3$ with $PbFe_{1/2}Nb_{1/2}O_3$," *Phys. Solid State*, vol. 7, no. 1, pp. 100–107, 1965.

[114] V. V. Zhdanova, "Dilatometric study of solid solutions in the system $BiFeO_3$–$PbFe_{1/2}Nb_{1/2}O_3$," *Phys. Solid State*, vol. 7, no. 1, pp. 108–111, 1965.

[115] I. O. Troyanchuk, M. V. Bushinsky, A. N. Chobot, O. S. Mantytskaya, N. V. Pushkarev and R. Szymczak, "Crystal-Structure and Magnetic Phase Transformations in Solid Solutions of $BiFeO_3$–$AFe_{0.5}Nb_{0.5}O_3$ (A = Ca, Sr, Ba, Pb)," *J. Exp. Theor. Phys.*, vol. 107, no. 2, pp. 245–250, 2008.

[116] D. Bochenek, R. Zachariasz, J. Ilczuk and J. Dudek, "Ferroelectromagnetic Smart Structures $(1–x)Pb(Fe_{0.5}Nb_{0.5})O_3$–$(x)BiFeO_3$," *Acta Phys. Pol. A*, vol. 116, no. 3, pp. 274–276, 2009.

[117] J. P. Patel, A. Senyshyn, H. Fuess and D. Pandey, "Evidence for weak ferromagnetism, isostructural phase transition, and linear magnetoelectric coupling in the multiferroic $Bi_{0.8}Pb_{0.2}Fe_{0.9}Nb_{0.1}O_3$ solid solution," *Phys. Rev. B*, vol. 88, no. 10, pp. 104108 1–9, 2013.

[118] L. A. Shilkina, A. V. Pavlenko, L. A. Reznitchenko and I. A. Verbenko, "Phase Diagram of the System $(1–x)BiFeO_3$–$xPbFe_{0.5}Nb_{0.5}O_3$ Solid Solutions at Room Temperature," *Crystallogr. Rep.*, vol. 61, no. 2, pp. 263–269, 2016.

[119] D. Bochenek, P. Niemiec, P. Guzdek and M. Wzorek, "Magnetoelectric and electric measurements of the $(1–x)BiFeO_3$–$(x)Pb(Fe_{1/2}Nb_{1/2})O_3$ solid solutions," *Mater. Chem. Phys.*, vol. 195, pp. 199–206, 2017.

[120] Curtesy of A. Bradeško and Electronic Ceramics Department, Jožef Stefan Institute, Ljubljana, Slovenia (unpublished work).

[121] A. Bradeško, L. Fulanović, M. Vrabelj, M. Otoničar, H. Uršič, A. Henriques, C.-C. Chung, J. L. Jones, B. Malič, Z. Kutnjak and T. Rojac, "Electrocaloric fatigue of lead magnesium niobate mediated by an electric-field-induced phase transformation," *Acta Mater.*, vol. 169, pp. 275–283, 2019.

[122] A. Bradeško, "Coupling of Electrocaloric and Electromechanical Response in Relaxor Ferroelectrics for Dielectric Cooling," PhD thesis, Jožef Stefan International Postgraduate School, 2019.

[123] C. Molin, J. Peräntie, F. L. Goupil, F. Weyland, M. Sanlialp, N. Stingelin, N. Novak, D. C. Lupascu and S. Gebhardt, "Comparison of direct electrocaloric characterization methods exemplified by $0.92Pb(Mg_{1/3}Nb_{2/3})O_3$-$0.08PbTiO_3$ multilayer ceramics," *J. Am. Ceram. Soc.*, vol. 100, no. 7, pp. 2885–2892, 2017.

Bibliography

Scientific Articles Related to the Thesis

U. Prah, M. Wencka, Z. Kutnjak, M. Vrabelj, S. Drnovšek, B. Malič and H. Uršič, "Multicaloric effect in polycrystalline $Pb(Fe_{0.5}Nb_{0.5})O_3$," *Informacije MIDEM,* vol. 47, no. 3, pp. 159–170, 2017.

H. Uršič, A. Benčan, U. Prah, M. Dragomir and B. Malič, "Structure and Dynamics of Ferroelectric Domains in Polycrystalline $Pb(Fe_{0.5}Nb_{0.5})O_3$," *Materials*, vol. 12, no. 8, pp. 1327 1–9, 2019.

U. Prah, T. Rojac, M. Wencka, M. Dragomir, A. Bradeško, A. Benčan, R. Sherbondy, G. Brennecka, Z. Kutnjak, B. Malič and H. Uršič, "Impoving the multicaloric properties of $Pb(Fe_{0.5}Nb_{0.5})O_3$ by controlling the sintering conditions and doping with manganese," *J. Eur. Ceram. Soc.*, vol. 39, no. 14, pp. 4122–4130, 2019.

U. Prah, M. Dragomir, T. Rojac, A. Benčan, R. Broughton, C.-C. Chung, J. L. Jones, R. Sherbondy, G. Brennecka ands H. Uršič, "Strengthened relaxor behavior in (1-x)$Pb(Fe_{0.5}Nb_{0.5})O_3$–$x$$BiFeO_3$," *J. Mater. Chem. C*, vol. 8, no. 10, pp. 3452–3462, 2020.

U. Prah, M. Wencka, T. Rojac, A. Benčan and H. Uršič, "$Pb(Fe_{0.5}Nb_{0.5})O_3$–$BiFeO_3$-based multicalorics with room-temperature ferroic anomalies," *J. Mater. Chem. C*, vol. 8, no. 32, pp. 11282–11291, 2020.

Other Scientific Articles

K. Radan, B. Kmet, S. Drnovšek, U. Prah, T. Rojac and B. Malič, "Mechanochemically-Assisted Synthesis of Lead-Free Piezoelectric $CaZrO_3$-Modified (K,Na,Li)(Nb,Ta)O_3-Solid Solution," *Ceramics,* vol. 1, no. 2, pp. 304–319, 2018.

M. Šadl, U. Tomc, U. Prah and H. Uršič, "Protective Alumina Coatings Prepared by Aerosol Deposition on Magnetocaloric Gadolinium Elements," *Informacije MIDEM,* vol. 49, no. 3, pp. 177–182, 2019.

O. A. Condurache, K. Radan, U. Prah, M. Otoničar, B. Kmet, G. Kapun, G. Dražič, B. Malič and A. Benčan, "Heterogeneity Challenges in Multiple-Element-Modified Lead-Free Piezoelectric Ceramics," *Materials,* vol. 12, no. 24, pp. 4049 1–12, 2019.

J. Walker, A. Mirjanić, U. Prah, M. Šadl, O. A. Condurache, A. Benčan, T. Rojac, M. Grigoras and H. Uršič, "Magnetic contributions in multiferroic gadolinium modified bismuth ferrite ceramics," *Scr. Mater.,* vol. 188, pp. 233–237, 2020.

Review Articles

H. Uršič and U. Prah, "Investigations of ferroelectric polycrystalline bulks and thick films using piezoresponse force microscopy," *Proc. R. Soc. A,* vol. 475, no. 2223, pp. 20180782 1–25, 2019.

Published Scientific Conference Contributions

N. Bartek, V. Shvartsman, D. C. Lupacsu, U. Prah and H. Uršič, "Influence of synthesis route on the properties of lead iron niobate," in *2019 IEEE International Symposium on Applications of Ferroelectrics (ISAF) proceedings*, Lausanne, Switzerland: Institute of Electrical and Electronics engineers, 2019.

Published Scientific Conference Contributions – Abstracts (Invited Lecture)

H. Uršič, T. Rojac, A. Benčan, J. Walker, E. Khomyakova, U. Prah, K. Vojisavljević, M. Vrabelj, S. Drnovšek and B. Malič, "Domain structure in ferroelectrics determined by piezo-response force microscopy," in *2. slovensko posvetovanje mikroskopistov*, Piran, Slovenia: Slovensko društvo za mikroskopijo, 2017.

H. Uršič, T. Rojac, M. Šadl, U. Eckstein, N. H. Khansur, K. G. Webber, U. Prah and B. Malič, "$Pb(Mg_{1/3}Nb_{2/3})O_3$–$PbTiO_3$ thick films prepared by aerosol deposition onto metal and polymer substrates," in *IEEE IFCS 2020 ISAF 2020 Virtual Conference*, Keystone, Colorado, USA: joint Conference of the IEEE International Symposium on Applications of Ferroelectrics, 2020.

Published Scientific Conference Contributions – Abstracts

U. Prah, M. Wencka, Z. Kutnjak, M. Vrabelj, S. Drnovšek, B. Malič and H. Uršič, "The coexistence of electrocaloric and magnatocaloric effects in $Pb(Fe_{1/2}Nb_{1/2})O_3$ ceramics," in *9th Jožef Stefan International Postgraduate School Students' Conference and 11th Young Researchers's Day*, Ljubljana, Slovenia: Jožef Stefan International Postgraduate School, Jožef Stefan Institute, 2017.

U. Prah, M. Wencka, Z. Kutnjak, M. Vrabelj, S. Drnovšek, B. Malič and H. Uršič, "Multicaloric effect in $Pb(Fe_{1/2}Nb_{1/2})O_3$ ceramics," in *15th Conference of the European Ceramic Socienty, ECerS 2017*, Budapest, Hungary: Akadémiai Kiadó, 2017.

U. Prah, M. Wencka, Z. Kutnjak, M. Vrabelj, S. Drnovšek, B. Malič and H. Uršič, "Multicaloric effect in polycrystalline $Pb(Fe_{0.5}Nb_{0.5})O_3$," in *53rd International Conference on Microelectronics, Devices and Materials and the Workshop on Materials for Energy Conversion and their Applications: Electrocalorics and Thermoelectrics*, Ljubljana, Slovenia: MIDEM – Society for Microelectronics, Electronic Components and Materials, 2017.

H. Uršič, U. Prah, M. Wencka, Z. Kutnjak, and B. Malič, "$Pb(Fe_{0.5}Nb_{0.5})O_3$-based multicaloric materials as a link between electrocaloric and magnetocaloric refrigeration," in *2018 ISAF-FMA-AMF-AMEC-PFM. International Symposium on Applications of Ferroelectrics (ISAF), Meeting on Ferroelectric Materials and Their Applications (FMA), The Asian Meeting on Ferroelectricity (AMF), 11th Asian Meeting on Electroceramics (AMEC), Piezoresponse Force Microscopy (PFM)*, Hiroshima, Japan: Institute of Electrical and Electronics Engineers (IEEE), 2018.

U. Prah, M. Wencka, T. Rojac, M. Vrabelj, Z. Kutnjak, B. Malič and H. Uršič, "Multicaloric properties of Mn and Li-doped $Pb(Fe_{0.5}Nb_{0.5})O_3$ ceramics," in *Thermag VIII, International Conference on Caloric Cooling*, Darmstadt, Germany: Technische Universität, 2018.

U. Prah, M. Wencka, T. Rojac, A. Bradeško, Z. Kutnjak, B. Malič and H. Uršič, "Multicaloric properties of $Pb(Fe_{0.5}Nb_{0.5})O_3$-based ceramics," in *54th International Conference on Microelectronics, Devices and Materials and the Workshop on Sensors*

and Transducers, Ljubljana, Slovenia: MIDEM – Society for Microelectronics, Electronic Components and Materials, 2018.

R. Sherbondy, U. Prah, H. Uršič, G. Brennecka, T. Rojac and B. Malič, "Sintering and dielectric study of the pseudobinary $Pb(Fe_{0.5}Nb_{0.5})O_3$–$BiFeO_3$ system," in *2019 Conference on Electronic Materials and Applications, EMA 2019*, Orlando, Florida: The American Ceramic Society, 2019.

K. Radan, B. Kmet, S. Drnovšek, T. Rojac, B. Malič, U. Prah, O. Condurache and A. Benčan, "Compositional inhomogeneity in Mn-doped (K,Na,Li)(Nb,Ta)O_3–$CaZrO_3$ lead-free piezoceramics," in *Piezo 2019: Electroceramics for End-Users X*, Špindlerův Mlýn, Czech Republic, 2019.

M. Šadl, U. Eckstein, N. H. Khansur, K. G. Webber, U. Prah, B. Malič and H. Uršič, "Aerosol deposition of relaxor-ferroelectric $0.9Pb(Mg_{1/3}Nb_{2/3})O_3$–$0.1PbTiO_3$ thick films onto low-cost metal substrates," in *11th Jožef Stefan International Postgraduate School Students' Conference and 13th Young Researchers's Day*, Planica, Slovenia: Jožef Stefan International Postgraduate School, Jožef Stefan Institute, 2019.

O. Condurache, K. Radan, B. Kmet, G. Dražić, U. Prah, B. Malič and A. Benčan, "Multiscale investigation of the role of manganese oxide addition in lead-free sodium potasium niobate based piezoelectrics," in *3. slovensko posvetovanje mikroskopistov*, Ankaran, Slovenia: Slovensko društvo za mikroskopijo, 2019.

U. Prah, T. Rojac, M. Wencka, R. Sherbondy, G. Brennecka, B. Malič and H. Uršič, "Multicaloric properties of $(1\text{-}x)Pb(Fe_{0.5}Nb_{0.5})O_3$–$xBiFeO_3$ solid solutions," in *XVI. Conference of the European Ceramic Socienty, ECerS 2019*, Torino, Italy: Akadémiai Kiadó, 2019.

O. Condurache, K. Radan, M. Otoničar, B. Kmet, G. Dražič, U. Prah, G. Kapun, B. Malič and A. Benčan, "Micro-, nano- and atomic structure investigation of alkaline niobate based solid solutions," in *XVI. Conference of the European Ceramic Socienty, ECerS 2019*, Torino, Italy: Akadémiai Kiadó, 2019.

U. Prah, T. Rojac, M. Wencka, R. Sherbondy, G. Brennecka, B. Malič and H. Uršič, "Toward efficient multicalorics; electrocaloric and magnetocaloric properties of $(1\text{-}x)Pb(Fe_{0.5}Nb_{0.5})O_3$–$xBiFeO_3$," in *Joint ISAF-ICE-EMF-IWPM-PFM meeting, 2019 IEEE International Symposium on Applications of Ferroelectrics (ISAF)*, Lausanne, Switzerland: IEEE Advancing Technology for Humanity, École Polytechnique Fédérale de Lausanne, 2019.

H. Uršič, U. Prah, T. Rojac, A. Benčan, R. Sherbondy, G. Brennecka and B. Malič, "Ferroelectric domain structure in polycrystalline $(1\text{-}x)Pb(Fe_{0.5}Nb_{0.5})O_3$–$xBiFeO_3$ investigated by piezoresponse force microscopy," in *Joint ISAF-ICE-EMF-IWPM-PFM meeting, 2019 IEEE International Symposium on Applications of Ferroelectrics (ISAF)*, Lausanne, Switzerland: IEEE Advancing Technology for Humanity, École Polytechnique Fédérale de Lausanne, 2019.

M. Šadl, U. Eckstein, N. H. Khansur, K. G. Webber, U. Prah, B. Malič and H. Uršič, "$0.9Pb(Mg_{1/3}Nb_{2/3})O_3$–$0.1PbTiO_3$ thick films prepared by aerosol deposition onto low-cost metal substrates," in *Joint ISAF-ICE-EMF-IWPM-PFM meeting, 2019 IEEE International Symposium on Applications of Ferroelectrics (ISAF)*, Lausanne, Switzerland: IEEE Advancing Technology for Humanity, École Polytechnique Fédérale de Lausanne, 2019.

U. Prah, T. Rojac, M. Wencka, M. Dragomir, A. Benčan, R. Sherbondy, G. Brennecka and H. Uršič, "Multicaloric properties of $(1\text{-}x)Pb(Fe_{0.5}Nb_{0.5})O_3$–$xBiFeO_3$ ceramic materials," in *E-MRS 2019 Fall Meeting*, Warsaw, Poland: Faculty of Materials Science and Engineering, 2019.

H. Uršič, A. Jazbec, L. Snoj, U. Prah, A. Bradeško, T. Rojac, S. Drnovšek, M. Vrabelj and B. Malič, "Influence of neutron and gamma irradiation on the electrocaloric properties of (1-x)Pb($Mg_{1/3}Nb_{2/3}$)O_3–$x$$PbTiO_3$ ceramic," in *E-MRS 2019 Fall Meeting*, Warsaw, Poland: Faculty of Materials Science and Engineering, 2019.

M. Šadl, U. Tomc, U. Prah, A. Bradeško, B. Malič, U. Eckstein, N. H. Khansur, K. G. Webber and H. Uršič, "Using the aerosol deposition method in the preparation of caloric-cooling elements," in *E-MRS 2019 Fall Meeting*, Warsaw, Poland: Faculty of Materials Science and Engineering, 2019.

U. Prah, T. Rojac, M. Wencka, M. Dragomir, A. Benčan, R. Sherbondy, G. Brennecka and H. Uršič, "Multicaloric properties of (1-x)Pb($Fe_{0.5}Nb_{0.5}$)O_3–$x$$BiFeO_3$ ceramic," in *55th International Conference on Microelectronics, Devices and Materials with the Workshop on Laser Systems and Photonics*, Bled, Slovenia: MIDEM – Society for Microelectronics, Electronic Components and Materials, 2019.

M. Šadl, U. Eckstein, N. H. Khansur, K. G. Webber, U. Prah, A. Bradeško, B. Malič and H. Uršič, "Pb($Mg_{1/3}Nb_{2/3}$)O_3–$PbTiO_3$ thick films prepared by aerosol deposition onto low-cost substrates," in *55th International Conference on Microelectronics, Devices and Materials with the Workshop on Laser Systems and Photonics*, Bled, Slovenia: MIDEM – Society for Microelectronics, Electronic Components and Materials, 2019.

K. Radan, B. Kmet, S. Drnovšek, U. Prah, T. Rojac and B. Malič, "Structural transformations during mechanochemically-assisted synthesis of potassium sodium niobate-based piezoceramics," in *25th Annual Meeting of the Slovenian Chemical Society*, Maribor, Slovenia: Slovensko kemijsko društvo, 2019.

B. Malič, H. Uršič, L. Fulanović, V. Bobnar, S. Drnovšek, U. Prah, A. Bradeško, T. Rojac, A. Jazbec and L. Snoj, "Ferroic perovskite oxides for caloric cooling applications," in *13th Pacific Rim Conference of Ceramic Society (PACRIM13)*, Okinawa, Japan: American Ceramic Society, 2019.

A. Mirjanić, U. Prah, M. Šadl, J. Walker, O. Condurache, A. Benčan, T. Rojac, M. Grigoras and H. Uršič, "Local piezoelectric and magnetic properties of ($Bi_{0.88}Gd_{0.12}$)FeO_3 ceramics," in *12th Jožef Stefan International Postgraduate School Students' Conference and 14th Young Researchers's Day*, Virtual Conference: Jožef Stefan International Postgraduate School, Jožef Stefan Institute, 2020.

U. Prah, M. Dragomir, T. Rojac, A. Benčan, R. Broughton, C.-C. Chung, J. L. Jones, R. Sherbondy, G. Brennecka and H. Uršič, "Strengthened relaxor behavior in (1-x)Pb($Fe_{0.5}Nb_{0.5}$)O_3–$x$$BiFeO_3$ solid solutions," in *IEEE IFCS 2020 ISAF 2020 Virtual Conference*, Keystone, Colorado, USA: joint Conference of the IEEE International Symposium on Applications of Ferroelectrics, 2020.

K. Radan, V. K. Vignaswaran, U. Prah, O. Condurache, M. Dragomir, T. Gindel, M. Deluca and B. Malič, "Structure and Temperature Induced Phase Transitions in Lead-Free Li- and Ta- modified alkaline niobate bases piezoceramics probed by raman spectroscopy," in *IEEE IFCS 2020 ISAF 2020 Virtual Conference*, Keystone, Colorado, USA: joint Conference of the IEEE International Symposium on Applications of Ferroelectrics, 2020.

A. Dubey, D. Lewin, U. Prah, M. Šadl, M. Escobar Castillo, H. Uršič, T. Rojac, V. Shvartsman and D. C. Lupascu, "Ferroelectric properties of Ba and Mn doped bismuth ferrite bulk and nanoparticles," in *IEEE IFCS 2020 ISAF 2020 Virtual Conference*, Keystone, Colorado, USA: joint Conference of the IEEE International Symposium on Applications of Ferroelectrics, 2020.

M. Šadl, U. Eckstein, N. H. Khansur, K. G. Webber, U. Prah, B. Malič and H. Uršič, "PMN-PT thick films on low-cost and flexible materials realized by aerosol deposition

method," in *Electroceramics 2020 Virtual Conference*, Darmstadt, Germany: Technische Universität, 2020.

K. Radan, V. K. Vignaswaran, U. Prah, O. Condurache, M. Dragomir, T. Gindel, M. Deluca and B. Malič, "Influence of MnO_2 addition on structural phase transitions and electrical properties of lead-free Li- and Ta-modified alkaline niobate based piezoceramics," in *Electroceramics 2020 Virtual Conference*, Darmstadt, Germany: Technische Universität, 2020.

O. Condurache, K. Radan, U. Prah, M. Otoničar, B. Kmet, G. Dražić, B. Malič and A. Benčan, "Electron microscopy study of lead-free piezoelectrics at different length scales," in *Electroceramics 2020 Virtual Conference*, Darmstadt, Germany: Technische Universität, 2020.

U. Prah, T. Rojac, M. Wencka, A. Benčan and H. Uršič, "Multicaloric properties of $0.8Pb(Fe_{0.5}Nb_{0.5})O_3$–$0.2BiFeO_3$-based ceramics," in *26th Annual Meeting of the Slovenian Chemical Society*, Portorož, Slovenia: Slovensko kemijsko društvo, 2020.

K. Radan, V. K. Vignaswaran, U. Prah, O. Condurache, M. Dragomir, T. Gindel, M. Deluca and B. Malič, "Structural Phase Transitions in Multiple-Element-Modified Lead-Free Piezoelectric Ceramics," in *26th Annual Meeting of the Slovenian Chemical Society*, Portorož, Slovenia: Slovensko kemijsko društvo, 2020.

Unpublished Scientific Conference Contributions (Invited Lecture)

H. Uršič, U. Prah, L. Fulanović, M. Vrabelj, A. Bradeško, T. Rojac, B. Rožič, Z. Kutnjak, M. Wencka, A. Kitanovski and B. Malič, "Electrocaloric and multicaloric materials for future cooling applications," in *Workshop on Green-process Research*, Hokaido, Japan: The Society of Powder Technology of Japan, 2018.

Unpublished Scientific Conference Contributions

H. Uršič, M. Šadl, O. Condurache, A. Benčan, M. Dragomir, U. Eckstein, N. H. Khansur, K. G. Webber, M. Deluca, U. Prah and B. Malič, "Aerosol-deposited $Pb(Mg_{1/3}Nb_{2/3})O_3$–$PbTiO_3$ films on metal and polymer substrates," in *Workshop Recent Advances in Nanoscience and It's Applications*, Zoom Seminar, 2020.

Invited Lecture at Foreign Universities

U. Prah, M. Wencka, Z. Kutnjak, M. Vrabelj, S. Drnovšek, B. Malič and H. Uršič, "The coexistence of electrocaloric and magnetocaloric effect in polycrystalline $Pb(Fe_{0.5}Nb_{0.5})O_3$," Poznań, Poland: Institute of Molecular Physics, Polish Academy of Sciences, 2017.

U. Prah, "Multicaloric properties of Mn-doped $Pb(Fe_{0.5}Nb_{0.5})O_3$ ceramics," Poznań, Poland: Institute of Molecular Physics, Polish Academy of Sciences, 2018.

U. Prah, "Ferroelectric-relaxor crossover in $(1\text{-}x)Pb(Fe_{0.5}Nb_{0.5})O_3$–$x BiFeO_3$ solid solutions," Poznań, Poland: Institute of Molecular Physics, Polish Academy of Sciences, 2019.

O. Condurache, H. Uršič, M. Šadl, K. Radan, U. Prah, M. Otoničar, B. Kmet, G. Dražić, B. Malič and A. Benčan, "Studies of different ceramic systems by means of electron microscopy techniques," Iasi, Romania: Laboratory for Dielectrics, Ferroelectrics and Multiferroics, Faculty of Physics, University "A.I. Cuza", 2019.

Biography

The author of this thesis was born on the 7th of May 1992 in Ljubljana, Slovenia. He received his BSc degree in 2014 at the Department of Inorganic Chemistry at the Faculty of Chemistry and Chemical Technology from the University of Ljubljana, Slovenia. During his undergraduate studies he participated in a project called *The preparation of high-temperature TiO_2 catalyst*, co-funded by the Slovenian Ministry of Education, Science and Sport, and the European Union. In 2016 he finished his MSc studies with a thesis entitled "The doping influence on characteristics of titanium dioxide powders and thin films" at the Department of Inorganic Chemistry at the Faculty of Chemistry and Chemical Technology from the University of Ljubljana, Slovenia. During that time, he was working as a student (lab work) at the Advanced Materials Department at Jožef Stefan Institute, Ljubljana.

Since October 2016 he has been employed at the Electronic Ceramics Department, Jožef Stefan Institute, Ljubljana. At the same time, he enrolled in a PhD study, program Sensor Technologies, at the Jožef Stefan International Postgraduate School under supervision of Asst. Prof. Dr. Hana Uršič Nemevšek and Assoc. Prof. Dr. Tadej Rojac. His research interests are the processing and characterization of functional ceramics, mainly $Pb(Fe_{0.5}Nb_{0.5})O_3$-based and $BiFeO_3$-based multiferroics. His particular interest was an investigation of how the structural, microstructural, ferroelectric and magnetic characteristics influence the functional properties, i.e., electrocaloric and magnetocaloric effects for solid-state cooling applications.